



Swansea University
Prifysgol Abertawe

OPTIMISATION OF NEXT GENERATION GALVANISING POT HARDWARE

Giovanni Paolo Alparone

Thesis submitted to Swansea University in fulfilment of the
requirements for the Degree of Doctor of Philosophy

Swansea University, November 2024

TATA STEEL



**Engineering and
Physical Sciences
Research Council**



Copyright: The author, Giovanni Paolo Alparone, 2024

Distributed under the terms of a Creative Commons Attribution 4.0 License (CC BY 4.0).

Abstract

The aim of this research is to study the corrosion behaviour and tribological properties of ceramics for use as roll bearing materials in the zinc bath of continuous galvanising lines.

Bulk ceramic materials were investigated, including hexagonal BN, BN Grade M26, Macor[®], AlN-BN, Y₂O₃-ZrO₂, Si₃N₄ and Al₂O₃, and their performance was compared to stainless steel 316L and WC-Co coatings. Microscopic examination after static testing in Zn-Al and Zn-Al-Mg found that Zn and Al diffusion occurred in stainless steel, and the thickness of WC-Co coatings was reduced from 150 to around 90 µm. Bulk ceramics, however, were observed to not react with the molten bath. Pin-on-disc testing was conducted on the ceramics and hexagonal BN displayed the lowest coefficient of friction (< 0.1).

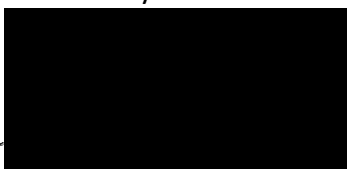
SiAlON, hexagonal and cubic BN ceramic composites were produced with Field Assisted Sintering Technology by varying the content of BN. Additions of hexagonal BN lubricant did not drastically improve the tribological properties, although static corrosion tests confirmed the corrosion resistance of the ceramic composites to molten Zn-Al and Zn-Al-Mg. Static testing was also conducted on Al₂O₃ coatings; however, the coatings were prone to damage caused by the large thermal expansion mismatch of $13 \times 10^{-6} \text{ K}^{-1}$ with steel and interactions with the Zn-Al-Mg bath occurred.

A bespoke rig enabled dynamic testing of two potential bearing system upgrades. The first upgrade involved replacing Wallex6TM with Wallex4TM and the second upgrade replaced WC-Co with Al₂O₃ coatings. All the WallexTM grades were similarly corroded, although the diffusion of Zn into the WallexTM alloys was reduced by approximately 60% in the Zn-Al-Mg bath compared to Zn-Al. The wear coefficient k determined that minimal wear damage in both Zn-Al ($k = 9.7 \times 10^{-6} \text{ K}^{-1} \text{ mm}^3 \text{ N}^{-1} \text{ m}^{-1}$) and Zn-Al-Mg ($k = 3.6 \times 10^{-6} \text{ mm}^3 \text{ N}^{-1} \text{ m}^{-1}$) was obtained when coupling Al₂O₃ coatings with Wallex6TM.

Declaration

This work has not previously been accepted in substance for any degree and is not being concurrently submitted in candidature for any degree.

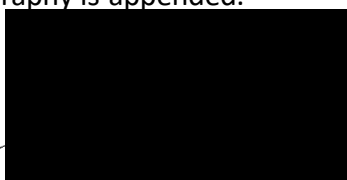
Signed



Date.....21/11/2024.....

This thesis is the result of my own investigations, except where otherwise stated. Other sources are acknowledged by footnotes giving explicit references. A bibliography is appended.

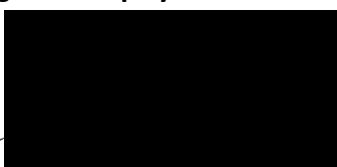
Signed



Date.....21/11/2024.....

I hereby give consent for my thesis, if accepted, to be available for electronic sharing **after expiry of a bar on access approved by the Swansea University.**

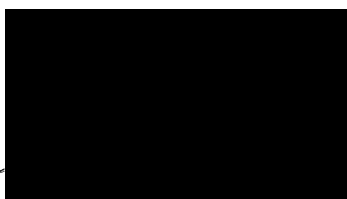
Signed



Date.....21/11/2024.....

The University's ethical procedures have been followed and, where appropriate, that ethical approval has been granted.

Signed



Date.....21/11/2024.....

Contents

Abstract	2
Declaration	3
Contents	4
Acknowledgments	7
List of Tables.....	8
List of Figures	10
Abbreviations	17
Chapter 1 Introduction.....	18
1.1 Scope of Research	18
1.2 Layout of Thesis.....	19
1.3 Galvanised Steel	20
1.4 Zn-Based Coating Systems.....	21
1.5 Metallurgy of Zn Coatings.....	23
1.5.1 Fe-Zn Systems.....	23
1.5.2 Al Additions	25
1.5.3 Zn-Al-Mg	27
1.6 The Continuous Galvanising Process	27
1.6.1 Operational Procedures of CG lines.....	29
1.6.2 Dross and Dross Build-up.....	37
1.6.3 Galvanised Coating Defects	38
1.7 Galvanising Pot Bearings	40
1.7.1 Design and Operation of Galvanising Pot Bearings.....	40
1.7.2 Lubrication of Journal Bearings	43
1.7.3 Wear of Journal Bearings.....	46
1.8 Material Selection for Galvanising Bath Hardware.....	48
1.8.1 Fe- and Co-based alloys.....	48
1.8.2 Ceramics	54
1.8.3 Effects of Changing Bath Composition	61
1.8.4 Dynamic Tests in Liquid Zn	63
1.9 Fabrication Processes of Materials.....	64
1.9.1 Field Assisted Sintering Technology	64
1.9.2 Thermal Spraying.....	66

1.9.3 Near Infrared (NIR)	67
1.10 Limitations and Project Objectives	68
Chapter 2 Experimental Methods	70
2.1.1 Commercially Available Materials	70
2.1.2 SiALON-BN Composites	71
2.1.3 Coatings	72
2.2.1 Sample Preparation	74
2.2.2 Etching	76
2.2.3 Imaging and Chemical Composition Analysis	78
2.2.4 X-ray Diffraction	80
2.2.5 Roughness Measurement	80
2.2.6 Density Measurement	81
2.2.7 Dilatometry	82
2.3 Mechanical Testing	82
2.3.1 Hardness Testing	82
2.3.2 Pin-on-disc Wear Testing	83
2.4 Corrosion Testing	86
2.4.1 Static Immersion Testing	86
2.4.2 Dynamic Testing	88
Chapter 3 Testing of Commercially Available Ceramics	95
3.1 Introduction	95
3.2 Material Characterisation of As-received Specimens	96
3.2.1 Benchmarks: SS 316L and WC-Co/Wallex6 TM	96
3.3 Static Immersion Testing	110
3.3.1 Problems with Preliminary Experiments	110
3.3.2 Characterisation of the Benchmarks After Testing	114
3.3.3 Characterisation of Ceramics After Testing	121
3.4 Pin-on-Disc Wear Testing	128
3.4.1 Introduction	128
3.4.2 Measurements of Friction Coefficient	128
3.4.3 Inspection of the Tested Specimens	133
3.4.4 Wear Scar Analysis	134
3.4.5 Wear Resistance and Hardness	140
3.5 Summary	142
Chapter 4 Novel Ceramic Materials and Coatings	145
4.1 SiALON-BN Composites	145

4.1.1 Introduction.....	145
4.1.2 Powder Characterisation	146
4.1.3 Problems with NIR	147
4.1.4 Fabrication of SiAlON-BN Composites with FAST	149
4.1.5 Effects of Changing Sintering Temperature and Time	152
4.1.6 Effects of Adding Sintering Additives.....	156
4.1.7 Static Immersion Testing	164
4.1.8 Pin-on-Disc Wear Testing	169
4.1.9 Summary of SiAlON-BN Composites.....	172
4.2 Al ₂ O ₃ Coatings.....	173
4.2.1 Introduction.....	173
4.2.2 Material Characterisation Before Testing.....	174
4.2.3 Static Immersion Testing	176
4.2.4 Analysis of Coating Failure.....	181
4.2.5 Summary of Al ₂ O ₃ Coatings	185
Chapter 5 Dynamic Testing of Materials in Zn Alloy	186
5.1 Introduction.....	186
5.2 Characterisation of As-received Samples	187
5.3 Dynamic Testing	190
5.3.1 Wallex6™ with HVOF WC-Co vs Wallex6™	192
5.3.2 Wallex6™ with HVOF WC-Co vs Wallex4™	202
5.3.3 SS 316L with HVOF Al ₂ O ₃ vs Wallex6™	211
5.3.4 Phase Identification	221
5.3.5 Wear Scar Analysis	223
5.4 Summary	229
Conclusions and Reflections.....	230
Conclusions	230
Novelty of the Research	231
Industrial Uptake	232
Future Work	232
Bibliography	234

Acknowledgments

This research was funded by the Engineering and Physical Sciences Research Council (EPSRC) with Tata Steel. I would like to thank my funders and the Materials and Manufacturing Academy (M2A) at Swansea University for giving me the opportunity to undertake a doctoral research degree.

The list of people who helped me in this project is endless, so I apologise if I am not including everybody. First, I am very grateful to all my academic and industrial supervisors, Professor David Penney, Professor James Sullivan, Dr Christopher Mills and Dr James Edy, who provided me guidance and feedback whenever was needed. Moreover, I want to thank my former academic supervisor, Dr Rhys Faulkner, for his help during the early stages of my research, Professor Eifion Jewell for his advice on pin-on-disc testing and Mr David Medway for the technical assistance in building the dynamic wear rig. I would also like to thank the members in the Steel and Metals Institute who allowed me to conduct my experiments in their lab, the Advanced Imaging Facility (AIM) and the MACH1 team at Swansea University, in particular Dr Shahin Mehraban for the dilatometry measurements.

I wish to acknowledge the support of the Henry Royce Institute for Advanced Materials through the Student Equipment Access Scheme for enabling access to FCT HP D 25 FAST facilities at The Royce Discovery Centre at the University of Sheffield and to the SENTECH Etchlab Reactive Ion Etcher at Imperial College, London.

Last but not least, I am deeply grateful to my family who encouraged me to embark on this journey and supported me along the way.

List of Tables

Chapter 1

Table 1.1 ZODIAC CG line operating conditions (Faulkner, 2020).	43
Table 1.2 ZODIAC bearing operating conditions (Faulkner, 2020).	43

Chapter 2

Table 2.1 Composition of commercially available ceramics for static testing.	71
Table 2.2 Particle size of the powders used for the fabrication of SiAlON/BN composites with FAST. The values reported were provided by the supplier.	72
Table 2.3 Preparation schedule for grinding and polishing metals and soft ceramics.	75
Table 2.4 Preparation schedule for grinding and polishing hard ceramic materials.	75
Table 2.5 Carpenter's etchant composition.	76
Table 2.6 Process conditions for thermal etching ceramic materials.	77

Chapter 3

Table 3.1 SS 316L composition (Davis, 1994).	97
Table 3.2 Wallex6™ alloy composition provided by the supplier.	97
Table 3.3 COF of the ceramics during steady-state regime.	131
Table 3.4 Measurements of the wear scar depths.	139
Table 3.5 Wear coefficients calculated from the volume loss at 9.42 m/min.	140
Table 3.6 Hardness values of the ceramic plates. The applied test load is reported in 'kgf' next to each numeric hardness value.	141

Chapter 4

Table 4.1 Measured particle size of SiAlON, hBN and cBN powder.	147
Table 4.2 Composition of the mixtures used to prepare the SiAlON-BN specimens with FAST.	150
Table 4.3 Composition and processing conditions for the initial FAST trials.	152
Table 4.4 Relative densities of the specimens prepared after performing the initial trials.	156
Table 4.5 Relative densities of the specimens prepared using sintering additives.	157
Table 4.6 COF of the SiAlON and SiAlON-BN specimens during steady-stage regime.	171

Chapter 5

Table 5.1 Material combinations chosen for dynamic testing.	187
Table 5.2 Wallex4™ alloy composition provided by the supplier.	189
Table 5.3 Main composition of the reaction layer of the pads after testing in Zn-Al.	220
Table 5.4 Main composition of the reaction layer of the pads after testing in Zn-Al-Mg. ...	220
Table 5.5 Wear coefficient and displacement after testing in Zn-Al.	223

Table 5.6 Wear coefficient and displacement after testing in Zn-Al-Mg.....	224
Table 5.7 Percentage change of wear coefficient and displacement after changing bath from Zn-Al to Zn-Al-Mg.....	224

List of Figures

Chapter 1

Figure 1.1 Phase diagram of the Fe-Zn binary system. Reproduced from (Okamoto, 2007).	24
Figure 1.2 Illustration showing the formation of intermetallic compounds in a Fe-Zn binary system. Reproduced from (Chakraborty et al., 2022).	25
Figure 1.3 Phase diagram of the Fe-Zn binary system, showing the Zn-rich corner of the 460°C isothermal section. Reproduced from (Marder, 2000).	26
Figure 1.4 Comparison between a GI coating (a) and a MagiZinc® coating (b). Reproduced from (Kuperus, 2018).	27
Figure 1.5 Main stages involved in galvanised steel production: (1) raw materials, (2) blast furnace, (3) basic oxygen furnace, (4) electric arc furnace, (5) casting, (6) hot rolling, (7) pickling, (8) cold rolling, (9) continuous galvanising.	28
Figure 1.6 Schematic of Tata Steel's ZODIAC CG line. (1) strip decoilers, (2) welders, (3) entry accumulator, (4) annealing, (5) zinc bath, (6) after pot cooling, (7) exit accumulator, (8) inspection, (9) strip coiling.	30
Figure 1.7 Sketch of the hot dip process in the Zn pot (a); galvanising bath hardware (b).	33
Figure 1.8 Outbursts at the interface between the steel and the coating (a); SEM image of a bare spot (b). Reproduced from (Azimi et al., 2012).	39
Figure 1.9 CAD renders of: stabiliser roll bearing sleeve (a) and bushing (b), sink roll bearing sleeve (c) and bushing (d). Reproduced from (Faulkner, 2020).	41
Figure 1.10 Photograph of the stabiliser roll journal bearing components used in ZODIAC. Reproduced from (Faulkner, 2020).	42
Figure 1.11 Sketch showing the cross-sectional view of a typical journal bearing.	44
Figure 1.12 Cross-section of SS 316L after immersion in GI for 8 days: (1) residual Zn, (2) intermetallic dross particles, (3) diffusion layer, (4) SS 316L specimen. Reproduced from (Kuperus, 2018).	49
Figure 1.13 Worn bearing sleeve and bushing with deep abrasive grooves present on the surface (a); characterisation of intermetallic dross particles (b). Reproduced from (Shi et al., 2018).	50
Figure 1.14 Cross-section of Wallex6™ after immersion in GI. The image was labelled to show the dross and reaction layer observed after testing, as well as the eutectic phases present in the alloy, which were found to disrupt the shape and uniformity of the diffusion layer. Reproduced from (Faulkner, 2020).	51
Figure 1.15 Cross-section of WC-coated SS 316L sleeve after immersion in Galvanneal. Corrosion products developed due to corrosion of the matrix (1) and cracks formed in the WC particles (2). Reproduced from (Tang et al., 2010).	53
Figure 1.16 Images showing Al ₂ O ₃ coating after 0 days (a), 10 days (b), 20 days (c) and 30 days (d) of dipping in liquid zinc. Reproduced from (Nag et al., 2021).	55
Figure 1.17 Composition of each gradient layer used to fabricate the ZrO ₂ -NiAl coating (a); SEM image showing the intermediate gradient layers (a). Reproduced from (Dong et al., 2006).	56

Figure 1.18 Comparison of the contact angles obtained for BN, Si ₃ N ₄ and Al ₂ O ₃ in molten Al at various temperatures. BN shows superior non-wetting properties up to a temperature of 1000°C. Reproduced from (Reusch et al., 2015).	58
Figure 1.19 Schematic of the pin-on-disk experimental setup (a): (1) weight, (2) clamp, (3) pin, (4) rotating direction of the disk, (5) abrasive disc and (6) moving direction of the sample; abrasive weight loss measurements showing the superior wear resistance of MoB/CoCr (b). Reproduced from (Chen et al., 2019).	59
Figure 1.20 Tribometer used for measuring the tribo-corrosion resistance of enamel (a); SEM image of the enamel coating after 30,000 cycles. The image shows the presence of a ~10 µm-thick glaze layer on the surface of the enamel (b). Reproduced from (Yu et al., 2019).	61
Figure 1.21 SEM images showing the difference between faceted (marked red) and curved (marked green) interfaces observed in the dross build-up structure when transitioning from GI to Zn-Al-Mg bath. Reproduced from (Kuperus, 2018).	62
Figure 1.22 Schematics of main FAST equipment. Graphite die showing punches in final position for manufacturing a turbine blade component (a); exploded die view (b). Reproduced from (Weston et al., 2020).	65
Figure 1.23 Schematics of the HVOF process. Reproduced from (El-Eskandarany, 2020).	67
Figure 1.24 Schematic illustrating the operation of NIR heating. The coating material is transparent to NIR radiation, which is absorbed by the underlying substrate, producing rapid heating and sintering of the coating. Reproduced from (Griffin et al., 2021).	68

Chapter 2

Figure 2.1 Example of a 60 mm diameter disc with 30wt.%cBN-SiAlON composition fabricated with FAST.	72
Figure 2.2 SS 316L samples with Al ₂ O ₃ coating (a); Al ₂ O ₃ coated bars (b); Wallex6™ bars (c).	73
Figure 2.3 Cracks formed after hot mounting a ceramic specimen.	74
Figure 2.4 Sentech RIE apparatus for plasma etching available at Imperial College, London.	77
Figure 2.5 Microscopes used for material characterisation: digital microscope (a); desktop SEM (b); ZEISS EVO SEM (c).	79
Figure 2.6 Solarus plasma cleaner (a); Agar sputter coater (b).	79
Figure 2.7 X-ray diffractometers used in this project: D8 Discover (a); D8 Advance (b).	80
Figure 2.8 Talysurf profilometer used for surface roughness measurement.	81
Figure 2.9 Experimental setup used to measure density with Archimedes' Principle.	82
Figure 2.10 Experimental set-up used to measure the coefficients of thermal expansion.	82
Figure 2.11 Innovatest hardness tester (a); image of an indent captured on the Keyence (b).	83
Figure 2.12 Pin-on-disk experimental apparatus for friction and wear testing.	84
Figure 2.13 Example of a line scan performed across the worn track.	86
Figure 2.14 Sketch of the experimental setup used for static dip testing (a); top loading furnace containing the Zn bath (b).	87
Figure 2.15 Samples prior to testing: first trial using bolts and nuts (a); second test using SS 316L wire only (b).	88

Figure 2.16 Existing bearing test rig (a); detail of the shaft for bearing sleeve specimens (b).	90
Figure 2.17 New test rig (a); details of the 'bar-on-pad' design (b).	91
Figure 2.18 3D drawing of the new test rig: isometric view (a); side view (b).	92
Figure 2.19 Drawing illustrating the new rig frame.	93

Chapter 3

Figure 3.1 Microstructure of SS 316L after etching with Carpenter's solution.	97
Figure 3.2 SEM image of Wallex6™ coated with HVOF WC-Co coating.	98
Figure 3.3 EDS analysis of each phase in Wallex6™ taken at marked location in Figure 3.2.	98
Figure 3.4 SEM image showing the CrCoWMo and CoWCr eutectic phases observed in Wallex6™.	99
Figure 3.5 Microstructure of as-received pure hexagonal BN at 800X magnification.	100
Figure 3.6 Microstructure of as-received BN Grade M26 at 800X magnification.	101
Figure 3.7 EDS maps of as-received BN grade M26.	101
Figure 3.8 Microstructure of as-received Macor® Machinable Glass Ceramic.	102
Figure 3.9 EDS maps of as-received Macor® Machinable Glass Ceramic.	103
Figure 3.10 SEM image of AlN-BN composite (a); average element composition of the phases observed in AlN-BN (b).	104
Figure 3.11 SEM image of as received 3YSZ (a); SEM image of 3YSZ after plasma etching (b).	105
Figure 3.12 SEM image of the microstructure of as-received 3YSZ after thermal etching.	106
Figure 3.13 SEM image of as received Si ₃ N ₄ (a); SEM image of Si ₃ N ₄ after thermal etching (b).	107
Figure 3.14 SEM image of Si ₃ N ₄ after plasma etching (a); Average element composition of plasma etched Si ₃ N ₄ (b).	108
Figure 3.15 SEM image of as received Al ₂ O ₃ (a); SEM image of plasma etched Al ₂ O ₃ (b).	109
Figure 3.16 SEM image of the microstructure of as-received Al ₂ O ₃ after thermal etching.	110
Figure 3.17 Inspection of the specimens after extraction from the Zn alloy bath.	111
Figure 3.18 Cross-section of Al ₂ O ₃ after immersion in Zn-Al-Mg for 5 weeks (a); EDS analysis of the phases observed in the specimen (b).	112
Figure 3.19 SS 316L after immersion in Zn-Al for 5 weeks, with solidified Zn on the surface.	113
Figure 3.20 Cross-section of SS 316L after 5 weeks of immersion in Zn-Al (a); EDS phase elemental analysis of the reaction products observed in SS 316L after immersion in Zn-Al (b).	114
Figure 3.21 Cross-section of SS 316L after 5 weeks of immersion in Zn-Al-Mg (a); EDS analysis of the reaction products observed in SS 316L after immersion in Zn-Al-Mg (b).	115
Figure 3.22 SEM image (a) and EDS elemental analysis performed on WC-Co/Wallex6™ after immersion in Zn-Al for five weeks (b).	119
Figure 3.23 SEM image (a) and EDS analysis of WC-Co/Wallex6™ after testing in Zn-Al-Mg (b).	120
Figure 3.24 Thickness reduction of WC-Co after immersion in Zn-Al (a) and Zn-Al-Mg baths (b). Note the difference in magnification between the two images.	120

Figure 3.25 SEM cross-sections of the ceramic specimens hBN (a), BN Grade M26 (b), Macor® (c), AlN-BN (d), 3YSZ (e), Si ₃ N ₄ (f) and Al ₂ O ₃ (g) after immersion in Zn-Al.	123
Figure 3.26 SEM cross-sections of the ceramic specimens hBN (a), BN Grade M26 (b), Macor® (c), AlN-BN (d), 3YSZ (e), Si ₃ N ₄ (f) and Al ₂ O ₃ (g) after immersion in Zn-Al-Mg.	124
Figure 3.27 EDS maps of pure hBN after testing in Zn-Al.	125
Figure 3.28 EDS maps of pure hBN after testing in Zn-Al-Mg.	125
Figure 3.29 Cross-sections of as-received Al ₂ O ₃ (a); Al ₂ O ₃ after exposure to Zn-Al (b); Al ₂ O ₃ after exposure to Zn-Al-Mg (c).	126
Figure 3.30 SEM images of Al ₂ O ₃ after immersion in Zn-Al for 5 weeks (a); EDS elemental analysis of Al ₂ O ₃ after testing (b).	126
Figure 3.31 As-received Macor® (a); Macor® after immersion in Zn-Al (b); Macor® after immersion in Zn-Al-Mg (c); EDS elemental analysis of Macor® after testing in Zn-Al-Mg (d).	127
Figure 3.32 COF curves for the tests performed at 3.14 m/min (a), 6.28 m/min (b) and 9.42 m/min (c).	130
Figure 3.33 Plot of the COF of the ceramics as a function of sliding speed.	133
Figure 3.34 Macroscopic examination of the tested specimens.	133
Figure 3.35 Optical images of the wear scars of pure hBN at 3.14 m/min (a), pure hBN at 9.42 m/min (b), BN M26 at 3.14 m/min (c) and BN M26 at 9.42 m/min (d).	135
Figure 3.36 Optical images of the wear scars of Macor® at 3.14 m/min (a), Macor® at 9.42 m/min (b), AlN-BN at 3.14 m/min (c) and AlN-BN at 9.42 m/min (d).	135
Figure 3.37 Images of the wear scars of 3YSZ at 3.14 m/min (a), 3YSZ at 9.42 m/min (b), Si ₃ N ₄ at 3.14 m/min (c), Si ₃ N ₄ at 9.42 m/min (d), Al ₂ O ₃ at 3.14 m/min (e) and Al ₂ O ₃ at 9.42 m/min (f).	137
Figure 3.38 Images of the SiC ball before testing (a) and after contact with Al ₂ O ₃ (b). The ball was worn during sliding, forming a 'flat-on-flat' contact.	137
Figure 3.39 3D scans of the worn surface of pure BN (a), BN M26 (b), Macor® (c), AlN-BN (d), 3YSZ (e), Si ₃ N ₄ (f), Al ₂ O ₃ (g) at 9.42 m/min sliding velocity.	138
Figure 3.40 Depth of the worn track section plotted against sliding speed.	139
Figure 3.41 Measured cross-sectional area of the wear scar at 9.42 m/min sliding speed.	140
Figure 3.42 Plot of the wear coefficient 'k' against the hardness of the ceramics.	142

Chapter 4

Figure 4.1 SEM images of SiAlON (a), hBN (b) and cBN powder (c).	147
Figure 4.2 AdPhos NIR unit (a); Inspection of the sample obtained at 0.5 m/min line speed and 100% lamp intensity (b).	149
Figure 4.3 FAST Furnace Type HP D25 (a); die assembly (b); specimen after FAST processing (c).	151
Figure 4.4 Graph illustrating the load and temperature profiles of a FAST cycle.	151
Figure 4.5 Microstructure of TRIAL1. The specimen was prepared using a dwell temperature of 1600 °C and a dwell time of 10 minutes.	153
Figure 4.6 Microstructure of TRIAL2. The specimen was prepared using a dwell temperature of 1800 °C and a dwell time of 30 minutes.	154
Figure 4.7 SEM image of TRIAL2 captured at 1000X, showing details of the SiAlON grains (darker contrast) separated by an intergranular phase (lighter contrast).	155
Figure 4.8 Photograph of the 100wt.% SiAlON specimen (TRIAL3) prepared at 1850 °C.	155

Figure 4.9 Microstructure of SiAlON after the addition of Y_2O_3 and Al_2O_3 sintering additives.	158
Figure 4.10 EDS phase elemental analysis of the phases present in SiAlON, which were previously highlighted in Figure 4.9.	159
Figure 4.11 Microstructure of 30wt.%hBN-SiAlON after the addition of Y_2O_3 and Al_2O_3 sintering additives.	160
Figure 4.12 Image of the 30wt.%hBN-SiAlON microstructure captured at 1000X magnification.	161
Figure 4.13 EDS mapping of 30wt.%hBN-SiAlON highlighting areas containing Y, O (a), Si (b), B (c) and N (d).	161
Figure 4.14 Microstructure of 30wt.%cBN-SiAlON after the addition of Y_2O_3 and Al_2O_3 sintering additives, showing BN rich (1) and SiAlON rich areas (2).	162
Figure 4.15 Magnified image of 30wt.%cBN-SiAlON showing details of the glassy phase (1).	163
Figure 4.16 EDS mapping of 30wt.%cBN-SiAlON highlighting areas containing Y, O (a), Si (b), B (c) and N (d).	163
Figure 4.17 Diffractograms of the SiAlON and SiAlON-BN composites after FAST processing.	164
Figure 4.18 SEM cross-sections of the specimens prepared with FAST, namely SiAlON (a), 10wt.%hBN-SiAlON (b), 20wt.%hBN-SiAlON (c), 30wt.%hBN-SiAlON (d) and 30wt.%cBN-SiAlON (e), after immersion in Zn-Al.	166
Figure 4.19 SEM cross-sections of the specimens prepared with FAST, namely SiAlON (a), 10wt.%hBN-SiAlON (b), 20wt.%hBN-SiAlON (c), 30wt.%hBN-SiAlON (d) and 30wt.%cBN-SiAlON (e), after immersion in Zn-Al-Mg.	167
Figure 4.20 Results of EDS analysis on 30wt.%hBN-SiAlON, showing the average element composition of the SiAlON and BN rich phases at the interface (1, 2) and in the bulk of the material (3, 4), after exposure to Zn-Al.	168
Figure 4.21 Results of EDS analysis on 30wt.%hBN-SiAlON, showing the average element composition of the SiAlON and BN rich phases at the interface (1, 2) and in the bulk of the material (3, 4), after exposure to Zn-Al-Mg.	169
Figure 4.22 COF curves of the SiAlON and SiAlON-BN specimens prepared with FAST.	171
Figure 4.23 As-received specimen (a); details of pores in the Al_2O_3 coating (b).	175
Figure 4.24 EDS average elemental composition of the as-received specimens.	175
Figure 4.25 X-ray diffraction patterns for the as-received Al_2O_3 coatings.	176
Figure 4.26 Cross-sections of Al_2O_3 coated SS 316L after 1 week (a, b) and 3 weeks (c, d) of static immersion testing in Zn-Al.	177
Figure 4.27 Details of the diffusion layer observed after the breakdown of the Al_2O_3 coating and subsequent contact with Zn-Al (a); EDS phase elemental analysis of the diffusion layer (b).	178
Figure 4.28 Cross-sections of the Al_2O_3 coatings after 4 weeks of immersion in Zn-Al-Mg: spallation of the coating (a); details of cracks and areas of the coating affected by degradation in molten metal (b); Zn diffusion through cracks (c); details of the three phases (d).	179
Figure 4.29 EDS maps of Al_2O_3 coating after immersion in Zn-Al-Mg.	181
Figure 4.30 CTE of SS 316L and Al_2O_3 as a function of temperature in the range of 35–465 °C.	183
Figure 4.31 Failure process of the Al_2O_3 coatings after exposure to molten metal at high temperature.	183

Chapter 5

Figure 5.1 Cross-sections of WC-Co/Wallex6™ (a) and Al ₂ O ₃ /SS 316L (b).	187
Figure 5.2 Cross-sections of Wallex6™ (a) and Wallex4™ (b) pad specimens.	188
Figure 5.3 Microstructure of Wallex4™ (a); Elemental phase composition of Wallex4™ (b).	189
Figure 5.4 Photograph of the Zn bath before testing (a); Dross formation during testing (b).	190
Figure 5.5 Cross-section of the WC-Co/Wallex6™ bar after immersion in Zn-Al-Mg, showing the oxide phases forming on the residual Zn layer (a); Composition of the oxide phases observed in this layer (b).	191
Figure 5.6 SEM image of WC-Co/Wallex6™ bar after testing in Zn-Al (a); high magnification image showing the intermetallic compounds (b); EDS phase elemental analysis of the intermetallic compounds (c).	193
Figure 5.7 (a) SEM image of Wallex6™ pad after testing in Zn-Al captured on the contact surface; (b) high magnification image; (c) Results of EDS phase elemental analysis.	195
Figure 5.8 SEM image of Wallex6™ pad after testing in Zn-Al within the unworn region (a); EDS point spectrum analysis of the phases present in the unworn region (b).	196
Figure 5.9 SEM image of WC-Co/Wallex6™ bar after testing in Zn-Al-Mg (a); high magnification image showing the intermetallic compounds (b); EDS phase elemental analysis of the intermetallic compounds (c).	198
Figure 5.10 Phase diagram showing the Zn-rich corner of the Zn-Al-Fe system at 460 °C. The diagram illustrates the Fe solubility limit for Al concentrations up to ~ 0.3 wt.% Al (McDermid et al., 2004).	199
Figure 5.11 Phase diagram of the Zn-Al-Fe system at 460 °C for 1.5 wt.% Mg additions. Fe solubility lines are shown in the temperature range between 450 °C and 500 °C (Kuperus, 2018).	200
Figure 5.12 SEM image of Wallex6™ pad after testing in Zn-Al-Mg captured on the contact surface (a); high magnification image (b); results of EDS phase elemental analysis (c).	201
Figure 5.13 SEM image of Wallex6™ pad after testing in Zn-Al-Mg captured on the unworn region (a); EDS point spectrum analysis of the phases present in the unworn region (b). .	202
Figure 5.14 SEM image of WC-Co/Wallex6™ bar after testing in Zn-Al (a); EDS phase elemental analysis of the intermetallic compounds (b).	204
Figure 5.15 SEM image of the contact region of Wallex4™ after testing in Zn-Al (a); EDS phase elemental analysis of the reaction layer (b).	205
Figure 5.16 SEM image captured within the unworn region of the Wallex4™ pad after testing in Zn-Al (a); EDS phase elemental analysis of the corrosion products (b).	206
Figure 5.17 EDS mapping of the elements present in Wallex4™ after testing in Zn-Al.	207
Figure 5.18 SEM image of WC-Co/Wallex6™ bar after testing in Zn-Al-Mg (a); high magnification image showing the reaction layer (b); EDS phase elemental analysis of the intermetallic compounds (c).	208
Figure 5.19 SEM image of the contact region of Wallex4™ after testing in Zn-Al-Mg (a); EDS phase elemental analysis of the reaction layer (b).	209
Figure 5.20 SEM image of the unworn region of Wallex4™ pad after testing in Zn-Al-Mg (a); EDS phase elemental analysis of the corrosion products (b).	210
Figure 5.21 EDS mapping of the elements present in Wallex4™ after testing in Zn-Al-Mg.	211
Figure 5.22 Visual inspection of the bar specimens tested in Zn-Al (a) and Zn-Al-Mg (b)...	212
Figure 5.23 Cross-section of the Al ₂ O ₃ /SS 316L bar after dynamic testing in Zn-Al.	213

Figure 5.24 Cross-section of the contact region of the Wallex6™ pad after testing in Zn-Al (a); EDS phase elemental analysis carried out at the interface with the molten metal bath (b).	214
Figure 5.25 Cross-section of the unworn region of the Wallex6™ pad after testing in Zn-Al (a); EDS phase elemental analysis of the corrosion products (b).	215
Figure 5.26 Cross-section of Al ₂ O ₃ /SS 316L bar after dynamic testing in Zn-Al-Mg.	216
Figure 5.27 Cracks within the Al ₂ O ₃ coating after dynamic testing in Zn-Al-Mg.	216
Figure 5.28 Cross-section of the contact region of the Wallex6™ pad after testing in Zn-Al-Mg (a); results of EDS phase elemental analysis of the contact surface (b).	217
Figure 5.29 Cross-section of the unworn region of the Wallex6™ pad after testing in Zn-Al-Mg (a); EDS phase elemental analysis of the corrosion products (b).	218
Figure 5.30 Concentration of Al, Co and Zn in the diffusion layer of the pad specimens after exposure to Zn-Al and Zn-Al-Mg.	220
Figure 5.31 Average thickness of the diffusion layers developed in the pads for each coupling.	221
Figure 5.32 XRD carried out on a Wallex6™ bar with WC-Co after immersion in Zn-Al.	222
Figure 5.33 XRD carried out on a Wallex4™ pad after immersion in Zn-Al.	223
Figure 5.34 Plot of the wear coefficients and values of displacement after dynamic testing.	224
Figure 5.35 3D imaging of the wear scars produced on the specimens tested in Zn-Al: Wallex6™ after sliding with Wallex6™/WC-Co (a); Wallex4™ after sliding with Wallex6™/WC-Co (b); Wallex6™ after sliding with SS 316L/Al ₂ O ₃ (c).	226
Figure 5.36 3D imaging of the wear scars produced on the pad specimens tested in Zn-Al-Mg: Wallex6™ after sliding with Wallex6™/WC-Co (a); Wallex4™ after sliding with Wallex6™/WC-Co (b); Wallex6™ after sliding with SS 316L/Al ₂ O ₃ (c).	228

Abbreviations

BOS – basic oxygen steelmaking
BSD – backscattered electron detector
CG – continuous galvanising
COF – coefficient of friction
CTE – coefficient of thermal expansion
EBSD – electron backscatter diffraction
EDM – electrical discharge machining
EDS – energy dispersive x-ray
FAST – field assisted sintering technology
HDG – hot dip galvanising
HVOF – high velocity oxygen fuel
ICP-MS – inductively coupled plasma mass spectrometry
NIR – near-infrared
SE – secondary electron
SEM – scanning electron microscopy
SPS – spark plasma sintering
SS – stainless steel
XRD – x-ray diffraction

Chapter 1

Introduction

1.1 Scope of Research

Modern steel manufacturers can apply coatings to the steel strip to impart corrosion resistance properties to the product. These coatings are produced on galvanising lines, such as the ZODIAC plant, which is Tata Steel's world-class coil galvanising line at Llanwern. ZODIAC serves the automotive industry, producing thin strips which automotive customers use for body panels. Continuous Galvanising (CG) involves the heat treatment and dipping of strip steel into a bath of molten Zn alloy at speeds of up to 180m/min.

The aim of this research is to optimise the galvanising bath journal bearings used in ZODIAC galvanising line, which are important components of the galvanising pot hardware. Modern automotive grade galvanised lines are increasingly focused on optimising galvanising line hardware to deliver increasing production yields while maintaining stringent quality requirements. The galvanising hardware guides the strip steel in and out the molten metal bath and has to survive in this challenging environment, operating with minimal vibrations which are detrimental to the galvanised coating quality. The galvanising line is able to continually operate for up to a five-week period, after which the hardware must be replaced. Therefore, the pot hardware itself can be considered a bottleneck to production and quality; if the operational capacity of hardware components, such as the pot roll bearings, were increased, the financial incentives would be significant.

The present research has analysed the next generation of materials for use as submerged hardware components in Tata Steel ZODIAC line at Llanwern. The work shown in this thesis was conducted for developing pot hardware which will use materials that minimise reactivity with the molten metal spelter, with a greater focus on the use of ceramics. The main objective of the project was the identification of

materials which remained inert and resistant to the attack of liquid Zn, so that they could be used for creating novel hardware and roll bearing designs. Research activities mainly focused on experimental testing of prospective materials with immersion testing inside molten Zn baths. Moreover, the project performed material characterisation to understand how the materials interacted with the molten metal bath.

1.2 Layout of Thesis

Chapter 1 provides background information on the CG process and it introduces the problem of pot roll bearing deterioration in liquid Zn alloy. The mechanisms limiting the operational capacity of the bearings are thoroughly explained, as well as the financial implications of using bath hardware with limited service life. Subsequently, the state-of-the-art technologies for making pot roll journal bearings with enhanced performance in the galvanising bath are reviewed. It emerged that ceramic materials have potential to outperform the bearing materials currently in use.

The procedures and materials experimented in this research are described in Chapter 2. This chapter provides information about the experiments conducted, including static testing, wear testing and dynamic testing. Moreover, the techniques used for material characterisation before and after testing are discussed.

The corrosion resistance in Zn alloy of a broad range of ceramic materials was investigated in Chapter 3 'Testing of Commercially Available Ceramics'. The ceramics were immersed in Zn alloy baths of different composition and, additionally, their wear resistance properties were also investigated. Chapter 4 'Novel Ceramic Materials and Coatings' highlights the manufacture, as well as the corrosion and wear resistant properties of novel materials and coatings, namely SiAlON-BN composites and HVOF Al_2O_3 coatings. A new technique for validating the results of static testing was discussed in Chapter 5 'Dynamic Testing of Materials in Zn Alloy'. This chapter provides a description of the design of a bespoke testing rig, which was used for dynamic testing of potential upgrades to the bearing system currently used in ZODIAC.

1.3 Galvanised Steel

Most materials are subjected to physical wear; however, effectively managing the challenges posed by physical wear is complex. This complexity arises due to the interplay of multiple factors that impact each other. The interaction between materials and specific environmental elements can lead to undesirable chemical reactions, causing corrosion. This deterioration process originates on the material surface, resulting in changes to their properties or even their failure. When unprotected steel is exposed to the atmosphere, it develops rust and undergoes corrosion (Maaß et al., 2011).

Zn is capable of protecting steel from corrosion, as it behaves as a sacrificial anode in most environments. Owing to its position in the galvanic series, Zn preferentially corrodes, while the cathode, i.e., Fe, becomes the site for oxygen reduction where no metal is lost. This means that when Zn-coated steel is exposed to an oxidising environment, Zn liberates its electrons before Fe does. For this reason, when Zn is deposited onto the surface of steel, a strong and adherent barrier is formed between the steel and the corrosive environment (Kuklik & Kudlacek, 2016). When freshly exposed galvanised steel comes into contact with the surrounding atmosphere, a series of Zn corrosion compounds is generated. In the presence of air, newly exposed Zn immediately interacts with oxygen, producing a thin layer of zinc oxide. When moisture is present, Zn and its oxide respond to water, leading to the formation of zinc hydroxide. The final product of this corrosion process is zinc carbonate, which is produced from the reaction between zinc hydroxide and carbon dioxide present in air. This zinc carbonate layer protects the underlying zinc, resulting in its minimal corrosion rate in most conditions. Due to the presence of this protective layer, the corrosion process is estimated to be around 7 to 10 times slower than that of Fe (Dallin, 2015).

Various techniques have been developed for coating Zn on to steel. These methods include electroplating, thermal spraying, hot-dip galvanising, sherardising, and mechanical plating. In electroplating, electrolytic deposition is used to apply a Zn coating from an electrolyte. Thermal spraying applies molten Zn using a flame or

electric arc, which is carried by a gas stream to the sand-blasted surface of the components to be coated. Hot-dip galvanising, or 'HDG', is a process in which the steel parts are immersed in molten Zn, leading to the formation of a Zn coating on the steel's surface during immersion. Sherardising is a diffusion-based method where small parts are sand-blasted and subsequently tumbled with a mixture of dust and sand in a rotary furnace. Regarding mechanical plating, it consists of tumbling pre-treated parts with Zn, dust and glass balls in a chemical environment. This leads the Zn particles to cold weld onto the steel, achieving galvanisation (Kuklik & Kudlacek, 2016).

HDG has several benefits, including the formation of a metallurgical bond with the steel substrate, high productivity and good economy. Its application ranges from small parts to steel structures. Two types of HDG technologies exist, namely batch hot-dip galvanising and continuous galvanising of steel strips. Continuous galvanising (CG) lines offer high productivity and an accurate setting of the process parameters. Basic parameters of the coating, such as appearance, structure and thickness can be efficiently checked. During the immersion in the molten Zn bath, a reaction between Fe and Zn occurs, leading to the formation of several Fe-Zn alloy phases. Al and other elements are typically added to the molten Zn bath (Kuklik & Kudlacek, 2016).

1.4 Zn-Based Coating Systems

Zn coatings on sheet steel, obtained by submerging the steel in a liquid Zn bath, can be grouped into four distinct categories:

1. Coatings with an Al content between 0.13% and 1%, which are referred to as GI coatings.
2. Coatings with Al content between 0% and 0.13% and 10%-18% Fe formed by diffusion of liquid Zn into solid Fe which occurs during heat treatment once the steel exists the molten metal bath. These coatings are termed galvanneal or GA coatings.

3. Coatings with >1% Al content which include Galfan (Zn-5% Al) and Galvalume (Zn-55% Al).
4. Coatings with Mg additions, with Mg content between 1% and 3.7% (Marder & Goodwin, 2023).

During a galvanising campaign, a continuous galvanising line has the capability to produce different coatings based on customer requirements and tailored to the customer's industry. Nowadays, automotive steel customers require strict tolerances of product geometry and higher standards for coating quality, particularly for visible parts, which must be free of any imperfections (Gossuin & Moreas, 2021). It is important for the automotive industry to apply paint coatings that play an important role in the car's purchasing decision making process. As a result, automotive customers require a product with a high quality surface finish (Beentjes et al., 2021). This product is referred to as 'full-finish' and it can be manufactured at the ZODIAC CG line. These coatings are typically applied to cold rolled steel, using GI bath composition. GI coatings have been commercially used for the automotive sector due to their excellent formability (Park et al., 2021). The ZODIAC line supplies full finish GI coated product to customers, including Nissan, BMW Mini and Vauxhall.

In recent decades, there has been an increasing effort on weight reduction within the automotive sector, in order to minimise fuel consumption (Chakraborty & Ghassemi-Armaki, 2021). In 2005, Tata Steel introduced the MagiZinc® coating to address this concern. This type of coating is a ZnAlMg-coating, containing Zn, Al (1.4-1.8wt%) and Mg (1.4-1.8wt%). The MagiZinc® coating exhibits enhanced resistance against corrosion and achieves a reduction in the use of valuable resources since it offers equivalent or superior corrosion protection while utilising only half of the coating thickness required compared to GI (Kuperus, 2018). Moreover, another driver for automotive manufacturers for using MagiZinc® coatings on their vehicles is its improved galling performance during press forming. Material transfer from the coated steel strip to the press tools is reduced, resulting in less tool pollution and less down time for cleaning these tools (Angeli et al., 2014). Manufacturers other than Tata Steel utilise Zn-Al-Mg coatings of different compositions; however, the Al and Mg contents are typically in the range 1%-3.7% (Marder & Goodwin, 2023).

1.5 Metallurgy of Zn Coatings

1.5.1 Fe-Zn Systems

When steel is immersed in the liquid Zn bath, a series of reactions takes place, depending on the specific composition of the bath. Therefore, it is important to understand the phase transformations occurring at the liquid Zn/steel interface; this enables to predict and control the microstructure of Zn coatings. Equilibrium phase diagrams can be used to predict the development of different phases in the coatings upon contact of several phases under equilibrium conditions. These diagrams are plots of elemental composition and temperature and exist as binary and ternary for two elements systems and three elements systems respectively (Kuperus, 2018).

The phase diagram of the Fe-Zn binary system is shown in Figure 1.1. Fe dissolves in liquid Zn when the steel strip is immersed in the molten metal bath, leading to the formation of intermetallic compounds with the elements present in the bath (Lee et al., 2017). The Zn bath temperature is typically held at 440-480°C and it is possible to observe that several intermetallic phases exist in this temperature range:

1. The gamma (Γ_1) phase with formula $\text{Fe}_3\text{Zn}_{10}$. The crystal structure is body-centered cubic and it contains 23.5-28 wt.% Fe.
2. A second gamma phase (Γ_2) with face-centered cubic structure and chemical composition containing 17-19.5 wt.% Fe.
3. The delta (δ) phase which is HCP and contains 7-11.5 wt.% Fe.
4. The zeta (ζ) phase with monoclinic crystal structure and composition containing 5-6 wt.% Fe (Marder & Goodwin, 2023).

During a typical galvanising process using a pure Zn bath, when the steel substrate reaches the galvanising temperature, Fe from the surface of the substrate and from the pot gear dissolves into the molten Zn bath. This results in a localised supersaturation of Fe in the proximity of the steel substrate and pot gear. The excess Fe combines with liquid Zn leading to the formation of the various intermetallic phases between Fe and Zn. Among these phases, the first one to nucleate is the zeta phase. This phase requires the minimum level of Fe supersaturation in the Zn bath

and it requires the lowest Gibbs free energy for nucleation at the typical galvanising temperatures. As the zeta phase forms on the steel substrate, the delta phase begins to nucleate at the interface between the steel and the zeta phase. Similarly, the gamma phase grows at the interface between the steel and the delta phase. Once these phases have achieved a considerable thickness, further growth is governed by the diffusion of Fe and Zn atoms through these layers of intermetallic compounds. The total thickness of the intermetallic layers accounts for a substantial portion, ranging from 50% to 80% of the entire coating thickness (Chakraborty et al., 2022). The process of nucleation and growth of the intermetallic compounds is schematically shown in Figure 1.2.

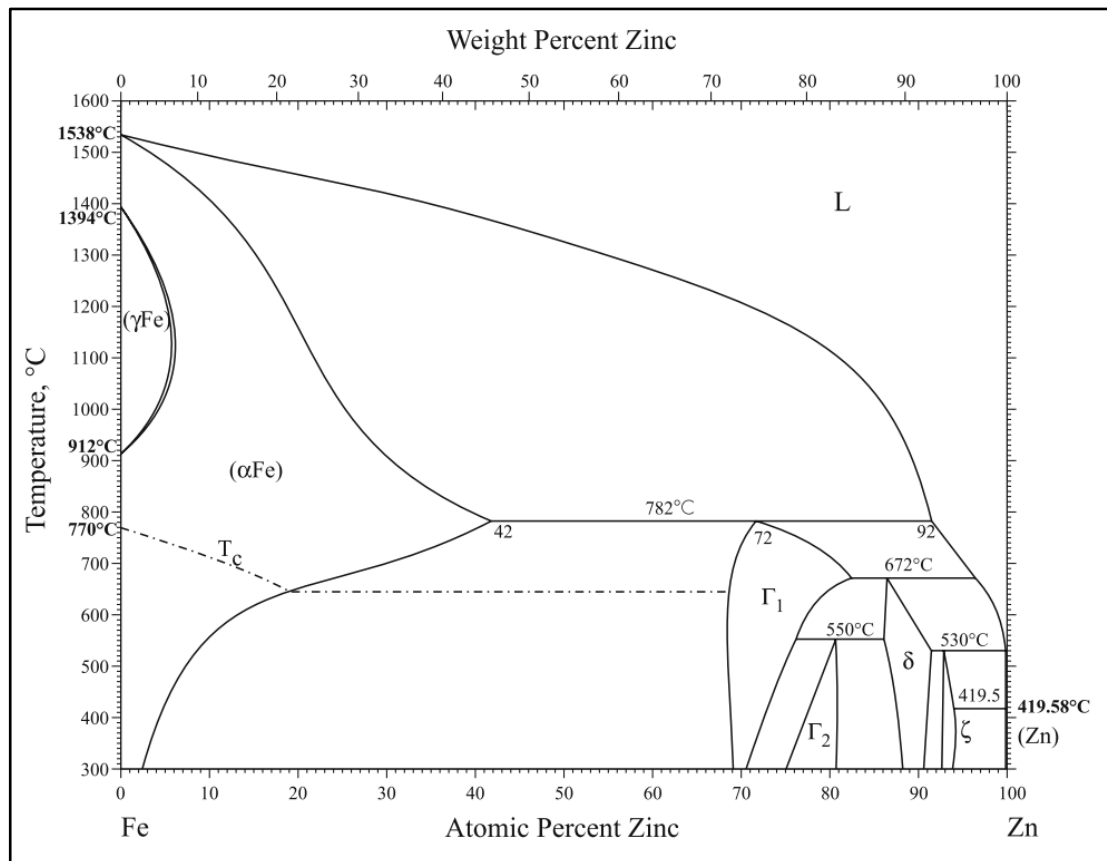


Figure 1.1 Phase diagram of the Fe-Zn binary system. Reproduced from (Okamoto, 2007).

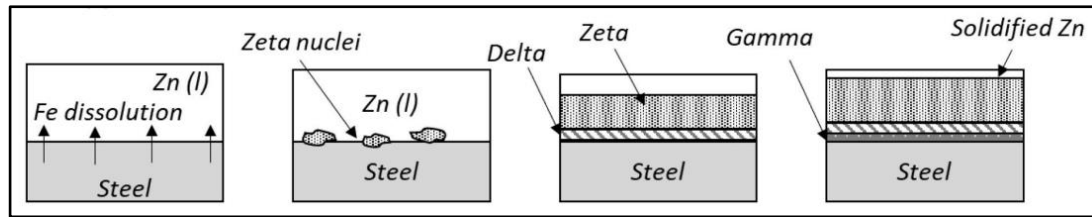


Figure 1.2 Illustration showing the formation of intermetallic compounds in a Fe-Zn binary system. Reproduced from (Chakraborty et al., 2022).

1.5.2 Al Additions

Al is introduced into the Zn bath for two primary purposes: first, to create a protective pure Zn overlay coating by inhibiting the formation of Fe-Zn phases at the interface between the Zn and Fe substrate. Second, it is used to produce multiphase microstructures within the Zn overlay coating for improving corrosion resistance. Additions of Al to the Zn bath are aimed at producing Zn-coated steel with a range of compositions, including GI, Galfan and Galvalume. In addition to generating a diverse array of overlay microstructures and properties, the introduction of Al into the various Zn baths prevents the formation of brittle Fe-Zn intermetallic compounds. This inhibition, which can be temporary, can also result in the formation of intermetallic compounds containing Fe and Al (Marder & Goodwin, 2023).

For the formation of the transient inhibition layer, it is necessary to review the Zn-Al-Fe ternary system (Figure 1.3). The Al concentration in the Zn bath affects the formation of the inhibition layer compound. Observing the Zn-Al-Fe phase diagram, it is possible to see that a minimum of around 0.15 wt.% Al is required for the formation of η -Fe₂Al₅(Zn) at a temperature of 460 °C. η -Fe₂Al₅ intermetallic is the only phase with the capability to inhibit the development of Fe-Zn intermetallic compounds. Managing the amount of Al in the Zn bath is complex due to the presence of Al in two distinct forms. Part of Al dissolves into the liquid Zn phase, while the remaining amount is found in the intermetallic particles present in the bath. The Al in liquid solution, often termed 'active' or 'effective' Al, is responsible for inhibiting the Fe-Zn reaction during the galvanising process. Active Al is significantly influenced by the quantity of dissolved Fe present in the bath. This is because supersaturated Fe

can combine with Zn and Al, resulting in the formation of Al-containing ζ , δ and η $\text{Fe}_2\text{Al}_5\text{Zn}_x$ phases. Consequently, the amount of Al available within the liquid Zn is reduced. Therefore, controlling this entrapment of Al particles within the molten Zn bath is a challenge and determining the concentration of active Al from the bath is problematic (Marder, 2000).

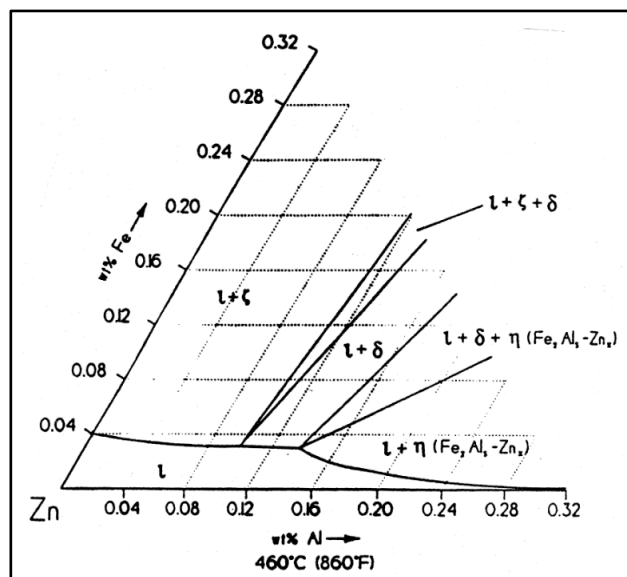


Figure 1.3 Phase diagram of the Fe-Zn binary system, showing the Zn-rich corner of the 460°C isothermal section. Reproduced from (Marder, 2000).

The inhibition of the formation of Fe-Zn intermetallic compounds is temporary. Al function is to not completely suppress the Fe-Zn reaction, but instead, to delay such interaction. Several models have been theorised to understand the breakdown of the inhibition layer. It has been demonstrated that lower Al content in the regions adjacent to the inhibition layer causes the dissolution and breakdown of the Fe_2Al_5 layer. In addition to this, diffusion of Zn through the inhibition layer can occur. Zn atoms reach the substrate, resulting in the nucleation and growth of Fe-Zn intermetallic phases at the interface between Fe_2Al_5 and the substrate. As previously explained, Al in the range of 0.1-0.3 wt.% is introduced into the Zn bath to inhibit the growth of brittle Fe-Zn intermetallic phases. The end of this incubation period occurs upon the breakdown of the Fe_2Al_5 layer, followed by the reaction between Fe and Zn.

For this reason, in industrial production, the immersion time is deliberately kept below the incubation period to achieve a highly ductile end product (Marder, 2000).

1.5.3 Zn-Al-Mg

The structure of Zn-Al-Mg coating is more complex than conventional GI (Figure 1.4). The microstructure consists of large grains of Zn surrounded by phases consisting of Zn-Al eutectic, Zn-Al-MgZn₂ ternary eutectic and some separate MgZn₂. In addition to this, a Fe-Al diffusion layer is also present on the steel surface, which is also observed in GI. The two types of eutectic phases in Zn-Al-Mg coatings are:

1. 'Zn-Mg-Al eutectic', which appears as grey stripes and/or dots of Zn-Al-Mg composition. Differences in grey scale are associated to slight differences in Zn-Mg-Al content. The ternary eutectic consists of Zn, MgZn₂ and/or Mg₂Zn₁₁.
2. 'Zn-Al eutectic', which appears as black phases containing Zn and Al. This phase is characterised by high Al content, which is approximately within the 20-40 wt.% range. Mg is present only at very low levels. This phase is also located at the boundaries of the Zn-Mg-Al eutectic phase (Kuperus, 2018).

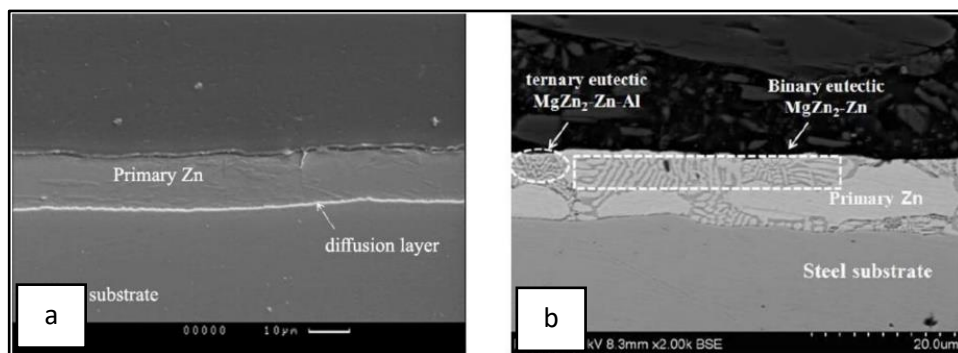


Figure 1.4 Comparison between a GI coating (a) and a MagiZinc® coating (b). Reproduced from (Kuperus, 2018).

1.6 The Continuous Galvanising Process

This section discusses the production of galvanised steel strip, which occurs at the end of the steel production process. The main stages required for the manufacturing

of coated coil from raw materials or steel scrap are schematically shown in Figure 1.5. The first process occurs in a tall, vertical shaft furnace called 'blast furnace', where iron ore is reduced by means of coke to produce 'pig iron'. Subsequently, the hot metal is refined into steel in the BOS (basic oxygen steelmaking) plant. This process route is often replaced with steel production from scrap utilising an electric arc furnace. This is followed by continuous casting to transform liquid steel into slabs, which undergo shaping in rolling machines containing cylindrical rolls. Modern integrated steel plants are equipped with facilities which further process the uncoated strip product through the applications of coatings to the steel strip to impart corrosion resistance properties to the product. These coatings are produced on galvanising lines, such as the ZODIAC plant, which is Tata Steel's world-class coil galvanising line at Llanwern. ZODIAC serves the automotive industry, producing thin strips which automotive customers use for body panels.

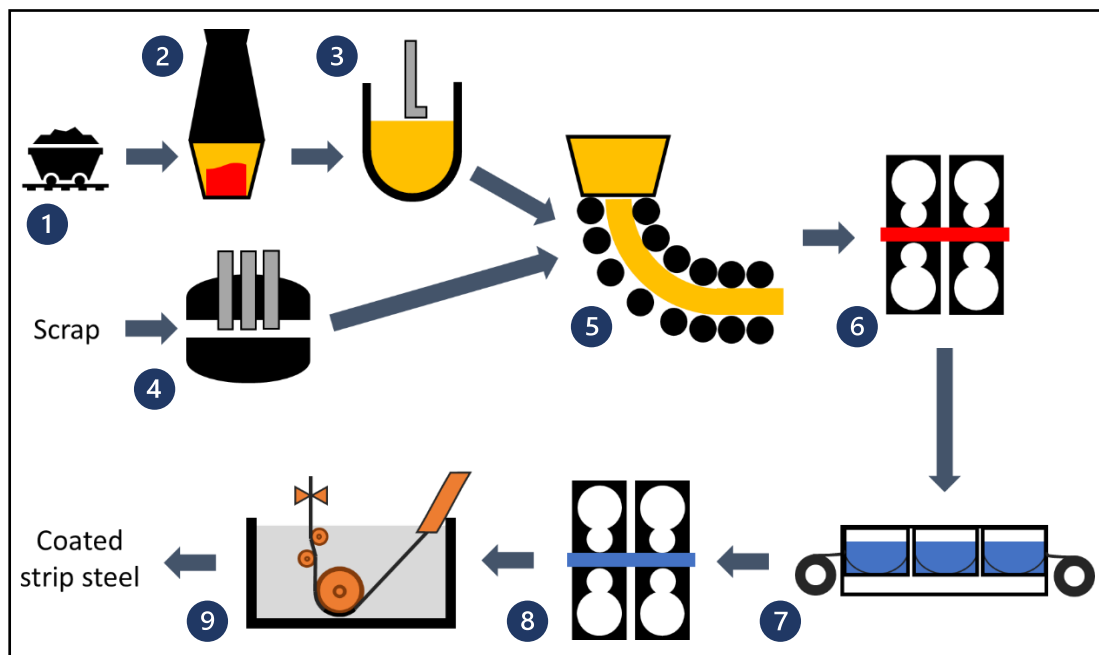


Figure 1.5 Main stages involved in galvanised steel production: (1) raw materials, (2) blast furnace, (3) basic oxygen furnace, (4) electric arc furnace, (5) casting, (6) hot rolling, (7) pickling, (8) cold rolling, (9) continuous galvanising.

1.6.1 Operational Procedures of CG lines

A schematic of the main operations found in a typical galvanising line can be found in Figure 1.7. Modern hot-dip galvanising lines enable the continuous manufacturing of strip steel coated with Zn alloy. These plants are capable of applying Zn coatings with various compositions on products of different width and gauges. The products manufactured on CG lines are categorised based on tolerance and defects specified by customer demands. CG lines operate according to a cyclical campaign schedule and maintenance is carried out between these campaigns. The duration of each campaign varies among different CG lines, although the duration of a typical campaign scheduled to produce GI coatings does not exceed five weeks.

The quality requirements of the products produced in CG lines differ depending on their application. For instance, products which are intended for use within the automotive sector require stringent quality control to ensure that the coatings have minimal defects and the desired surface roughness tolerance. Meeting these standards is important in order to prevent aesthetic issues when the galvanised sheet is formed and painted into automotive panels. As a result, quality control is a fundamental part of CG when automotive-grade galvanised product is manufactured. In contrast, stringent quality requirements are not needed for the production of construction-grade coatings. This distinction is due to the nature of the products processed; automotive panels demand a surface critical product, whereas construction-grade products can allow a less stringent range of thickness differences (Pearcey et al., 2021).

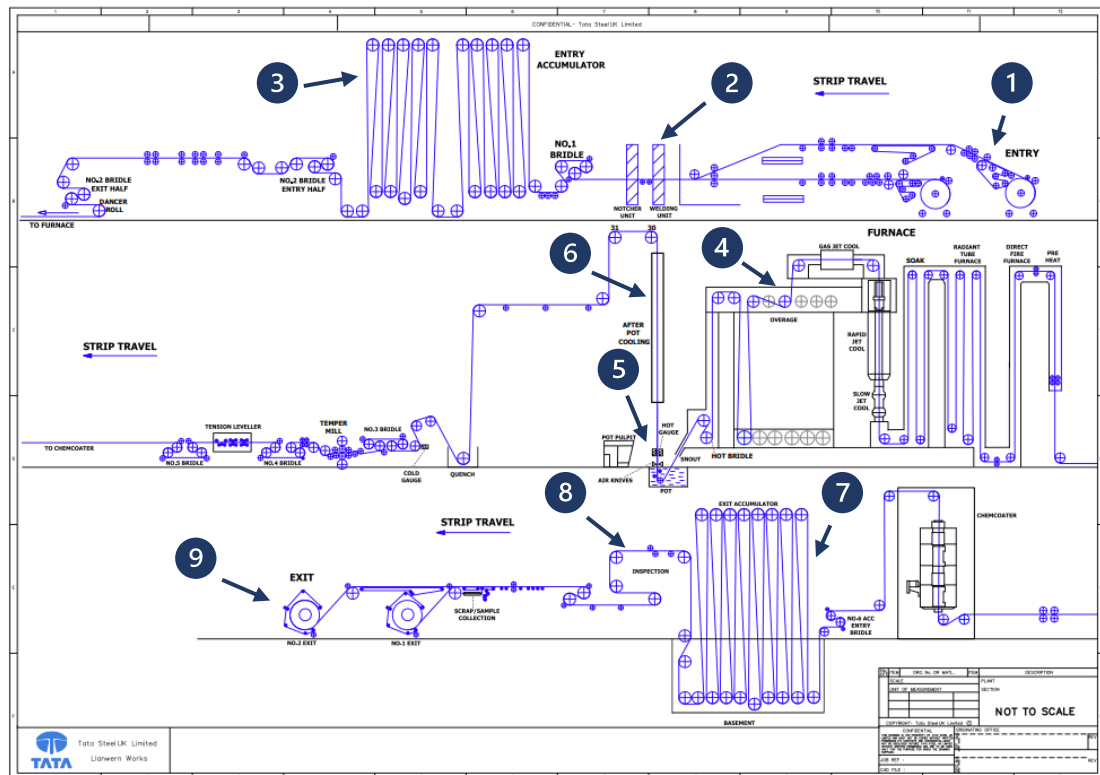


Figure 1.6 Schematic of Tata Steel’s ZODIAC CG line. (1) strip decoilers, (2) welders, (3) entry accumulator, (4) annealing, (5) zinc bath, (6) after pot cooling, (7) exit accumulator, (8) inspection, (9) strip coiling.

1.6.1.1 Entry Accumulator and Cleaning

Strip steel is fed continuously through the CG production line using strip de-coilers and accumulators situated at the line’s entrance. Once uncoiled, the steel strips are welded together end to end to create a continuous strip of steel. Tension along the line is provided by a series of rolls called ‘bridles’, which are located at the entry and further down the line. When the steel coil is getting changed, the accumulators can change in height, ensuring the uninterrupted operation of the line while a new coil is being joined to the strip steel feed and, therefore, they are a key components in the CG process (Pagilla et al., 2001).

Strip steel that is delivered from rolling mills often contains surface residues in the range of 100-200 mg/m². It is crucial to eliminate these residues to prevent any interference with the galvanising reaction or any increase in dross levels within the

galvanising bath, which will be discussed in Section 1.6.2. Surface residues typically contain Fe fines, which may exist in metallic or oxidised forms. Achieving the required level of cleanliness for automotive products, typically 20 g/m² per side of Fe fines and oil, necessitates a wet cleaning process. This procedure involves the application of an alkali solution, initially through spraying. Subsequently, the strip undergoes mechanical cleaning using brushes combined with a feed of sodium hydroxide (NaOH) solution and surfactants. Subsequently, a water jet is used for a final rinsing step (Marder & Goodwin, 2023).

1.6.1.2 Annealing and Entry Snout Control

The ZODIAC line utilises an annealing section where heating occurs using two sets of furnaces: a direct fired furnace and a radiant tube furnace.

When a direct fired furnace is used for heating, it leads to the phenomenon of selective surface oxidation of alloying elements in the substrate, such as Mn, Si, Al and Cr. Additionally, external oxidation of Fe to FeO (wustite) occurs. It is reported that these oxides do not create a continuous layer covering the entire surface and, instead, they are present as islands (Marder & Goodwin, 2023; Marder, 2000).

After the direct fired furnace section, the steel strip moves into the radiant tube furnace, where the temperature is raised to values higher than 700°C, which is above the recrystallization temperature (Marder, 2000). The use of radiant tube heating elements has improved the purity of the annealing furnace environment. This advancement also enables a more accurate regulation of the furnace atmosphere since the combustion by-products from the burner are not introduced into the furnace. Annealing occurs in a N₂/H₂ environment and from this point the atmosphere is maintained inert until the steel is immersed in the Zn pot. The N₂/H₂ is also used to further eliminate residual organic compounds and surface oxides. FeO compounds are transformed to metallic Fe, making the steel surface suitable for galvanising (Marder & Goodwin, 2023).

Preheating is not only used to prepare the surface of the steel for galvanising, but also its function is to achieve the desired microstructure and mechanical properties (Marder & Goodwin, 2023). After the annealing section, the steel strip is cooled to the Zn bath temperature of 465°C using a gas jet. On exiting the cooling section, the steel is introduced to the molten metal bath via the snout and tundish hardware under a reducing HN_x environment. The atmospheric conditions within the snout influence the quality of the coating surface. Vaporised Zn may condense in the snout and potentially fall onto the strip steel before it enters the Zn bath. Coating defects caused by this process are controlled if the partial pressure of oxygen in the snout is increased to a level higher enough to promote the oxidation of the liquid Zn layer present in the snout, but below the level required for oxidising metallic Fe surface that is immersed in the Zn pot. This process is typically referred to as 'wet snout practice' (Marder & Goodwin, 2023).

1.6.1.3 Galvanising Coating Section

Following the cleaning and annealing processes, a layer of Zn alloy is applied to the steel strip upon immersion in the hot dip galvanising bath, as illustrated in Figure 1.7a. There are several components guiding the steel strip through the zinc bath, which include a series of rolls and the journal bearings attached to each side of the rolls. These components are referred to as the 'pot hardware' and are shown in Figure 1.7b.

The steel strip is guided in and out of the Zn bath using three distinct rolls, namely a sink roll, a correction roll and a stabilising roll. The large sink roll is located at the bottom and it is approximately 800 mm in diameter. The function of the sink roll is to change the direction of the steel strip so that it exits the bath upward. The correction and stabilising rolls measure approximately 230 mm in diameter. They are located above the sink roll, providing stability to the strip steel as it exits the Zn pot. This process aims to minimise vibrations to allow excess Zn coating to be efficiently removed by the gas knives and to enhance the overall quality of the final product. The stabiliser roll has the same pass line as the sink roll and they are both fixed in positions. The corrector roll is independent of the other two rolls and it is able to

move forward and backward parallel to the Zn surface (Bright & Ensminger, 2004). Therefore, it enables to correct any strip shape issues.

The material used to make the submerged rolls is stainless steel grade 316L coated with a thin layer consisting of WC embedded in a Co based matrix at a ratio of 90% WC to 10% Co. The WC/Co coating is applied via a thermal spraying process called 'high velocity oxy-fuel' (HVOF), which is described in Section 1.9.2.

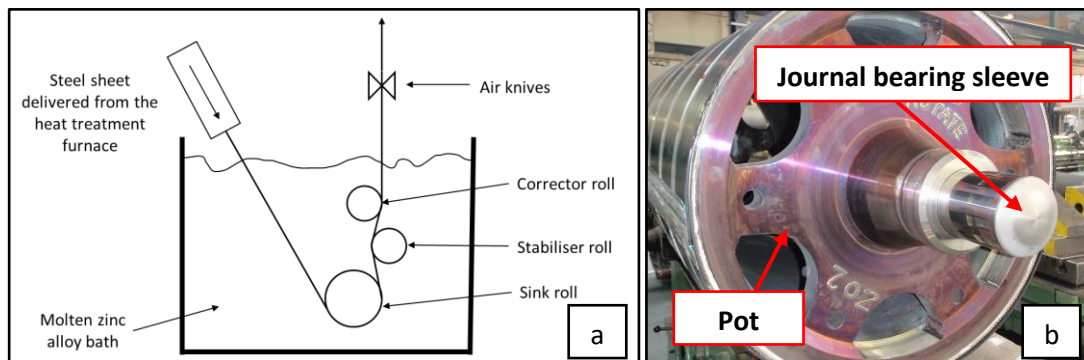


Figure 1.7 Sketch of the hot dip process in the Zn pot (a); galvanising bath hardware (b).

Bearing assemblies are used to support the submerged pot rolls. A bushing is attached to the roll support arm and a journal bearing sleeve is directly attached to each end of the roll shaft. In the ZODIAC CG line at Llanwern, the bushing and the roll support arm are joined by welding, whereas the bearing sleeve is mounted using an assembly mechanism which eliminates the need to weld the component to the roll (Faulkner, 2020). The ZODIAC line utilises journal bearings that are manufactured from Wallex6™ alloy, whose composition can be found in Chapter 3, and the bearing sleeve component is coated with a 150 µm HVOF WC-Co coating.

The temperature of the galvanising bath is maintained at around 465°C, which is above the melting point of Zn to ensure that the metal is in the liquid state. The speed of the ZODIAC CG line is kept at 150m/min and the immersion time of the strip steel in the Zn pot is approximately 1-3 seconds. The liquid Zn or Zn alloy is first required to wet the steel surface in order to obtain a galvanised coating. For this reason, the wetting angle is an important property to determine the wetting behaviour of steel with liquid Zn. The wetting angle was found to be a function of the surface oxides

present on the steel surface, hence why they are eliminated during annealing to promote the reduction to Fe, achieving a surface that is ready for galvanising. Another parameter which affects the wetting angle with Zn is the immersion time; as the steel enters and subsequently exits the Zn bath, nucleation and growth of the intermetallic phases occurs on the strip steel surface, as previously described in Section 1.5. As a result, the wetting angle physically 'flattens' (Marder & Goodwin, 2023).

Control of the Zn coating thickness and uniformity is achieved by using gas wiping knives that blow two jets of pressurised gas onto the surface of the strip steel. As the strip exits the galvanising bath, excess Zn is sent back into the pot to produce the desired coating thickness, which is monitored using on-line X-ray measuring equipment (Marder, 2000). The ZODIAC galvanising line uses air knives that are enclosed in a N₂ shroud in order to produce a shielded atmosphere between the liquid Zn level and the knives. The coating thickness is determined by several parameters, including gas pressure, knife height, air knife to strip distance and contact angle of the gas. Variations of the nozzle to strip distance can be detrimental to coating weight uniformity, as the coating thickness varies linearly with distance. These variations are observed during excessive strip vibration, which defines the amount of horizontal movement occurring in the direction perpendicular to the strip surface (Pearcey et al., 2021). Therefore, it is important keep vibrations at a minimum to ensure that the correct thickness is achieved and minimal surface defects are present.

Although novel materials and coatings have emerged for manufacturing journal bearing components, effectively addressing the challenges linked to increased vibration levels resulting from deteriorated bearings remains unresolved. Even with the application of stabilising and correcting rolls to minimize strip movement, increased Zn levels are frequently employed to counteract strip movement, enabling to produce a consistent coating thickness. Strip movement is predominantly associated with vibrations resulting from degraded journal bearing components. The deterioration of the bearings surface is responsible for causing vibrations in the gas

knives section of the CG line, compromising the quality of the coating (Escott et al., 2021).

It was earlier discussed the requirements dictated by the automotive industry are very stringent regarding product quality. As a result, the production window for premium 'full-finish' product manufactured for the automotive sector is restricted. Due to their limited service time, degraded pot roll journal bearings are typically replaced every 5 weeks. Therefore, the consequences related to bearing induced strip vibrations are quality issues and loss of yield with high financial reward. (Escott et al., 2021). In addition to this, replacing the degraded hardware with new components significantly increases the costs required for maintenance of the CG line. For this reason, achieving a reduction of the 'down days' required for maintenance leads to substantial financial interest for Tata Steel, hence the importance of developing a material for producing pot roll journal bearings with extended durability.

Product and downtime costs are dependent on the type of product being processed. It was estimated that downtime costs around €8,400 (~ £6,960) per hour for an automotive-grade galvanising line and between €3,300-€4,700 (~ £2730-£3890) per hour for a non-automotive grade galvanising line. Similarly, full-finish coatings can be up to five higher than the average cost. These figures do not include lost opportunity costs; however, the typical cost of full-finish product is approximately €800 (~ £660) per ton, resulting in profits ranging from €100 (~ £82) to €200 (~ £165) per ton. Given a production speed of 1 ton/min, it was estimated that the sales value of production is roughly €48,000 (~ £40,000) per hour and during downtime the lost profits range from €6,000 (~ £4,970) to €12,000 (~ £9,940) per hour. Therefore, a four-hour stop for changing the pot hardware leads to a lost opportunity between €24,000 (~ £19,880) to €48,000 (~ £39,760), which adds to the actual costs of downtime mentioned earlier (Faulkner et al., 2017).

1.6.1.4 After Pot Cooling

Coating solidification occurs in a cooling tower, where the strip steel proceeds vertically. It is shown that for GI-coated strip, the Zn crystal (spangle) size and the

dominant crystallographic orientation (texture) of the Zn coating are affected by the cooling rate. Conventional air cooling on GI-coating produced a spangle size of 700-800 μm and a roughness R_a of 0.57 μm , provided that spangle-formers such as Pb and Sb are not present. On the other hand, using an electrostatically charged water spray, which results in a more rapid cooling through the solidification range, produces a reduced spangle size of 80-200 μm with an R_a of 0.32 μm . Furthermore, there is evidence that rapid cooling leads to a reduced intensity of the basal (0001) plane in the GI coating, which determines the strength of adhesion of paint to the coating (Marder & Goodwin, 2023).

After exiting the cooling tower, the thickness of the strip is reduced to typically 0.5%-1.5%. This process is called temper rolling, but it is also known as 'skin passing'. Temper rolling is performed utilising 1%-2% water soluble lubricant for GI-coated product. The temper rolling process is carried out for several reasons. First of all, the process introduces dislocations into the steel, pinning C and other interstitial elements and preventing the discontinuous yielding associated with the formation of Lüders lines. Secondly, the strip is conditioned at the surface for subsequent treatments by imparting a texture onto it. Lastly, temper rolling enables to improve strip shape and its flatness (Marder & Goodwin, 2023). Tata Steel's ZODIAC CG line uses non-contact technology for online measurement of surface roughness. After tempering, the strip steel passes through tension levelers, where a bending force is applied to improve shape and mechanical properties of the product. A passivate layer for additional corrosion protection is applied to construction grade product. The thickness of this coating is very small (50 mg/m^2) and the composition used in ZODIAC is phosphate-based, which replaced the old chromate-based layer used in the past.

The last stage in the CG process is a final inspection stage, which is conducted before the steel exits the line. Visual inspection is performed manually as well as by a CognexTM imaging system consisting of a series of cameras used to capture images of the strip surface. The defects detected are recorded and if the product quality requirements set by both Tata Steel and the customer are met, the coated strip steel is coiled and finally released.

1.6.2 Dross and Dross Build-up

In the CG process, the strip steel is continuously fed into the Zn pot and this process is accompanied by constant dissolution of Fe from the steel into the bath. As the strip steel enters the galvanising bath, dissolution of Fe occurs rapidly and the regions with high Fe content in the Zn bath are those located near the strip surface (Marder & Goodwin, 2023). The amount of dissolved Fe is always higher than that removed from the bath by the coating, producing a saturation of the bath in Fe. When Al is added to the bath with a concentration above its solubility limit in liquid Zn and the solubility limit of Fe from the strip steel is surpassed, dross particles start to develop at the bath-steel interface. Intermetallic compounds can precipitate as Fe-Al, whose density is lower than that of liquid Zn and, as a result, it is found near the surface of the galvanising bath; therefore, this phase is referred to as 'top dross'. In addition to this, intermetallic compounds can precipitate as Fe-Zn, which is known as 'bottom dross' as it is found at the bottom of the bath. However, the formation of bottom dross is completely inhibited when the Al content in the bath is above 0.135 wt%. Dross can also be categorised as oxides involving ZnO and/or AlO (Kuperus, 2018).

Top dross particles consist of Fe-Al intermetallic particles with Fe_2Al_5 base structure. The average size of these dross particles is typically between 10-30 μm and since they float at the surface of the bath, they can potentially interact with the surface of the strip, causing production issues. Bottom dross is characterised by FeZn_7 (σ_1 phase) and FeZn_{13} (ζ phase) and its content vary depending on the composition of the galvanising bath used (Kuperus, 2018; Marder & Goodwin, 2023).

Dross can grow on the surface of the pot rolls, resulting in defects in the coated product, which gradually increase throughout the galvanising campaign. Stainless steel 316L is widely used as a pot roll material due to its corrosion resistance and the molybdenum (Mo) additions to its composition. However, the material is not inert to liquid Zn and it undergoes degradation over the course of the galvanising campaign. The reaction between stainless steel and the molten metal bath produces dross build-up on the surface of the rolls. Dross build-up impacts the production and quality of galvanised strip steel as it can lead to malfunctioning of the bath hardware and

degradation of the surface of the Zn coating due to the higher hardness of the dross particles. For this reason, a WC-Co layer is typically applied to the surface of the sink and stabiliser rolls to improve the corrosion resistance in liquid Zn (Kuperus, 2018; Seong et al., 2001). There is evidence that the bath geometry and other operating variables have an impact on dross production. In order to design galvanising pot equipment and operating condition practices that can lead to a reduction in dross production, different variations from the base configuration were studied. It was shown that a smaller bath volume resulted in a higher concentration of precipitates; moreover, increasing coating weight enabled to minimise dross production, as there is a greater Al consumption with the higher coating weight and, therefore, the Al levels in the bath are lowered (Marder & Goodwin, 2023).

1.6.3 Galvanised Coating Defects

Although nowadays it is possible to obtain galvanised coatings with superior surface quality, the production of defect-free coatings for the automotive industry is still a challenge (Tang & Goodwin, 2001). On CG lines, such as ZODIAC, tonnes of coils are rejected as they fail to meet the quality standards, limiting the financial potential of CG lines. The presence of defects in the coating is dependent on the operation of the galvanising bath; in addition to this, defects can be developed during the other stages involved in the production of galvanised steel strip.

Defects that are already present in the steel surface before immersion in the galvanising bath are magnified by the application of the Zn coating. Imperfections caused by upstream process such as hot strip mill mechanical defects, scratches or surface damage during cold rolling produce Zn-Fe alloy outbursts at the interface between the steel and the coating (Figure 1.8a) or variations of the dendritic Zn crystal orientation. If mill scale, rusts, oxides, oils and cleaning solutions are not removed from the steel surface prior to immersion in the galvanising bath, incomplete wetting can occur. This results in areas which remain uncoated, known as 'bare spots' (Figure 1.8b). Another issue is the local discoloration of the coatings caused by stains or small patches of oxide skin. Surface contaminants can be

responsible for reducing the adhesion between the coating and the steel causing 'exfoliation' or 'peel off', which refers to the delamination of the Zn coating upon the application of an external force (Saravanan & Srikanth, 2018; Tang & Goodwin, 2001).

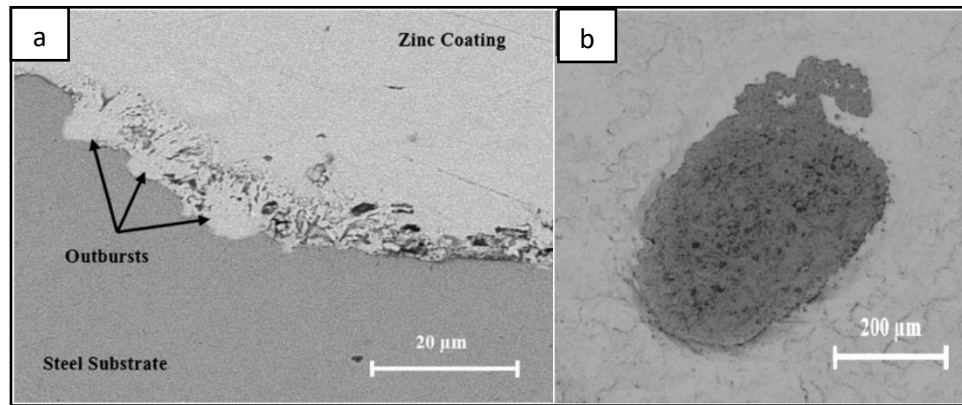


Figure 1.8 Outbursts at the interface between the steel and the coating (a); SEM image of a bare spot (b). Reproduced from (Azimi et al., 2012).

Coating defects are also related to the operational procedures of the galvanising bath. When Zn vapours form in the snout, condensation of Al-free Zn takes place, forming Zn-Fe alloy outbursts which appear as raised spots in the coating. For this reason, it is important to maintain the correct partial pressure of oxygen in the snout, as discussed earlier in this section. When dross particle entrapment through the coating thickness is observed, high spots or bumps are produced. Entrapment of large dross particles in the coating is typically observed when the Al content in the bath is rapidly increased to a higher concentration, for example during transition from GA to GI. If significant dross pickup occurs on the submerged pot rolls, dents can be produced on the strip surface (Saravanan & Srikanth, 2018; Tang & Goodwin, 2001). Moreover, when the effective Al content in the galvanising bath is relatively low, Zn-Fe crystallites can form in the coating. Crystallites can dissolve if the immersion time is increased; however, the typical dipping time in CG lines is less than 5 seconds, which is insufficient for completely dissolving Zn-Fe crystallites. In addition to this, the content of these crystallites depends on the strip entry temperature and substrate chemistry. If a relatively high entry temperature is used and if the substrate chemistry is complex, Zn-Fe crystallites are formed with effective Al content as high as 0.18%.

Although the existence of crystallites does not compromise the adherence of the coating to the substrate, some galvanisers are concerned about their presence in the coating (Tang & Goodwin, 2001).

Defects originating during air jet wiping include jet lines and coating sags. The former is characterised by longitudinal bands where the coating is slightly thinner or thicker than the surrounding areas and are formed should Zn dust block the knife slot, causing an air jet disturbance. Sags or ripples are caused by high strip and bath temperatures or excessive strip vibrations. If the Zn does not wet the surface of the strip uniformly, the so-called 'caterpillar' defects are observed (Saravanan & Srikanth, 2018).

1.7 Galvanising Pot Bearings

1.7.1 Design and Operation of Galvanising Pot Bearings

Submerged pot roll bearings are important for maintaining stability within the coating section of a CG line. The function of these components is to allow unhindered rotation of the galvanising pot rolls used to guide the strip steel into the molten Zn bath. The ZODIAC CG line utilises journal bearings which are illustrated in the CAD renders shown in Figure 1.9a,b for the stabiliser roll and Figure 1.9c,d for the larger sink roll. It is possible to observe that the bearing design differs for each type of roll, as the stabiliser roll bearing is characterised by a closed end with an opposing end open and flanged. On the other hand, the design of the sink roll bearing sleeve is simpler and is open ended. For both geometries, the sleeve is partially surrounded by a bushing; the stabiliser roll utilises a bushing with a half circle design of 180 degrees and the sink roll utilises a bushing with a partial circle of 120 degrees (Faulkner, 2020).

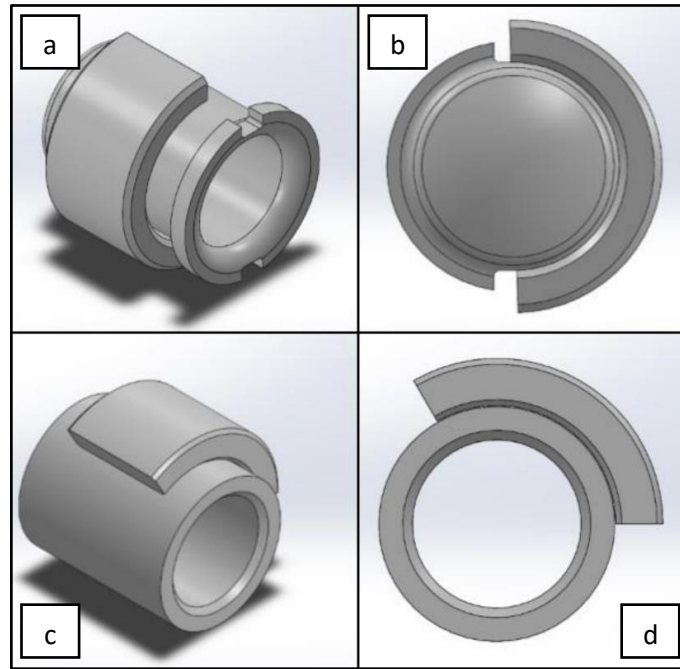


Figure 1.9 CAD renders of: stabiliser roll bearing sleeve (a) and bushing (b), sink roll bearing sleeve (c) and bushing (d). Reproduced from (Faulkner, 2020).

An example of journal bearings installed on the end of a stabiliser pot roll is shown in Figure 1.10. The placement of the journal bearing bushing and sleeve components is achieved by the load applied by the tension of the strip steel. At the ends of the galvanising bath rolls, the journal bearing sleeves are welded taking the form of a basic cylindrical sleeve. These sleeves come into contact with a journal bearing bushing of a slightly larger diameter, with typical clearance values of 2 mm circumferentially, and both components share a common centre. The tension of the strip steel in the galvanising pot is responsible for positioning the bearing sleeves against the bushing components, as the steel is continuously fed in the Zn bath through the submerged rolls. Therefore, the journal bearing sleeve and bushing are crucial for the stability of the strip steel passing through the coating section of the line and the stable operation of these two components enables the production of galvanised coatings with superior quality required for the manufacturing of full finish product (Faulkner, 2020).

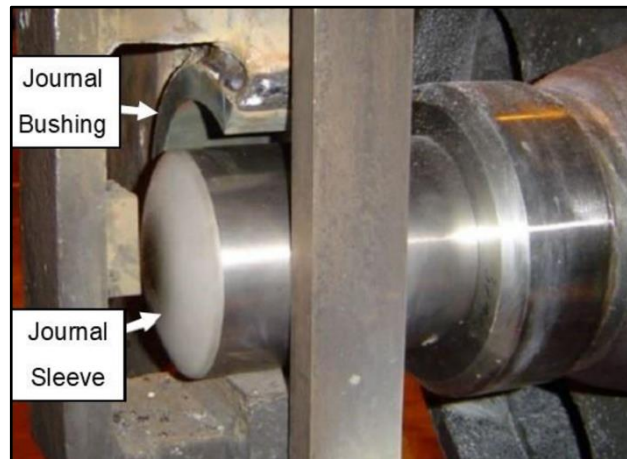


Figure 1.10 Photograph of the stabiliser roll journal bearing components used in ZODIAC. Reproduced from (Faulkner, 2020).

The strip, as it travels around the sink roll, corrector roll and stabiliser roll within the Zn bath, experiences a line tension that regulates the position and movement of the strip throughout the CG line. The line tension varies across different sections of the line, with the lowest tensions applied in the annealing segments where preventing strip deformation is crucial. Intermediate tensions are employed in the coating section to impart sufficient turning torque to the submerged rolls, preventing skidding and managing vibrations. The highest tensions occur in the temper mill and tension levelling sections. In the coating section, the highest tensions are typically employed during the production of automotive products. These tensions are sustained by the two support bearings located at each end of the submerged pot rolls (Marder & Goodwin, 2023).

A model (Faulkner, 2020) of the load conditions of submerged pot rolls was used to resolve bath roll loads into bearing rolls using data captured on the ZODIAC CG line. The load on submerged pot rolls is related to line tension, which is determined by product schedule. In this model, the rotational speed was assumed to be analogous to the bearing rotational speed for corresponding roll and bearing couplings. In addition to this, for determining the bearing load over the examined campaign length, it was assumed that each bearing supported half of the total load exerted on each respective roll. Considering both of the two assumptions, pot roll and bearing load were found to be directly proportional to line tensions. The line and bearing

operating conditions calculated in this study are summarised in Table 1.1 and Table 1.2 respectively. The maximum value of the sink, corrector and stabiliser bearing loads are 35.78 kN, 14.34 kN, 13.86 kN, which were determined for a maximum line tension of 40 kN. The average force for line tension recorded was 22.1 kN, which corresponds to average sink, corrector and stabiliser bearing loads of 19.1 kN, 7.96 kN and 7.5 kN. The sink roll was found to have a maximum and average rotational speed of 67.13 and 48.94 RPM respectively. The maximum and average rotational speed of the stabiliser and corrector rolls were measured to be 195.78 RPM and 268.5 RPM. It was also reported that the average and maximum line speeds were 123.01 m/min and 168.7 m/min.

Table 1.1 ZODIAC CG line operating conditions (Faulkner, 2020).

Maximum Tension [kN]	Average Tension [kN]	Average Line Speed [m/min]	Maximum Line Speed [m/min]
40.0	22.1	123.0	168.7

Table 1.2 ZODIAC bearing operating conditions (Faulkner, 2020).

Bearing	Maximum Load [kN]	Average Load [kN]	Maximum Rotational Speed (RPM)	Average Rotational Speed (RPM)
Sink	35.78	19.12	67.13	48.94
Corrector	14.34	7.96	268.50	195.78
Stabilising	13.86	7.51	268.50	195.78

1.7.2 Lubrication of Journal Bearings

Bearings are elements used to support a certain load that generally is applied to a shaft, enabling the relative movement between two components of a machine (Childs, 2019). Different examples of bearings exist, as they can be categorised by the type of the relative motion required and type of constraints applied to the bearing (e.g. about a point, about a line, along a line, etc.) (Neale, 2013). One of the most

common types of bearings are journal bearings, whose function is to support a rotating journal or shaft (Balakrishnan et al., 2010).

Typically, in sliding bearings the relative movement is facilitated by the presence of a thin layer film of lubricant. A lubricant is interposed in a bearing to minimise friction between two surfaces and to dissipate heat (Childs, 2019). Therefore, the use of lubricants leads to a reduced wear and prolonged lifetime of the bearing components. Lubricants can be used in liquid form as well as in the solid state; examples of these include polytetrafluoroethylene (PTFE) and molybdenum sulphide (MoS), which can be found in static bushing components. The pot roll bearing systems used in the ZODIAC galvanising line are open and completely submerged in liquid Zn alloy. In addition to this, the surfaces of the bearing components are in contact. Figure 1.11 illustrates a schematic of a typical construction of a two-component journal bearing with interposed lubricant. The distance separating the two components with differing diameters is known as clearance.

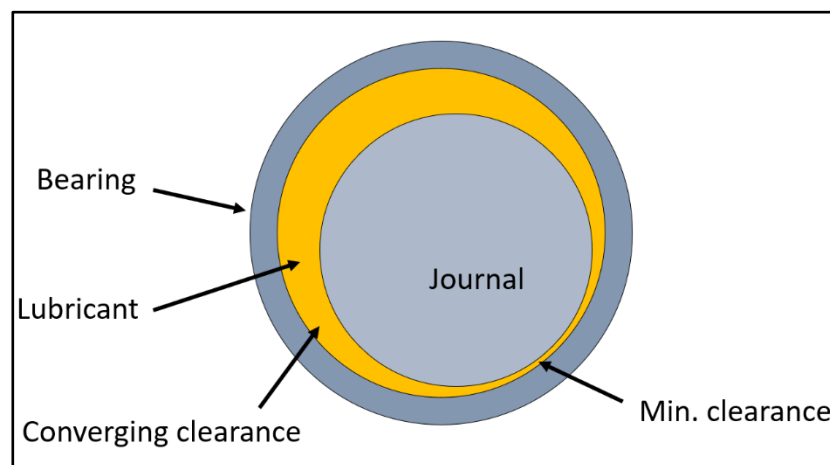


Figure 1.11 Sketch showing the cross-sectional view of a typical journal bearing.

When liquid lubricants are used, three different types of lubrication regimes are possible, namely boundary, mixed and hydrodynamic lubrication. Hydrodynamic lubrication regime is observed when the interposed lubricant separates completely the two surfaces in relative motion. The amount of separation between the journal and bearing components in this regime is represented by a film thickness; when

hydrodynamic lubrication occurs, the film is thick enough to avoid direct or metal-to-metal contact between the friction-coupled elements (Zhang, 2014). In the hydrodynamic lubrication regime, the journal rotates forming a convergent and divergent geometry with the static bushing component. In the convergent region, the fluid is forced to pass into an ever decreasing cross-sectional area due to the journal rotation; as a result, pressure increases, causing the film to push against the journal sleeve (Dhande & Pande, 2018).

When two or more lubrication mechanisms are present, mixed lubrication occurs. Typically, this regime is associated with frequent physical contact between the two solids; however, part of the bearing surface will develop a partial hydrodynamic fluid film (Zhang, 2014). A portion of the load is carried by that partial hydrodynamic lubricant film and, for this reason, it will contribute to achieve a reduced friction and wear compared to the unlubricated condition. Moreover, mixed lubrication can be considered a transitional phase from boundary to hydrodynamic lubrication regime (Abdelbary & Chang, 2023).

In some circumstances, the solid surfaces are so close to each other that contact is dominated by the asperities present at the surface of the two solids or interactions between monomolecular or multi-molecular films of lubricants (liquids or gases); this regime is referred to as boundary lubrication (Zhang, 2014). When a journal bearing operates in the boundary lubrication regime, complete contact between the sleeve and bushing components of the bearing occurs. The causes for such contact are numerous and they include heavy loads, low running speeds, high surface roughness or insufficient supply of lubricant required to produce a thick fluid film to separate the two surfaces (Rahnejat, 2010).

A hydrodynamic feasibility study was conducted by (Faulkner, 2020) to improve the design of the journal bearing systems used in ZODIAC. It was found that the stabiliser and corrector bearings require a diameter of 200 mm, a width of 175 mm and a clearance of 100 μm to produce pressurised fluid film lubrication in submerged pot roll bearings. Regarding the sink roll bearings, a 300 mm diameter bearing of 400 mm width and 100 μm clearance were specified. The dimensions required for the sink roll bearings are larger as the load supported by the bearings is greater and the rotational

speed of the sink roll is lower. It was concluded that building bearing systems with these dimensions could enable the production of a film with minimum thickness of 10 μm at average line speed and tension values.

1.7.3 Wear of Journal Bearings

Failure of the film compromises the relative motion of solid bodies, resulting in inevitable damage to the surfaces in contact. Therefore, film failure ultimately leads to significant wear (Stachowiak & Batchelor, 2013). Wear is a phenomenon that can be difficult to understand and the wear process is complicated by various factors, including changing conditions at the interface during service and the formation of reaction products. In certain cases, multiple wear mechanisms can be present (Bruce, 2012). The main types of wear are sliding wear, abrasive wear, fatigue wear and chemical wear.

1.7.3.1 Sliding Wear

Sliding wear refers to the deterioration that arises when two solid surfaces move across each other. In most practical scenarios, the sliding surfaces are typically lubricated and the resulting wear is termed 'lubricated sliding wear'. However, in certain engineering applications, surfaces interact in the absence of lubrication, leading to wear termed as 'dry sliding wear'. While the term adhesive wear is sometimes used to characterise sliding wear, it can be misleading. Adhesion is a significant factor in sliding wear, but it is one of many physical and chemical processes that can be observed. Severe sliding wear is frequently described with terms like 'scuffing', 'scoring' and 'galling'. Scuffing occurs in metallic contacts lacking adequate lubrication, resulting in changes in surface texture aligned with the direction of relative motion. Scoring refers to the formation of grooves and scratches in the direction of sliding, potentially involving abrasion by particles. Galling is used to describe a severe scuffing, involving local welding and causing substantial surface

damage. Galling occurs in unlubricated sliding at low speeds and can also be observed in lubricated systems if the lubricant film fails.

As surfaces move relative to one another, mechanical stresses arise, leading to material damage through processes such as plastic deformation or fracture. This damage can occur both at the microscopic and macroscopic level. Additionally, as two surfaces undergo sliding, frictional work is dissipated in the form of heat, causing the temperature in each body to increase. Another concern arises when the surface of the material interacts with the surrounding environment through chemical reaction. This interaction may result in the formation of reaction layers which can be subsequently broken down during sliding, producing debris and altering the nature of the contact (Hutchings & Shipway, 2017).

1.7.3.2 Abrasive Wear

Regarding abrasive wear, the surface of a material is removed or displaced due to the interaction with hard particles or hard asperities present on the contacting surface. The mechanisms involved in abrasive wear include both plastic deformation and brittle fracture. Two categories commonly identified are 'two-body abrasive wear' and 'three-body abrasive wear.' Two-body abrasion results from hard protrusions or attached hard particles on the counterface, while three-body abrasion involves freely moving hard particles that can roll and slide between sliding surfaces, possibly of different materials. When corrosion coincides with abrasive wear, the combined material removal rate may exceed that of corrosion or wear alone, and it is possible to use the term 'tribocorrosion'. The impact of lubrication on abrasive wear differs significantly from what is observed during sliding wear. Lubrication in sliding wear typically minimises wear by reducing tangential stresses on the surface and mitigating the frequency and severity of contact between asperities. However, as the abrasive particles are larger than the hydrodynamic film thickness developed in lubricated systems, contact between the particle and the counterface still occurs even when a lubricant is present (Hutchings & Shipway, 2017).

1.7.3.3 Rolling Contact Wear and Fatigue

The expression 'contact fatigue' is typically found in the literature to describe surface damage resulting from repeated rolling contact. Surface defects form after a specific number of rolling contact cycles, leading to contact fatigue. Once pits are observed on the rolling surface of a bearing, they pass through the rolling contact causing excessive vibration, which prevents further use of the bearing. Failure of the bearing induced by contact fatigue is typically sudden and must be avoided. Available evidence indicated that fatigue wear arises from the development of cracks in the deformed surface layer. As rolling occurs, local contact stresses are high and the wear mechanisms are predominantly influenced by material properties and operating conditions (Stachowiak & Batchelor, 2013).

1.8 Material Selection for Galvanising Bath Hardware

1.8.1 Fe- and Co-based alloys

An onsite investigation study (Wang et al., 2015) was conducted to determine the dominant influencing factors in the failure of a sink roll system, including its sleeves and bushings, in a CG line. The study, which analysed the abrasions between the bearing components of the pot roll system, concluded that the wear between the sleeves and bushings was the dominant factor for the on-line cycle life of the sink roll system. The consequences of the premature failure of the pot roll bearings are increased costs of production and limited production efficiency.

It was reported that one of the most common failure modes for sink roll bearings is severe abrasive wear that is manifested as deep grooves with a size of up to 1 cm developed on the surface of the bearings. The pot roll bearings used by the galvanising industry are designed so that their operating stress is always below the yield strength of the bearing materials at the service temperature. Therefore, a mechanism other than accumulation of low cycle fatigue damage must be responsible for the premature failure of the pot roll bearing components (Tang et al., 2010). Recent research (Shi et al., 2018) concluded that the failure mechanism

responsible for the serious abrasion and instability of a sink roll system is the poor corrosion resistance of the hardware materials in liquid Zn.

Stainless Steel 316L (SS 316L) has been one of the main materials of choice for the fabrication of galvanising pot hardware, as it provides good corrosion resistance in molten Zn at a convenient price. Other materials, including Fe-based and Co-based, were considered for components demanding greater wear resistance, such as roll bearings. Although Fe rapidly dissolves in pure Zn, a bath with Al content above 0.15 wt.% causes the Al-Fe reaction to prevail over the Zn-Fe reaction. As a result, Fe-Al phases form at the surface of the alloy (Matthews & James, 2010). Figure 1.12 shows SEM images of SS 316L after immersion in GI; it is possible to observe two distinct reaction layers. Over the whole surface of the sample, a layer of intermetallic dross particles was observed. These particles were found to be attached to the surface of the steel, instead of 'floating' in the solidified Zn. The second layer is a diffusion layer and formed due to Al diffusion and Fe dissolution from the steel specimen (Kuperus, 2018).

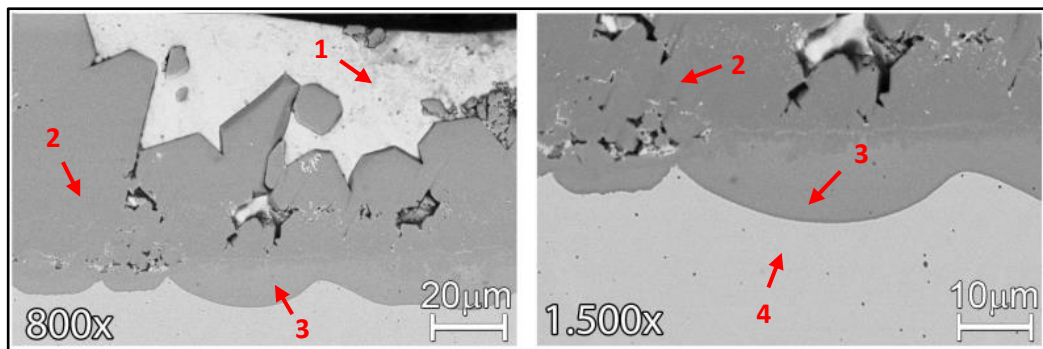


Figure 1.12 Cross-section of SS 316L after immersion in GI for 8 days: (1) residual Zn, (2) intermetallic dross particles, (3) diffusion layer, (4) SS 316L specimen. Reproduced from (Kuperus, 2018).

After nucleation and growth of the reaction layers, physical material loss occurs, as the hardware material is diffused into the galvanising bath. Introducing intermetallic dross particles between the sleeve and bushing components of the bearing will transform the system from a two-body wear to a three-body wear system (Faulkner,

2020). When the intermetallic dross particles are introduced in the clearance between the bearing components, they would contribute to the observed abrasive wear mechanisms, forming grooves on the surface of the bearings, as shown in Figure 1.13a.

Investigations (Shi et al., 2018) of the sleeves of a sink roll-system were conducted to verify the role of liquid Zn corrosion in the serious abrasion observed between the bearing components. The sleeves analysed in this study were manufactured from SS 316L and the formation of intermetallic phases after immersion testing in molten Zn was confirmed. This reaction with the molten metal bath could decrease the hardness of the bearing surfaces, accelerating the wear of these components. In addition to this, evidence of dross particle entrapment in the clearance between the sleeves and bushings was found. The dross particles were removed from the clearance and characterised (Figure 1.13b). The size of the particles was found to be approximately 500 μm and it was reported that the hardness of the particles reached a micro Vickers hardness of 700 HMV. For this reason, it was postulated that they influenced the wear of the bearings surface, producing uneven abrasion and leading to failure of the sleeve and bushing components.

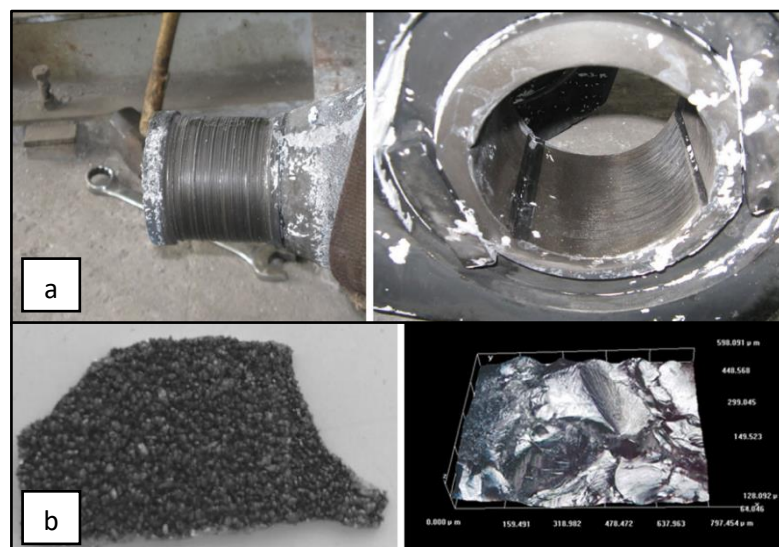


Figure 1.13 Worn bearing sleeve and bushing with deep abrasive grooves present on the surface (a); characterisation of intermetallic dross particles (b). Reproduced from (Shi et al., 2018).

Co-based alloys have a similar dissolution mechanism and the high affinity between Co and Al is responsible for the formation of a surface dross layer (Matthews & James, 2010). The additions of elements such as Mo results in the formation of Laves phases which inhibit the formation of Co-Al reaction products. Therefore, the high Mo content of some Co-based alloys, such as Tribaloy T400 and T800, improves the corrosion resistance of the material (Goodwin et al., 2002; Matthews & James, 2010). The galvanising industry currently makes an extensive use of Co-based ‘Stellite’ alloys (or equivalent ‘Wallex™’ grades). Wallex™ alloys, including Wallex6™, Wallex4™ and Wallex180™, were tested in GI and their performance was compared after 5 weeks of immersion. Wallex6™, which is used as bearing material in ZODIAC, was reported to react with molten Zn and Al. An FeAl and a CoAl intermetallic phase nucleated on the sample surface and a subsurface reaction layer was observed, whose shape and uniformity was disrupted only when the CrCoWMo phases of the alloy were present, as shown in Figure 1.14. Similarly, Wallex4™ and Wallex180™ reacted with the molten metal bath; however, roughness measurements, which were used to determine the amount of deterioration after testing, showed that Wallex4™ and Wallex180™ performed better than Wallex6™ (Faulkner, 2020).

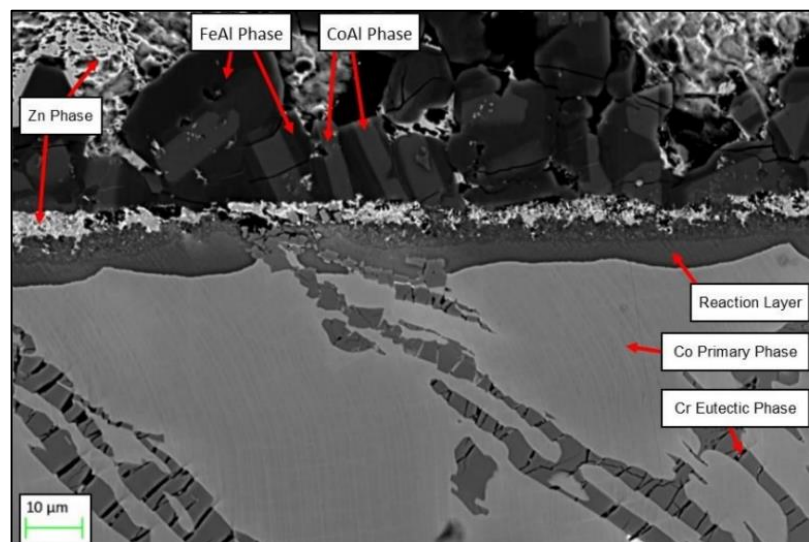


Figure 1.14 Cross-section of Wallex6™ after immersion in GI. The image was labelled to show the dross and reaction layer observed after testing, as well as the eutectic phases present in the alloy, which were found to disrupt the shape and uniformity of the diffusion layer. Reproduced from (Faulkner, 2020).

It is reported that severe abrasive wear still occurs in bearing sleeves and bushings manufactured from Co-based alloys. Unlike steels and other pot roll bearing materials, the hardness of Stellite and equivalent WallexTM alloys is superior compared to that of the intermetallic dross particles formed in the liquid Zn bath. Therefore, the entrapment of dross particles was not believed to be responsible for the damage caused by severe abrasion. The hardness of the dross particles formed in industrial baths with low Al content is significantly lower than the hardness of Stellite alloys at the galvanising temperature of approximately 460°C, suggesting that it was impossible for them to inflict severe damage to the Stellite bearings used (Tang et al., 2010).

A number of experiments (Tang et al., 2010) were performed to understand what other mechanisms could have resulted in the severe abrasive wear observed in Stellite bearings. The study concluded that the damage accumulation process was caused by the high affinity of Co in the alloy towards Al present in the molten metal bath. The authors of the study reported that nucleation and growth of CoAl particles occurred upon immersion in liquid Zn-Al. Due to their superior hardness, these particles were responsible for removing the bearing materials forming wear debris, which rapidly reacted with Al present in the bath and it is partially converted to CoAl fibres. The fibres deposited onto the surface of the bearings and the wear process proceeded with generation and subsequent deposition of wear debris with increased size; for this reason, the dimensions of the wear grooves increased with time during a galvanising campaign until damage was sufficient to cause pot instability.

As previously mentioned, the surface of several hardware components used in ZODIAC, including the surface of the pot roll and the journal bearing sleeve are coated with a HVOF thermal sprayed coating consisting of WC embedded in a Co based matrix at a ratio of 90% WC to 10% Co. WC-Co coatings, which have been used to protect Fe and Co-based alloys from molten Zn attack, are composite structures containing a soft Co-based matrix in which hard WC particles having load-bearing capability are embedded. WC-Co showed superior wear resistance when paired against superalloys in galvanising baths. However, corrosion of the matrix was

reported to occur, which combined with cracking of the WC particles caused failure of the coating (Zhang et al., 2004).

An example of this behaviour was reported in the literature (Tang et al., 2010), which examined the corrosion of SS 316L sleeves with laser-clad WC coating. The WC carbide particles were dispersed in a Fe-based matrix and the deterioration of this matrix was identified to be one of the possible failure mechanisms. When the coating was characterised after testing, evidence of corrosion of the matrix was observed (Figure 1.15) and, therefore, the matrix was no longer capable of supporting the spherical WC particles, which started to crack. In addition to this, fragments of the WC particles were found in the residual Galvanneal alloy on the sleeve as a result of the corrosion of the matrix, leading to failure of the coating.

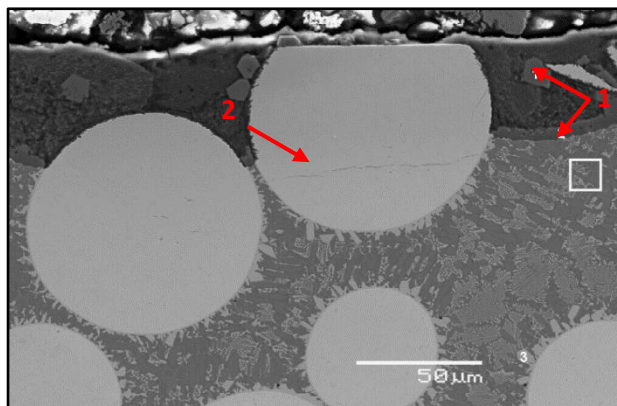


Figure 1.15 Cross-section of WC-coated SS 316L sleeve after immersion in Galvanneal. Corrosion products developed due to corrosion of the matrix (1) and cracks formed in the WC particles (2). Reproduced from (Tang et al., 2010).

The deterioration of the pot roll bearing materials is responsible for causing strip vibrations, leading to quality issues around the gas knives section of the CG line (Escott et al., 2021; Rachamalla, 2006). For this reason, materials with excellent resistance properties, such as Co-based alloys, have been selected for making the journal sleeve and bushing components of pot roll systems in CG lines. Despite their wear resistance properties, these alloys suffer from severe degradation in molten Zn alloy. The literature reviewed in this section showed that the reaction between the bearing materials and the molten metal bath is the main mechanism which leads to

wear and degradation of the journal bearing components. Fe-based and Co-based alloys experience corrosion in liquid Zn alloy and, therefore, the bearings have a limited service life. It was discussed that WC coatings were introduced to enhance wear resistance; however, WC coatings were still observed to degrade in molten Zn alloy due to corrosion of the matrix, which reacted with the molten metal bath.

As a result, the existing literature suggests the importance of using a material with improved corrosion resistance in liquid Zn to obtain bearings with extended service life and to prevent strip vibrations. Furthermore, materials inert in liquid Zn will prevent the formation of reaction products which could close the gap between the sleeve and bushing components, enabling the use of bearings with reduced clearance designed for preventing direct metal on metal contact, as discussed in Section 1.7.2.

1.8.2 Ceramics

The use of ceramics as materials for galvanising pot hardware has gained a strong interest due to their high melting point, high hardness, wear resistance and chemical stability when used at elevated temperatures and in molten metal applications. The poor wetting behaviour of many oxides such as alumina and yttria-stabilized zirconia in molten Zn confirmed the strong resistance to corrosion of these materials (Matthews & James, 2010). However, the high hardness of ceramics could become a problem when used as pot bearings, as they could damage the metallic counter component. In addition to this, ceramics are brittle and they could easily fail when tension is applied or under mechanical and thermal shock (Zhang, 2005). In order to overcome these limitations, ceramics were paired with softer and tougher materials and their performance in liquid Zn-Al was discussed in the literature. A ceramic coating could be applied onto steel to protect the metal from the attack of Zn-Al, as shown by (Nag et al., 2021), (Liu et al., 2020) and (Wang et al., 2019). The ceramic materials were coated via a thermal spraying or electrodeposition processes. Several ceramic materials were discussed in the literature, such as oxides, carbides and borides, which are reviewed in this section.

1.8.2.1 Al₂O₃

The durability of pure aluminium oxide or alumina (Al₂O₃) in molten Zn was investigated by (Nag et al., 2021) against that of WC-12Co coating. Al₂O₃ was plasma sprayed onto SS 316L, as the ceramic is reported to have good bonding with stainless steel. According to the results of this study, Al₂O₃ showed superior performance over WC-Co, as the integrity of the coating was not compromised even after 30 days of dipping (Figure 1.16). Unlike WC-Co, thickness reduction or roughness variation were not observed during the testing period and SEM images of the samples showed no significant change in porosity and confirmed the absence of new phases on the surface of the coating. In addition to this, no vertical cracks were detected, thus no Zn-Al penetration occurred in the coating (Nag et al., 2021).

Experiments also confirmed that Al₂O₃ was non-wetting to molten Zn. The sessile drop method was used by (Shinozaki et al., 1999) to measure the contact angle of Al₂O₃ at 873 and 973K. A Zn sample was placed on top of an Al₂O₃ substrate and subsequently the Zn was allowed to melt. The contact angles were obtained from the shape of the Zn droplet and the measurements taken were in the range of 150-160°. Since the contact angle exceeded 90°, the material exhibited non-wetting behaviour. Moreover, the Al₂O₃ samples were analysed after the measurements and no Zn diffusion into the ceramic substrate was observed (Shinozaki et al., 1999).

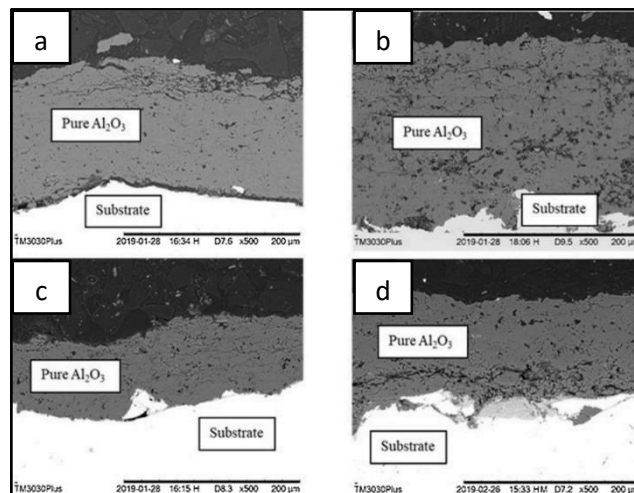


Figure 1.16 Images showing Al₂O₃ coating after 0 days (a), 10 days (b), 20 days (c) and 30 days (d) of dipping in liquid zinc. Reproduced from (Nag et al., 2021).

1.8.2.2 ZrO₂

The wettability experiments described by (Shinozaki et al., 1999) were also conducted on zirconia (ZrO₂) samples containing 3 mol% or 8 mol% Y₂O₃. Again, the measured contact angles were greater than 90° and almost identical to those obtained on the Al₂O₃ samples. The corrosion resistance of yttria-stabilised zirconia was confirmed by the immersion tests carried out by (Dong et al., 2006) in a bath of molten Zn at 620 °C, which is above the bath temperature used in ZODIAC. ZrO₂ and a NiAl binder were thermal sprayed onto carbon steel to form a gradient coating by varying the composition ratios of the feedstock powder as illustrated in Figure 1.17a. Graded transition layers were observed when the coating was analysed on the SEM (Figure 1.17b). It was reported that the presence of the NiAl binder affected the performance of the coating in liquid Zn, as the Zn atoms reached the NiAl gradient intermediate layer and reacted with the NiAl alloy particles. EDS showed that the products of this interaction are ultra-fine grains enriched in Zn and Ni atoms, which also contain smaller amounts of Zr and Al. It was observed that the reaction products expand in the ZrO₂-NiAl gradient coatings as diffusion of liquid Zn atoms along grain boundaries occurs. Once the NiAl binder completely reacts with the molten metal, the gradient coatings were destroyed by growth of corrosion products (Dong et al., 2006).

Composition and thickness of the ZrO ₂ -Ni/Al gradient coating				
Gradient composite ceramic coating	Layer	Composition (wt.%)		Thickness (mm)
		Ni/Al	ZrO ₂	
ZrO ₂ -Ni/Al gradient coating	No. 1	100	0	~0.1
	No. 2	85	15	0.2
	No. 3	70	30	0.2
	No. 4	50	50	0.2
	No. 5	30	70	0.2
	No. 6	15	85	0.2
	No. 7	0	100	0.3

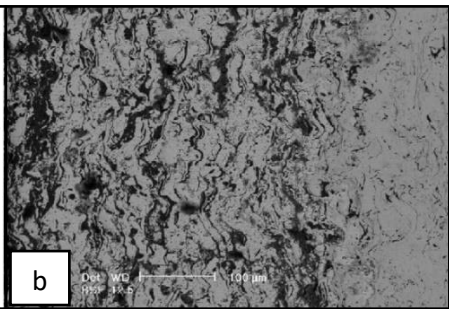


Figure 1.17 Composition of each gradient layer used to fabricate the ZrO₂-NiAl coating (a); SEM image showing the intermediate gradient layers (a). Reproduced from (Dong et al., 2006).

1.8.2.3 Si₃N₄ and SiAlONs

Silicon Nitride (Si₃N₄) is a ceramic used for the development of anti-friction bearings (Popp & Sternagel, 1999). A composite structure made up of Si₃N₄/SiC and stainless steel was studied by Ma et al. (2014) for use as an immersion heater for heating hot dip galvanising baths. The properties of Si₃N₄/SiC include low friction coefficient, high hardness, heat stress resistance and Zn corrosion resistance (Ma et al., 2014; Ma et al., 2010). SiAlON are Si₃N₄-based ceramics whose structure also contains some fractions of Al and O (Adeniyi et al., 2019). They offer excellent wear and chemical corrosion resistance and, for this reason, they could be suitable for high-temperature engineering applications, such as roll bearings (Wang et al., 2020).

The use of SiAlON bearings for galvanising sink rolls was reported to reduce the maintenance required between different galvanising campaigns. Following the recent trend to use dissimilar materials for the bearing components, a test showed that SiAlON bushings could be paired with sleeves of a wide range of superalloys and coatings, such as SS 316L with WC coating. However, the wear rate was observed to be twice as high in SiAlON than it was in a WC coating when these two materials were paired together (Tang et al., 2010). This behaviour was explained to be a consequence of the brittleness of the WC particles, which cracked because of the contact pressure during sliding. As a result, they could act as debris and form surface grooves on the SiAlON bushing, whose hardness is lower than the WC particles (Parthasarathy et al., 2004). Currently, a Wallex4™ sleeve is used against a SiAlON bushing in CG lines outside the UK, such as in the US.

1.8.2.4 BN

Another material with excellent corrosion resistance to molten metals is boron nitride (BN), which is a non-oxide ceramic typically employed in the fabrication of high-temperature crucibles. At room conditions, BN has a hexagonal structure (hBN), which changes to a cubic zinc blende structure (cBN) at higher temperatures and pressures. Compared to other nitrides, such as AlN, hBN has greater chemical and thermal stability (Brant et al., 2013; Reusch et al., 2015). BN has potential to remain

inert to many metallic melts, including Zn, Al and Mg. In addition to this, BN shows non-wetting properties against these metals (Reusch et al., 2015; Stavros, 1999), as observed in Figure 1.18.

Praxair S.T. Technology Inc. filed a patent (Jarosinski et al., 2013) application for the use of BN coatings onto the surface of galvanising rolls. The invention relates to rolls for use in contact with molten Zn, which are coated with a blend of BN and silicate via a thermal spray process. The main function of the silicate is to maintain the BN attached to the surface of the roll. According to the patent, the coating improves the corrosion resistance of the steel roll when immersed in a bath containing Zn and 0.05-5 wt.% Al (Jarosinski et al., 2013). This suggests that it is possible to take advantage of the corrosion resistance of BN to maximise the service time of the galvanising pot bearings.

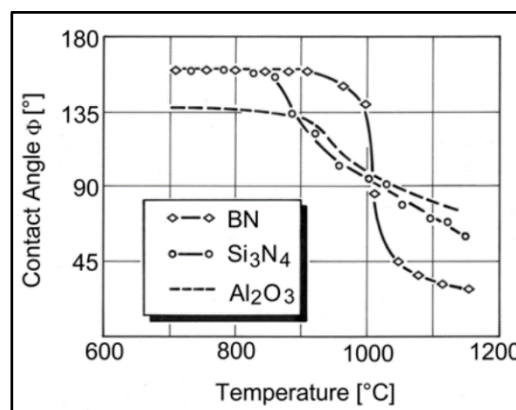


Figure 1.18 Comparison of the contact angles obtained for BN, Si₃N₄ and Al₂O₃ in molten Al at various temperatures. BN shows superior non-wetting properties up to a temperature of 1000°C. Reproduced from (Reusch et al., 2015).

1.8.2.5 Other Types of Ceramics

Other examples of ceramic materials have been discussed in the literature. For instance, silicates have been applied to galvanising pot rolls to enhance the corrosion resistance of the roll materials in liquid Zn (Jarosinski et al., 2013). In addition to this, boron containing thermal spray coatings have shown superior performance in Zn alloy baths compared to conventional WC-Co coatings (Matthews & James, 2010).

These ceramics were typically sprayed together with a metallic binder to obtain a 'cermet' coating, such as those tested by (Chen et al., 2019), who performed static immersion tests of MoB/CoCr, MoB/NiCr and TiB/CoCr cermets coatings. The study was conducted using a bath of liquid Zn at a temperature of 460°C for 360 hours. It was reported that the coating showed high durability and non-wetting behaviour during the 360 hours of testing. The observed performance was correlated to the presence of several inert borides ($\text{Cr}_2\text{Ni}_3\text{B}_6$, CoMo_2B_2 , and CoMoB) in the coatings, which minimised the formation of intermetallic phases during the static immersion tests. The formation of reaction products occurred when Zn penetrated the pores of the thermal sprayed coatings and, for this reason, MoB/NiCr showed the highest durability owing to its lower porosity. Moreover, pin-on-disc testing was performed on the three coatings to analyse their wear resistance, using the set up in Figure 1.19. Among the three coatings tested, MoB/NiCr was found to also have superior wear resistance compared to the other two coatings (Figure 1.18b) (Chen et al., 2019). MoB-based coatings were also experimented in other studies, such as in Lv et al. (2010), Hiroaki Mizuno and Junya Kitamura (2007) and Zhang et al. (2013).

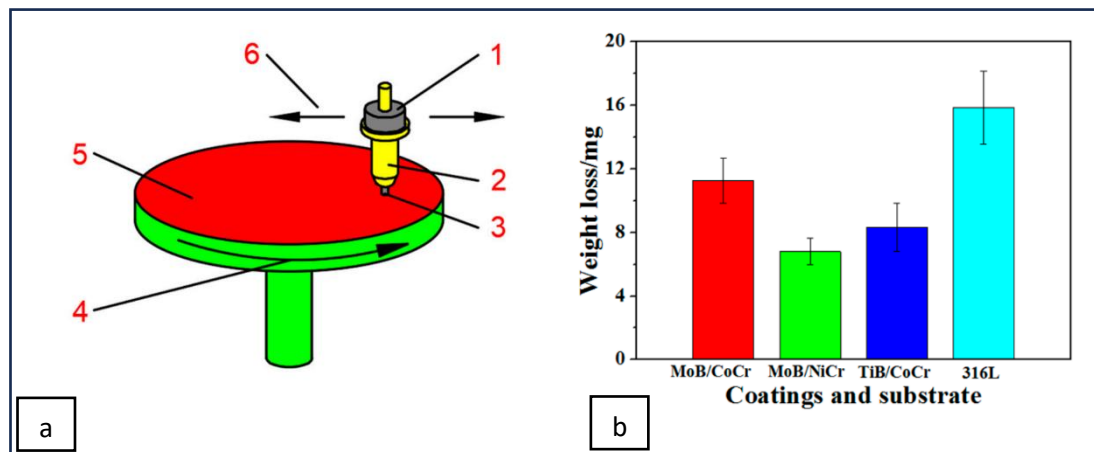


Figure 1.19 Schematic of the pin-on-disc experimental setup (a): (1) weight, (2) clamp, (3) pin, (4) rotating direction of the disk, (5) abrasive disc and (6) moving direction of the sample; abrasive weight loss measurements showing the superior wear resistance of MoB/CoCr (b). Reproduced from (Chen et al., 2019).

Another ceramic with potential for use in a liquid Zn environment is zirconium diboride (ZrB_2). This material was electrodeposited by Wang et al. (2019) onto stainless steel and immersed in pure Zn for up to 120 hours. The results of the test showed that ZrB_2 has good chemical stability in liquid Zn and shielded the stainless steel substrate from the attack of molten metal. However, it was reported that the coating failed due to growth of defects, which led to the disintegration of the coating.

A recent study (Yu et al., 2021) compared the performance of enamel coating against that of WC-Co. Tribo-corrosion tests were carried out in Zn-0.2 wt% Al liquid metal at 460°C using a SS 304 disc containing the coating and a Q235 steel pin. Figure 1.20a illustrates the experimental setup for tribo-corrosion testing. The enamel mainly contained SiO_2 with some additions of CaF_2 and oxides including Al_2O_3 and B_2O_3 , which enhanced the wear resistance of the material. The experimental results showed that enamel was more effective in providing corrosion resistance to steel compared to WC-Co. The dense morphology of the coating and the amorphous structure of the enamel eliminated the occurrence of fast inward diffusion of the liquid metal through pores or grain boundaries. No microcracks were identified in the coating, which remained bonded to the substrate even after 30,000 cycles. However, a glaze layer was detected at the surface of the enamel due to the formation of (Al, Zn)-rich oxides compatible with enamel (Figure 1.20b). The oxides seemed to have formed despite fresh alloy melt being renewed at 0.5 h intervals (Yu et al., 2021). If the formation of these oxides is prevented, the experiments performed on enamel coatings further confirmed the chemical stability of certain ceramics in liquid Zn.

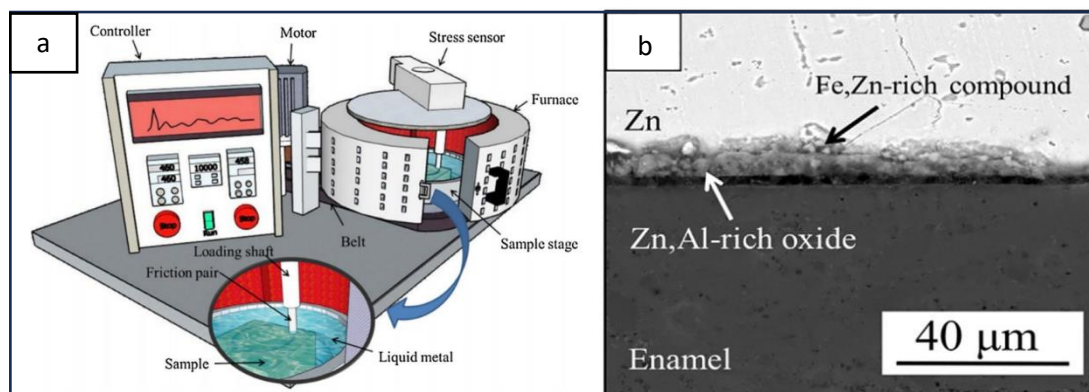


Figure 1.20 Tribometer used for measuring the tribo-corrosion resistance of enamel (a); SEM image of the enamel coating after 30,000 cycles. The image shows the presence of a $\sim 10\ \mu\text{m}$ -thick glaze layer on the surface of the enamel (b). Reproduced from (Yu et al., 2019).

1.8.3 Effects of Changing Bath Composition

The composition of the Zn alloy bath affects the performance of hardware materials. For instance, Liu et al. (2005) and Bright (2007) showed that the addition of small amount of Al content in the bath plays an important role in reducing the corrosion rate of the pot hardware material. Tests were carried out using SS 316L specimens which were tested in galvanising (Zn-0.18Al), Galfan (Zn-5Al) and Galvalume (Zn-55Al) baths. It was found that small Al additions can reduce the activity of Zn and form an inhibition layer, therefore reducing the corrosion rates of the pot hardware materials. If the Al amounts are above the critical value, the dominant process in the molten metal bath is changed from a Fe-Zn reaction to a Fe-Al reaction. As a result, baths with high Al content increase the activity of Al and accelerate the corrosion reaction (Liu et al., 2005). When Stellite 6 is used as hardware material, it reacts with the Al-containing bath, leading to the formation of an Al-rich intermetallic layer. If the Al amounts present in the baths are increased, the dominant intermetallic compound in the bath changes from $\zeta(\text{FeZn}_{13})$ to the $\delta(\text{FeZn}_9)$ and to the $\eta(\text{Fe}_2\text{Al}_5\text{Zn}_x)$ phase (Zhang & Tang, 2003).

CG lines can be designed to operate baths of different composition. For example, a galvanising line can have one GI bath and one Zn-Al-Mg bath, which will switch

depending on which coating is required on the final product. Sometimes the pot hardware is not replaced before the bath is switched and the performance of the hardware materials can be affected. A study (Kuperus, 2018) was conducted to analyse the behaviour of dross-build up formed on the galvanising bath hardware when transitioning from GI to Zn-Al-Mg. Experiments confirmed that a dross build-up layer formed when SS 316L hardware was immersed in GI. It was found that this layer diminished after immersion in Zn-Al-Mg and, therefore, the study focused on determining the nature of this change. It was observed that the dross-build up structure formed in GI was very flat and it was referred to as a faceted interface, which was characterised by high stability. If the intermetallic dross particles and liquid Zn are in equilibrium, the surface tension between the interfaces is low. When the hardware was subsequently immersed in Zn-Al-Mg, the surface tension increased as the liquid became more thermodynamically stable when 1.5 wt.% Mg was present (Kuperus, 2018). As a result, when the hardware was immersed in Zn-Al-Mg, a curved interface is formed instead of a faceted interface (Figure 1.21), showing that the transition to baths of different composition can alter the corrosion behaviour of the hardware materials.

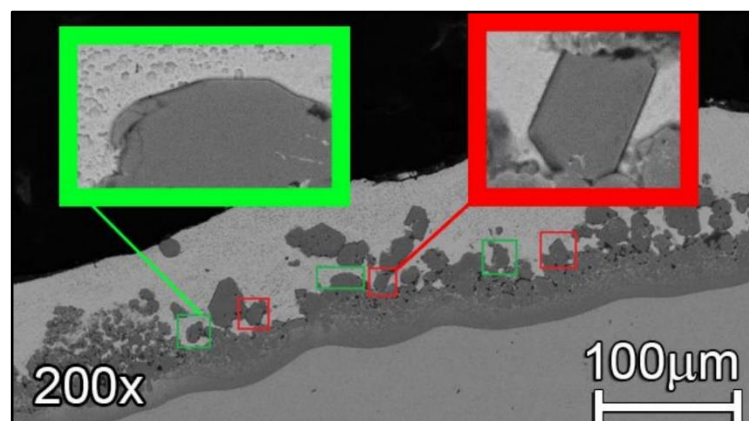


Figure 1.21 SEM images showing the difference between faceted (marked red) and curved (marked green) interfaces observed in the dross build-up structure when transitioning from GI to Zn-Al-Mg bath. Reproduced from (Kuperus, 2018).

1.8.4 Dynamic Tests in Liquid Zn

The majority of the studies reviewed previously investigated the corrosion behaviour of prospective materials in liquid Zn by conducting static tests, where the materials were not tested in motion and were only immersed in baths containing the liquid metal. However, the journal sleeve component of the galvanising hardware is in motion and, in addition to this, the bearings operate in a Zn alloy bath which is larger than the pots used for lab-scale static tests. There is evidence in the literature that conducting dynamic testing allows to better understand the performance of materials in molten metal.

For example, experiments were performed on various alloys, including SS 316L and Fe_3Al , to determine their corrosion rates in a bath of Al-8Si composition. Liu et al. (2005) performed these experiments in both static and industrial baths, where on-line dynamic testing was conducted. It was found that for the same bath composition, the corrosion rates measured in industrial baths are higher than those obtained for static baths. The corrosion rate of SS 316L was measured to be approximately three times larger than the rate observed in the static bath. Moreover, the static corrosion rate of Fe_3Al was also found to be lower than the corrosion rate received from the dynamic test. This reduction is due to the small volume of the static baths, which become saturated with elements dissolved from the specimen, leading to a slower corrosion of the specimen. On the other hand, industrial baths have a larger volume and, therefore, the effect of the dissolution of solid metal becomes minimal. In addition to this, the intermetallic layers developed on the outside of the corroded specimens were brittle and spalled off into the melt during dynamic testing, resulting in the growth of new reaction products and faster corrosion in industrial baths (Liu et al., 2005). Although the experiments were performed in baths of composition containing Al and Si, this analysis is expected to be applicable to baths containing liquid Zn alloy as well.

1.9 Fabrication Processes of Materials

The techniques used to fabricate specimens for testing materials in liquid Zn are various and they differ depending on the type of material used as feedstock or structure that need to be achieved. For example, ceramic materials, which were earlier explained to be prospective materials for use as galvanising bearing components, require different fabrication processes compared to metals. The techniques which are available today are numerous and allow to manufacture both bulk materials as well as coatings. This section discusses the main processes that are used to produce the specimens relevant to the project.

1.9.1 Field Assisted Sintering Technology

Field Assisted Sintering Technology (FAST), also known as Spark Plasma Sintering (SPS), is a powder metallurgy technique where an electric current and an uniaxial load are applied simultaneously to a powder specimen and die assembly. The application of electric current induces Joule heating in the die and/or specimen, enabling fast heating rates and a decrease in processing time.

FAST typically utilises low voltage and high current to generate elevated temperatures while applying axial load within a vacuum or gas atmosphere. The powder is enclosed in a conductive die assembly (Figure 1.22), commonly made of graphite, facilitating the Joule heating which plays an important role in the process. Die configurations can vary, the simplest design consists of placing the powder in a ring between two punches and utilising spacers to make contact with the electrodes. These electrodes are activated to apply the load. A standard processing cycle involves gradually heating and loading the die and powder sample to a specified maximum temperature and load, holding for a predetermined duration and then initiating the cooling phase. Temperature measurement is typically conducted at one of these three locations: close to the upper surface of the sample using a pyrometer, on the external surface of the ring, again using a pyrometer, or via a thermocouple embedded within the ring. Maintaining a minimum load is essential to ensure

consistent electrical contact, and the electric current (DC) can be either continuous or pulsed (Weston et al., 2020).

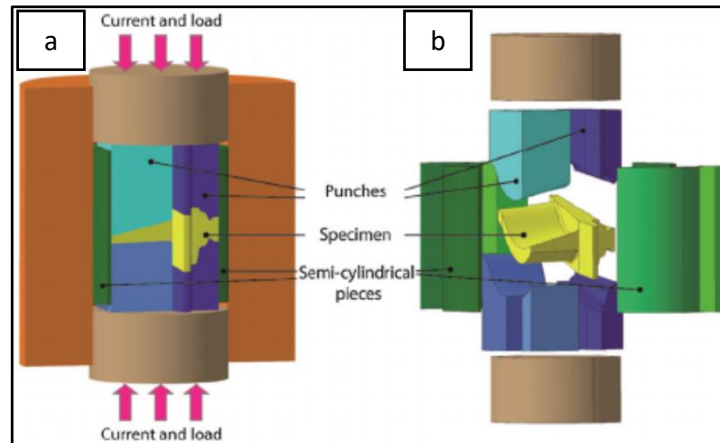


Figure 1.22 Schematics of main FAST equipment. Graphite die showing punches in final position for manufacturing a turbine blade component (a); exploded die view (b). Reproduced from (Weston et al., 2020).

FAST is known to provide technological and economic advantages when compared to traditional sintering methods. When FAST processing was used, materials were observed to achieve higher density at lower temperatures and/or in reduced timeframes, as well as enhanced performance and properties. Specifically, FAST can generate ultra-fine grain (UGF) or nanoscale microstructures that are not achievable through conventional methods, such as hot pressing or hot isostatic pressing. FAST has successfully processed materials that were previously considered challenging or impossible to handle with traditional sintering routes. A diverse range of materials have been effectively processed using FAST, due to its ability to use feedstock of various morphologies, size and size distribution through adjustment of process parameters. Therefore, FAST enables to overcome the difficulties of conventional material processing and has the capability to develop novel materials (Weston et al., 2020).

1.9.2 Thermal Spraying

Thermal spraying refers to a broad range of coating techniques that inject a feedstock material into a high-temperature gas or plasma; subsequently, the feedstock is heated up to a partial or complete melting and sprayed onto a substrate to obtain a coating. Various thermal spray methods exist, including powder and wire flame spraying, electric arc wire spraying, plasma spraying and high-velocity oxy-fuel spraying (HVOF). The majority of feedstock materials used for thermal spraying processes, including HVOF, are powders. Ceramics and other coating materials can be easily manufactured as powders, which are reported to produce denser coating microstructures (Nouri & Sola, 2019).

HVOF is a technique which is relative new compared to other thermal spraying processes. A schematic of the process is illustrated in Figure 1.23. HVOF is not a solid-state process, as it involves depositing feedstock materials onto the substrate in a molten or semi-molten state to fabricate the desired coating. The process differs from flame spraying due to the expansion of the jet at the gun exit. Various gases can be used as fuels, such as propane, propylene, acetylene, hydrogen and natural gas; liquid fuels, including kerosene, can also be used. Powder coating materials are heated to their molten state and propelled by a high-temperature, high-velocity gas stream towards the substrate. The molten powder stream impacts the substrate, forming droplets within the high-energy gas stream. These droplets flatten or deform on the substrate, creating layers known as 'splats'. The accumulation of multiple layers of splats results in the formation of the coating (El-Eskandarany, 2020).

One of the benefits of using HVOF is that it allows to achieve higher particle velocity and lower particle temperature compared to other thermal spraying techniques, such as plasma spraying. As a result, HVOF is characterised by high deposition efficiency, leading to the fabrication of coatings with good adhesion (Łatka et al., 2020).

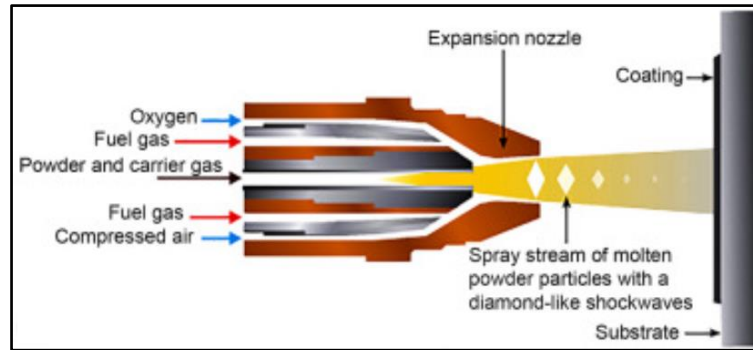


Figure 1.23 Schematics of the HVOF process. Reproduced from (El-Eskandarany, 2020).

1.9.3 Near Infrared (NIR)

Near infrared, or NIR, is a modern rapid thermal curing technique which has recently become a popular option to produce coatings for the pre-painted steel markets. Its main advantage is the ability to significantly reduce curing time compared to conventional heating processes (Mabbett et al., 2014). NIR radiation is located between visible and infrared in the electromagnetic spectrum (Watson et al., 2011). NIR machines operate at wavelengths between 700-1500 nm, typically using lamps of tungsten-halogen filaments. The process is schematically show in Figure 1.24. The power setting of the lamp can be set to adjust the emitted spectrum, as heating the material is linked to its ability to absorb the emitted radiation (Griffin et al., 2021).

NIR machines have been successfully used for ultrafast sintering of titanium dioxide (TiO_2) layers on metal substrates. A TiO_2 paste containing a solvent and a binder was used to produce the film. TiO_2 is a material which is transparent to NIR radiation and, for this reason, it passed through the material without heating. The metal substrate, which was in direct contact to TiO_2 absorbed these wavelengths, leading to rapid heating of the substrate. This process drove off the solvent and binder from the substrate upward resulting in rapid sintering of TiO_2 (Watson et al., 2011).

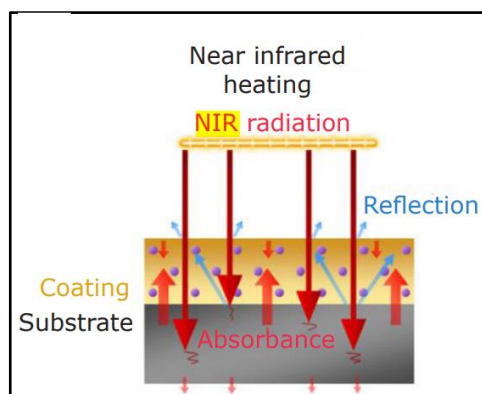


Figure 1.24 Schematic illustrating the operation of NIR heating. The coating material is transparent to NIR radiation, which is absorbed by the underlying substrate, producing rapid heating and sintering of the coating. Reproduced from (Griffin et al., 2021).

1.10 Limitations and Project Objectives

The identification of materials that remain inert in liquid Zn alloy is one of the main technical challenges of the sheet steel galvanising industry. Therefore, studies have been conducted recently to determine the corrosion behaviour of metals and ceramics in liquid Zn alloy. However, the studies reviewed in this chapter showed some limitations.

Although ceramics have been demonstrated to have potential to remain inert in liquid Zn environments, the available literature lacks comprehensive studies evaluating the performance of a diverse range of ceramics with potential for use as galvanising hardware materials. Existing research has primarily focused on a limited selection of ceramics, which is a broad class of materials. There are no comparative studies which examine the performance of different types of ceramics in molten Zn. Another gap in the literature arises from the predominant use of baths containing pure Zn or Zn-Al for testing the performance of prospective materials. However, there is no information regarding the behaviour of these ceramics when immersed in baths containing Mg additions. Given the use of Zn-Al-Mg baths in many CG lines, including ZODIAC, the effects of changing bath composition on the corrosion behaviour of the materials need to be understood. In addition to this, several experiments in the available literatures utilised short testing durations. This is a critical limitation as

materials may not show signs of reaction with the Zn bath immediately. For this reason, it is important that test duration align with the length of a typical galvanising campaign, allowing the comprehensive evaluation of the corrosion resistance properties of the ceramics against the pot hardware materials currently in use. Furthermore, the performance of the ceramics in liquid Zn cannot be determined from the use of static immersion testing alone, as several studies showed that dynamic testing allowed to better replicate the behaviour observed in real industrial baths.

In addressing these limitations, future studies are needed for a more robust understanding of the suitability of ceramics as galvanising bearing materials. The present project examines a broad selection of various ceramics materials, including those commercially available as well as novel materials and structures, in order to achieve superior properties. Experiments are performed in two baths of different composition, namely GI and Zn-Al-Mg, that are currently used in ZODIAC for the production of galvanised strip steel. Moreover, the performance of the tested ceramic materials is investigated by conducting both static and dynamic testing in liquid Zn, obtaining a more comprehensive understanding of the potential of ceramic bearing materials.

Chapter 2

Experimental Methods

2.1 Materials

This project investigates a broad selection of different materials, ranging from metals to ceramics. During the early stages of this research, experiments in liquid Zn alloy were performed on materials available commercially, which are cast into components of various sizes and shapes. However, it will be later explained that superior properties can be obtained by combining different materials. For this reason, novel materials and structures, including composites containing SiAlON and BN ceramics, and Al₂O₃ coatings were explored in this research.

2.1.1 Commercially Available Materials

The materials available commercially that were tested in this project include stainless steel (SS) grade 316L, two Co-based alloys (Wallex4TM and Wallex6TM) and seven different ceramic materials, namely pure hexagonal boron nitride (hBN), BN grade M26, aluminium nitride-boron nitride composite (AlN-BN), Macor[®] machinable glass ceramic, yttria-stabilised zirconia (3YSZ), alumina (Al₂O₃) and silicon nitride (Si₃N₄). The composition of the ceramics is listed in Table 2.1. SS 316L specimens for static immersion tests were EDM cut from round bars of 20 mm diameter procured from Metalex (Poole, UK). Wallex4TM and Wallex6TM pads of 50 × 50 × 5 mm dimension were supplied by Wall Colmonoy (Swansea, UK) and were used for dynamic testing in liquid Zn alloy. The seven ceramic materials were procured from Precision Ceramics (Birmingham, UK) and they were supplied as components of various sizes and shapes, which were, subsequently, cut with a diamond wheel to obtain specimens for static testing. In addition to this, 80 × 80 × 5 mm plates were procured for each ceramic for pin-on-disc wear testing.

Table 2.1 Composition of commercially available ceramics for static testing.

Name	Composition
Pure Boron Nitride (hexagonal)	hBN
Boron Nitride Grade M26	40wt.%SiO ₂ , 60wt.%BN
Macor Machinable Glass Ceramic	46wt.%SiO ₂ , 17%MgO, 16%Al ₂ O ₃ , 10%K ₂ O, 7%B ₂ O
AlN-BN composite	AlN, BN
Yttria-stabilised zirconia (3YSZ)	3 mol.% Y ₂ O ₃ -ZrO ₂
Silicon Nitride	Si ₃ N ₄
Alumina	Al ₂ O ₃

2.1.2 SiAlON-BN Composites

SiAlON composites containing additions of hexagonal (hBN) and cubic BN (cBN) were fabricated using FAST facilities available at the Henry Royce Institute in Sheffield University (Sheffield, UK). The fabrication of these samples, which is discussed in detail in Chapter 4, required the use of α -SiAlON, BN, Y₂O₃ and Al₂O₃ powders, which were procured from PI-KEM (Tamworth, UK) with particle size in the range between 1-20 μ m (Table 2.2). Mixtures of the following compositions were prepared:

- Pure SiAlON
- 10wt.%hBN-SiAlON
- 20wt.%hBN-SiAlON
- 30wt.%hBN-SiAlON
- 30wt.%cBN-SiAlON.

Subsequently, a total amount of 8 wt.% Y₂O₃-Al₂O₃ mixture with molar ratio of 3:5 was used as sintering additive and was added to each SiAlON-BN blend. FAST was used to fabricate 60 \times 3 mm discs from the mixtures previously prepared (Figure 2.1).

The discs were sectioned using a diamond wheel to obtain smaller specimens for static testing in liquid Zn.

Table 2.2 Particle size of the powders used for the fabrication of SiAlON/BN composites with FAST. The values reported were provided by the supplier.

Material	Particle size [μm]
α -SiAlON	Unknown
hBN	5-10
cBN	10-20
Al_2O_3	1-10
Y_2O_3	1-10

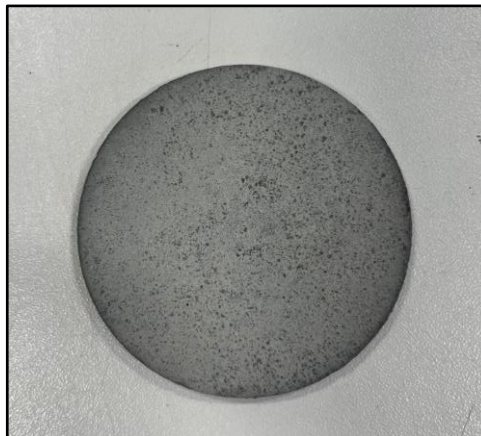


Figure 2.1 Example of a 60 mm diameter disc with 30wt.%cBN-SiAlON composition fabricated with FAST.

2.1.3 Coatings

Two different coatings were tested in this project, namely WC-Co and Al_2O_3 . 90% WC-Co coatings with 150 μm thickness were applied to the surface of Wallex6™ via HVOF technology (Chapter 1, Section 1.9.2). The coated samples were supplied by Wall Colmonoy (Swansea, UK) as discs with $\varnothing 30 \times 10$ mm dimension that were used for static testing, as well as $\varnothing 20 \times 150$ mm bars for dynamic testing. Al_2O_3 was coated to

a nominal thickness of 250 μm onto the surface of SS 316L using HVOF spraying. The process was conducted by Engineered Performance Coatings (Cardiff, UK) which also provided the feedstock material for the coating. The coating thickness was determined according to the relationship formulated by Mizuno and Kitamura (2007), which was obtained for thermal sprayed coatings for molten metal applications. They reported the following relationship (Equation 1):

$$C_d = \alpha_1 / (t \times \alpha_2) \quad (1)$$

where t is the optimal thickness of the coating in μm , α_1 and α_2 are the coefficients of thermal expansion of the coating and of the base material respectively, and $C_d \geq 0.15 \times 10^{-2}$. Al_2O_3 was sprayed onto $20 \times 20 \times 5$ mm plates for static testing as well as $\varnothing 20 \times 150$ mm rods for dynamic testing.

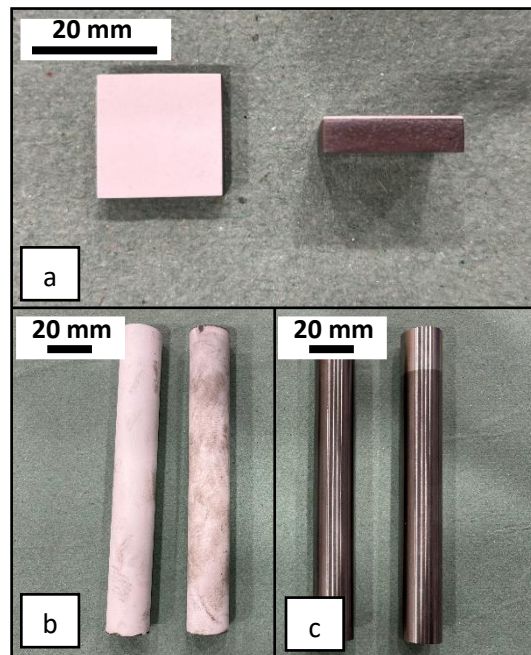


Figure 2.2 SS 316L samples with Al_2O_3 coating (a); Al_2O_3 coated bars (b); Wallex6™ bars (c).

2.2 Material Characterisation

2.2.1 Sample Preparation

If necessary, samples were first cut to size. Metallic materials were precision cut with electrical discharge machining (EDM) and hard ceramic materials required the use of a diamond wheel. Stainless steel and Co-based alloys were hot mounted in Bakelite conductive resin before grinding and polishing were performed. Due to cracking of the samples after hot mounting (Figure 2.3), brittle ceramic materials were cold mounted using a conductive acrylic resin (CEM3070, Cloeren Technology GmbH) based on methyl methacrylate. Samples were ground using SiC grinding papers and diamond grinding discs, depending on the hardness of the materials being prepared. Polishing was carried out using polishing pads and solutions specific to the materials to be polished. Examples of the sample preparation procedures followed are outlined in Table 2.3 and Table 2.4. Samples were rinsed in warm water and cleaned with ethanol in between each grinding and polishing step, in order to minimise any possible contamination from the samples. Polishing cloth pads were washed thoroughly using water and detergent before each usage to avoid cross contamination of grinding and polishing debris.



Figure 2.3 Cracks formed after hot mounting a ceramic specimen.

Table 2.3 Preparation schedule for grinding and polishing metals and soft ceramics.

Material	Pad	Lubricant	Base Plate Speed (RPM)	Time
Grinding	P120 Grit SiC Paper	Water	200	Variable – Until Flat
	P200 Grit SiC Paper	Water	200	1 minute per sample
	P400 Grit SiC Paper	Water	200	1 minute per sample
	P800 Grit SiC Paper	Water	200	1 minute per sample
	P1200 Grit SiC Paper	Water	200	1 minute per sample
	P2500 Grit SiC Paper	Water	200	1 minute per sample
Polishing	Cloth Pad	9 μ m Diamond Particle Solution	200	4 minutes per sample
	Cloth Pad	3 μ m Diamond Particle Solution	200	4 minutes per sample
	Cloth Pad	0.05 μ m Colloidal Silica Solution	200	2 minutes per sample

Table 2.4 Preparation schedule for grinding and polishing hard ceramic materials.

Material	Pad	Lubricant	Base Plate Speed (RPM)	Head Speed (RPM)	Time
Grinding	P120 Grit SiC Paper	Water	200	60	Variable – Until Flat
	P1200 Grit SiC Paper	Water	200	60	1 minute per sample
	Diamond disc	9 μ m Diamond Particle Solution	200	60	20 minutes per sample
	Diamond disc	3 μ m Diamond Particle Solution	200	60	20 minutes per sample
Polishing	Cloth Pad	3 μ m Diamond Particle Solution	200	60	15 minutes per sample
	Cloth Pad	1 μ m Diamond Particle Solution	200	60	10 minutes per sample
	Cloth Pad	0.05 μ m Colloidal Silica Solution	200	60	2 minutes per sample

2.2.2 Etching

Several materials required etching in order to reveal their microstructural features. These samples were removed from the mount after polishing before etching was performed. Stainless steels were immersed in Carpenter's etchant at room temperature for 4 seconds. The composition of the etchant used is found in Table 2.5. Due to concerns related to safety, chemical etching was not performed on ceramics as it required the use of acids above their boiling point. In addition to this, it was not possible to use electrolytic etching techniques as the ceramics used in this work were not electrically conductive. Therefore, other etching methods were experimented as an alternative to chemical etching. There is evidence that ceramics can be thermal etched (annealing) or plasma etched to delineate the grain boundaries of the material (Chinn & Chinn, 2002).

Table 2.5 Carpenter's etchant composition.

Name of Etchant	Composition
Carpenter's stainless steel etch	FeCl ₃ – 7 g
	CuCl ₂ – 2g
	Hydrochloric acid – 100 ml
	Nitric acid – 4.9 ml
	Ethanol – 100 ml

Ceramics were thermal etched using a tube furnace. After removing the encapsulations, the specimens were placed in a boat, which was positioned inside the chamber. Subsequently, the furnace was closed and vacuum pumped, before being heated to the etching temperature, which typically lies 100-200K below the sintering temperature of the ceramic. The processing conditions required for etching were obtained from the literature (Chinn & Chinn, 2002) and are summarised in Table 2.6. The furnace was heated and cooled gradually to minimise thermal shock failures of the heating elements.

Table 2.6 Process conditions for thermal etching ceramic materials.

Material	Annealing conditions
Nitrides	Temperature = 1250 °C Time = 15 min
Oxides	Temperature = 1500 °C Time = 20 min

Plasma etching was carried out using the SENTECH (Berlin, Germany) Etchlab Reactive Ion Etching (RIE) setup located at the Department of Materials at Imperial College (London, UK) through the Royce Institute. The apparatus, which is shown in Figure 2.4, is capable of etching materials through bombardment of ions and the use of multiple gases, including C_4F_8 , Ar, O_2 and N_2 . The literature showed that ceramics such as Sialons and Si_3N_4 were plasma etched from superheated $CF_4 + O_2$ gas (Chinn & Chinn, 2002). As the RIE apparatus did not have a CF_4 gas supply, etching was conducted using C_4F_8 gas at 50 Pa pressure and 70 W forward power for 3 minutes. During the plasma etching process, the gas mixture was admitted into the vacuum chamber and ionised to form a plasma, which attacked the grains in the ceramic. At the end of the etching process, the chamber was cleaned with O_2 gas to remove volatile etch products before opening the chamber.



Figure 2.4 Sentech RIE apparatus for plasma etching available at Imperial College, London.

2.2.3 Imaging and Chemical Composition Analysis

Polished specimens were analysed using both light and electron microscopes. When quick and accurate images needed to be captured, digital microscopy was often utilised; the analysis was performed using a Keyence VHX-7000 (Osaka, Japan) digital microscope (Figure 2.5a), which enabled to perform 3D depth profiling of the surface morphology of the specimen. For capturing more details, scanning electron microscopy (SEM) was used. The SEM images obtained in this study were captured using a Hitachi (Tokyo, Japan) TM4000 desktop SEM (Figure 2.5b) and a ZEISS (Jena, Germany) EVO SEM (Figure 2.5c). Both instruments were equipped with secondary electron (SE) and backscattered electron (BSD) detectors. In addition to this, Oxford Instruments (Abingdon, UK) EDS detectors were installed on the microscopes with Aztec software (version 6.1) for performing chemical analysis.

All the specimens analysed on the SEM were plasma cleaned using the Gatan (Pleasanton, USA) Solarus machine shown in Figure 2.6a, in order to remove any contamination from the surface. Mounted specimens were attached to a range of different sized stubs using two-sided carbon tape. Non-conductive specimens, such as ceramic materials, were coated with a 5 nm thick layer of Pt using an Agar (Stansted, UK) sputter coater (Figure 2.6b). If charging was still present, conductive tape was used to bridge the surface of the specimen to the stub, avoiding the electrons fired from the SEM gun to build up on the surface.

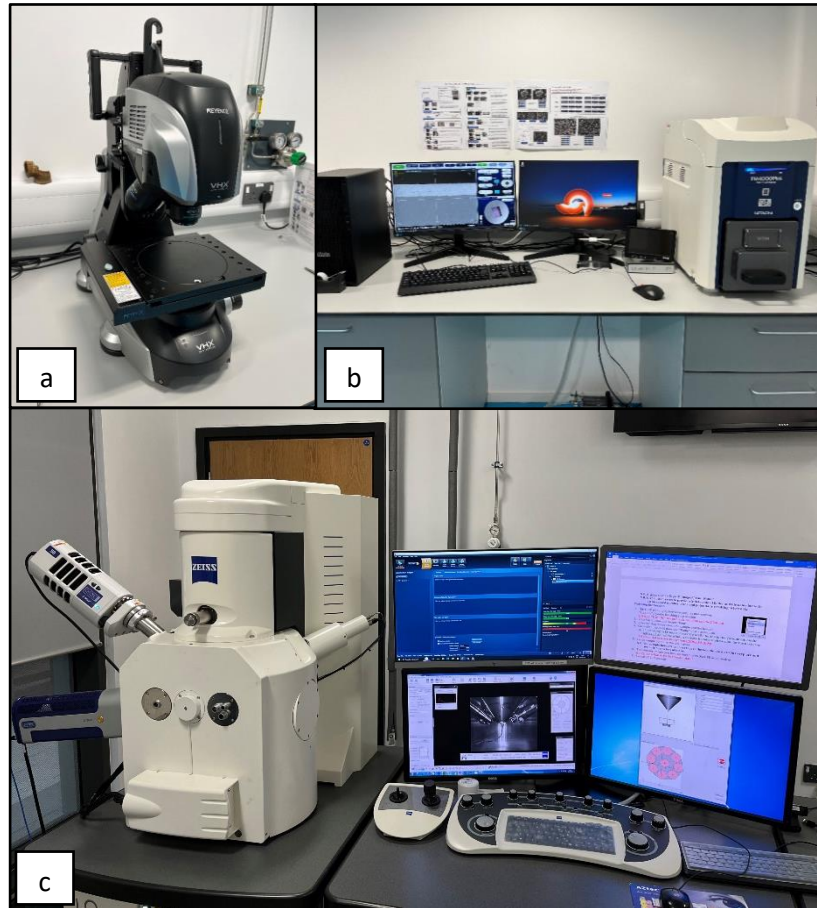


Figure 2.5 Microscopes used for material characterisation: digital microscope (a); desktop SEM (b); ZEISS EVO SEM (c).

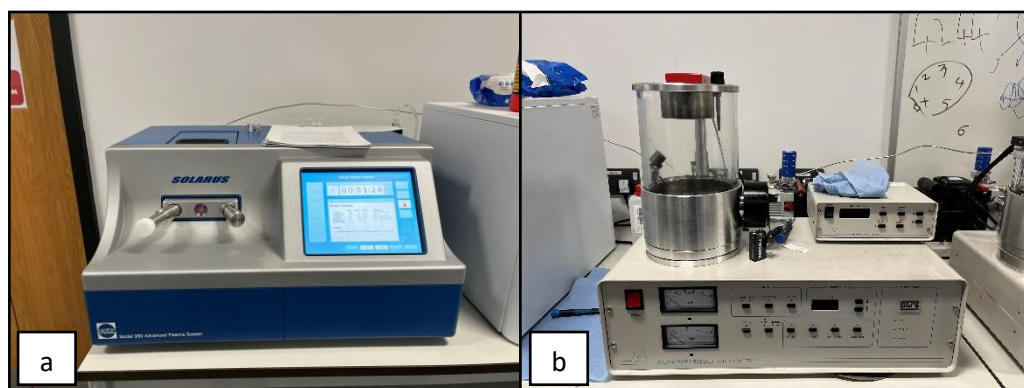


Figure 2.6 Solarus plasma cleaner (a); Agar sputter coater (b).

2.2.4 X-ray Diffraction

X-ray diffraction (XRD) was used for materials and phase identification. Two different Bruker (Billerica, USA) X-ray diffractometers were used in this project, namely the D8 Discover (Figure 2.7a) and the D8 Advance (Figure 2.7b). Diffraction patterns were collected at room temperature, over an angular range of 20° to 80° with a count time per step of 1 s and 0.03° step size. The diffraction data generated was analysed with DIFFRAC.EVA software (version 7.0.0.4) and the diffraction patterns were compared to the reference patterns of known phases available in the Crystallography Open Database (Gražulis et al., 2009).

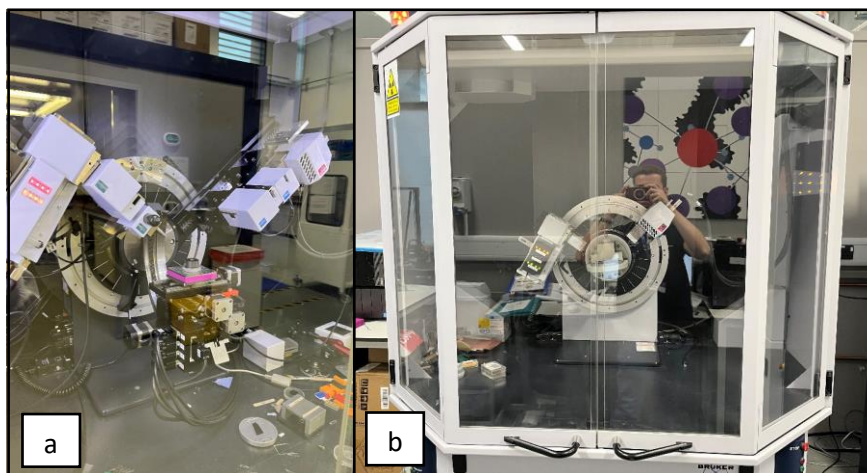


Figure 2.7 X-ray diffractometers used in this project: D8 Discover (a); D8 Advance (b).

2.2.5 Roughness Measurement

The roughness of the specimens was assessed using linear measurements on a surface profilometer. In this project, roughness measurements were obtained using a Taylor Hobson (Leicester, UK) Talysurf Form 2 surface profilometer (Figure 2.8) and the roughness was described in terms of arithmetic mean roughness value (R_a). To determine the roughness of a specimen, multiple linear measurements were carried out by rotating the specimen at 45° angles and the R_a values obtained were averaged. The profilometer was also used to determine the depth and area of a groove on the

surface (e.g. after wear testing), as well as to generate 3D scans of the surface, which were processed using the Talymap Gold software.

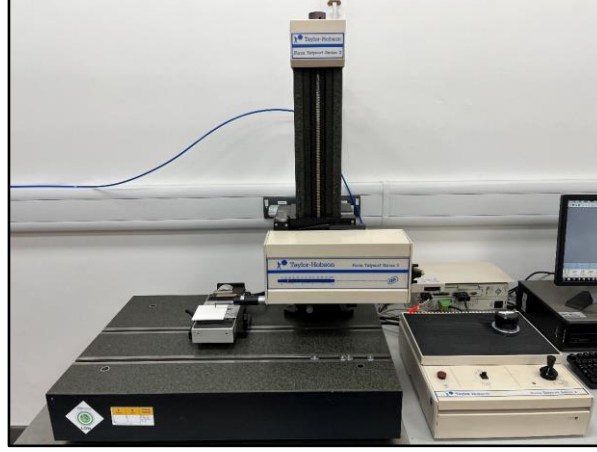


Figure 2.8 Talysurf profilometer used for surface roughness measurement.

2.2.6 Density Measurement

The bulk density of specimens was measured via the Archimedes' Principle using the setup shown in Figure 2.9. The specimens were weighed in air and the mass was recorded. Subsequently, the mass was recorded when the same specimens were submerged into a beaker of water. The difference between the two readings corresponds to the weight of fluid displaced and it allows to determine the bulk density. In this thesis, the relative density is reported, which was obtained from the ratio of the measured bulk density to the theoretical density obtained from the literature. For specimens fabricated by combining dissimilar materials, the theoretical density was calculated using the rule of mixtures (Equation 2):

$$\rho_c = \sum_i \rho_i \phi_i \quad (2)$$

where ρ_c is the density of the composite, and ' ϕ ' the volume fraction of i constituents.

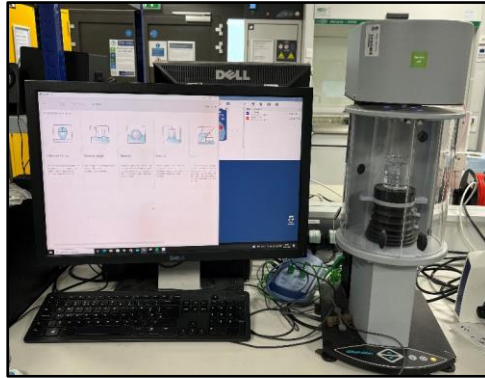


Figure 2.9 Experimental setup used to measure density with Archimedes' Principle.

2.2.7 Dilatometry

The coefficients of thermal expansion (CTEs) were measured with dilatometry, using a NETZSCH (Selb, Germany) DIL402C dilatometer. The experimental set-up is shown in Figure 2.10. Samples were sectioned into bars with a diameter of 5 mm and a length of 20 mm. The length change of the bars was analysed in the temperature range between room temperature and 465 °C on heating at a rate of 10 K min⁻¹. Curves were acquired to illustrate the variation of the CTE as a function of temperature.



Figure 2.10 Experimental set-up used to measure the coefficients of thermal expansion.

2.3 Mechanical Testing

2.3.1 Hardness Testing

The hardness of the specimens tested in this project was measured using an Innovatest (Maastricht, Netherlands) hardness indenter, which is shown in Figure

2.11a. All the specimens were first hot or cold mounted and were prepared according to the preparation procedure outlined in Section 2.2.1. The readings were measured via Vickers Hardness (HV) using indentation loads between 3 and 5 kgf. Images of the indents were taken on the digital microscope (Figure 2.11b). The HV values were determined by measuring the average diagonal length of the indent ‘ d ’ according to Equation 3 (Zhou et al., 2013):

$$HV = 1.854 F/d^2 \quad (3)$$

where ‘ F ’ is the load applied in [kgf]. Ten readings were taken on each specimen and the values measured were averaged.

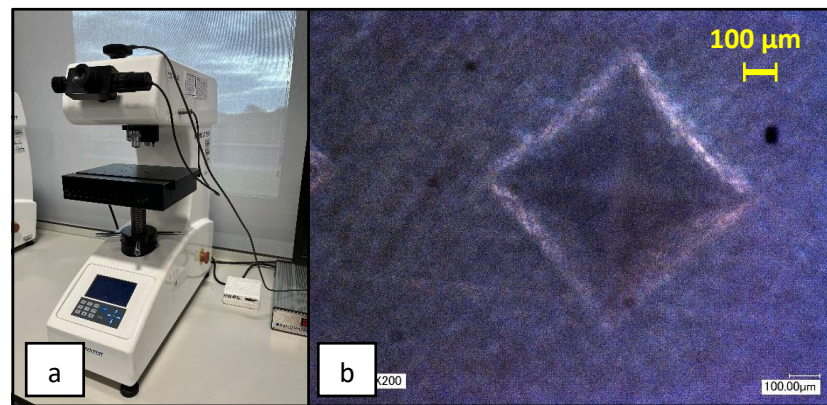


Figure 2.11 Innovatest hardness tester (a); image of an indent captured on the Keyence (b).

2.3.2 Pin-on-disc Wear Testing

Wear testing was performed on a bespoke pin-on-disc apparatus developed by Williams (2023). The experimental setup is illustrated in Figure 2.12. In this project, pin-on-disc wear testing was carried out to investigate the tribological properties of ceramic materials. Tribological properties are typically investigated using tribometers such as the pin-on-disc, four-ball and Timken apparatuses (Carrapichano et al., 2002; Rai et al., 1999; Stachowiak & Batchelor, 2004; Xiao et al., 2014). A limitation of the four-ball and Timken tribometers is that the contact stress can vary during testing. In this study, friction and wear characterisation was performed using a pin-on-disc

tribometer, which offers better control of the experimental conditions compared to the other two techniques (Stachowiak & Batchelor, 2004).

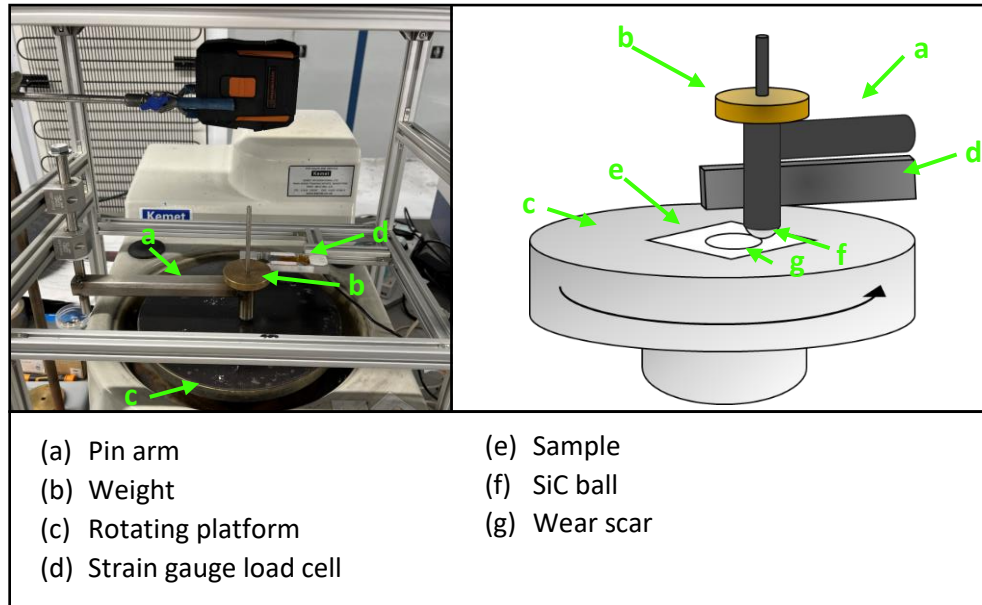


Figure 2.12 Pin-on-disc experimental apparatus for friction and wear testing.

Testing was performed on $80 \times 80 \times 5$ mm plates and 60×3 mm discs. All the specimens were polished to a roughness of $<1 \mu\text{m}$ (Ra) according to the preparation procedure outlined in Section 2.2.1. Silicon carbide (SiC) ball bearings with a hardness of 2200–2800 HV and 10 mm diameter were used as the pin. SiC was chosen due to its superior hardness compared to that of the ceramic ‘discs’, making the disc the expected sacrificial counterpart. The setup consisted of a rig where an arm was weighted down onto the ceramic specimens with a known constant load of 2 N to press the pin against the rotating specimen, as shown in the previous experiments (Williams, 2023). Higher loads were avoided to prevent the softer ceramics from breaking during the tests. The SiC sphere was attached to the arm, as shown in the figure, and the applied force was controlled by adding weights to the ball holder. The rig was fitted with a strain gauge load cell, which measured the friction force upon contact with the pin arm. The pin-on-disc apparatus was positioned above the rotating platform of a polishing machine, where the test sample was fixed. Testing was performed in the ‘upper-pin-on-bottom-disc’ mode without lubrication and at

room temperature. The rotations of the platform were set between 50-150 rpm. Details of the sliding speeds and duration of sliding contact are provided in the relevant experimental sections. The ball bearing was replaced before starting each test so that each time the ceramic ‘discs’ were sliding against a new, untested SiC pin.

The friction force was recorded automatically by the data processing software and was divided by the normal force to obtain the coefficient of friction. To determine the wear loss of the samples, 3D scans of the wear scars were recorded using a surface profilometer. The wear volume loss of the discs ‘ V ’ was obtained according to Equation 4:

$$V = A \times L \quad (4)$$

where ‘ A ’ is the measured cross-sectional area of the wear scar and ‘ L ’ is the length of the stroke and is equal to the circumference of the circular trace left after the test. The worn track section ‘ A ’ was obtained by performing a line scan across the worn track. An example of a line scan is illustrated in Figure 2.13. The total sliding distance ‘ S ’ was obtained by multiplying the sliding speed ‘ v ’ in [m/min] with the duration of the test ‘ t ’ in [min], as shown in Equation 5:

$$S = v \times t \quad (5)$$

Subsequently, the sliding distance was used to calculate the wear rate ‘ k ’ as shown in Equation 6 (Yin et al., 2022):

$$k = \frac{V}{F \times S} [mm^3/Nm] \quad (6)$$

where ‘ F ’ is the normal contact load and ‘ S ’ is the sliding distance.

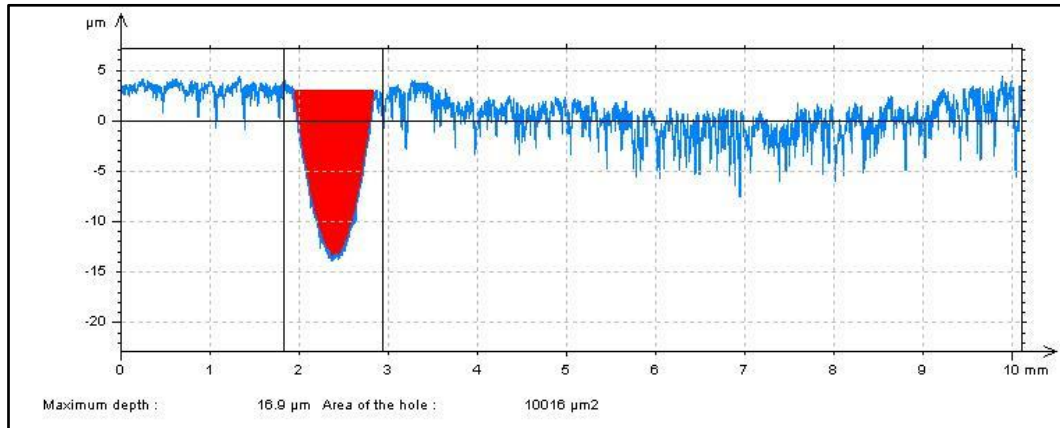


Figure 2.13 Example of a line scan performed across the worn track.

2.4 Corrosion Testing

2.4.1 Static Immersion Testing

Static immersion tests were conducted to study the corrosion behaviour of the materials in liquid Zn alloy. A schematic of the experimental set up is illustrated in Figure 2.14a. The tests were conducted using two top loading furnaces (Figure 2.14b). Two graphite crucibles (184 × 232 mm) were filled with approximately 20 kg of Zn alloy ingots taken from ZODIAC to obtain Zn-0.3wt%Al and Zn-1.5wt%Al-1.5wt%Mg bath compositions supersaturated in Fe. Samples of each bath were sent to Element Materials Technology (London, UK) for ICP-MS to check whether the target compositions were met, prior to submerging the samples in Zn. Two specimens for each material were immersed separately in each bath to study the effect of bath composition on the corrosion behaviour of the ceramics. The specimens were suspended in the bath from above using metallic wire, which was wrapped around a threaded bar positioned above each crucible.

During the first iteration of the experiment, molybdenum (Mo) wire was used to hold the samples, as well as a series of steel bolts and nuts to secure the samples onto the wire (Figure 2.15a). The wire material was later replaced with SS 316L due to the brittleness of Mo, which snapped during the first trial. In addition to this, bolts and nuts were eliminated after the first trial and the samples were secured only using the

steel wire (Figure 2.15b). During testing, SS 316L wire was attacked by the bath, forming a mixture of intermetallic particles and liquid Zn, and it was observed that the reaction climbed out of the bath. This process is termed 'supermeniscus intermetallic climb' (Brunnock et al., 1996; Marder & Goodwin, 2023) and it exposed the threaded bar to the attack of molten metal. For this reason, the threaded bar was replaced after each test; however, the corrosion behaviour of the specimens being tested was not affected.

Prior to immersion in the Zn alloy bath, the specimens were preheated in an oven at 300 °C for one hour. Subsequently, they were introduced in each Zn bath ensuring that all the specimens were submerged below the Zn level. Thermocouples were used to monitor the furnace temperature, which was kept at a constant value of 465 °C during the test. After 5 weeks, the samples were removed from the molten Zn bath and cooled naturally to room temperature. Each sample was pickled in HCl acid (35%) solution to remove the Zn solidified on the surface. The samples were mounted in conductive resin and the top surface was ground and polished according to the procedure described in Section 2.2.1, starting with coarse SiC grinding paper to obtain cross-sections for metallographic examination with optical microscopes and SEM-EDS.

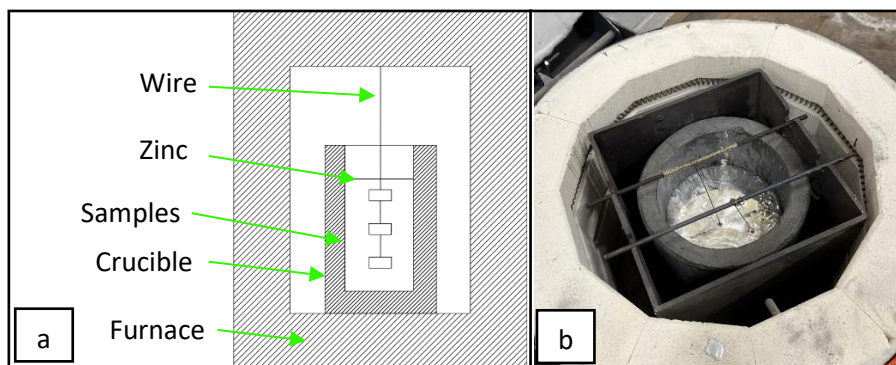


Figure 2.14 Sketch of the experimental setup used for static dip testing (a); top loading furnace containing the Zn bath (b).

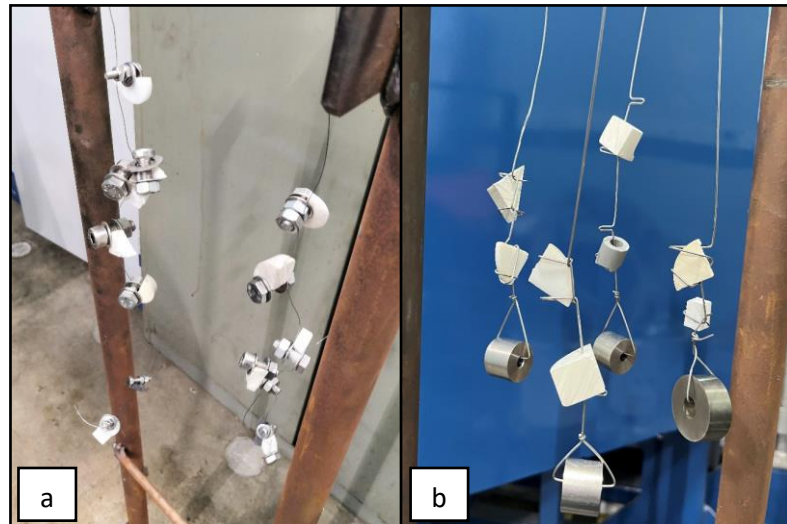


Figure 2.15 Samples prior to testing: first trial using bolts and nuts (a); second test using SS 316L wire only (b).

2.4.2 Dynamic Testing

2.4.2.1 Existing Bearing Test Rig

The importance of conducting dynamic testing was discussed in Section 1.9.4 (Chapter 1). In order to perform dynamic tests where the materials are tested in motion inside a molten metal bath, a bespoke testing rig is required. It was determined that a suitable process of validating submerged galvanising pot roll bearings would consist of offline trials on the bespoke testing rig prior to online trials on the pot rolls on the ZODIAC galvanising line. If these trials were successful, the new bearing could be installed on the ZODIAC CG line.

During the initial stages of the project, a pre-existing test rig was considered for dynamic testing of prospective bearing materials. The rig was designed and constructed for a previous doctorate project on galvanising bath bearings (Faulkner, 2020). This rig was developed to allow offline testing of full-scale journal bearings. The rig was designed for validating bearing materials and design before being installed on the line, where unplanned maintenance stops can cost thousands of pounds per hour in unplanned downtime. In addition to this, the rig was designed to test full-size correct roll bearings of accurate geometry and to operate under load and

environmental conditions used on the line. As discussed in Chapter 1, Section 1.6.1.3, the corrector roll is independent of the other two rolls, as it is attached to a separate support framework. This specific arrangement facilitates the removal of the bearing and should failure occur, the associated financial losses would be less significant compared to the corrector roll and the stabiliser roll, which share a common supporting framework. For this reason, the rig was developed to test full-size corrector roll bearings using known loading and rotational velocity conditions (Faulkner, 2020).

A photograph of the existing bearing testing rig is shown in Figure 2.16. The rig was designed to bring both bearing sleeve and bushing components into contact. The bearing sleeve was mounted to a driveshaft simulating the pot roll end. The two bearing components are brought into contact with frictionless linear motion of the testing frame. The rig is equipped with a 7 kW motor and is capable of producing a maximum speed of 300 rpm and a maximum torque of 245 Nm. A loading mechanism consisting of a system of suspended weights is used to continuously apply a maximum load of 9810 N (Faulkner et al., 2021).

Throughout the present research, several issues were identified on the existing bearing test rig. As previously mentioned, the rig was designed to test full-size bearing components. Testing multiple bearing sleeve-bushing material combinations required substantial investments, considering the high costs associated with fabrication of samples of the required bearing geometry and material, which are estimated to be around £2000 per test. Additionally, more time would be required for procuring bearings with size and geometry that were equivalent to components used on ZODIAC, compared to using smaller-scale components of simpler geometry. For this reason, using the existing rig for dynamic testing would have required time and financial resources that were beyond those allocated for this project. In order to overcome these limitations, a decision was made to replace full-size bearing sleeve and bushing components with smaller-scale bars and pads of simpler geometry. This more simplistic approach would still account for the molten metal media, which was absent in other methods of wear testing, such as pin-on-disc tests, and would still allow the assessment of the tribo-corrosion behaviour of prospective bearing materials,

overcoming the limitations of static immersion testing. Redesigning the existing rig to allow testing of a 'bar-and-pad' system was considered initially. However, it was decided to design and build a new machine due to difficulties in upgrading the existing rig.

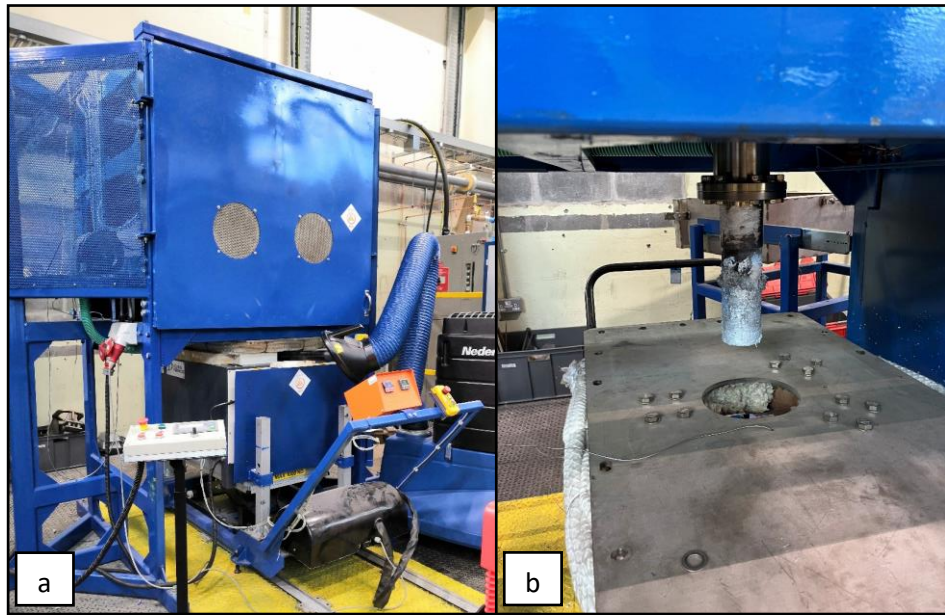


Figure 2.16 Existing bearing test rig (a); detail of the shaft for bearing sleeve specimens (b).

2.4.2.2 New Test Rig Design

The new rig (Figure 2.17a) was built at Swansea University and designed with two design objectives in mind. The first objective was to enable rapid, smaller-scale dynamic testing of a pair of materials in liquid Zn alloy. Like the journal bearings used in the CG line, the system consists of a component in relative movement against a static component. The new design utilises a rotating shaft, or bar, which is sliding against a static component which takes the form of a square pad, as shown in Figure 2.17b. Specimens with this simplified geometry are less expensive and easier to manufacture compared to full-size bearings, enabling rapid dynamic testing of prospective galvanising pot bearing materials. The second objective was to simplify the operation of the machine, which was designed for smaller scale dynamic tests and, therefore, it was no longer necessary to simulate the load and speed utilised on

the line. The loading mechanism present on the existing rig was eliminated; instead, the applied load is provided by the shaft assembly, which pushes the bar onto the static pad under the effect of gravity. A 3D drawing of the new design is illustrated in Figure 2.18.

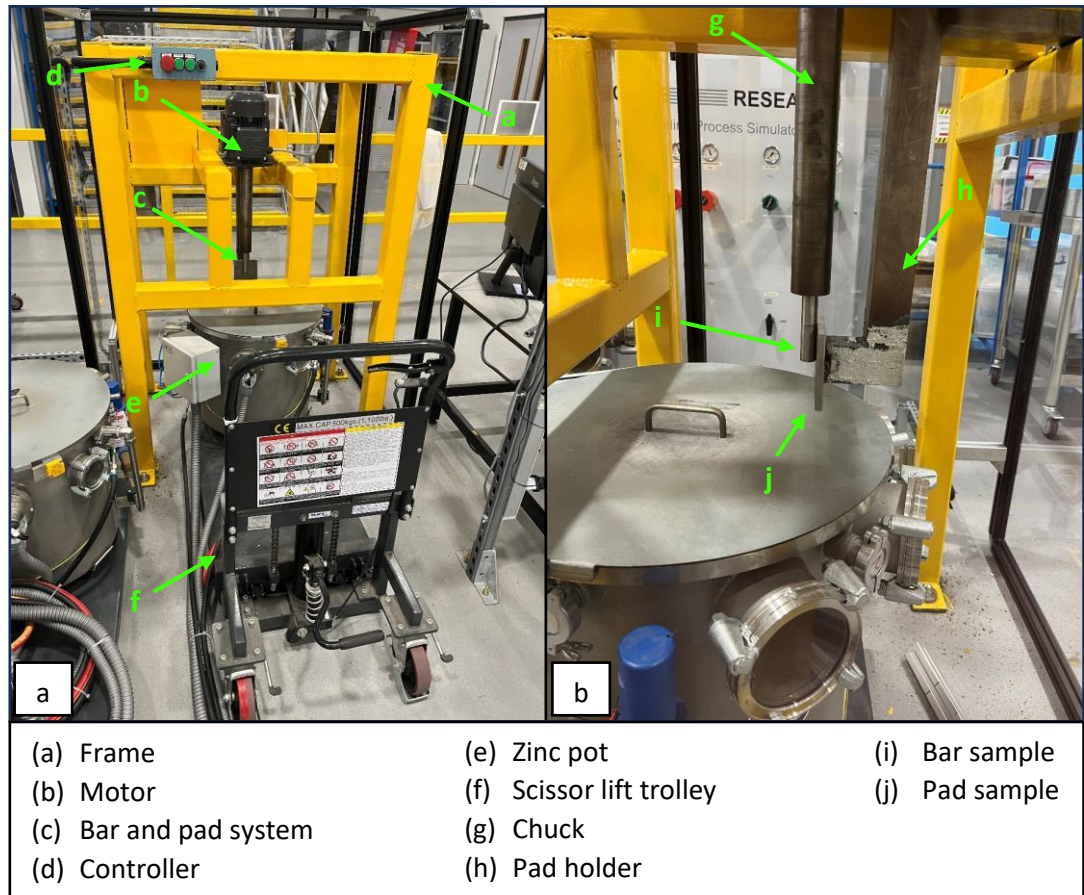


Figure 2.17 New test rig (a); details of the 'bar-on-pad' design (b).

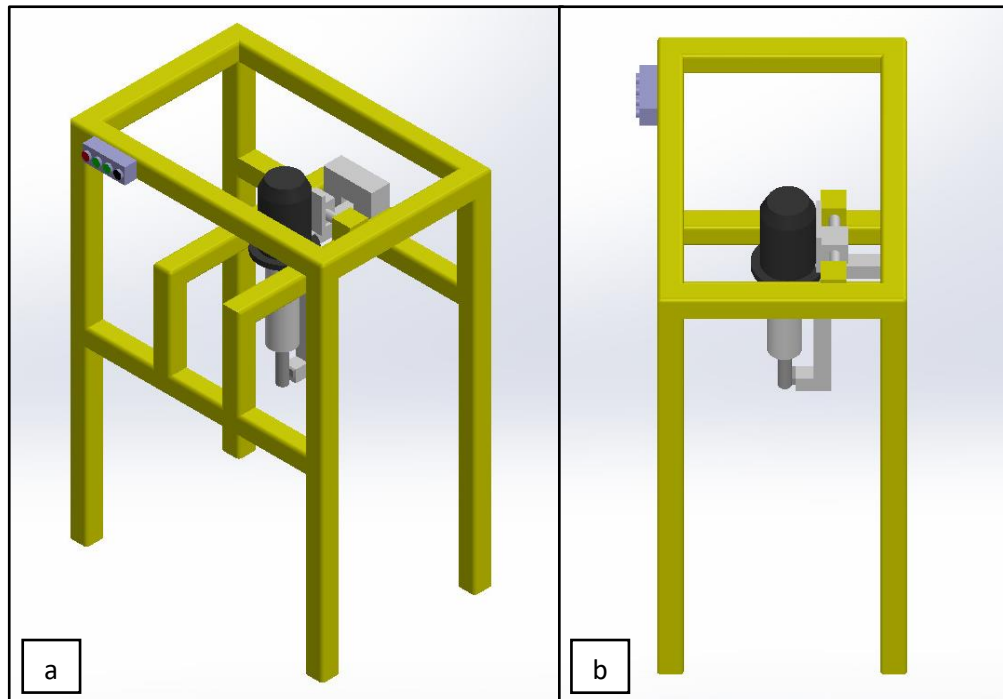


Figure 2.18 3D drawing of the new test rig: isometric view (a); side view (b).

The frame, which is sketched in Figure 2.19, was fabricated from mild steel box section of 75 mm width and 3 mm wall thickness. A control panel was mounted on one side of the frame with buttons to control the speed and direction of the shaft rotation. A 0.55 kW motor was located to run parallel to the shaft, as shown in Figure 2.17. The bar sample is bolted to a mild steel chuck which is attached to the motor. The chuck was fabricated to accommodate bars of 20 mm diameter and is not submerged in liquid Zn, so that the upper portion of the bar is just above the Zn level. This system allows to reuse the chuck after each test. The bar is capable of rotating up to a speed of 300 rpm. The pad is tack welded to a mild steel structure which is bolted onto the frame at the rear of the rig. In order to determine the load applied onto the pad, several measurements were taken by pulling the shaft at different distances from the pad holder using a crane scale. An average load of approximately 60 N was recorded and the load was not found to vary significantly at different distances from the pad holder; therefore, it can be assumed to remain constant during testing. The zinc pot used for the new rig consisted of an existing furnace which had already been procured as a spare furnace for the hot-dip simulator. The pot is equipped with a thermocouple for temperature measurement inside the furnace and is heated by resistance coils

around the outside of a graphite crucible. The pot was mounted on a scissor lift and mobile trolley. Two lids were used to cover the pot, which were laser cut to create a central opening for the shaft and pad holder.

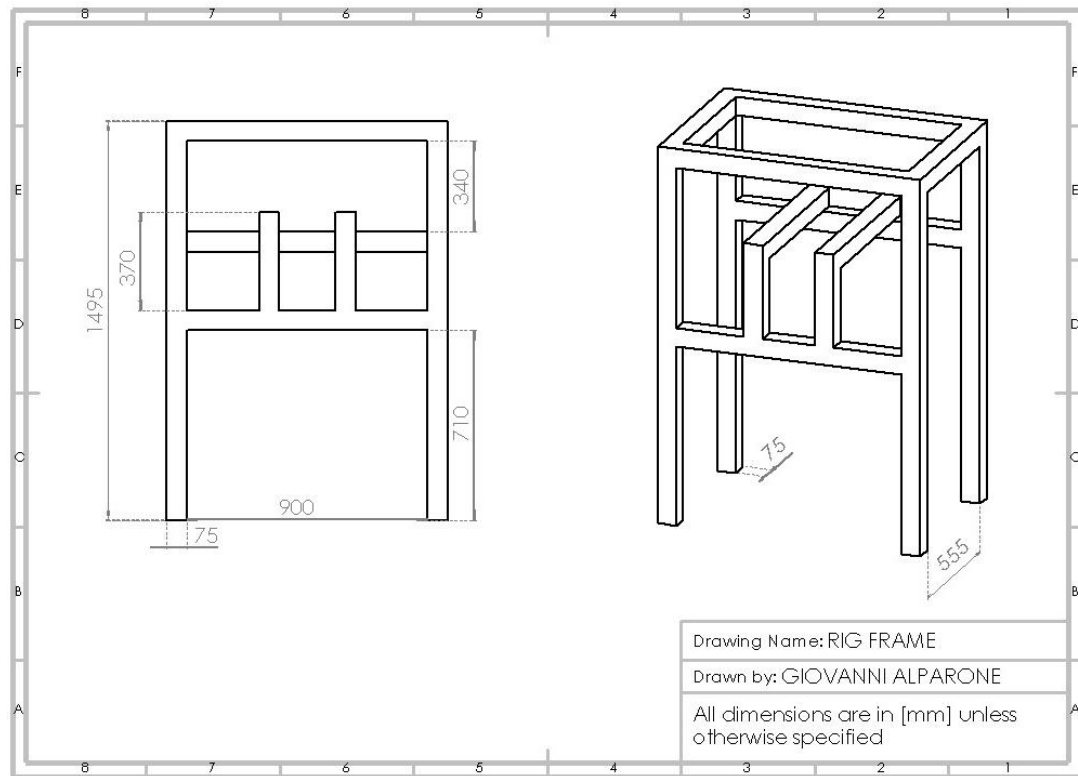


Figure 2.19 Drawing illustrating the new rig frame.

2.4.2.3 Dynamic Testing Experimental Procedure

The bar and pad specimens were mounted on the rig as described in Section 2.4.2.2. The Zn pot was loaded with approximately 40 kg of Zn alloy ingots. Like static immersion testing, each material combination was tested in both Zn-0.3wt%Al and Zn-1.5wt%Al-1.5wt%Mg bath compositions and the bath chemistry was checked by sending samples to Element Materials Technology (London, UK) for ICP-MS. The pot was set at a temperature of 465 °C, which was monitored using thermocouples installed inside the pot. As the Zn melted, dross formed on top of the bath, which was removed before starting the test. Once the Zn was fully molten, the pot was raised so that the bar was just above the Zn level and was held for 24 hours to preheat the

specimens and to minimise the effects of thermal shock. Subsequently, the pot was raised slightly to submerge the bar and the pad in liquid Zn and the lid was closed. The bar was rotated in the clockwise direction with a speed of 300 rpm for 48 hours. Subsequently, the pot was lowered and the specimens were removed from the holders. Samples from the bar and the pad were cut as described in Section 2.2.1 for characterisation. Zn was removed from portions of the tested pad specimens with HCl to measure volume loss. The displacement of the bar specimen after 48 hours of sliding against the pad specimen was determined by measuring the depth of the wear scar left on the pad specimen. The volume loss was obtained from the cross-sectional area and the length of the scar, enabling to calculate the wear coefficient according to Equation 6. 3D maps of the wear scar were generated using the Keyence VHX-7000 (Osaka, Japan) digital microscope (Section 2.2.3).

Chapter 3

Testing of Commercially Available Ceramics

3.1 Introduction

As discussed in Chapter 1, Section 1.8, ceramics are potential materials for manufacturing galvanising pot roll bearings with extended durability, as they can remain unreactive in molten metals. However, several issues were identified in the literature, since not only a small selection of ceramics were investigated, but also the effects of changing bath composition on the performance of the ceramics in liquid Zn was not examined. Ceramics are a broad class of materials that includes oxides, nitrides, carbides, etc. These materials have dissimilar properties and composition, and, for this reason, a decision was made to test a broad selection of ceramic materials that are typically used in engineering applications.

An initial study was conducted on materials that were sourced from Precision Ceramics (Birmingham, UK) and include a selection of seven different ceramics, whose names and composition were provided in Table 2.1 (Chapter 2). The choice of these materials is supported by the information found in the literature, which is discussed in detail in Chapter 1, Section 1.8.2. It was shown that oxides, such as Al_2O_3 and ZrO_2 , as well as nitrides, such as BN and Si_3N_4 , were previously experimented in baths containing Zn and showed potential to remain unreactive. In addition to this, it was decided to test materials, such as Macor® and AlN-BN, which are available commercially; however, there is no information regarding their reactivity with molten Zn. The corrosion behaviour of the ceramics was compared to that of two galvanising hardware materials, namely SS 316L and Wallex6™ coated with HVOF 90% WC-Co layer; these two materials were used as benchmarks. All the samples were characterised before and after testing using the microscopy techniques discussed in Chapter 2, Section 2.3.3. The corrosion behaviour of the materials was investigated by conducting static immersion tests in liquid Zn-Al and Zn-Al-Mg at 465 °C. In

addition to this, mechanical testing, including hardness and pin-on-disc wear testing was conducted on as-received ceramic specimens.

The findings presented in this chapter were used to write the following papers:

- “Static Immersion of Ceramics in Zn-Al and Zn-Al-Mg for Optimised Galvanising Bath Bearings”. In: Proceedings of the 13th International Conference on Zinc & Zinc Alloy Coated Steel Sheet (Galvatech), Seoul.
- “The Effect of Sliding Speed on the Tribological Properties of Ceramic Materials”. In: *Materials* 2023, 16(23), 7252. DOI: 10.3390/ma16237252.

3.2 Material Characterisation of As-received Specimens

3.2.1 Benchmarks: SS 316L and WC-Co/Wallex6TM

SS 316L is an Fe-based alloy and is classified as an austenitic stainless steel. Its constituents are Cr, Ni and Mo. SS 316L refers to the low-carbon variant of grade 316. The typical composition of SS 316L is found in Table 3.1. Wallex6TM is a Co-Cr-W-C alloy and it is the equivalent of Stellite6TM. The composition of Wallex6TM is found in Table 3.2. Wallex6TM was coated with a 150 µm thick layer of WC-Co applied via the HVOF thermal spray process. This coating provides greater chemical resistance to liquid Zn, as previously explained in Chapter 1, Section 1.8.1. SEM images of SS 316L and Wallex6TM coated with WC-Co are shown in Figures 3.1 and 3.2 respectively. SS 316L was etched to reveal the microstructural features, following the process outlined in Section 2.2.2.

The microstructure of the SS 316L and WC-Co/Wallex6TM benchmarks are respectively shown in Figure 3.1 and Figure 3.2. The SEM image obtained for the etched SS 316L specimen shows that the microstructure of the material is characterised by polygonal grains as well as annealing twins. Regarding Wallex6TM, the material is a Co-based alloy and Figure 3.2 shows the presence of several eutectic phases in the material. EDS analysis was performed to measure the elemental composition of the

microstructure of the alloy and the WC-Co coating (Figure 3.3). C peaks were excluded from the analysis due to difficulties in measuring C content accurately with EDS.

Table 3.1 SS 316L composition (Davis, 1994).

Material	%Fe	%Cr	%Ni	%Mn	%Si	%S	%C	%P	%Mo
SS 316L	BAL	16.0-18.0	10.0-14.0	0-2.0	0-1.0	0-0.03	0-0.03	0-0.045	2.0-3.0

Table 3.2 Wallex6™ alloy composition provided by the supplier.

Material	%Fe	%Cr	%Ni	%Mn	%Si	%Co	%C	%W	%Mo
Wallex6™	2.3	28.4	2.6	0.8	1	BAL	1.2	3.8	0.8

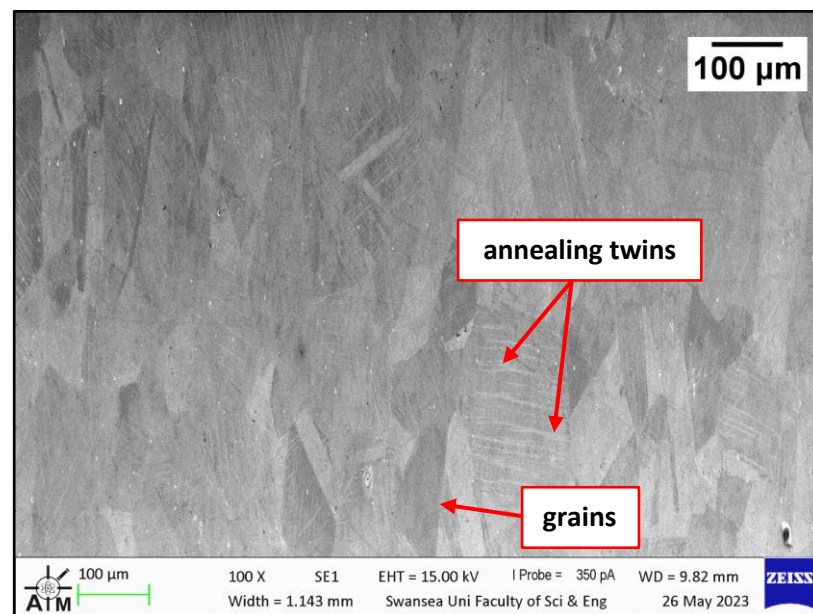


Figure 3.1 Microstructure of SS 316L after etching with Carpenter's solution.

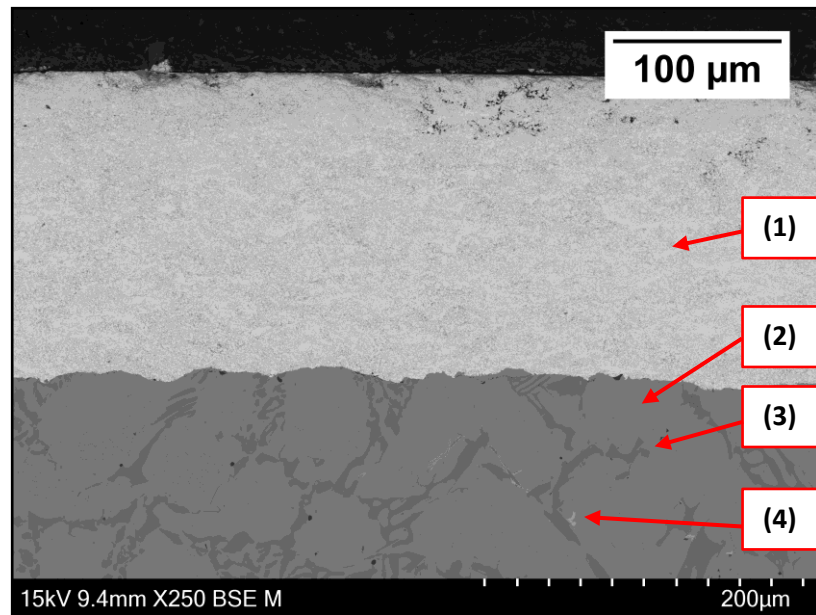


Figure 3.2 SEM image of Wallex6™ coated with HVOF WC-Co coating.

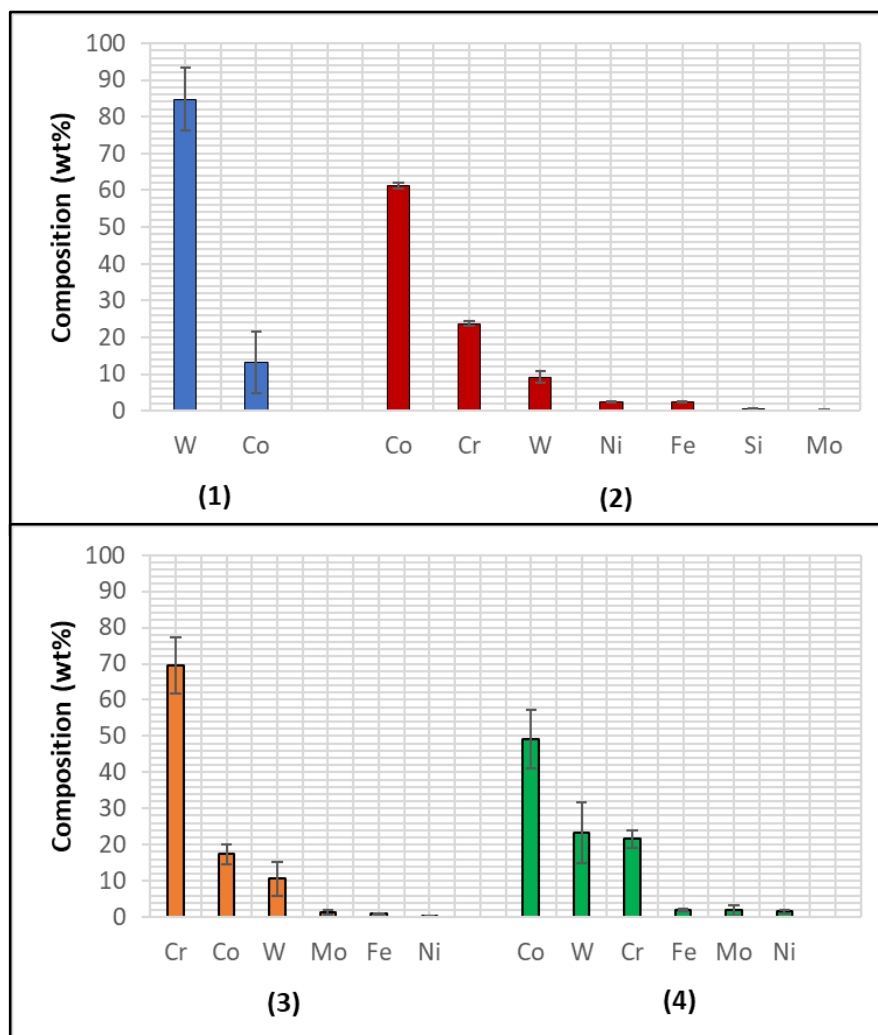


Figure 3.3 EDS analysis of each phase in Wallex6™ taken at marked location in Figure 3.2.

Figure 3.2 and Figure 3.3 show that Wallex6™ is coated with a WC-Co layer that is of uniform thickness and free of cracks (1). The alloy is characterised by a Co solid solution matrix phase (2), with Co, Cr and W as the main constituents. EDS found that the average element composition of this phase is Co (61.3 ± 0.8 wt.%), Cr (23.8 ± 0.6 wt.%) and W (9.3 ± 1.5 wt.%). Two eutectic phases were observed in the Co matrix phase: a primary CrCoWMo phase (3) and a secondary eutectic phase of CoWCr (4). The results of EDS elemental analysis showed that the primary eutectic phase comprised of Cr (69.6 ± 7.8 wt.%), Co (17.3 ± 2.8 wt.%), W (10.6 ± 4.6 wt.%) and Mo ($1.4 \pm$ Mo wt.%) with traces of Fe and Ni. The secondary phase mainly contained Co (49.2 ± 8.1 wt.%), W (23.2 ± 8.4 wt.%) and Cr (21.6 ± 2.5 wt.%). Details of both eutectic phases are shown in Figure 3.4.

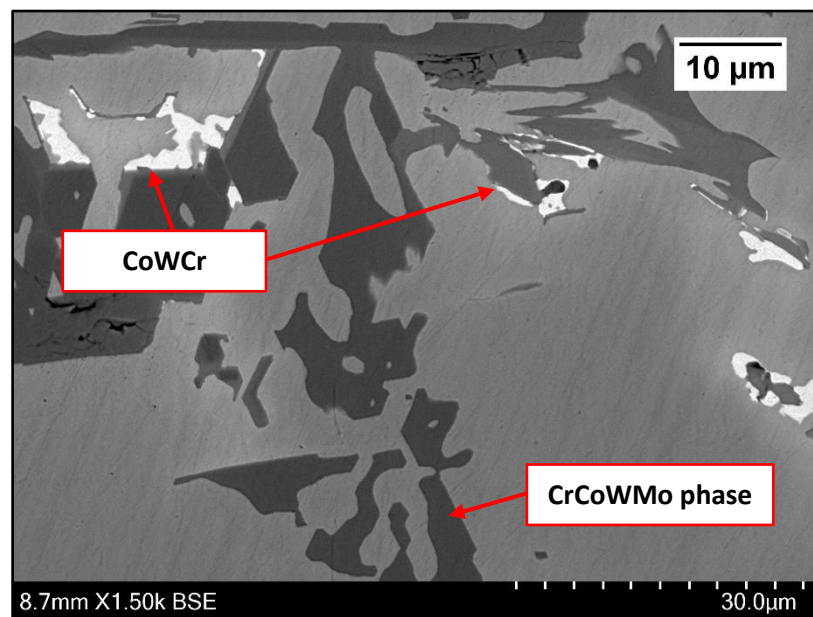


Figure 3.4 SEM image showing the CrCoWMo and CoWCr eutectic phases observed in Wallex6™.

3.2.2 Ceramic Materials

As-received specimens of hBN, BN Grade M26, Macor®, AlN-BN, 3YSZ, Si₃N₄ and Al₂O₃ were characterised with SEM and EDS. As mentioned in Chapter 1, Section 1.8.2.4, BN is a ceramic material that can exist as multiple phases. Its hexagonal phase (hBN)

is characterised by a microstructure which is similar to that of graphite. It consists of a series of layers which are bound by weak Van der Waals forces. Each layer is formed by B and N atoms held together by strong covalent bonds (Reid, 2018; Roy et al., 2021). As a result, the material is easily machinable and can be used as a lubricant, even in dry conditions. In this experiment, two BN grades were tested, namely pure hBN and BN Grade M26, whose microstructure is shown in Figure 3.5 and Figure 3.6 respectively. The microstructure of hBN is platelet-like, with pores separating the anisotropic grains. BN Grade M26 is a ceramic material containing 60% BN and 40% SiO₂. The SEM image of the as-received specimen (Figure 3.6) illustrates the presence of a bright phase which is dispersed in a darker phase. EDS elemental maps (Figure 3.7) show that the dark phase is the BN matrix, which surrounds the brighter SiO₂ phase. The SiO₂ grains have grown with irregular shape and non-uniform size. Porosity is less apparent in the BN M26 specimen compared to the pure hBN.



Figure 3.5 Microstructure of as-received pure hexagonal BN.

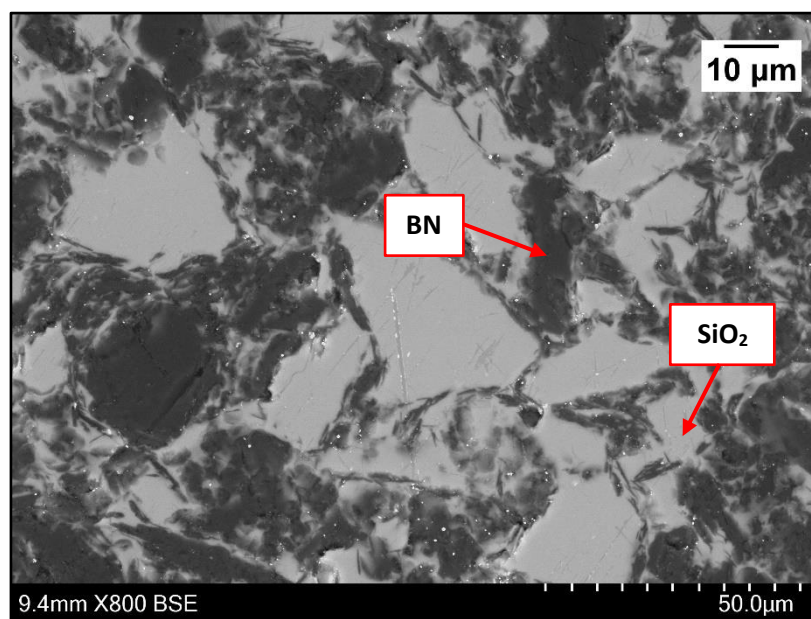


Figure 3.6 Microstructure of as-received BN Grade M26.

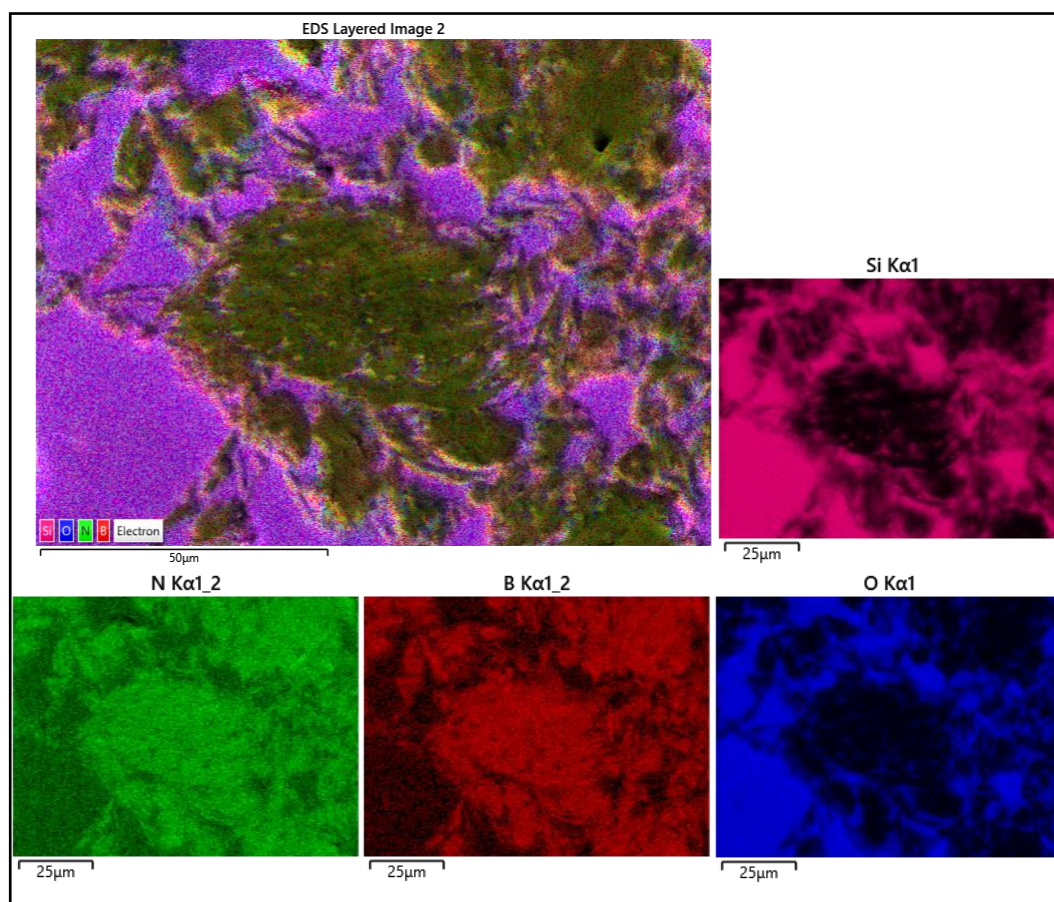


Figure 3.7 EDS maps of as-received BN grade M26.

Macor[®] is a machinable glass ceramic containing 55% fluorophlogopite ($\text{KMg}_3\text{AlSi}_3\text{O}_{10}\text{F}_2$) mica and 45% borosilicate glass (Eiceman et al., 2013). The microstructure of the as-received Macor[®] specimen is found in Figure 3.8. The SEM image shows the presence of randomly-oriented flakes embedded in a glass matrix. This type of structure is typically referred to as ‘house of cards’ microstructure and it makes the material machinable by means of conventional tooling (Henry et al., 2018). In addition to this, the SEM image shows the presence of areas free from flakes or laths. EDS maps (Figure 3.9) confirm that the fluorophlogopite mica flakes are rich in Mg and are surrounded by the glass matrix; however, the mica free areas are found to have the same composition of the flakes, and for this reason, it is likely they are chunks of fluorophlogopite rather than mica free regions. Moreover, it was observed from Figure 3.8 that a spheroidal phase was present and the results of EDS showed that this phase was rich in Mg and F, suggesting that it was spheroidal magnesium fluoride (Figure 3.9).

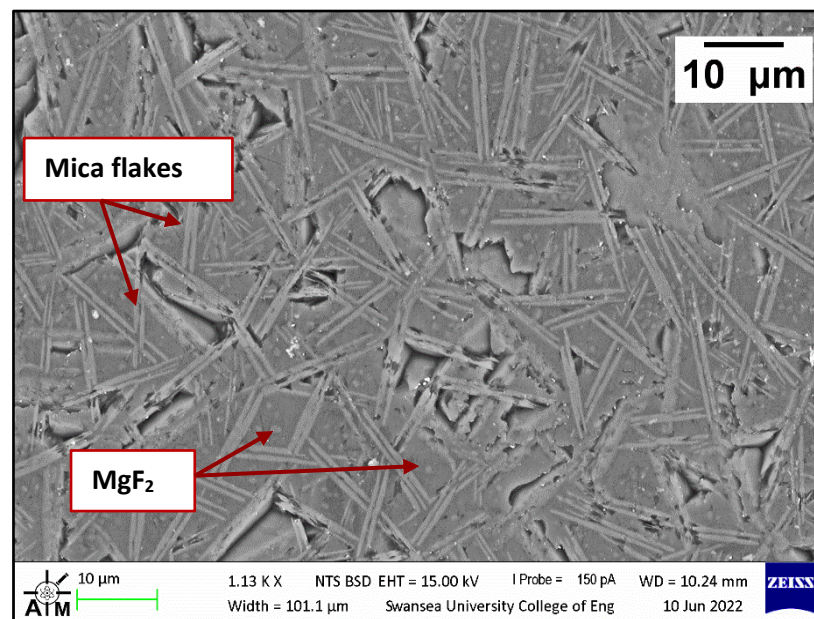


Figure 3. 8 Microstructure of as-received Macor[®] Machinable Glass Ceramic.

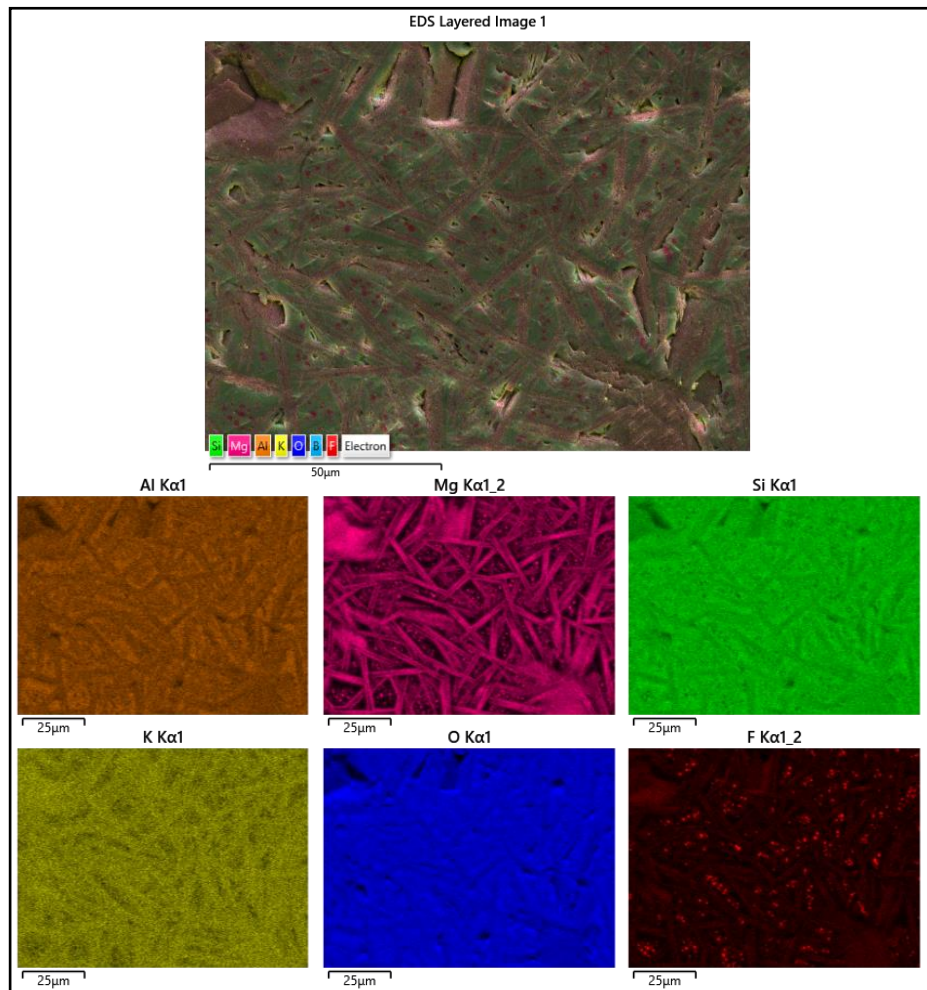


Figure 3.9 EDS maps of as-received Macor® Machinable Glass Ceramic.

Figure 3.10a shows the microstructure of as-received AlN-BN as it appears on the scanning electron microscope. The material is also known as 'SHAPAL Hi-M Soft™' and is a machinable AlN ceramic with BN additions. The microstructure of AlN-BN is characterised by the presence of two phases: a bright matrix with crystalline grains and a darker phase which is surrounded by the bright grains. EDS measurement of both phases (Figure 3.10b) revealed that the dark regions are rich in BN, whereas the bright crystalline grains are the AlN matrix.

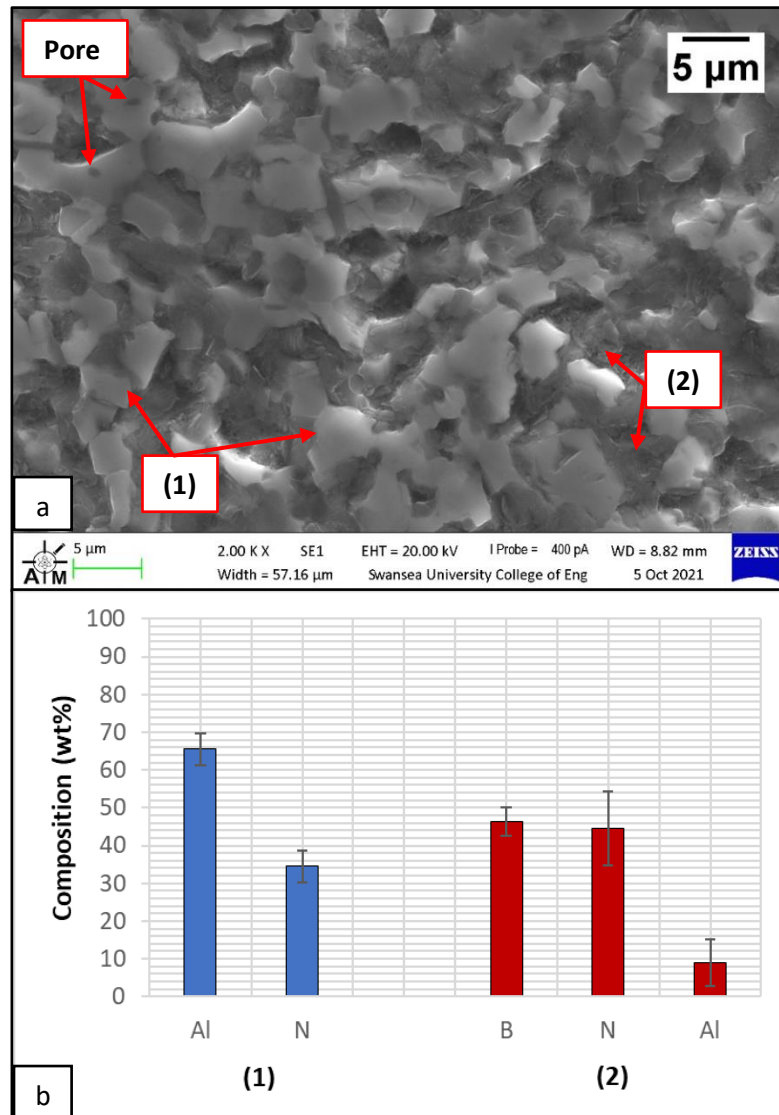


Figure 3.10 SEM image of AlN-BN composite (a); average element composition of the phases observed in AlN-BN (b).

It was observed from the SEM image that the grains have grown without uniform size, which was possibly influenced by the conditions of the sintering process used to manufacture the specimen. The average length of the grains was measured to be $3.8 \pm 1.2 \mu\text{m}$. In addition to this, small pores ($0.7 \pm 0.2 \mu\text{m}$) can be observed within the AlN grains.

Figure 3.11a shows the microstructure of as received 3YSZ. The SEM image illustrates the presence of pores with approximately $0.5 \mu\text{m}$ in diameter. However, the microstructural features of the material were not visible in the as received 3YSZ specimen. There is evidence that ceramic specimens are typically etched to reveal the

microstructural features and several techniques have been proven to etch ceramic materials successfully, including chemical etching, plasma etching and thermal etching or annealing. Two specimens were prepared to compare different etched microstructures. Due to the hazards associated with chemical etching, which often requires the use of acids above their boiling point, it was decided to etch one sample of 3YSZ with a plasma and to carry out an annealing cycle on the other sample, following the procedures outlined in Chapter 2, Section 2.2.2. An SEM image of 3YSZ after plasma etching is shown in Figure 3.11b. It is observed that the image is very similar to that captured on the unetched sample, as the microstructural features were not enhanced by the plasma etching process. On the other hand, thermal etching was very effective in revealing the microstructure of the material, as it can be seen in Figure 3.12. The 3YSZ specimen now presents grains with an average size of around 50 nm, which seem to have grown with an equiaxed structure.

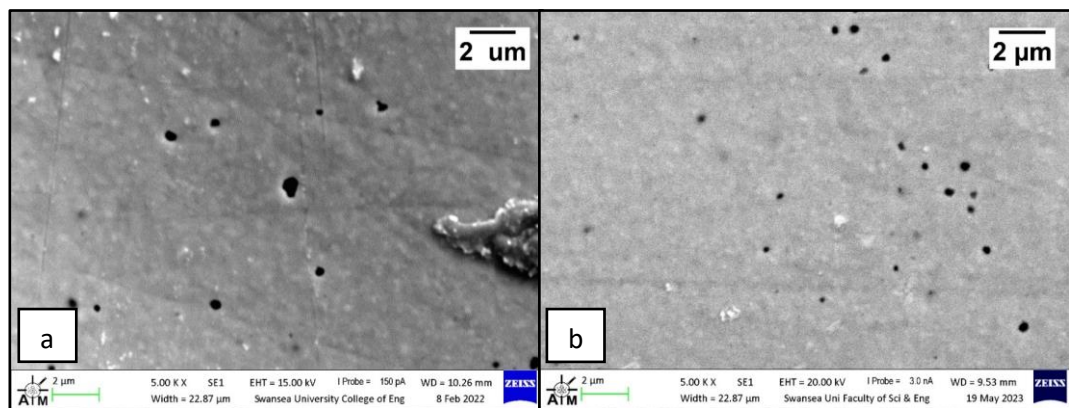


Figure 3.11 SEM image of as received 3YSZ (a); SEM image of 3YSZ after plasma etching (b).

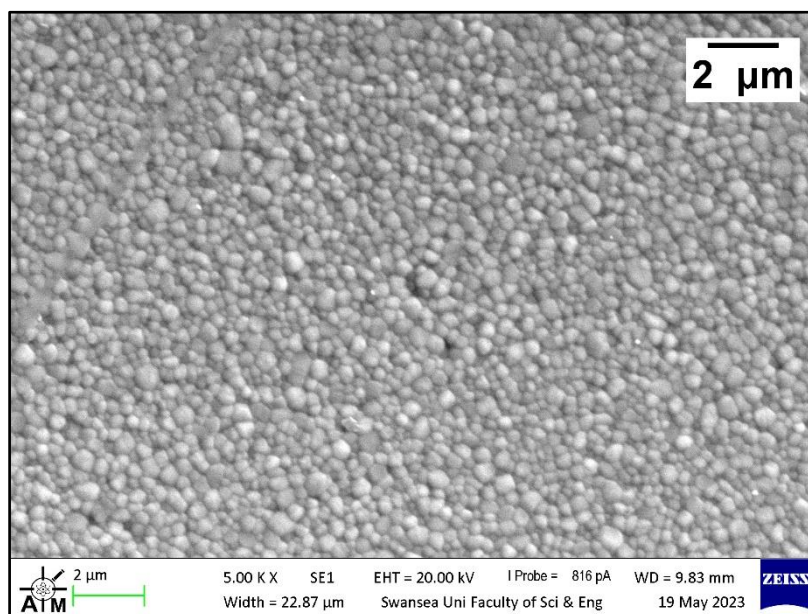


Figure 3.12 SEM image of the microstructure of as-received 3YSZ after thermal etching.

Figure 3.13a shows an image of the as-received Si_3N_4 specimen obtained on the scanning electron microscope. Like 3YSZ, the Si_3N_4 ceramic was etched to enhance the microstructural features. Figure 3.13b and Figure 14a respectively show the microstructure of Si_3N_4 after annealing and after plasma etching. It was observed that the effect of thermal etching was quite dramatic in Si_3N_4 , as Figure 3.13b shows that the features and the phases present in the material have changed. These changes could be the result of dissolution or precipitation of phases, which is sometimes observed in thermally etched ceramics and it leads to over etching of the microstructure (Chinn & Chinn, 2002). On the other hand, Figure 3.14a illustrates that plasma etching did not alter the microstructural features, which appeared more defined and the Si_3N_4 grains remained intact after the etching process.

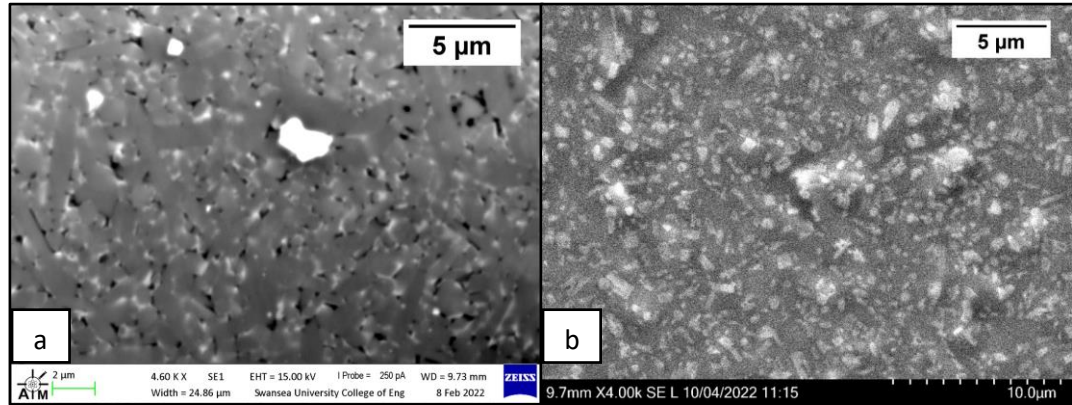


Figure 3.13 SEM image of as received Si_3N_4 (a); SEM image of Si_3N_4 after thermal etching (b).

It was observed that the microstructure was characterised by two types of grains with different morphology. The SEM image of plasma etched Si_3N_4 shows the presence of large rodlike grains (1) as well as smaller equiaxed grains with hexagonal morphology. EDS was performed to reveal the composition of Si_3N_4 in these areas (Figure 3.14b). The large, elongated grains (1) mainly contained Si (65.2 ± 0.2 wt.%), N (29.4 ± 0.5 wt.%), O (2.3 ± 0.3 wt.%), Y (1.6 ± 0.2 wt.%) and Al (1.5 ± 0.1 wt.%). The smaller grains contained Si (66.2 ± 1.7 wt.%), N (27.0 ± 1.4 wt.%), O (3.3 ± 0.3 wt.%), Y (1.8 ± 0.2 wt.%) and Al (1.6 ± 0.1 wt.%) and, therefore, no significant difference in composition was detected between location (1) and location (2).

It is reported that Si_3N_4 exists as two major crystalline phases with hexagonal structure, known as α - Si_3N_4 and β - Si_3N_4 . The α grains typically have an equiaxed structure; however, due to its chemical instability, this phase always transforms into the β phase at around 1600°C , forming the interlocking microstructure with elongated grains (Messier et al., 1978; Zhu & Sakka, 2008). The grains shown in Figure 3.14b are β - Si_3N_4 grains, where the large rodlike grains have grown more than the small equiaxed grains. Therefore, the α - β transformation resulted in a microstructure characterised by large, elongated grains embedded in a small grained matrix. The average length of the large elongated grains in Figure 3.14a was measured to be $4.2\ \mu\text{m}$ with an aspect ratio of approximately 4:1, whereas the smaller β - Si_3N_4 grains measured approximately $1.2\ \mu\text{m}$.

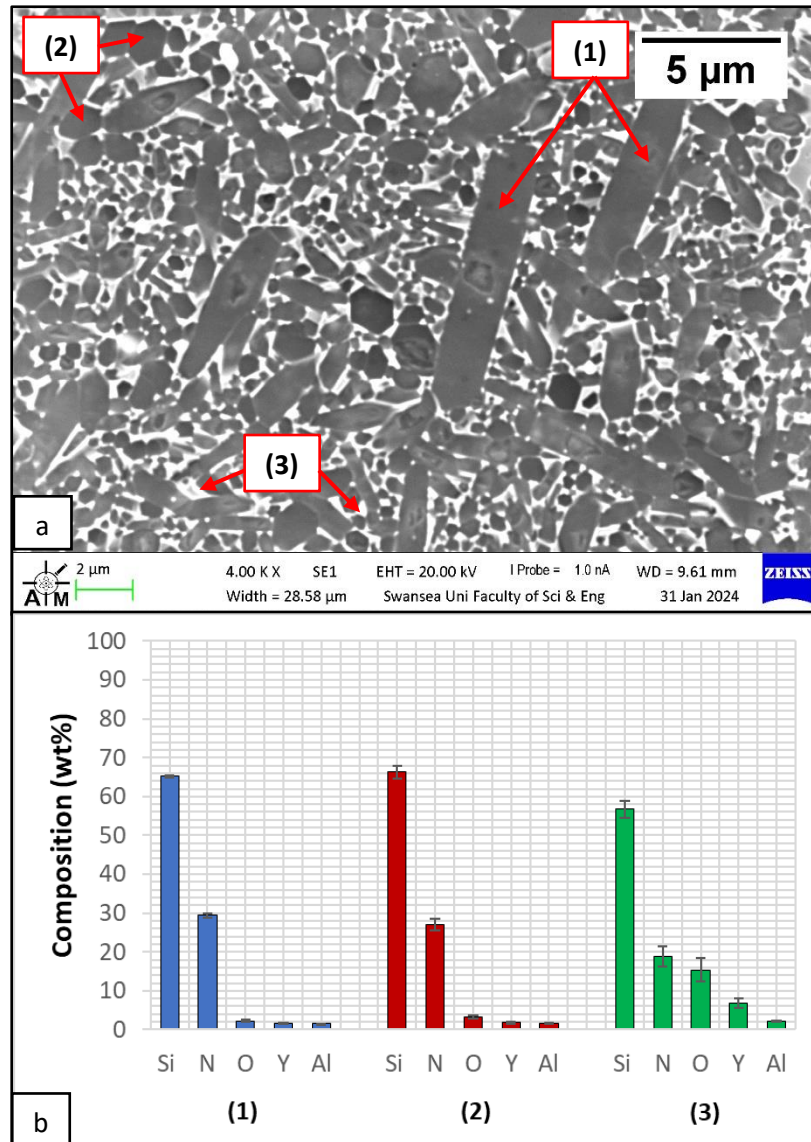


Figure 3.14 SEM image of Si_3N_4 after plasma etching (a); Average element composition of plasma etched Si_3N_4 (b).

In addition to this, it was noticed the presence of a secondary phase in the material, as the Si_3N_4 grains (darker contrast) are separated by an intergranular phase (lighter contrast), which is a glassy grain-boundary phase. The glassy phase plays an important role to fully sinter the ceramic and achieve high densification. For this reason, sintering additives, such as Al_2O_3 and Y_2O_3 are added during the sintering process, which react with the SiO_2 on the surface. This process leads to the formation of a glassy phase at the Si_3N_4 grain boundaries. EDS analysis (Figure 3.14b) was performed in these regions (3) and it was observed that the grain boundary phase contained Si

(56.7 ± 2.1 wt.%), N (18.8 ± 2.6 wt.%), O (15.4 ± 3.1 wt.%), Y (6.8 ± 1.2 wt.%) and Al (2.3 ± 0.2 wt.%). The average element composition showed that the O, Y and Al content is higher in the grain boundary phase compared to the Si_3N_4 grains.

Etching was performed on the as-received Al_2O_3 specimen as well. SEM images of the microstructure of as-received Al_2O_3 and the microstructure of Al_2O_3 after plasma etching are shown in Figure 3.15a and Figure 3.15b respectively. It was observed that plasma etching did not produce any significant enhancement of the microstructural features. On the other hand, the microstructure of Al_2O_3 was enhanced after thermal etching, as shown in Figure 3.16. The SEM image of the annealed specimen shows that the material is characterised by grains that appear to have grown discontinuously as their size ranges from an average of approximately 90 nm for the smaller grains, to an average of approximately 3 μm for the larger grains.

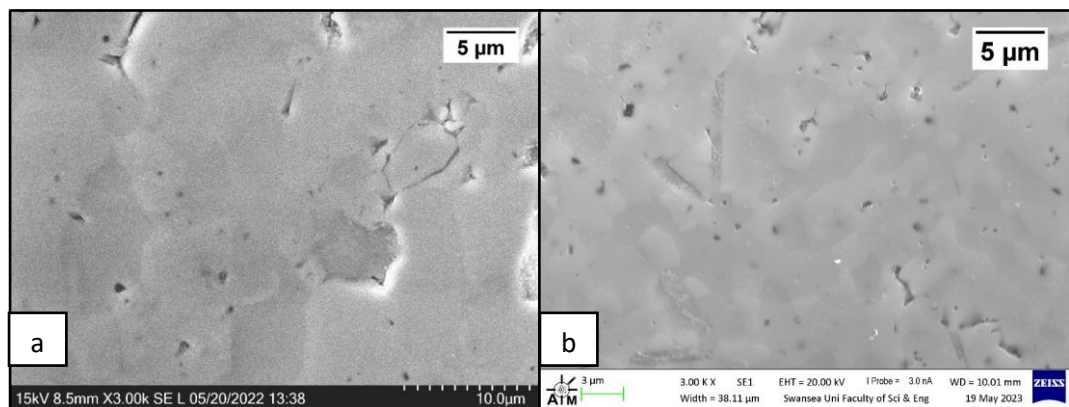


Figure 3.15 SEM image of as received Al_2O_3 (a); SEM image of plasma etched Al_2O_3 (b).

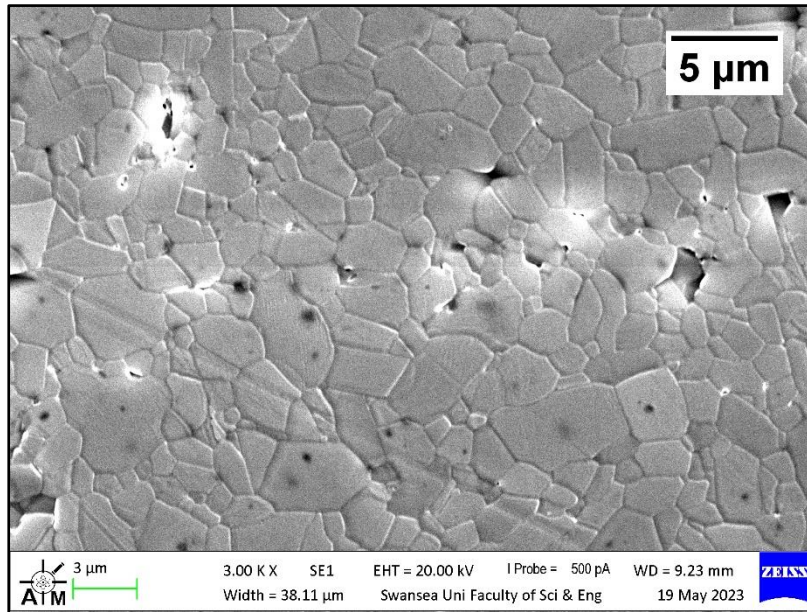


Figure 3.16 SEM image of the microstructure of as-received Al_2O_3 after thermal etching.

3.3 Static Immersion Testing

3.3.1 Problems with Preliminary Experiments

Static immersion tests were performed according to the experimental procedure outlined in Chapter 2, Section 2.4.1. The first test did not involve the removal of the residual Zn from the specimens after extraction from the molten metal bath. Therefore, the pickling step discussed in Chapter 2 was not performed prior to characterisation with SEM and EDS. While handling the ceramic specimens, it was noticed that the Zn started to peel off easily (Figure 3.17), suggesting that the ceramics specimens were not wetted by molten metal. On the other hand, the residual Zn remained firmly attached to the surface of the benchmark materials, such as the SS 316L specimens.

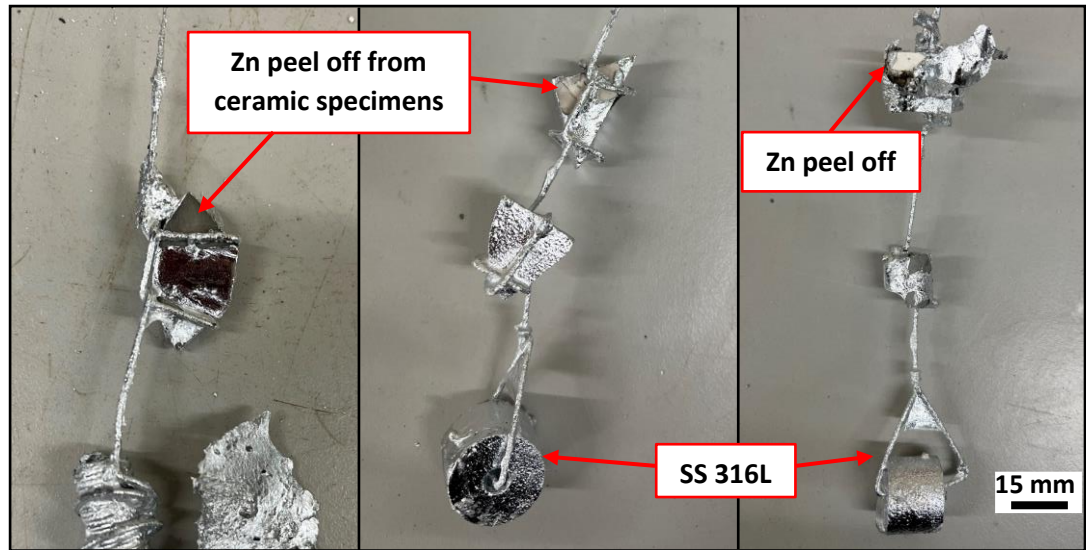


Figure 3.17 Inspection of the specimens after extraction from the Zn alloy bath.

The specimens covered in Zn were prepared for characterisation, as described in Chapter 2, Section 2.2.1. All the specimens were analysed with SEM after immersion in Zn-Al and Zn-Al-Mg and several anomalies were identified on the ceramic samples from the analysis of the cross-sections after static immersion testing. Figure 3.18a shows an image of the cross-section of Al_2O_3 after immersion in Zn-Al-Mg for five weeks. The results of EDS analysis conducted on this specimen are shown in Figure 3.18b. The image confirmed that residual Zn alloy solidified on the samples after extraction from the molten metal baths. In addition to this, the SEM image revealed the presence of an intermediate layer located at the ceramic-Zn alloy interface, which is characterised by both vertical and horizontal cracks. This layer was approximately $23\text{ }\mu\text{m}$ thick and EDS phase elemental analysis revealed that it mainly contained O ($49.7 \pm 5.0\text{ wt.}\%$), Si ($45.8 \pm 4.8\text{ wt.}\%$), Zn ($2.8 \pm 2.0\text{ wt.}\%$) and Mg ($1.4 \pm 0.2\text{ wt.}\%$). The presence of Si in the examined sample is peculiar; samples of the Zn bath were sent to Element Materials Technology (London, UK) for ICP-MS to analyse and no Si was detected. Moreover, EDS confirmed that Si was absent in the Al_2O_3 specimen (3), as shown in Figure 3.18b. Therefore, it is unlikely that this phase is a product of a reaction between the ceramic and the molten metal bath.

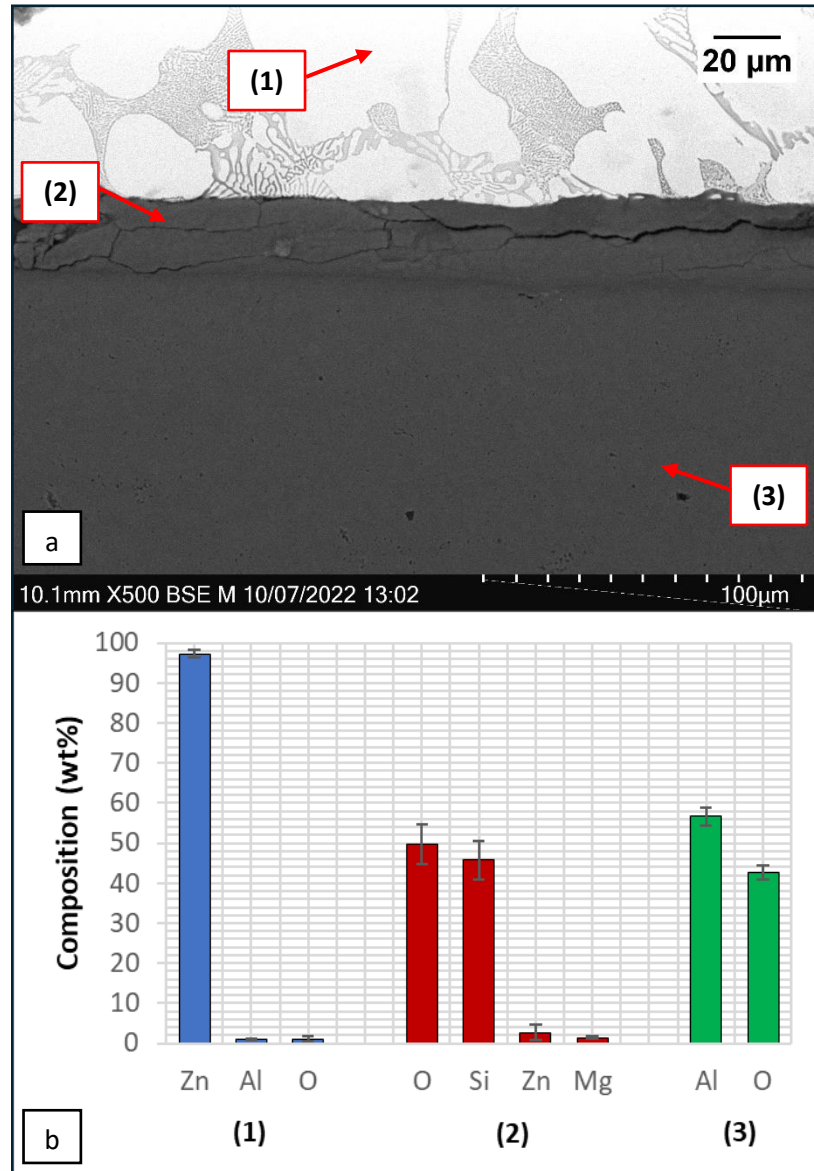


Figure 3.18 Cross-section of Al_2O_3 after immersion in Zn-Al-Mg for 5 weeks (a); EDS analysis of the phases observed in the specimen (b).

The presence of a Si-rich layer was observed in the other ceramic specimens tested in this experiment, including the materials, which did not contain Si in the microstructure; on the other hand, it was not observed in the benchmark materials, such as SS 316L. The SEM image of SS 316L after immersion in Zn-Al showed that some phases were present at the steel-Zn interface (Figure 3.19); however, these layers did not contain Si, unlike the phases present in the ceramic specimens. It will be later discussed that the new phases observed in SS 316L were reaction products

and the analysis of the composition of these corrosion layers is found in Section 3.3.2. The difference between steel and the ceramic materials is that the solidified Zn remained firmly attached on the steel surface, whereas the Zn easily peeled off from the ceramic specimens, as previously discussed. When the ceramic specimens were prepared for material characterisation, the detached Zn formed a gap with the ceramic surface. In addition to this, polishing of the specimens required the use of pastes containing Si, as shown in Chapter 2, Section 2.2.1 and this is considered to be the potential reason for the detection of Si-rich regions in the tested ceramic samples. These regions were initially confused with reaction layers and its presence could hinder the identification of corrosion products in the ceramics after immersion in molten metal. For this reason, it was decided to repeat the experiments in both Zn-Al and Zn-Al-Mg and to remove the residual Zn from the tested specimens, following the procedure outlined in Chapter 2, Section 2.4.1.

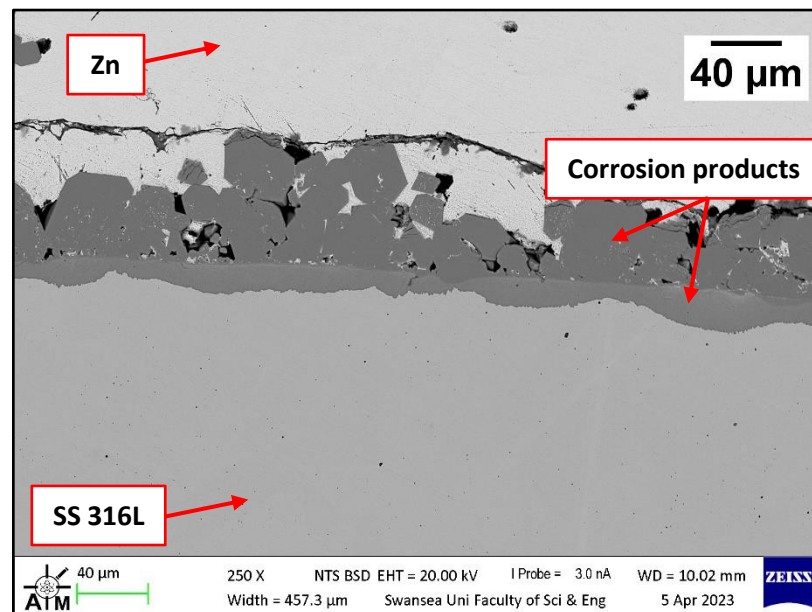


Figure 3.19 SS 316L after immersion in Zn-Al for 5 weeks, with solidified Zn on the surface.

3.3.2 Characterisation of the Benchmarks After Testing

3.3.2.1 SS 316L

SEM images and EDS analysis of SS 316L after immersion in Zn-Al and Zn-Al-Mg baths are shown in Figure 3.20 and Figure 3.21 respectively.

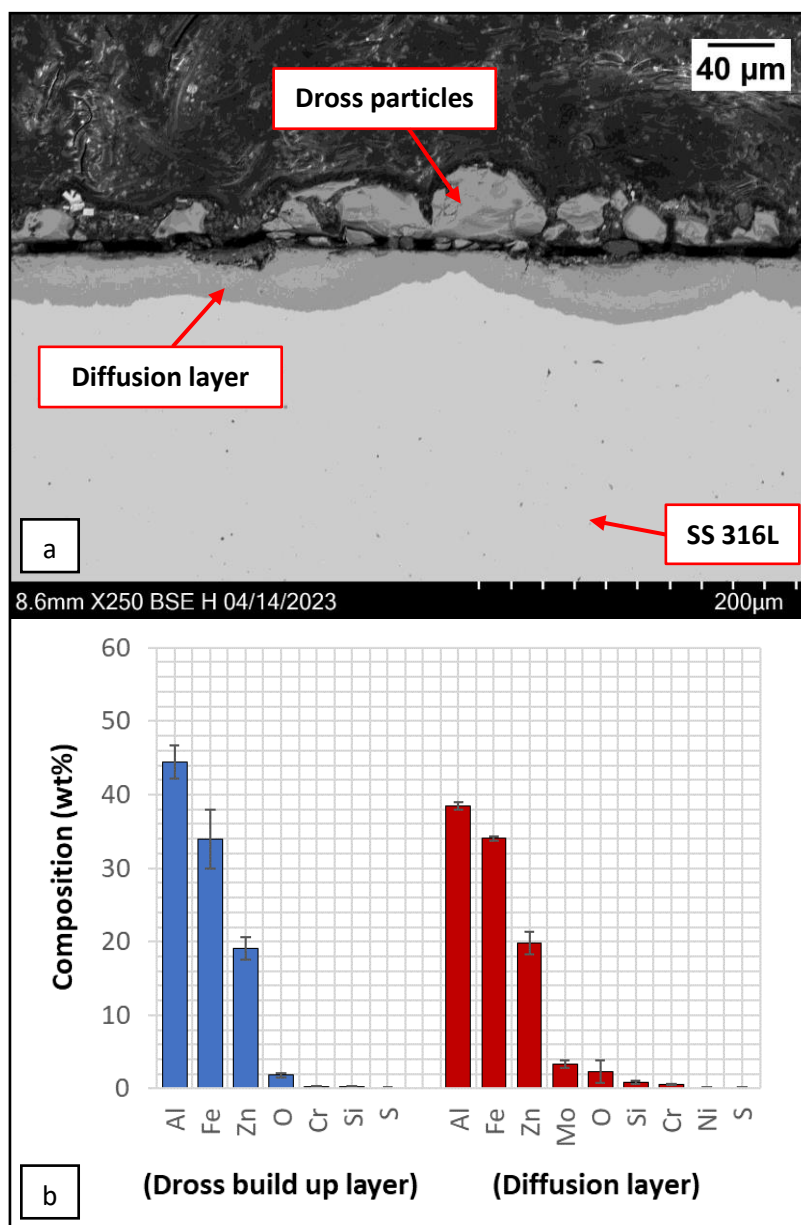


Figure 3.20 Cross-section of SS 316L after 5 weeks of immersion in Zn-Al (a); EDS phase elemental analysis of the reaction products observed in SS 316L after immersion in Zn-Al (b).

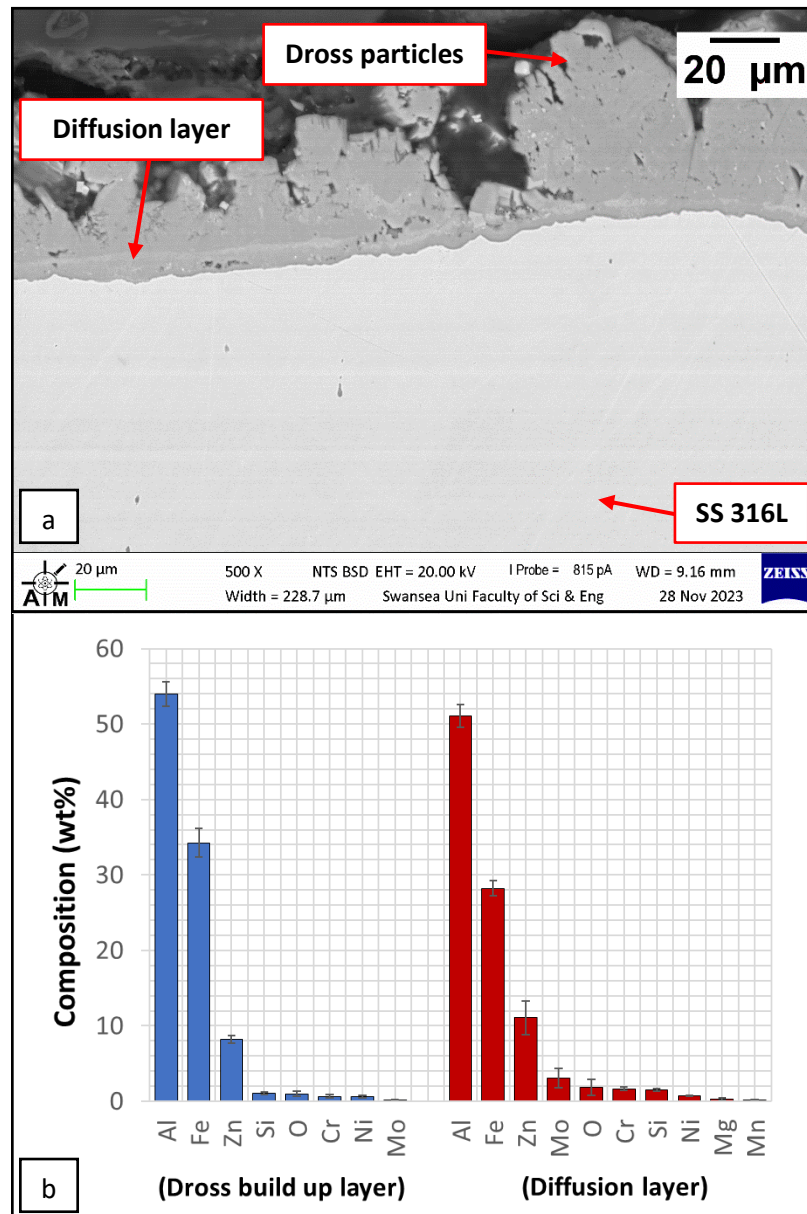


Figure 3.21 Cross-section of SS 316L after 5 weeks of immersion in Zn-Al-Mg (a); EDS analysis of the reaction products observed in SS 316L after immersion in Zn-Al-Mg (b).

It was observed that pickling the tested samples with HCl before grinding/polishing did not remove the corrosion products which were identified on the SS 316L specimens after exposure to liquid Zn alloy. Figure 3.20 showed that the SS 316L specimen was attacked by liquid Zn-Al. The corrosion of SS 316L occurring in baths containing Zn and Al was reported in other studies (Khaliq et al., 2022; Liu et al., 2005; Yu et al., 2020; Yu et al., 2021; Zhang et al., 2007). A diffusion layer developed beneath the steel surface whose thickness was measured to be around 30 μm , determined

from an average of ten measurements taken on the analysed area. However, the thickness of the diffusion layer was nonuniform and it was observed that the layer grew with an undulating pattern. EDS phase elemental analysis was performed at different locations in this layer and the average composition is given in Figure 3.20b.

EDS revealed that the subsurface reaction layer mainly contained Al (38.4 ± 0.5 wt.%), Fe (34.0 ± 0.3 wt.%), Zn (19.9 ± 1.5 wt.%), and Mo (3.4 ± 0.5 wt.%). The formation of this layer was the result of Al diffusion from the molten metal bath into the SS 316L specimen due to the high affinity of Al for Fe (Matthews & James, 2010). It was reported that when the Al content in the bath was below 0.15 wt.%, the dominant chemical process was the Zn-Fe reaction. If the Al content was above 0.15 wt.%, the Al-Fe reaction became the dominant process, leading to the formation of a diffusion layer at the interface of SS 316L and the Zn alloy (Liu et al., 2005). In addition to this, Figure 3.20a showed the presence of reaction products distributed over the surface of SS 316L. This layer was characterised by a build-up of intermetallic dross particles and was found to predominantly contain Al (44.4 ± 2.3 wt.%), Fe (33.9 ± 4.0 wt.%), and Zn (19.1 ± 1.5 wt.%).

The thickness of the dross build up layer was measured to be approximately 30 μm . The formation of the intermetallic particles was attributed to the dissolution of the steel by Zn. Zn reacted with the Fe from the specimen, forming a layer of intermetallic dross particles. Figure 3.20b suggests that the intermetallic dross particles were chemically the same as the subsurface reaction layer, except for the absence of Mo. Diffusion coefficients of Mo into liquid Zn were calculated in other studies (Kuperus, 2018), which concluded that Mo took more time to diffuse into the melt compared to the other elements present in the steel.

Figure 3.21a shows a cross-section of the uncoated SS 316L after immersion in Zn-Al-Mg for 5 weeks. SS 316L reacted with the Zn-Al-Mg and corrosion products were identified at the interface, as observed in the specimen tested in Zn-Al. A diffusion layer developed beneath the steel surface, again following an undulating pattern. The results of EDS phase elemental analysis of this layer are shown in Figure 3.21b. It was found that the composition of this layer was similar to that of the specimen immersed in Zn-Al, as it mainly contained Al (51.1 ± 1.5 wt.%), Fe (28.2 ± 1.0 wt.%) and Zn (11.1

± 2.2 wt.%). However, it was observed that the diffusion layer in the Zn-Al-Mg bath was significantly thinner ($\sim 6 \mu\text{m}$) than that for the sample immersed in the Zn-Al bath. EDS analysis showed that the diffusion layer in the sample immersed in the Zn-Al contained a higher amount of Zn (20%) compared to the diffusion layer observed in the sample immersed in Zn-Al-Mg ($\sim 8\%$). The Al levels were measured to be approximately 10% higher in the Zn-Al-Mg bath compared to the Zn-Al bath.

A number of studies identified a relationship between the Al content in the liquid Zn bath and the formation of FeZn compounds (Bright, 2007; Liu et al., 2005; Marder, 2000). The Al was found to delay the FeZn reaction by segregating to the surface of the steel and forming an 'inhibition layer'. In addition to this, the time for the FeZn phases to develop increased with increasing level of Al in the bath. Since the Zn-Al-Mg bath used in this study contained ten times more Al than in the Zn-Al bath, it was concluded that the higher Al levels reduced the diffusion of Zn into the SS 316L specimen, leading to the formation of a thinner reaction layer. Therefore, the Zn-Al-Mg bath composition provided greater inhibition of the reaction between the SS 316L and the molten Zn in the bath.

3.3.2.2 Wallex6TM Coated with WC-Co

SEM images of the Wallex6TM specimens coated with HVOF WC-Co after immersion in Zn-Al and Zn-Al-Mg baths are shown in Figure 3.22 and Figure 3.23 respectively. Evidence of deterioration of the WC-Co coatings was observed after testing, as large horizontal cracks are present (Figure 3.22a) and parts of the coating are missing (Figure 3.23a). However, the underlying Wallex6TM alloy was still covered by the WC-Co layer. The EDS analysis of the coating after immersion in Zn (Figure 3.22b and Figure 3.23b) revealed the presence of W, Co and O and the formation of an oxide layer on top of the coating in both specimens (location 1), which is absent in the as-received specimen (Figure 3.2).

The presence of oxygen in WC-Co after exposure to Zn was previously reported by Nag et al. (Nag et al., 2021), who theorised that Co and WC reacted with oxygen dissolved in liquid Zn. It is known that Co and WC form oxides at high temperatures

(Chen et al., 2016; Gulbransen & Andrew, 1951). In addition to this, Co may have dissolved into the melt, leaving the WC particles exposed (Nag et al., 2021). These particles could have also detached from the coating, resulting in the regions missing coating, as shown in Figure 3.23a.

The coating thickness was measured on different areas of the sample. From these measurements, it was found that the WC-Co coating was affected by thickness reduction. For instance, Figure 3.24 illustrates that the thickness was reduced to around 90 μm on the sample exposed to Zn-Al (Figure 3.24a) and to 96 μm on the sample immersed in Zn-Al-Mg (Figure 3.24b). Traces of Zn (Figure 3.22b) and Mg (Figure 3.23b) below 0.2 wt.% were detected in the coating, which may have penetrated through pores and cracks present in this layer. The Wallex6TM alloy remained protected by the coating as no Zn, Al or Mg were found on the Co solid solution phase (location 3) as well as on the CrCoW eutectic phases (location 4). However, further deterioration of the coating could have left the underlying material exposed to the attack of the liquid metal, as it was previously reported that Wallex6TM is not inert in Zn and Al (Faulkner, 2020).

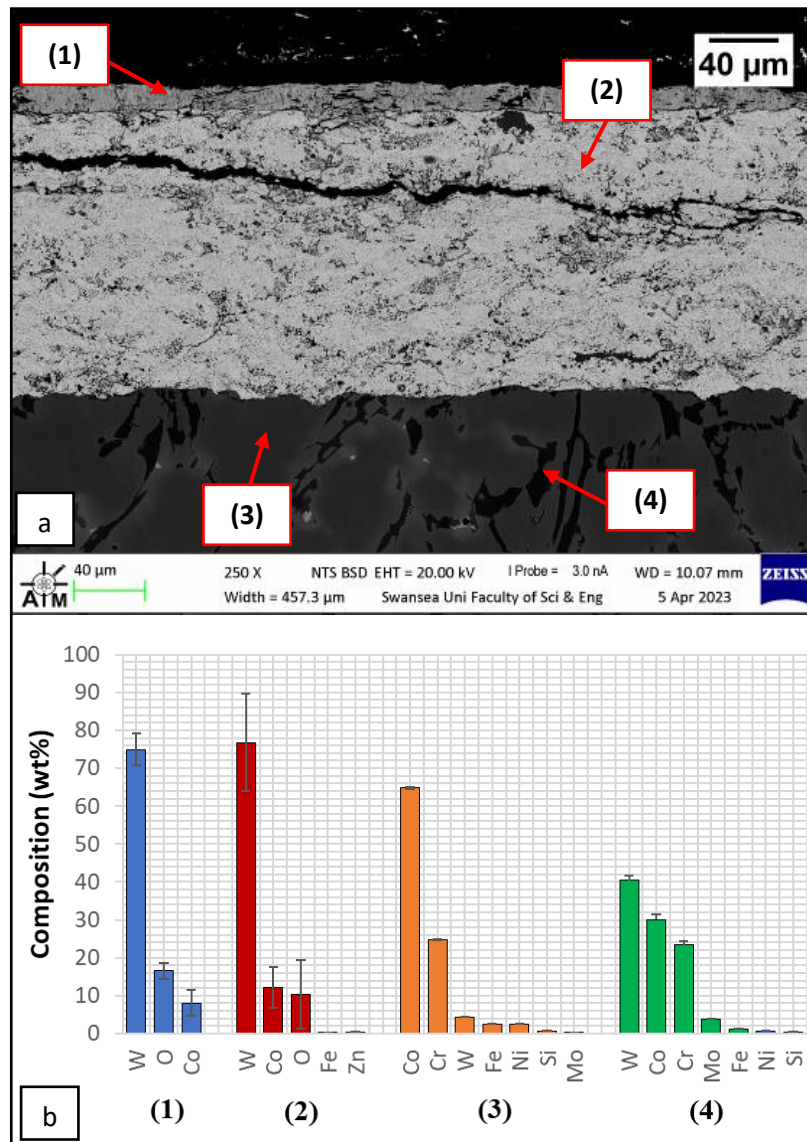


Figure 3.22 SEM image (a) and EDS elemental analysis performed on WC-Co/Wallex6™ after immersion in Zn-Al for five weeks (b).

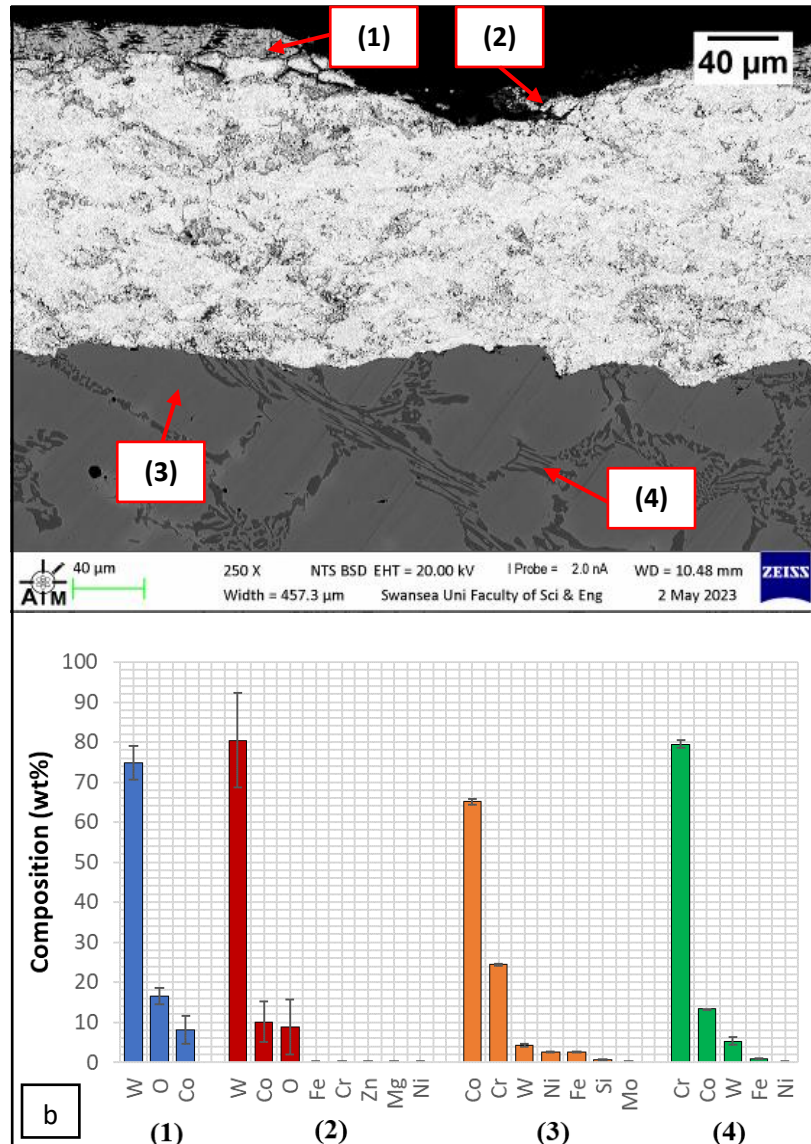


Figure 3.23 SEM image (a) and EDS analysis of WC-Co/Wallex6™ after testing in Zn-Al-Mg (b).

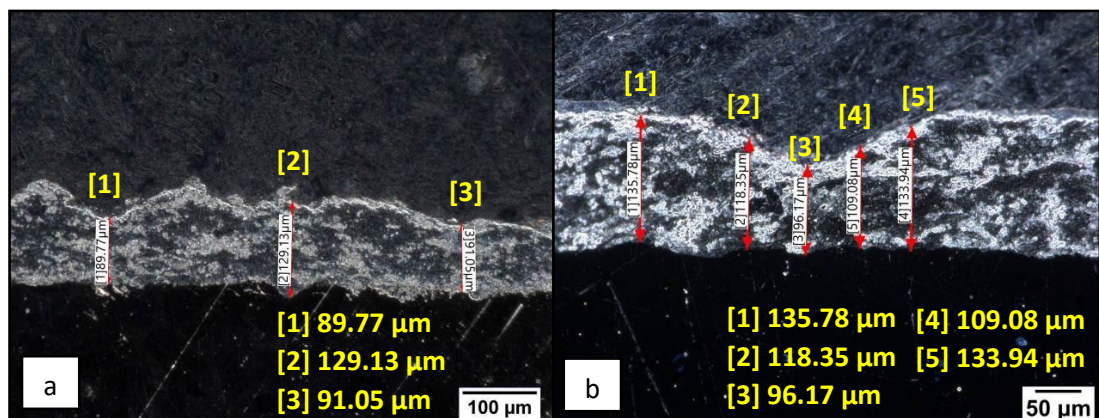


Figure 3.24 Thickness reduction of WC-Co after immersion in Zn-Al (a) and Zn-Al-Mg baths (b).

Note the difference in magnification between the two images.

3.3.3 Characterisation of Ceramics After Testing

SEM images of the ceramic specimens after immersion in Zn-Al and Zn-Al-Mg baths are shown in Figure 3.25 and Figure 3.26 respectively. The specimens were pickled in HCl solution to remove the residual Zn, as illustrated for the benchmark materials. Once again, the cross-sections were analysed in the regions in proximity of the surface of the material, where contact with molten metal occurred. It was observed that the formation of layers containing Si during sample preparation was avoided and the examination of the cross-section revealed that all the ceramics tested in this experiment did not corrode in both Zn alloy baths.

Unlike SS 316L, no dross build up layer or intermetallic particles were observed at the interface, where contact with Zn alloy occurred. In addition to this, no sub-surface diffusion layers were found, suggesting that hBN, BN Grade M26, Macor®, AlN-BN, 3YSZ, Si₃N₄ and Al₂O₃ were resistant to molten metal dissolution-diffusion with Zn, Al and Mg. The absence of corrosion products in the ceramics suggests that the formation of extremely hard intermetallic particles can be prevented and it will be less likely for abrasive debris to form and become entrapped between the bearing and bushing surfaces, as observed by Shi et al. (2018). As a result, ceramic materials could solve the problems related to the use of degraded journal bearings, including strip vibrations around the gas knives section of the line. In addition to this, due to their inertness to molten Zn, Al and Mg reaction, ceramics have potential to enable hydrodynamic operation of submerged pot roll bearings, as the absence of dross formation on the bearing surface could allow the use of tight radial clearances necessary for achieving hydrodynamic lubrication.

Three ceramics, namely hBN, Al₂O₃ and Macor® presented some characteristics which needed further analysis. The SEM images of the hBN samples immersed in Zn-Al (Figure 3.25a) and in Zn-Al-Mg (Figure 3.26a) show the presence of a new phase between the BN grains. EDS mapping was performed to determine the nature of this phase and the results after immersion in Zn-Al and Zn-Al-Mg are shown in Figure 3.27. and Figure 3.28 respectively. The elemental maps illustrated in both figures confirmed that no reaction layers developed in the material. Some Zn was observed in the

samples, which was located between the BN grains near the surface (Figure 3.28) as well as in the bulk of the material (Figure 3.27 and Figure 3.28) as illustrated by the EDS layered image of all the elements. The microstructure of hBN is platelet-like and pores were identified, observing the SEM image of the as-received hBN surface (Figure 3.5). Therefore, it is believed that Zn reached the bulk of the material because of diffusion through these pores. However, the absence of intermetallic phases in the sample confirmed that the material was not attacked by the liquid metal after 5 weeks of immersion.

Regarding the Al_2O_3 specimens, a different microstructure was noticed in regions beneath the surface of the sample as opposed to the rest of the surface. Figure 3.29 shows a comparison between the cross-section of as-received Al_2O_3 (Figure 3.29a), Al_2O_3 after immersion in Zn-Al (Figure 3.29b) and Al_2O_3 after immersion in Zn-Al-Mg (Figure 3.29c). It is possible to observe that these microstructural features were present in the as-received specimen. For this reason, they were not caused by the exposure to the liquid Zn alloy and it is believed that they formed when the sample was sectioned prior to testing. In addition to this, EDS analysis was conducted in these regions and the results for the specimen tested in the Zn-Al bath are shown in Figure 3.30. The analysis showed that Zn did not diffuse into the ceramic, as it is present at very low levels in both specimens. Although the concentration of O was found to be slightly higher at the interface compared to the bulk, there is no indication of a reaction between the ceramic and the molten Zn bath. Figure 3.30 shows that traces of Fe below 4 wt.% were detected in the surface of the sample immersed in Zn-Al (location 2). Fe is not present in the ceramic but it may have dissolved from the SS 316L specimens into the liquid melt, as discussed previously. Moreover, stainless steel wire was used to hold the sample during testing, as previously discussed in Chapter 2, Section 2.4.1 hence why Fe was detected.

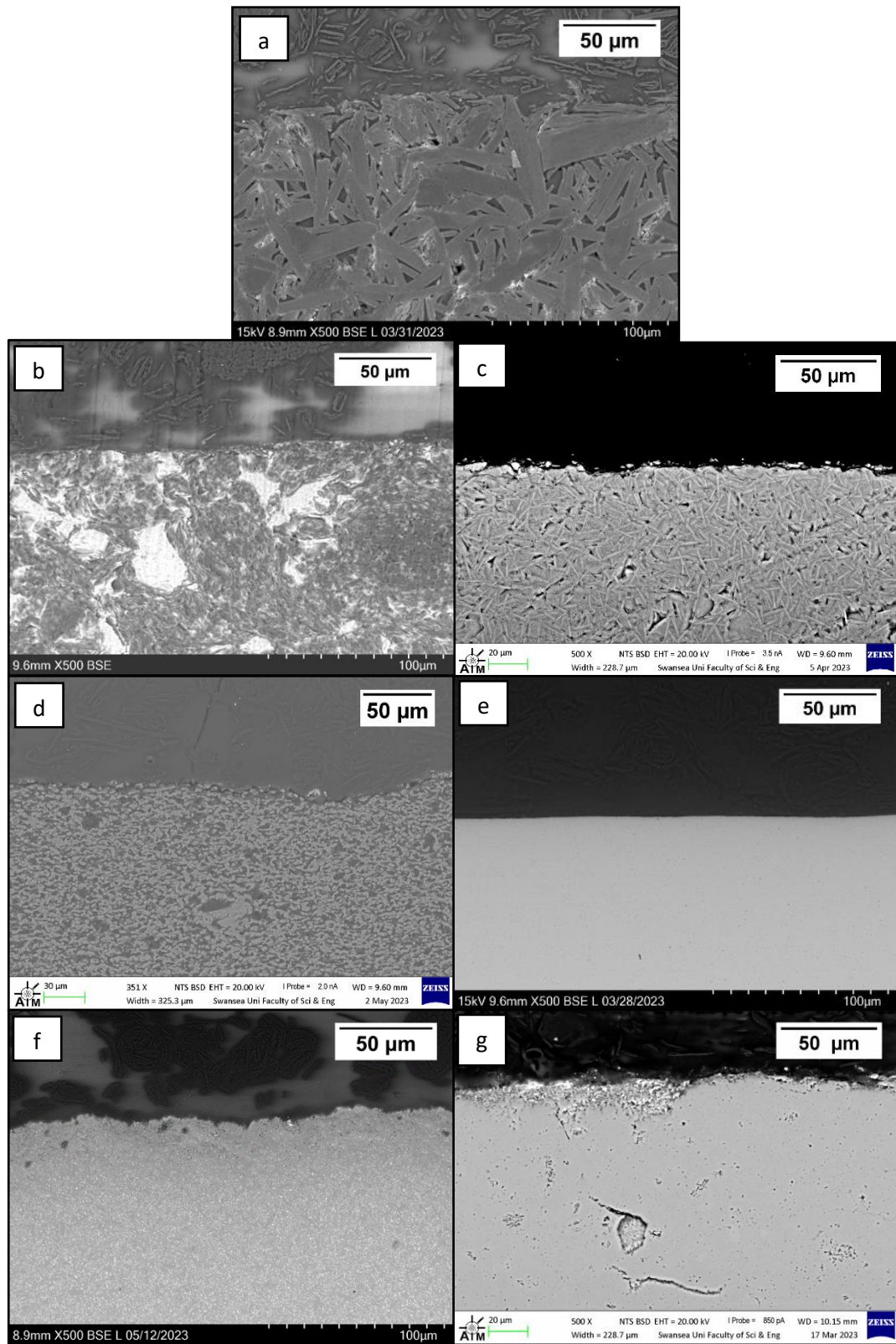


Figure 3.25 SEM cross-sections of the ceramic specimens hBN (a), BN Grade M26 (b), Macor® (c), AlN-BN (d), 3YSZ (e), Si₃N₄ (f) and Al₂O₃ (g) after immersion in Zn-Al.

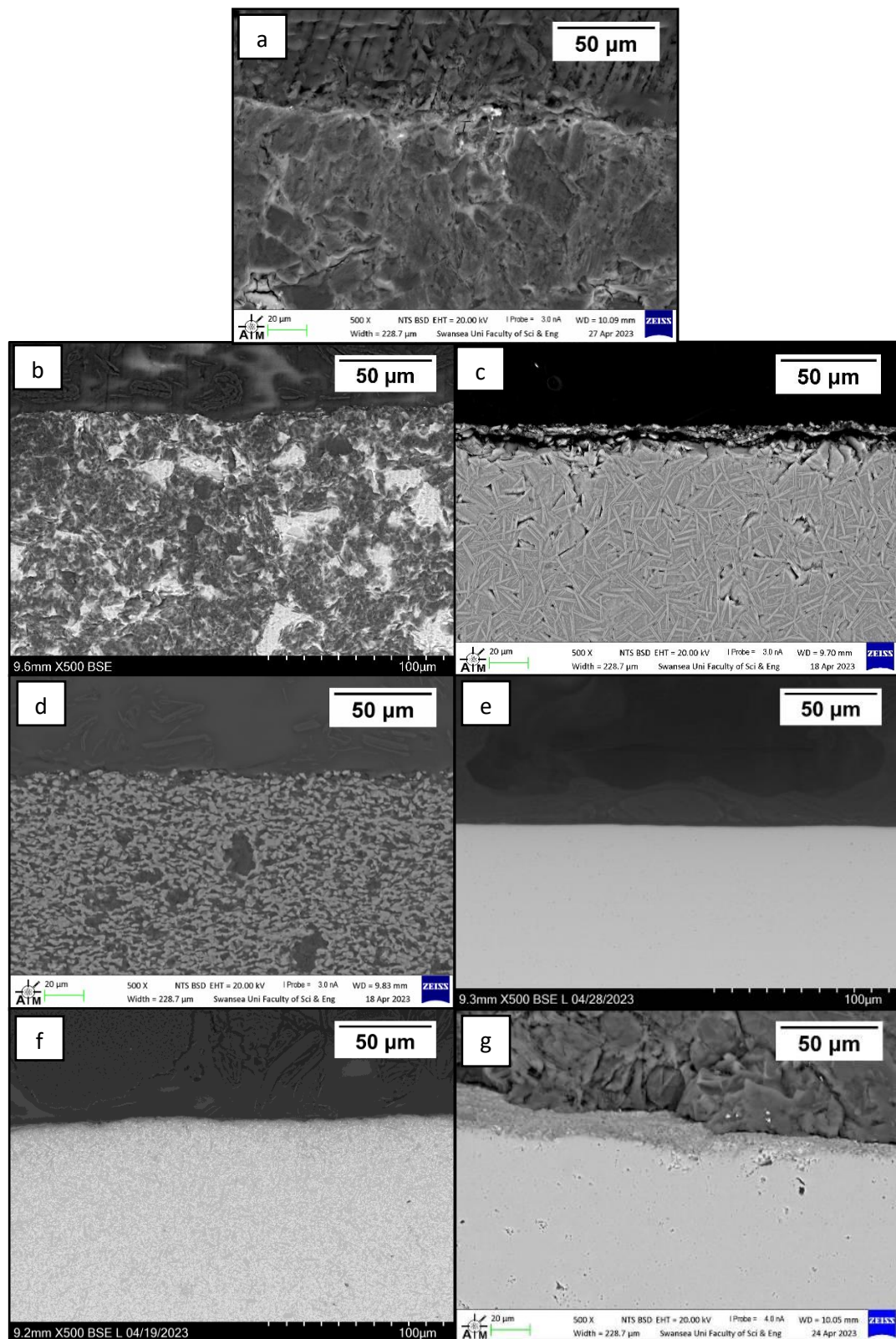


Figure 3.26 SEM cross-sections of the ceramic specimens hBN (a), BN Grade M26 (b), Macor® (c), AlN-BN (d), 3YSZ (e), Si₃N₄ (f) and Al₂O₃ (g) after immersion in Zn-Al-Mg.

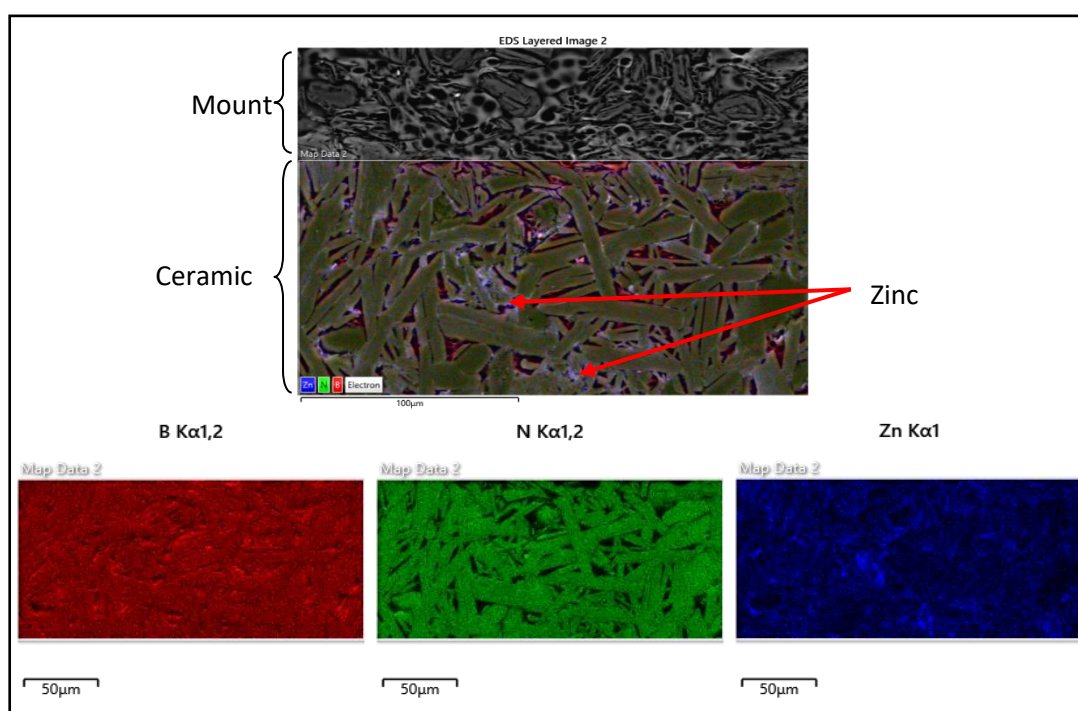


Figure 3.27 EDS maps of pure hBN after testing in Zn-Al.

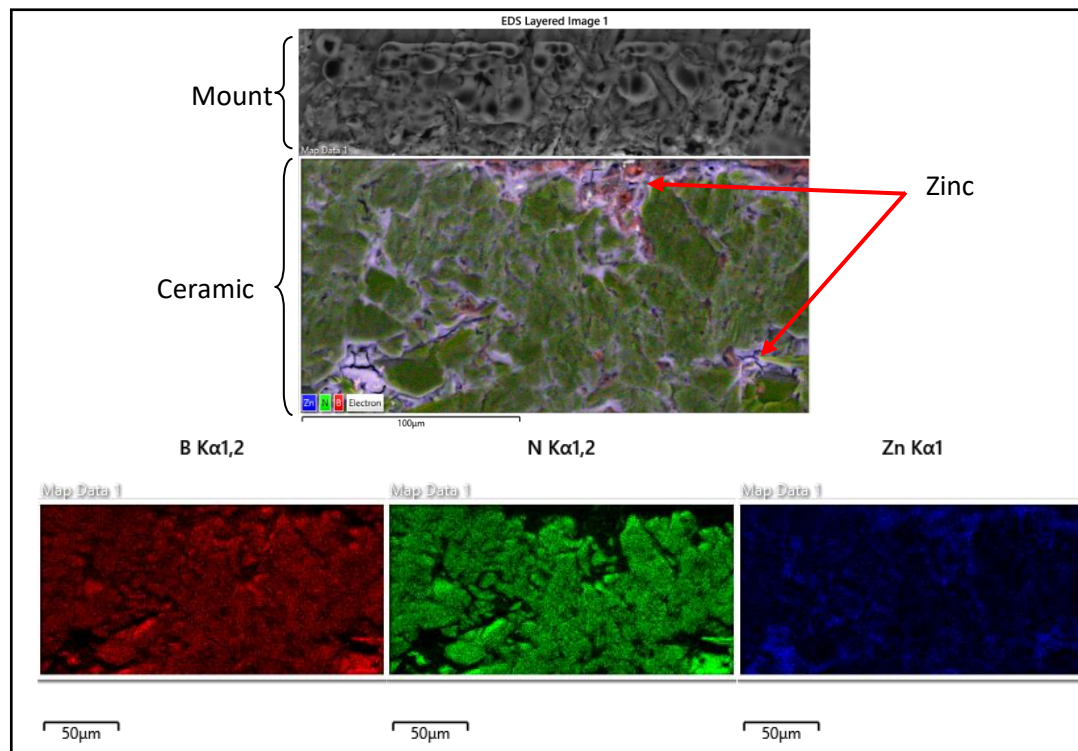


Figure 3.28 EDS maps of pure hBN after testing in Zn-Al-Mg.

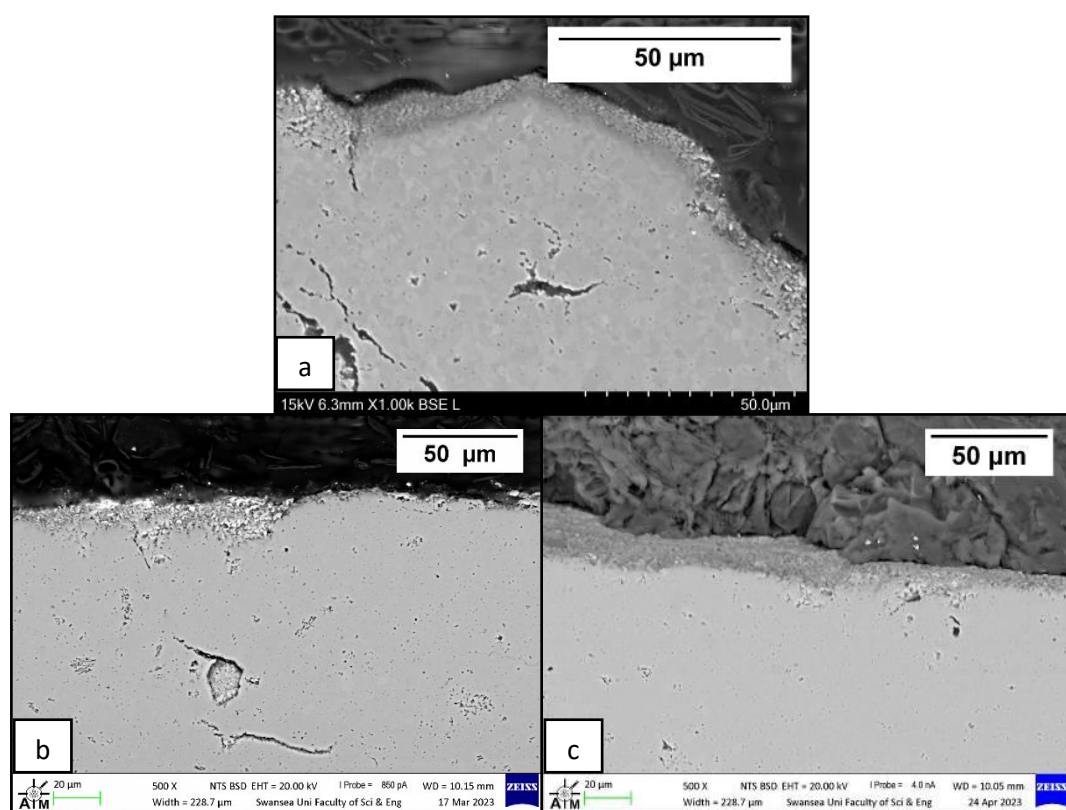


Figure 3.29 Cross-sections of as-received Al_2O_3 (a); Al_2O_3 after exposure to Zn-Al (b); Al_2O_3 after exposure to Zn-Al-Mg (c).

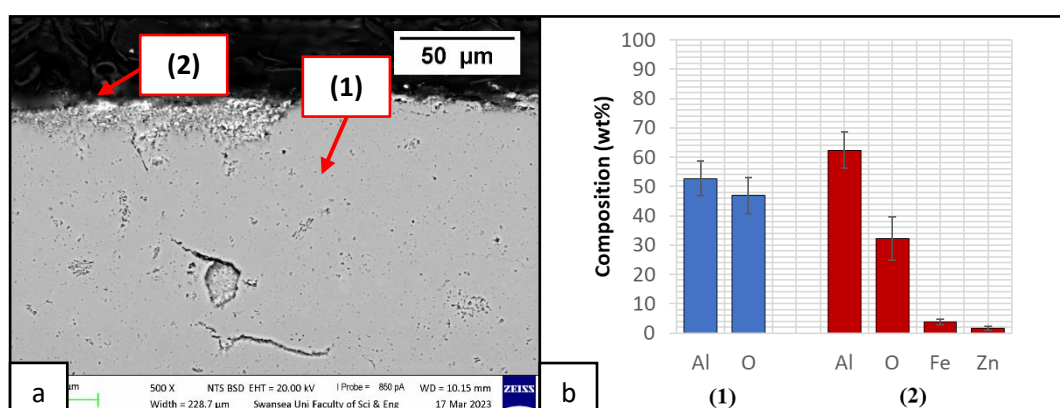


Figure 3.30 SEM images of Al_2O_3 after immersion in Zn-Al for 5 weeks (a); EDS elemental analysis of Al_2O_3 after testing (b).

Like Al_2O_3 , the Macor[®] glass ceramic specimens displayed a different microstructure near the interface compared to the bulk of the material, which is more noticeable for the specimen tested in Zn-Al-Mg (Figure 3.26c). The samples tested in both Zn-Al and

Zn-Al-Mg baths were compared to the cross-section of an as-received Macor[®] specimen to verify whether this phase was the result of exposure to molten metal. Once again, the comparison (Figure 3.31a-c) allowed to exclude the occurrence of a reaction with the Zn alloy baths, as this microstructure was found in the as-received specimen as well.

This observation was confirmed by the result of EDS analysis conducted on the specimen immersed in Zn-Al-Mg (Figure 3.31d), which revealed that the elemental composition measured on the surface of the material is similar to that measured on the bulk. The analysis suggested that no diffusion of the elements present in the molten metal bath occurred as the Al and Mg levels do not vary from those detected in the bulk of the material and only low levels of Zn were present, which were found to be approximately 0.6 wt.%. Therefore, it was concluded that the Zn detected in the analysis refers to traces of Zn solidified on the sample after removal from the molten metal bath which were not eliminated completely during pickling.

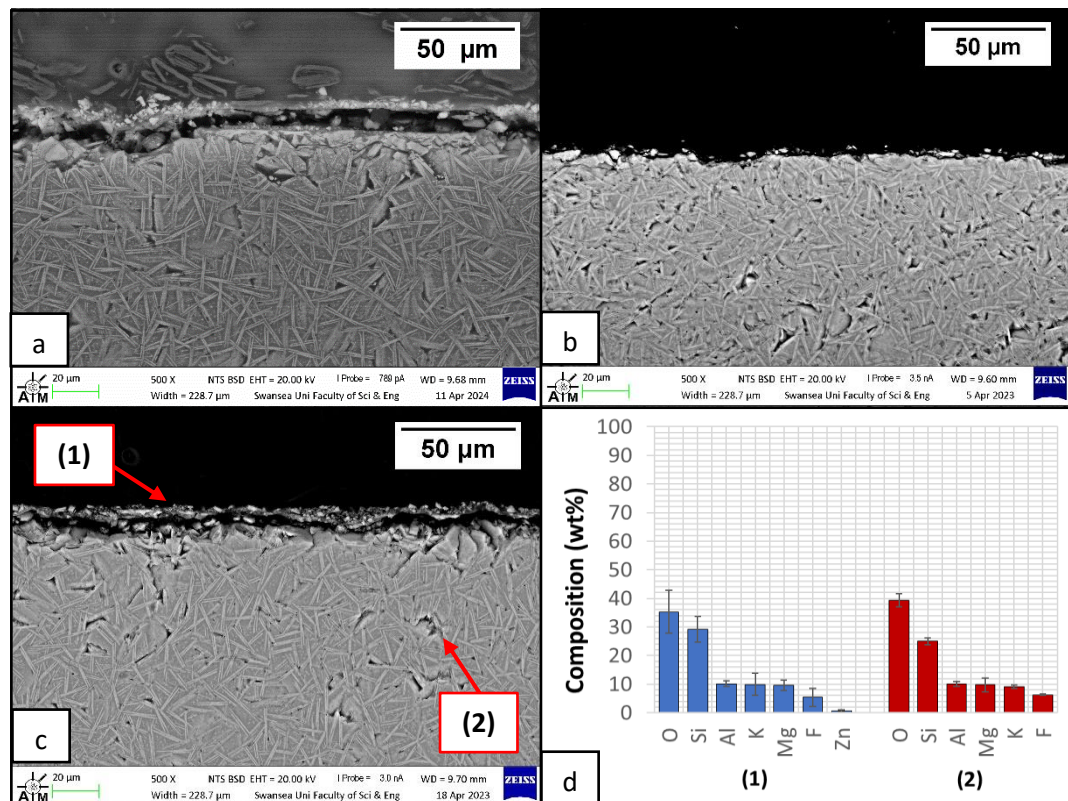


Figure 3.31 As-received Macor[®] (a); Macor[®] after immersion in Zn-Al (b); Macor[®] after immersion in Zn-Al-Mg (c); EDS elemental analysis of Macor[®] after testing in Zn-Al-Mg (d).

3.4 Pin-on-Disc Wear Testing

3.4.1 Introduction

The process of selecting a material suitable for reducing the wear damage of the galvanising pot roll bearings should not be limited to the examination of the corrosion resistance of prospective bearing materials, as optimal tribological properties, such as excellent resistance to wear, are required for reducing the levels of wear damage in service. The wear resistance of metals has been extensively discussed in the literature; for instance, experiments were performed to determine the influence of certain heat treatments on the wear behaviour of steel (Kara et al., 2023; Özbek & Özbek, 2022; Toboła, 2019). However, there is a lack of comparative studies on technical ceramics (Niebuhr, 2007). Therefore, after investigating the corrosion behaviour of prospective bearing materials, it was decided to conduct wear testing to study the tribological properties of ceramics. Tribological properties are typically investigated using tribometers such as the pin-on-disc, four-ball and Timken apparatuses (Carrapichano et al., 2002; Rai et al., 1999; Stachowiak & Batchelor, 2004; Xiao et al., 2014). A limitation of the four-ball and Timken tribometers is that the contact stress can vary during testing. In this study, friction and wear characterisation were performed using a pin-on-disc tribometer, which offers better control of the experimental conditions compared to the other two techniques (Stachowiak & Batchelor, 2004).

3.4.2 Measurements of Friction Coefficient

The coefficient of friction (COF) was measured according to the procedure outlined in Chapter 2, Section 2.3.2, in order to study the effect of changing sliding conditions on the tribological behaviour of the ceramics. The COF was recorded at 50 rpm, 100 rpm and 150 rpm, which correspond to 3.14 m/min, 6.28 m/min and 9.42 m/min sliding speeds, respectively. Friction coefficient curves were obtained and are shown in Figure 3.32. It is possible to notice that the COF varied with time until it reached constant values, which is a behaviour typically associated with a steady state of

tribological conditions (Ba et al., 2021). The values of the COF presented in this study were extrapolated from this region. As the ceramics reached a steady state at different sliding times, averages of the COF were taken between 960 and 1200 s (Table 3.3), when the COF was constant for all the ceramics.

The curves obtained at a 3.14 m/min sliding speed, Figure 3.32a, show that the COF of 3YSZ and AlN-BN increased slowly with time until a maximum value was reached when a steady state occurred. For the pure hBN specimen, the steady-state regime was immediately reached as soon as sliding with the SiC pin occurred. Si₃N₄, Al₂O₃, Macor® and BN M26 showed a different behaviour, as the COF increased more rapidly and the maximum peak was reached at shorter sliding times. This was followed by a sudden drop in the COF values, which subsequently stabilised as steady-state conditions were approached. The COF of Macor® increased again after the first drop to reach a second peak before decreasing to the steady-state values. Similar behaviours were observed when the sliding speed was increased to 6.28 m/min and 9.42 m/min, as illustrated in Figure 3.32b-c, except for those of pure hBN, whose COF reached a maximum peak followed by a rapid decrease.

When sliding was initiated, the increase in the COF values was due to an increased interaction between the asperities of the two materials, as the surface layer of the 'disc' was removed. The COF reached a peak when maximum adhesion was achieved, which occurred when the asperities in the material deformed and the wear rate was increased due to a higher presence of worn particles. If the asperity deformation processes decreased after reaching the maximum peak, the COF dropped until the interfacial steady state of tribological conditions was achieved (Ba et al., 2021). At a 3.14 m/min sliding velocity, the ceramic which displayed the lowest friction with the SiC ball was pure hBN. The COF recorded for this material was 0.06, which is significantly lower compared to the COF values recorded for the other ceramic materials tested in this study.

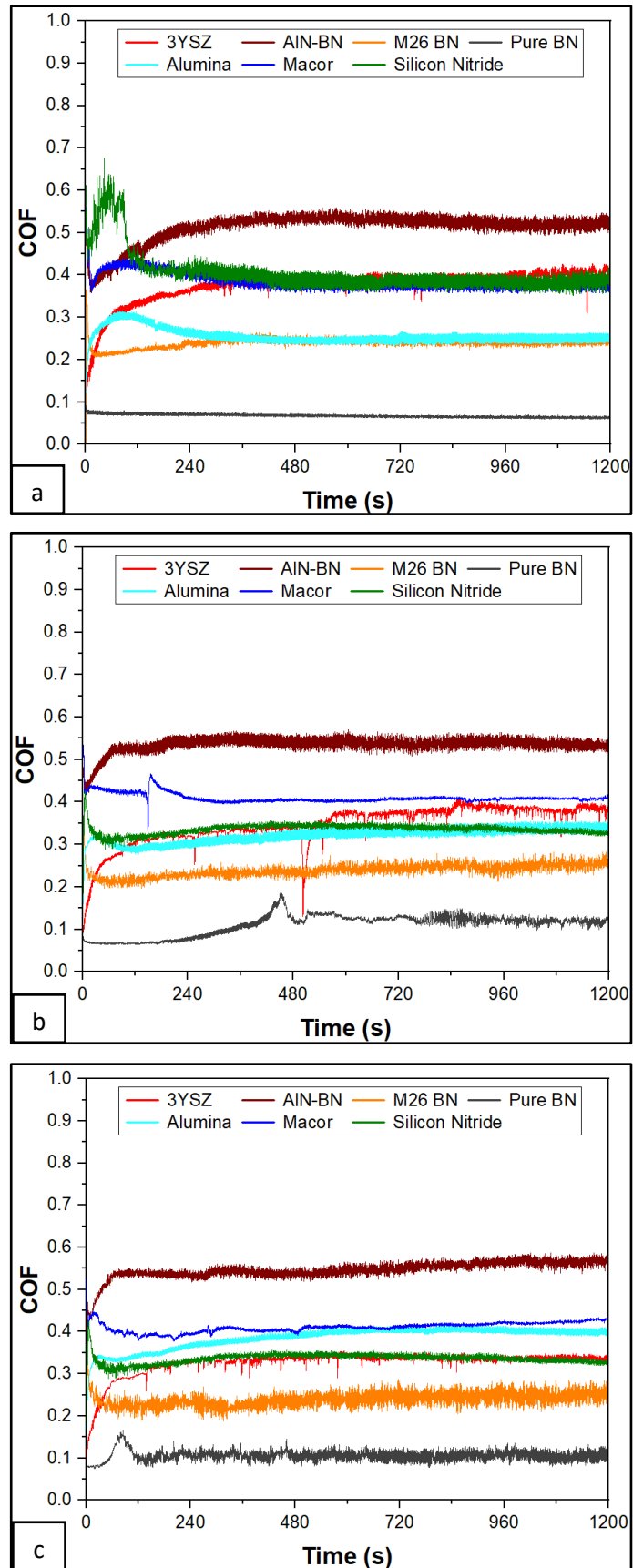


Figure 3.32 COF curves for the tests performed at 3.14 m/min (a), 6.28 m/min (b) and 9.42 m/min (c).

Table 3.3 COF of the ceramics during steady-state regime.

Material	3.14 m/min	6.28 m/min	9.42 m/min
Pure hBN	0.06±0.00	0.12±0.01	0.11±0.01
BN M26	0.24±0.00	0.25±0.01	0.25±0.01
Macor®	0.38±0.01	0.41±0.00	0.42±0.00
AlN-BN	0.52±0.01	0.54±0.01	0.57±0.01
3YSZ	0.40±0.01	0.38±0.01	0.34±0.00
Si ₃ N ₄	0.38±0.01	0.33±0.00	0.35±0.00
Al ₂ O ₃	0.25±0.01	0.34±0.01	0.40±0.01

The hexagonal form of BN is known for its ability to provide lubrication as a result of the sliding of the hBN layers that are held by weak Van der Waals interactions (Carrapichano et al., 2002; Menezes et al., 2013; Yin et al., 2022). Other studies have confirmed that the COF of pure hBN can assume values less than 0.1, which is a distinct feature of lubricious materials (Cao et al., 2011; Zhang, 2016). Moreover, Figure 3.32 shows that the steady-state condition was reached immediately, which may be the result of the formation of a tribolayer between the two contacting surfaces as soon as sliding with the SiC pin was initiated. BN grade M26 also showed a low COF, although it stabilised to a constant value of 0.24 at a 3.14 m/min sliding speed. This value is higher than that recorded for pure hBN due to the presence of SiO₂ in the material, which is believed to increase the friction with the SiC pin.

Among the three ceramics containing BN, the AlN-BN composite is the material with the largest COF, which was recorded to be 0.52 at a 3.14 m/min sliding speed. In addition to this, the COF was higher than those recorded for all the other ceramics, and it is theorised that the large difference in hardness with the SiC counterpart led to higher friction. Although several studies concluded that the tribological properties of materials can be improved by BN additions to their structure (Carrapichano et al., 2002; Chen et al., 2017; Li et al., 2015; Yanar et al., 2022; Yin et al., 2022), in this case, BN did not provide sufficient lubrication to the system in question. This behaviour could be related to the composition of the ceramic, as the formation of a protective tribolayer in a material is reported to be linked to the amount of BN present (Chen et al., 2017). Si₃N₄, Macor® and 3YSZ showed a similar COF at 3.14 m/min and when a

steady state was reached. The COF was measured to be around 0.4 for 3YSZ and 0.38 for Macor[®] and Si₃N₄. Regarding Al₂O₃, although the COF recorded was higher than that of pure hBN, it matched the values obtained for BN-grade M26. Therefore, low friction was observed in the Al₂O₃ ceramic at the lowest sliding speed, and this behaviour was observed without benefitting from the lubrication effect provided by hBN.

As the sliding speed was increased to 6.28 m/min and 9.42 m/min, changes in the COF of the ceramics were observed. Figure 3.33 shows the COF as a function of the sliding velocity for all the materials tested. The COF of pure hBN increased from 0.06 to values slightly higher than 0.1. However, the COF value recorded was still low, considering that the specimen was sliding at a rate three times higher than the first test. The COF of BN M26 showed minimal variations with velocity, and, therefore, the lubrication provided by BN seemed to not be affected by the higher sliding speeds. On the other hand, an increased friction value was observed for AlN-BN, which remained the material with the highest COF among the ceramics tested. The same trend was followed by Macor[®] and Al₂O₃, with Al₂O₃ being the material that most severely suffered from the higher sliding velocities. The COF no longer matched the values recorded for BN M26 and was found to increase to 0.34 and 0.4 at 6.28 m/min and 9.42 m/min, respectively. The opposite trend was observed for Si₃N₄ and 3YSZ, as the COF decreased from the values recorded at the lowest sliding speed. Due to its low thermal conductivity, 3YSZ was expected to suffer the high velocities worse compared to the ceramics with higher thermal conductivity (e.g., Al₂O₃), which can better dissipate the higher heat from the contact caused by the higher speed (Basu et al., 2020; Stachowiak & Batchelor, 2013). However, the results collected in this work show that the COF of 3YSZ decreased from 0.4 at 3.14 m/min to 0.34 at 9.42 m/min, indicating that the friction of 3YSZ with the SiC counterface was reduced at high speeds.

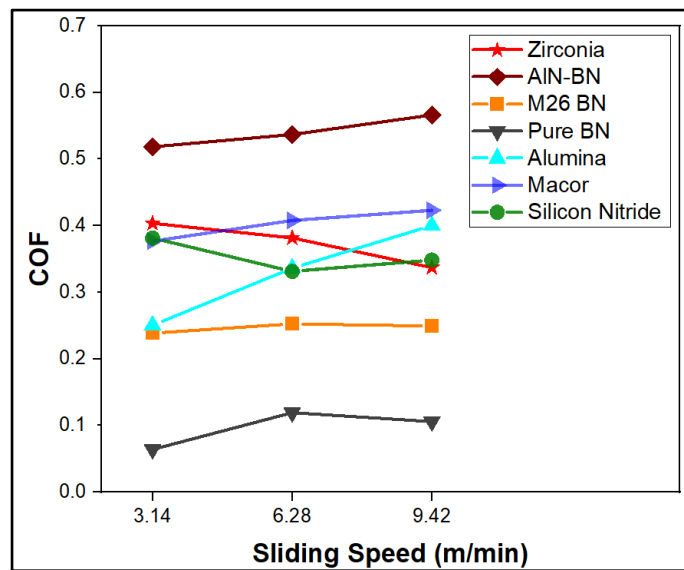


Figure 3.33 Plot of the COF of the ceramics as a function of sliding speed.

3.4.3 Inspection of the Tested Specimens

Debris formation was observed when the specimens were visually inspected during testing. Debris deposited on each side of the wear track, as shown in Figure 3.34. The photographs were taken on a pure hBN specimen during testing and more debris accumulated as the sliding time was increased. Debris formation was observed in hBN, BN M26, AlN-BN and Macor®. No debris was observed on a macroscopic level when 3YSZ, Al₂O₃ and Si₃N₄ were tested.

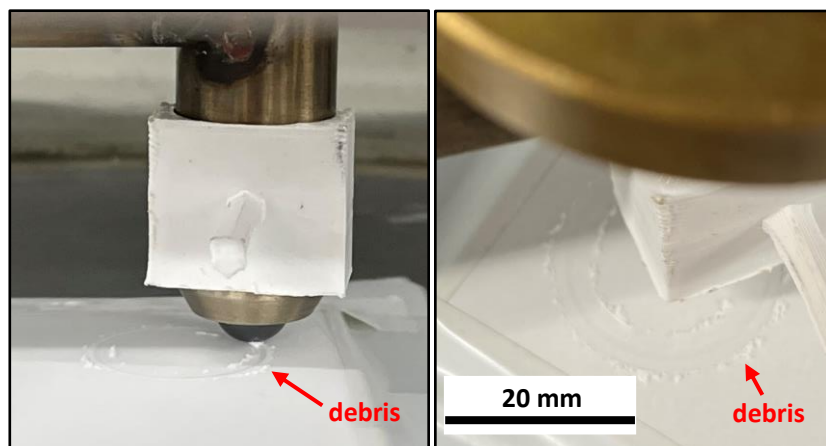


Figure 3.34 Macroscopic examination of the tested specimens.

3.4.4 Wear Scar Analysis

Images of the wear scars left on the ceramics at 3.14 m/min and at 9.42 m/min were compared. Figure 3.35 shows the surfaces of pure hBN and BN grade M26 after testing. On the pure hBN sample, it is possible to notice the appearance of multiple parallel grooves when the sliding velocity was increased to 9.42 m/min (Figure 3.35b). The grooves were the result of the cutting of the softer hBN specimen by the hard asperities present in the SiC pin. Multiple grooves formed due to the presence of multiple asperities in contact at the interface. The cut material was removed as wear debris, which could also be found inside the wear track, and it was mainly present on the sample tested at a high speed. For the BN M26 specimen, grooving started to occur at a 3.14 m/min sliding speed, and a large amount of debris could be found inside the wear track, suggesting that the grooves provided space for particle entrapment (Figure 3.35c-d). The width of the scar on the two BN grades was found to increase when higher velocities were used. The width of the scar on the pure hBN ceramic increased from approximately 885 μm to 1660 μm as the speed was varied from 3.14 m/min to 9.42 m/min. Regarding BN M26, the width increased from approximately 1010 μm to 1940 μm , suggesting that the BN grades suffered from severe wear, particularly at a high speed.

Figure 3.36a-b and Figure 3.36c-d respectively show the surface of Macor® and the AlN-BN composite. Both of the two materials showed evidence of ploughing, as deep grooves were observed at 3.14 m/min and at 9.42 m/min sliding speeds. Large amounts of debris were found on the examined surface, which deposited on the sides as well as on the inside of the wear scar. Furthermore, debris entrapment was more pronounced on the specimens tested at a high sliding speed. On the AlN-BN ceramic, the width of the scar increased slightly from around 662 μm at 3.14 m/min to 876 μm at 9.42 m/min. A similar behaviour was observed on the Macor® specimen, as the width increased from around 530 μm to 671 μm when the sliding speed was increased to 9.42 m/min.

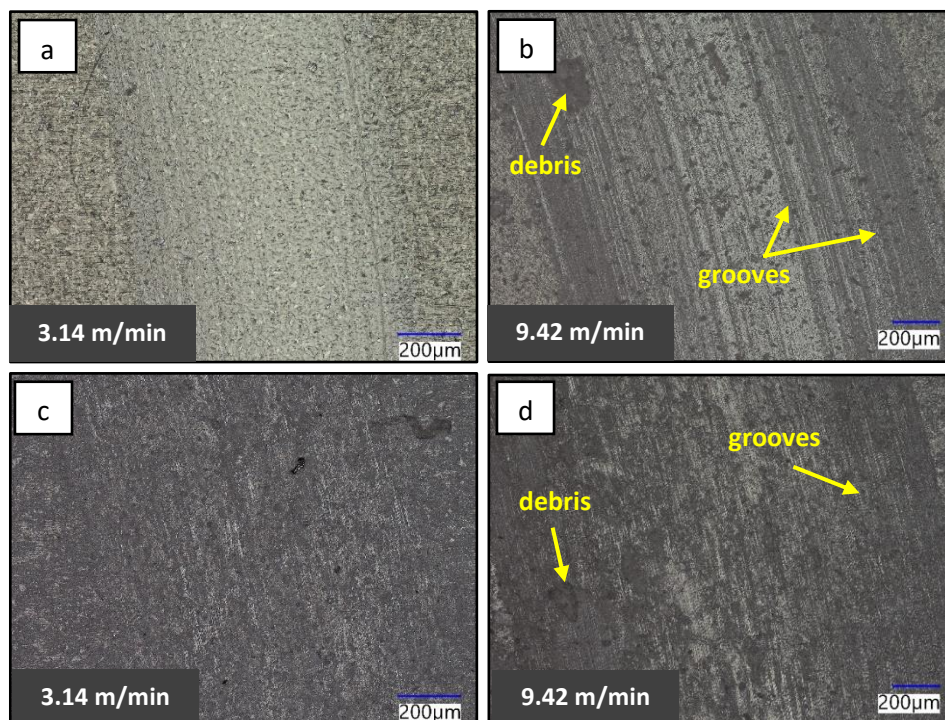


Figure 3.35 Optical images of the wear scars of pure hBN at 3.14 m/min (a), pure hBN at 9.42 m/min (b), BN M26 at 3.14 m/min (c) and BN M26 at 9.42 m/min (d).

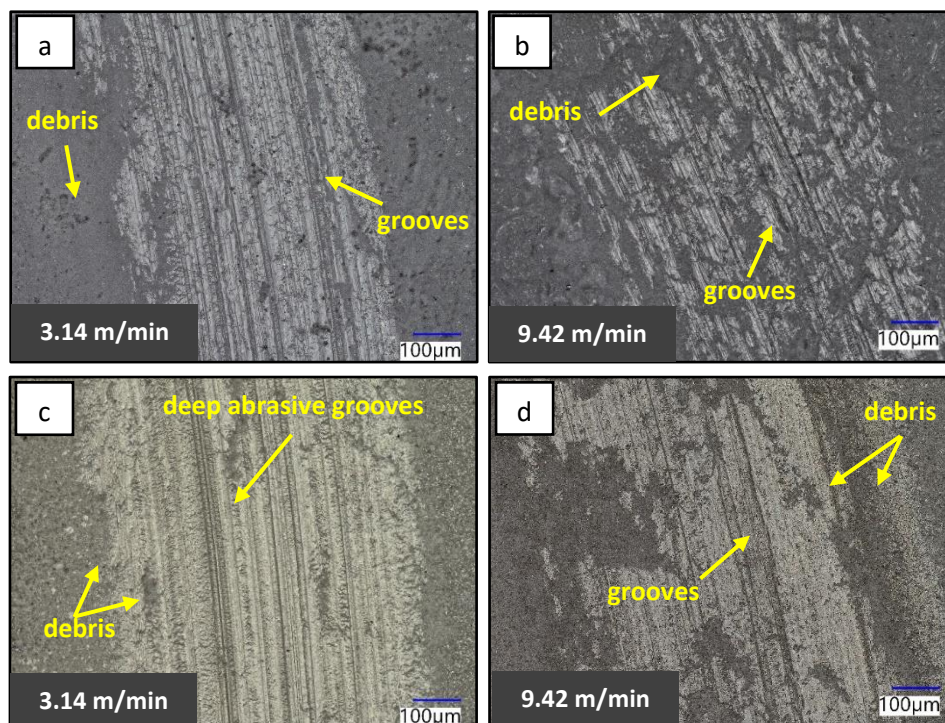


Figure 3.36 Optical images of the wear scars of Macor® at 3.14 m/min (a), Macor® at 9.42 m/min (b), AlN-BN at 3.14 m/min (c) and AlN-BN at 9.42 m/min (d).

The wear tracks left on the 3YSZ, Si_3N_4 and Al_2O_3 specimens are shown in Figure 3.37. Several differences can be noticed compared to the images previously discussed. The features of the wear scar do not appear as distinct, except for the presence of scratch marks on the 3YSZ (Figure 3.37 a-b) and Si_3N_4 (Figure 3.37 c-d) specimens, and small pits on the Al_2O_3 sample (Figure 3.37 e-f). The scratches are oriented with the sliding direction, and, therefore, it is likely they were caused by the SiC ball, which was worn by the three hard ceramics tested in this study (3YSZ, Si_3N_4 and Al_2O_3), as show in Figure 3.38. It is postulated that the flattening of the ball resulted in the increase in the COF of Al_2O_3 observed at the higher sliding speeds, as reported in Section 3.4.2.

Figure 3.37e-f show that the width of the scar increased from around 330 μm at 3.14 m/min to approximately 570 μm at 9.42 m/min, and it is believed that the increase in the surface in contact was due to the flattening of the counterface. The images captured on 3YSZ and Si_3N_4 showed that the scratching became less severe at high sliding speeds, suggesting a reduced interaction between the asperities of the two materials. The COF dropped when the asperity deformation processes decreased, as previously explained. Therefore, it is postulated that this reduced interaction observed at 9.42 m/min resulted in a decrease in the COF of 3YSZ and Si_3N_4 as the speed was increased. In addition to this, it was noticed that the surface of the as-received Si_3N_4 specimens contained a considerable amount of pores, and their presence could be related to the sintering process conditions used to manufacture the plates. The ceramics were procured as finished components from the supplier, and, for this reason, the origin of these features could not be identified with the information available. The absence of debris on the surface of the materials after testing suggests that the wear on these ceramics was less severe.

To further investigate the wear scar morphology, 3D scans of the worn surface were obtained for the ceramics tested at 9.42 m/min and are shown in Figure 3.39. The scans confirmed that the soft BN grades suffered from severe wear, as the scar was wide and deep (Figure 3.39a-b). The worn surface decreased on the Macor[®] and AlN-BN specimens, and the scar was narrower and less deep, as shown in Figure 3.39c-d. On the other hand, Al_2O_3 , 3YSZ and Si_3N_4 did not develop a ‘channel’ upon sliding with the SiC pin (Figure 3.39e–g).

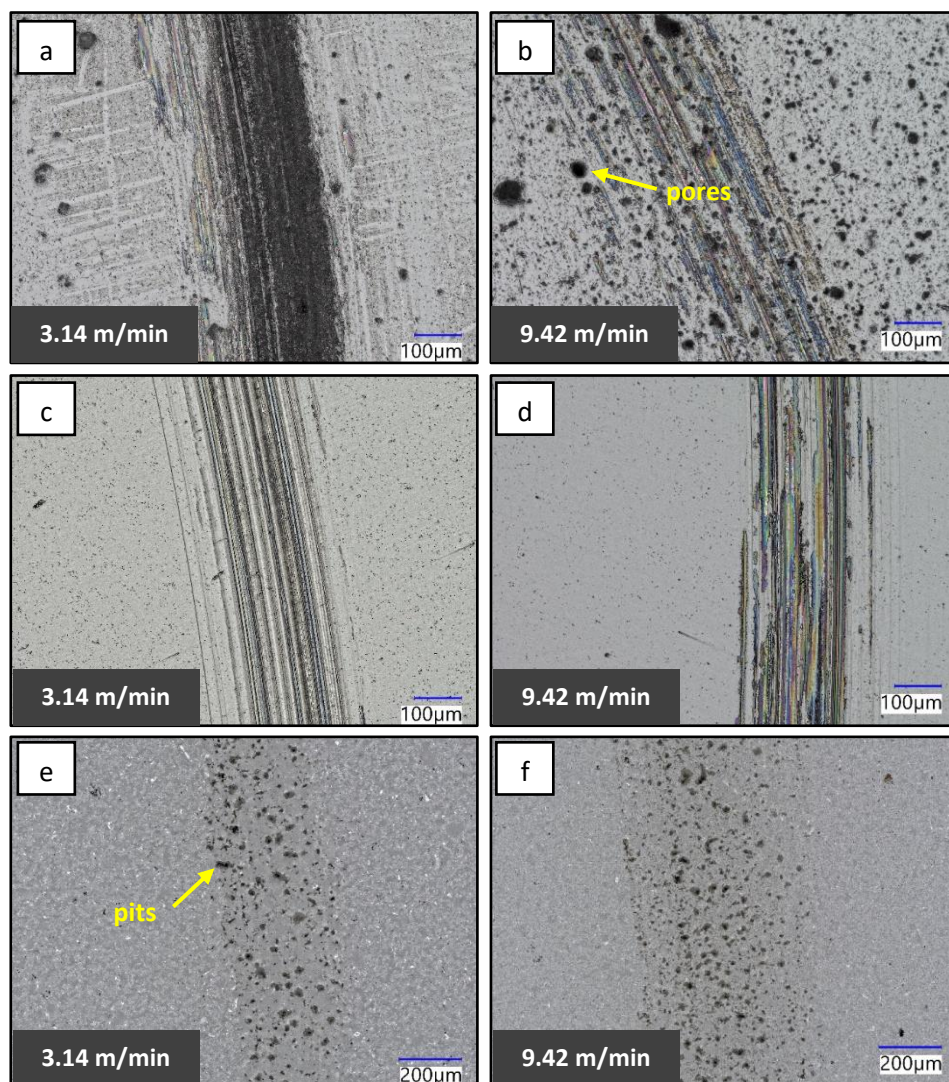


Figure 3.37 Images of the wear scars of 3YSZ at 3.14 m/min (a), 3YSZ at 9.42 m/min (b), Si_3N_4 at 3.14 m/min (c), Si_3N_4 at 9.42 m/min (d), Al_2O_3 at 3.14 m/min (e) and Al_2O_3 at 9.42 m/min (f).

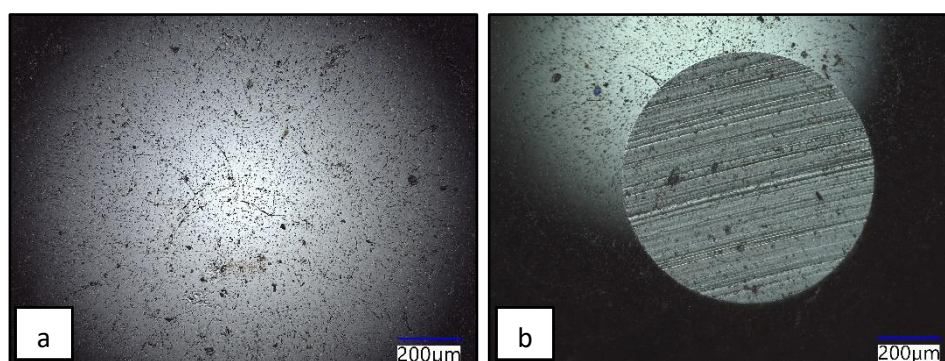


Figure 3.38 Images of the SiC ball before testing (a) and after contact with Al_2O_3 (b). The ball was worn during sliding, forming a 'flat-on-flat' contact.

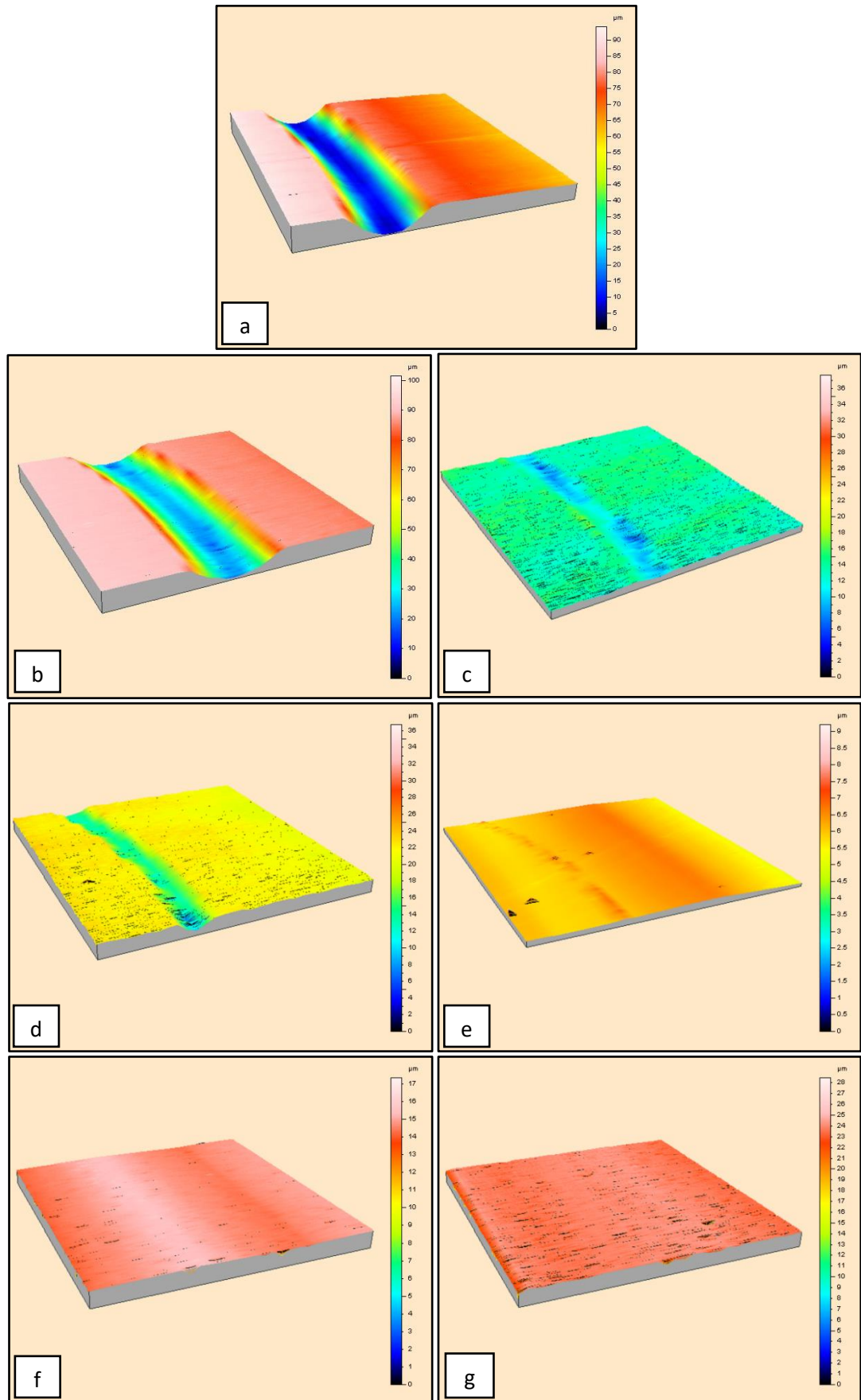


Figure 3.39 3D scans of the worn surface of pure BN (a), BN M26 (b), Macor® (c), AlN-BN (d), 3YSZ (e), Si₃N₄ (f), Al₂O₃ (g) at 9.42 m/min sliding velocity.

The depth of the scar was measured on the ceramics that suffered from severe volume loss after testing (Table 3.4), and the depths were plotted against the three different sliding velocities (Figure 3.40). The measured cross-sectional areas for the materials tested at a 9.42 m/min sliding velocity are plotted in Figure 3.41. The measurements confirmed that pure hBN and BN M26 were the materials with more damage, and they were also the ceramics which most suffered from the higher sliding speeds. Figure 3.40 shows that there was a steeper increase in the scar depth with speed for the pure hBN and BN M26 specimens compared to Macor® and AlN-BN.

Table 3.4 Measurements of the wear scar depths.

Material	3.14 m/min	6.28 m/min	9.42 m/min
Pure BN	16.9 μm	52.2 μm	64.8 μm
M26 BN	26.0 μm	57.2 μm	86.2 μm
Macor®	11.5 μm	16.0 μm	21.7 μm
AlN-BN	6.92 μm	9.19 μm	9.49 μm

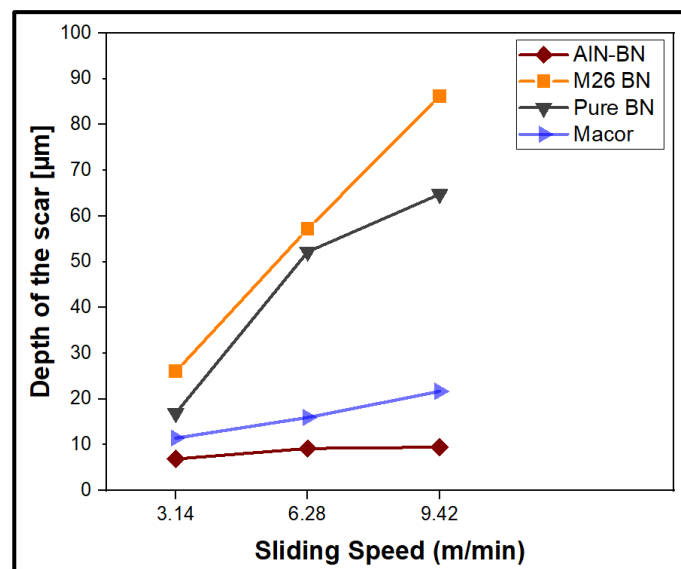


Figure 3.40 Depth of the worn track section plotted against sliding speed.

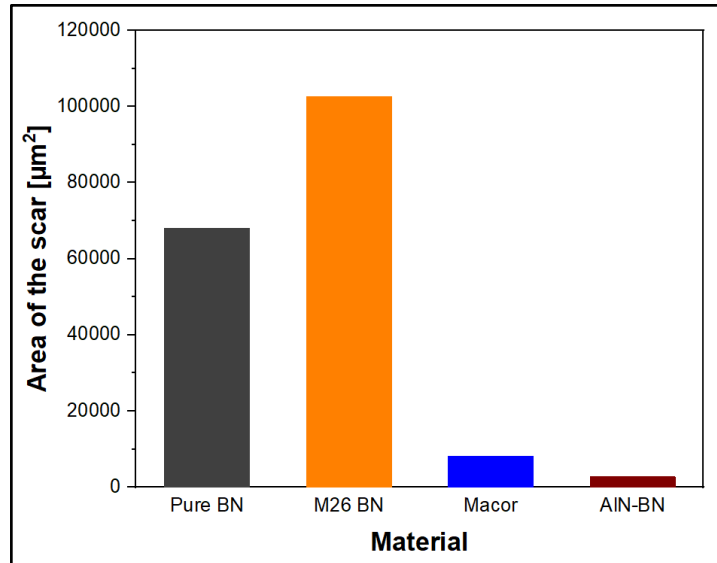


Figure 3.41 Measured cross-sectional area of the wear scar at 9.42 m/min sliding speed.

3.4.5 Wear Resistance and Hardness

The wear of the ceramics was measured using the wear coefficient ‘k’, which was determined in terms of volume loss per unit force per unit distance, as shown by Equation 6 in Chapter 2, Section 2.3.2. The higher the wear coefficient, the less the wear resistance of the material. The values of k for all the ceramics tested at 9.42 m/min are provided in Table 3.5. The wear coefficients of Al_2O_3 , 3YSZ and Si_3N_4 were significantly lower compared to the other ceramics, as minimal volume loss was detected under the conditions stated here, and they are considered to have superior wear resistance. The ceramics with the highest wear were the two BN grades, which were severely damaged by the harder SiC pin.

Table 3. 5 Wear coefficients calculated from the volume loss at 9.42 m/min.

Material	$k \times 10^{-6} [\text{mm}^3\text{N}^{-1}\text{m}^{-1}]$
Pure BN	11.331
M26 BN	17.115
Macor®	1.355
AlN-BN	0.455
3YSZ	0.02
Si_3N_4	0.021
Al_2O_3	0.018

The hardness of the ceramics tested in this work was measured according to the procedure outlined in Chapter 2, Section 2.3.1. Ten measurements were taken on each ceramic material and the average hardness values of the ceramics tested in this study are summarised in Table 3.6. The wear coefficients at a 9.42 m/min sliding speed were plotted against the hardness of the ceramics (Figure 3.42) and a correlation between these two material properties was found. The softer materials, namely, pure hBN and BN M26, displayed poor wear resistance compared to the hard ceramics, Al_2O_3 , 3YSZ and Si_3N_4 . The hardness of AlN-BN and Macor[®] was intermediate, falling between the low hardness of hBN and the high hardness of Al_2O_3 , 3YSZ and Si_3N_4 , and, therefore, they showed moderate wear. Moreover, the graph suggests that there is an exponential relationship between the wear rate and hardness; however, more experiments need to be performed to confirm this trend.

Table 3.6 Hardness values of the ceramic plates. The applied test load is reported in 'kgf' next to each numeric hardness value.

Name	Hardness
hBN	10±1 HV/4
BN M26	20±2 HV/4
Macor [®]	248±27 HV/5
AlN-BN	361±25 HV/4
3YSZ	1375±8 HV/3
Si_3N_4	1537±16 HV/3
Al_2O_3	1679±10 HV/3

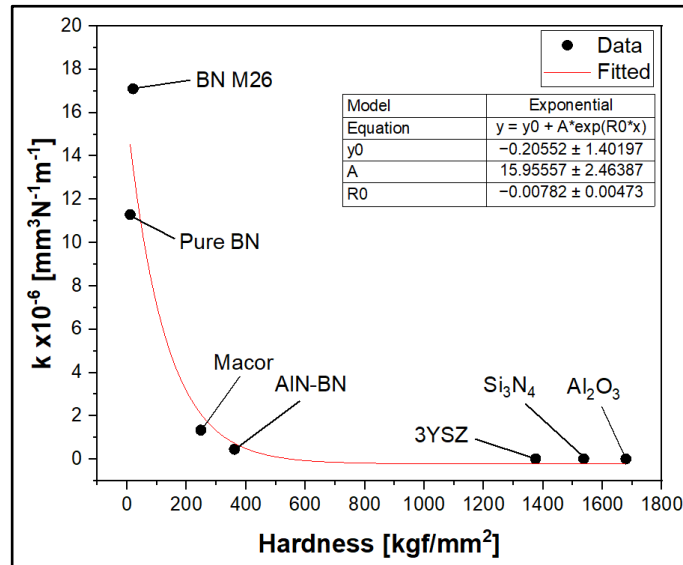


Figure 3.42 Plot of the wear coefficient 'k' against the hardness of the ceramics.

3.5 Summary

In this chapter, the corrosion behaviour of commercially available ceramics in liquid Zn alloy was compared to that of SS 316L and WC-Co/Wallex6™. The results of static immersion testing in Zn-Al and Zn-Al-Mg showed that the bath composition did not affect the corrosion behaviour of the ceramics tested in this study. SS 316L was severely attacked by molten Zn due to dissolution-diffusion processes occurring in the metal after contact with Zn. This confirmed the use of unprotected SS 316L hardware in the hot-dip galvanising bath is not recommended. The WC-Co coating shielded the base metal from liquid Zn in this experiment, but the formation of an oxide layer on top of the coating and the reduction of the coating thickness suggested that WC-Co was deteriorated and further degradation could expose the Wallex6™ base metal to the attack of liquid Zn. Conversely, all the sintered bulk ceramics tested in this work were not observed to react after exposure to liquid Zn alloy. hBN, BN Grade M26, Macor®, AlN-BN, 3YSZ, Si₃N₄ and Al₂O₃ remained inert, although Zn diffused into pure hBN through pores present in the material. The results of the corrosion test revealed that, due to their superior performance in Zn-Al and Zn-Al-Mg, ceramics outperformed the SS 316L and WC-Co benchmarks and, therefore, they hold promise that ceramics can be used to increase the service life of galvanising pot roll bearings.

Moreover, this chapter investigated the tribological properties of ceramics by performing a pin-on-disc wear test at different sliding velocities. Journal bearings require high wear resistance and the results earlier discussed suggested that Si_3N_4 , 3YSZ and Al_2O_3 can be used in the development of bearings with extended durability, due to their superior wear resistance. Among the ceramics tested, hexagonal BN had the lowest COF, which reached values < 0.1 at a low sliding speed. This result confirmed that hBN is a lubricious material and the presence of BN may reduce the COF between two materials in relative sliding.

The experiments discussed so far were conducted on sintered bulk ceramics, whose use as bearing materials could become problematic due to the well-known brittleness of ceramics. To solve this problem, it was decided to apply a thin Al_2O_3 coating onto the surface of materials with higher ductility, i.e., steel, with the aim of combining the superior ductility of steel with the inertness to molten metal of the ceramic. In addition to this, it was decided to fabricate novel materials containing BN, with a view of improving the lubrication of the bearings system, thereby reducing the wear damage on journal bearings in service. For this reason, SiAlON-BN composites were fabricated. Both SiAlON-BN composites and Al_2O_3 coating are discussed in Chapter 4.

Furthermore, several improvements were identified regarding the experiments to be conducted in this study. So far, the corrosion behaviour of materials in liquid Zn alloy was investigated by conducting static immersion, in which prospective bearing materials were not tested in motion; however, it was earlier discussed (Chapter 1, Section 1.8.4) that the components of a journal bearing system are in relative movement and the corrosion behaviour in molten metal could differ from static conditions. As result, it is important that dynamic testing is conducted to validate the results of static immersion testing. Moreover, the pin-on-disc wear tests were carried out at room temperature and under dry sliding condition. The experiments were carried out on an existing pin-on-disc set up which could only enable testing at room temperature to be conducted. High-temperature wear testing would have required substantial upgrades to the existing tribometer or the use of a significantly different machine. However, it is known that the bearings operate in liquid Zn alloy at 465°C and it is reported that, typically, ceramics are subjected to more severe wear and

friction at elevated temperatures (Stachowiak & Batchelor, 2013). Therefore, it was evident that a machine capable of performing dynamic wear testing in liquid Zn at high temperature was required to conduct further investigations and it was decided to build a rig for investigating the tribo-corrosion behaviour of prospective bearing materials. The wear testing rig, whose design is described in Chapter 2, Section 2.4.2.2, enabled to conduct rapid, small-scale tests of specimens in relative movement at the conditions found in the hot-dip galvanising bath (Chapter 5).

Chapter 4

Novel Ceramic Materials and Coatings

4.1 SiAlON-BN Composites

4.1.1 Introduction

Chapter 3 focused on experimenting a broad selection of technical ceramics available commercially and the results of static immersion testing demonstrated that ceramic materials are inert to Zn-Al and Zn-Al-Mg. Pin-on-disc testing of these ceramics showed that the lowest value of the COF was obtained using hBN due to its lubricious properties (Chapter 3, Section 3.4.2,). However, it was shown that the hexagonal form of BN is very soft; as a result, the wear resistance of this material is poor, especially compared to ceramics, such as Si_3N_4 , which displayed negligible volume loss after wear testing. For this reason, hBN is used as a solid-lubricating agent and is often introduced as a second phase to other materials to enhance their tribological performance. Ceramic composites obtained with hBN additions have already been experimented in other studies (Carrapichano et al., 2002; Chen et al., 2019; Subramanian et al., 2021; Yin et al., 2022; Zhao et al., 2018). Benefits in terms of friction and wear resistance were achieved, as the hBN particles can be released continuously upon sliding contact, which fill into the pores, grooves and cracks of the surface. If a suitable content of hBN is added, the formation of a smooth lubricating film occurs, which is reported to enhance the tribological properties of the material (Zhao et al., 2018).

The first part of this chapter focuses on investigating the tribo-corrosion behaviour of SiAlON-hBN composites fabricated with FAST (Chapter 1, Section 1.9.1). SiAlON is a ceramic made of Al, Si, N and O and it originates from Si_3N_4 . SiAlON has already been experimented as a material for submerged journal bearings in CG lines outside the UK, as previously mentioned in Chapter 1, Section 1.8.2.3. hBN was added to SiAlON

to promote the development of a lubricating film between the contacting surfaces of the bearings. The content of hBN was varied and the effects of increasing hBN additions on the COF as well as the corrosion in liquid Zn alloy were determined. Moreover, the tribo-corrosion behaviour of SiAlON-hBN composites was compared to that of pure SiAlON specimens, as well as that of SiAlON-cBN, which was prepared using the hard cubic form of BN.

4.1.2 Powder Characterisation

As mentioned in Chapter 2, Section 2.1.2, ceramic powders were used for preparing SiAlON-BN specimens. The powders were characterised with SEM prior to processing and images of the SiAlON, hBN and cBN powders are shown in Figure 4.1a, Figure 4.1b and Figure 4.1c respectively. The particle size was determined from these images by measuring the length of a sample of 10 particles in each material. These measurements are found in Table 4.1 and it was observed that the average particle size of both BN powders lied in the range of values indicated by the supplier, which were provided in Table 2.2 (Chapter 2, Section 2.1.2); no information was provided by the supplier regarding the size of the SiAlON particles. Figure 4.1a shows that the particles in the SiAlON powder have formed many agglomerates and, for this reason, measuring the size of isolated particles was difficult. Figure 4.1b revealed that the morphology of the hBN particles was near-spherical and the average particle size was measured around 6 μm . The cBN powder was made of particles with blocky shape and sharp edges. The average particle size was measured to be approximately 14 μm , meaning that it was slightly larger compared to the hexagonal form.

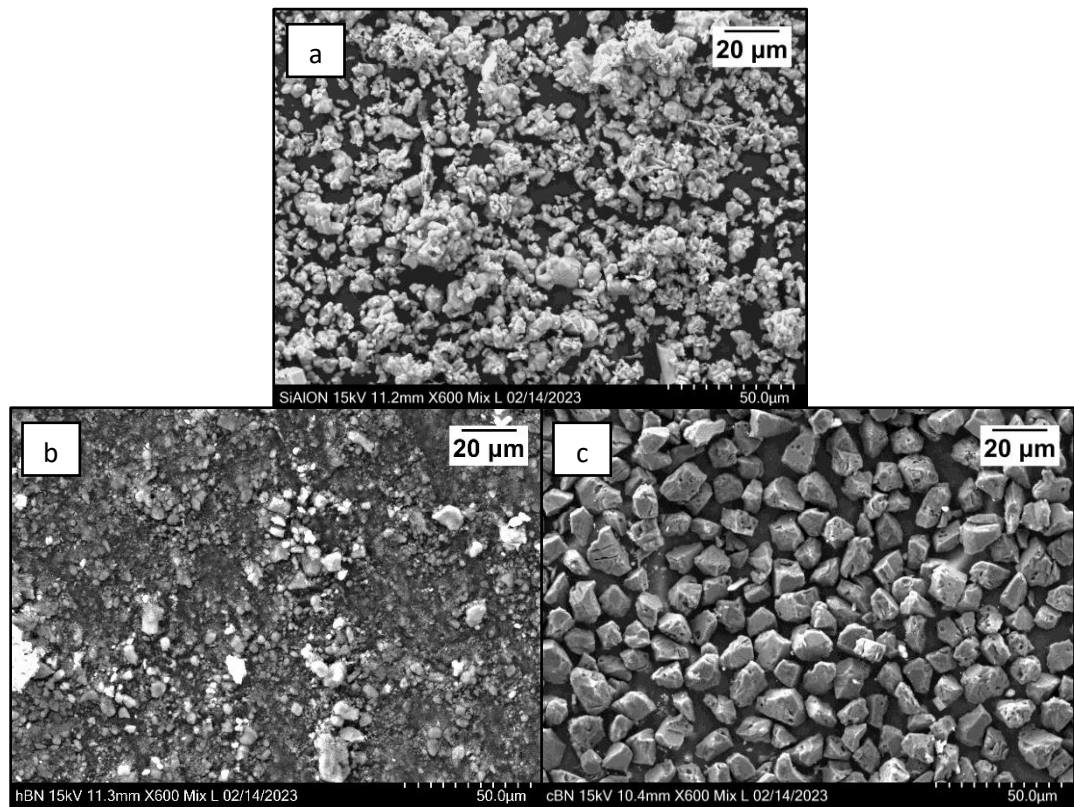


Figure 4.1 SEM images of SiAlON (a), hBN (b) and cBN powder (c).

Table 4.1 Measured particle size of SiAlON, hBN and cBN powder.

Material	Min particle size [μm]	Max particle size [μm]	Average Particle size [μm]
SiAlON	2.15	5.87	3.96 ± 1.15
hBN	2.70	10.69	5.87 ± 2.40
cBN	9.61	18.78	13.79 ± 2.95

4.1.3 Problems with NIR

Previous research conducted at Swansea University utilised NIR for sintering TiO_2 for dye sensitised solar cells (Watson et al., 2011); for this reason, it was initially decided to fabricate the SiAlON-BN composites with this technology, whose details were previously discussed in Chapter 1, Section 1.9.3. Trials were conducted to sinter the SiAlON-BN powders and to apply the mixture as a thin coating onto steel, at the same

time. An AdPhos (Bruckmühl, Germany) NIR unit was used for these trials, which is shown in Figure 4.2a.

SiAlON and hBN powders were mixed at a ratio of 50:50 by weight to obtain 30 g of SiAlON-hBN, which was subsequently added to ethanol and stirred to form a slurry. A 25×25 mm steel plate was used as the substrate and a thermocouple was spot welded onto the underside of the plate to record the temperature during heating. To enable deposition of the slurry, two layers of Scotch™ adhesive tape were applied to the surface of the steel plate on opposite sides, leaving the middle exposed. The slurry was poured onto the sample and was spread evenly using a glass rod. At this point, the tape was removed to obtain a layer of mixture ready for thermal processing via NIR.

The plate was positioned on top of a moving platform located at one end of the unit (Figure 4.2a). The platform was designed to move at a set speed under an NIR lamp with adjustable intensity. The heating process started once the sample platform was under the NIR lamp. A trial was conducted using a lamp intensity of 100% and a line speed of 0.5 m/min, which respectively correspond to the highest power and slowest movement of the platform. The sample exited the NIR lamp region on the other end and was allowed to cool down before inspection.

Figure 4.2b shows a photograph of the sample after heating with NIR. It was observed that the ethanol evaporated, as expected. However, damages on the ceramic coating occurred when the sample was handled; for example, when it was moved from the NIR unit to a workbench, fragments of the coating detached from the plate, suggesting that there was poor bonding with steel. Further handling caused the coating to completely disintegrate. The thermocouple recorded a maximum temperature of 1000 °C during NIR heating, which may be insufficient to fully sinter the ceramic mixture. Other studies which prepared SiAlON-BN composites utilised sintering temperatures above 1550 °C. (Ye et al., 2010; Yin et al., 2022). Changing the line speed and lamp intensity did not solve the issue, as lower temperatures were produced and, therefore, it was decided to test different techniques other than NIR heating.

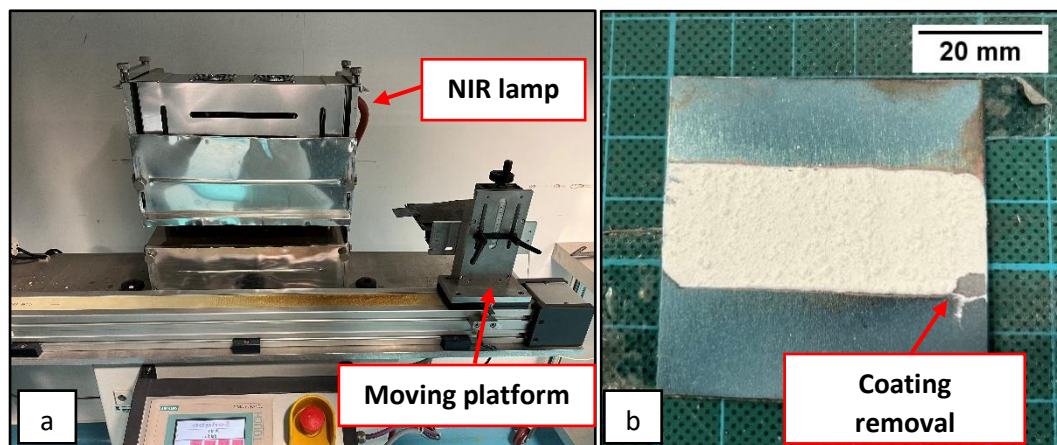


Figure 4.2 AdPhos NIR unit (a); Inspection of the sample obtained at 0.5 m/min line speed and 100% lamp intensity (b).

4.1.4 Fabrication of SiAlON-BN Composites with FAST

NIR heating did not produce the temperature required for sintering the ceramic powders and the specimens prepared were not suitable for testing due to poor bonding with the steel substrate and breakdown of the coating during sample handling. For this reason, other sintering technologies were explored for fabricating the SiAlON-BN specimens required for this study. There is evidence in the available literature that ceramic powders can be sintered with Field Assisted Sintering Technology (FAST), also known as Spark Plasma Sintering, whose details were discussed in Chapter 1, Section 1.9.1. Previous studies showed that this technique successfully enabled the fabrication of samples made of SiAlON and BN ceramics (Ye et al., 2010; Yin et al., 2022). Therefore, it was decided to prepare the SiAlON-BN composites using the FAST equipment at the University of Sheffield (Sheffield, UK), through the Royce Institute. Before preparing the specimens required in the present study, several trials were conducted to optimise the processing conditions.

SiAlON-BN discs of 60 mm diameter and 3 mm thickness were prepared using a FAST Furnace Type HP D25 (FCT Systeme GmbH, Rauenstein, Germany), which is shown in Figure 4.3a. The feedstock was prepared by mixing SiAlON and BN powders at the desired weight ratios and the required mass of powder was poured into the die shown in Figure 4.3b. The compositions of the blends prepared for FAST are listed in Table

4.2. All the internal surfaces of the die assembly in contact with the powder were lined using graphite foil in order to minimise bonding between the components. The die assembly was subjected to a cold pre-pressing of 20 MPa to achieve good electrical contact between the surfaces and, subsequently, it was loaded into the furnace and placed between the hydraulic rams of the process chamber. At this point, the chamber was evacuated and the predefined FAST cycle was initiated. The FAST processing parameters included heating rate, dwell temperature, dwell load and dwell period.

An initial contact load of 5kN was applied by the hydraulic rams to the die assembly and the temperature was measured and controlled using an optical pyrometer. Although a current is applied as soon as the cycle is initiated, temperature could not be controlled until a value of approximately 300 °C was reached, due to limitations of the pyrometer. In this study, all the SiAlON-BN ceramics were consolidated by increasing the temperature and the load simultaneously until the respective dwell setpoints were reached. Once the dwell period is complete, the voltage was removed and the die assembly was left to cool down to room temperature. In addition to this, the load is gradually decreased throughout this cooling period. Once the load was removed, the chamber was vented and opened to extract the die assembly. The graphite films were removed and the consolidate SiAlON-BN specimen was retrieved (Figure 4.3c). An example of a FAST cycle used to prepare the specimens is shown in Figure 4.4.

Table 4.2 Composition of the mixtures used to prepare the SiAlON-BN specimens with FAST.

Blend no.	SiAlON [wt.%]	hBN [wt.%]	cBN [wt.%]
1	100	0	0
2	90	10	0
3	80	20	0
4	70	30	0
5	70	0	30

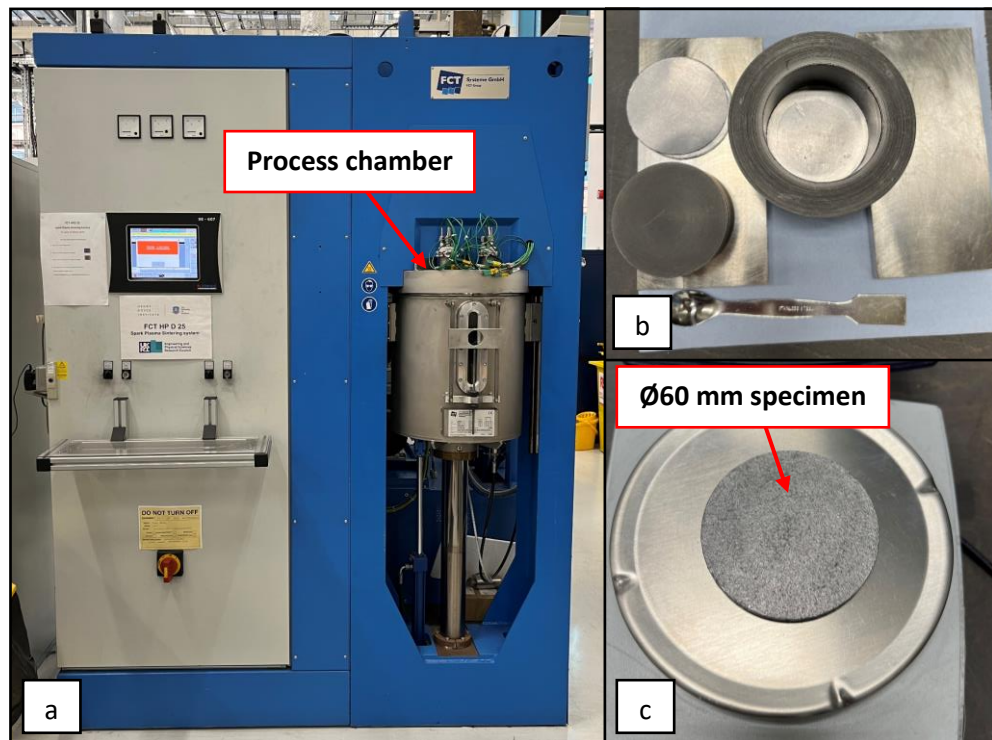


Figure 4.3 FAST Furnace Type HP D25 (a); die assembly (b); specimen after FAST processing (c).

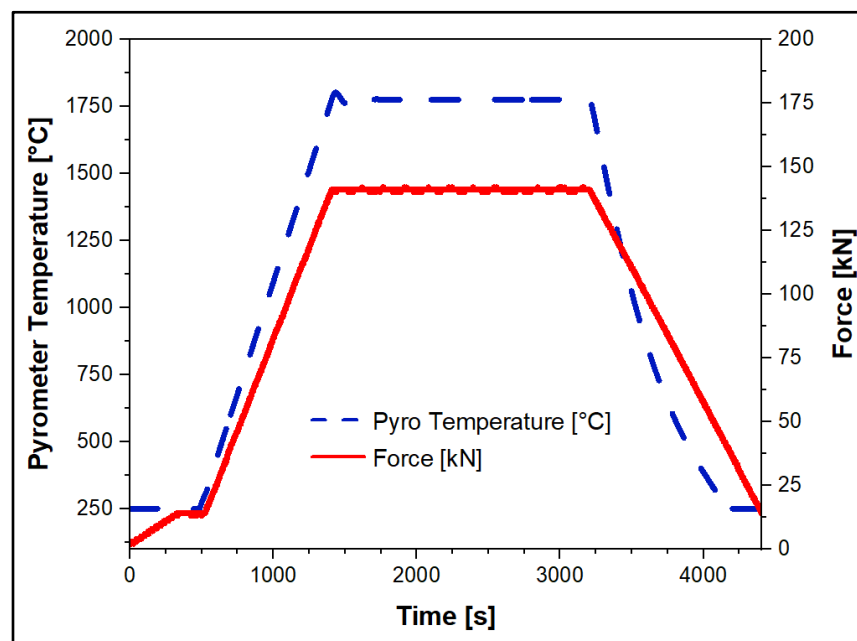


Figure 4.4 Graph illustrating the load and temperature profiles of a FAST cycle.

4.1.5 Effects of Changing Sintering Temperature and Time

Before preparing samples for static testing and pin-on-disc wear testing, initial trials were conducted with FAST to test the technique and to optimise the processing conditions required for sintering. A total of five specimens were fabricated by varying the dwell temperature, dwell time and BN content. The composition and processing conditions used for these trials are found in Table 4.3. The dwell load was fixed at 141 kN for all the specimens and the dwell load and temperature profiles are those illustrated in Figure 4.4., i.e., the load is increased as the temperature in the furnace is increased and, subsequently, it is gradually removed during the cooling period.

Table 4.3 Composition and processing conditions for the initial FAST trials.

Specimen name	Composition	Dwell Temperature [°C]	Dwell Time [min]
TRIAL1	SiAlON	1600	10
TRIAL2	SiAlON	1800	30
TRIAL3	SiAlON	1850	30
TRIAL4	30wt.%hBN-SiAlON	1850	30
TRIAL5	30wt.%cBN-SiAlON	1850	30

The discs were sectioned and samples were prepared for material characterisation. Specimens for examination with SEM and EDS were ground and polished according to the procedure outlined in Chapter 2, Section 2.2.1. Figure 4.5 and Figure 4.6 respectively show the microstructures of TRIAL1 and TRIAL2 specimens, which were manufactured using 100wt.% SiAlON feedstock. TRIAL1 was fabricated using a dwell temperature of 1600 °C and a dwell time of 10 minutes, which were used in a previous study (Yin et al., 2022) to sinter SiAlON-BN. Figure 4.5 shows that the microstructure of TRIAL1 is characterised by grains separated by regions of incomplete densification. This type of structure was observed in spark plasma sintered Si₃N₄ ceramics and was referred to as ‘snow flake’ structure, as it consists of a grain skeleton without the presence of an intergranular glassy phase separating the Si₃N₄ grains (Herrmann et

al., 2008). Moreover, the SEM image of TRIAL1 sample revealed that the material is characterised by a significant amount of porosity.

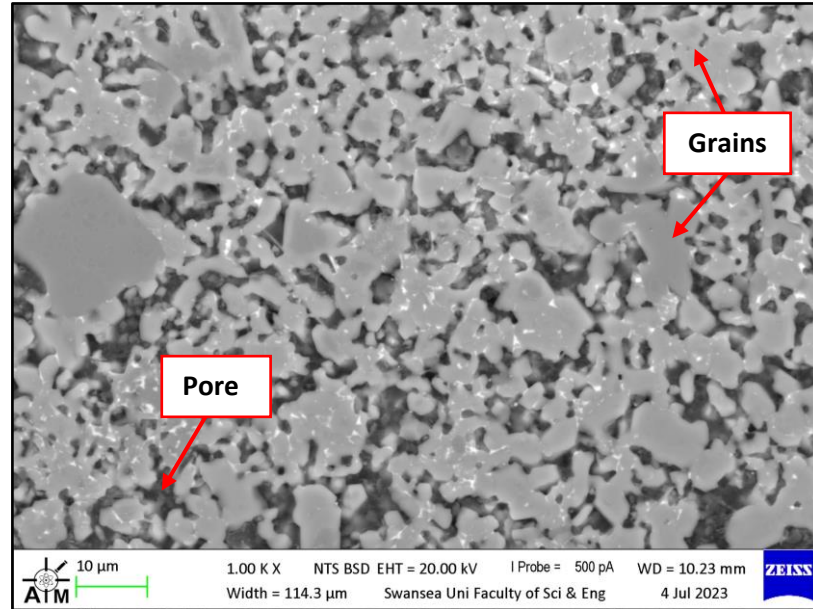


Figure 4.5 Microstructure of TRIAL1. The specimen was prepared using a dwell temperature of 1600 °C and a dwell time of 10 minutes.

The experiments conducted in previous studies demonstrated that the densification of SiAlON-BN composites prepared with FAST/SPS is highly dependent on the processing conditions (Yin et al., 2022). For this reason, TRIAL2 was prepared by increasing both the dwell temperature and dwell time to 1800 °C and 30 minutes respectively. The SEM image of the microstructure of TRIAL2 (Figure 4.6) shows that the material is now characterised by areas of good densification. These areas are made of SiAlON grains (darker contrast) which are separated by an intergranular phase (light contrast), as it was observed previously in the Si_3N_4 specimens tested in Chapter 3 (Figure 3.14). The presence of the intergranular glassy phase is more evident in the magnified image of the microstructure (Figure 4.7). However, Figure 4.6 and Figure 4.7 show that pores are still present in the material. When the sintering temperature was further increased to 1850 °C (TRIAL3), the 100wt.% SiAlON specimen cracked, as soon as the moulds were disassembled after FAST processing (Figure 4.8). Cracking did not occur in the SiAlON specimens prepared at lower dwell

temperatures (TRIAL1 and TRIAL2), suggesting that stresses were induced in the material when the temperature was raised to 1850 °C.

TRIAL4 and TRIAL5 were prepared at 1850 °C and 30 min holding time with the addition of hBN and cBN powders to obtain 30wt.% hBN-SiAlON and 30wt.% cBN-SiAlON, respectively. Although the temperature was the same as that used for TRIAL3, no cracking of the specimens occurred after sintering; therefore, adding BN may have a beneficial effect during FAST processing of SiAlON in preventing the development of stresses. The microstructure of SiAlON-BN composites is discussed in Section 4.1.6.

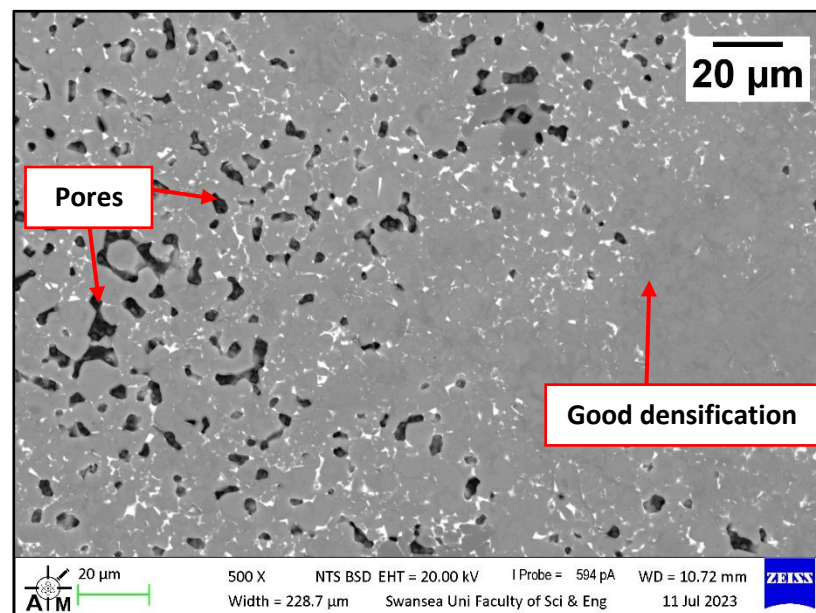


Figure 4.6 Microstructure of TRIAL2. The specimen was prepared using a dwell temperature of 1800 °C and a dwell time of 30 minutes.

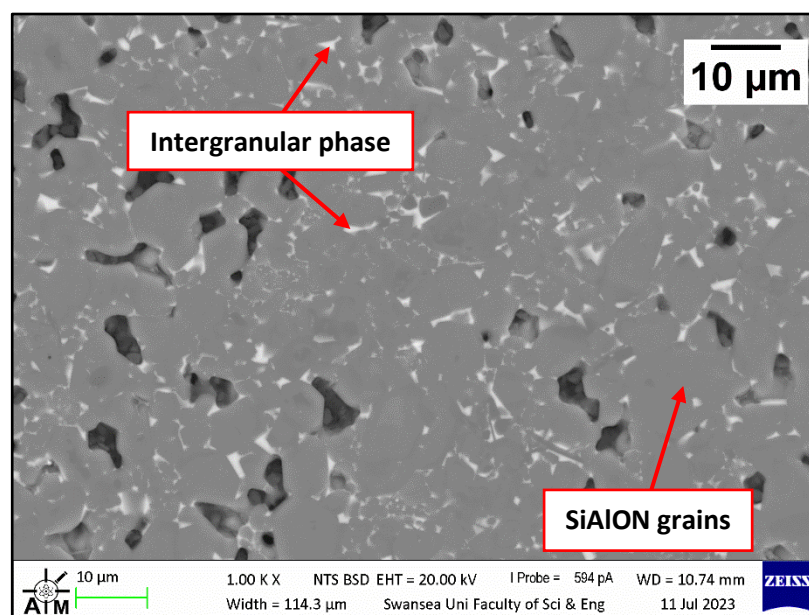


Figure 4.7 SEM image of TRIAL2, showing details of the SiAlON grains (darker contrast) separated by an intergranular phase (lighter contrast).

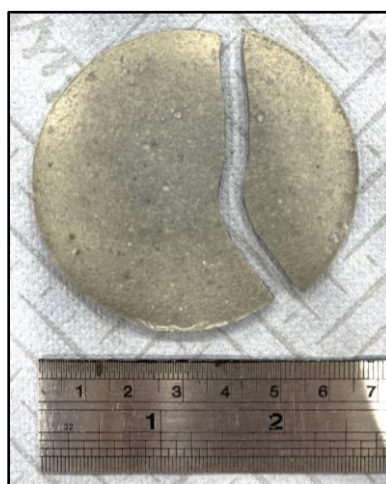


Figure 4.8 Photograph of the 100wt.% SiAlON specimen (TRIAL3) prepared at 1850 °C.

The density of the specimens prepared in the trials was measured using the Archimedes' method, with the exception of the cracked sample (TRIAL3). The relative densities of the materials were calculated according to the procedures discussed in Chapter 2, Section 2.2.6 and are found in Table 4.4. It was observed that the bulk densities measured with Archimedes' method were lower than the theoretical densities of SiAlON and SiAlON-BN composites, hence why the relative densities were

not 100%. This difference was caused by the open porosity present in the samples prepared during the trials, which was previously observed when the microstructure of the materials was characterised with SEM (Figure 4.4 - Figure 4.6). It is ideal for prospective galvanising pot roll bearing materials to have low levels of open porosity because Zn can infiltrate through pores, as discussed previously in Chapter 3, Section 3.3.3. Therefore, it was decided to further optimise the FAST processing and to focus on reducing the porosity in the samples. Additives are typically used during sintering to promote densification and a mixture of Y_2O_3 and Al_2O_3 was used in another study as the sintering additive to prepare SiAlON-BN composites with FAST/SPS (Yin et al., 2022). For this reason, the specimens used for testing in the present work were prepared by adding a total amount of 8 wt.% of sintering additives to each blend listed in Table 4.2. The mixture consisted of Y_2O_3 - Al_2O_3 with a molar ratio of 3.5.

Table 4.4 Relative densities of the specimens prepared after performing the initial trials.

Specimen name	Relative density [%]
TRIAL1	83.43 ± 0.68
TRIAL2	90.88 ± 0.95
TRIAL4	93.99 ± 0.06
TRIAL5	92.53 ± 1.54

4.1.6 Effects of Adding Sintering Additives

Five samples, namely SiAlON, 10wt.%hBN-SiAlON, 20wt.%hBN-SiAlON, 30wt.%hBN-SiAlON and 30wt.%cBN-SiAlON, were prepared by adding a mixture of Y_2O_3 - Al_2O_3 sintering additive to improve densification. The materials were sintered using a load of 141 kN and a dwell time of 30 minutes, like the specimens characterised in the previous section. Regarding the dwell temperature, it was decided to lower the value to 1775 °C for the SiAlON-BN composites and to 1700 °C for the pure SiAlON specimen, in order to prevent cracking of the specimens after FAST processing. The temperature and load profiles used for preparing these specimens are analogous to those of the trials and were illustrated previously in Figure 4.4.

As done for the initial trials, the specimens were sectioned for material characterisation and testing. The Archimedes' method was performed on samples prepared with the sintering additives and the relative densities of the materials were determined (Table 4.5). It was observed that the majority of the materials benefitted from the addition of $Y_2O_3-Al_2O_3$: the relative density of pure SiAlON increased from 83.43% to 94.53% and all the SiAlON-hBN specimens displayed a higher relative density, meaning that the measured density of these materials was closer to their theoretical density and that a decrease in open porosity was achieved. The highest density was measured on 20wt.%hBN-SiAlON, as a value of 99.58% was recorded. The only specimen which showed a lower density compared to the trials was 30wt.%cBN-SiAlON, as shown in Table 4.5. This suggested that the sintering additives did not enhance densification of the materials containing cBN and the lower measured density was the result of decreasing the sintering temperature from 1850 °C to 1775 °C.

Table 4.5 Relative densities of the specimens prepared using sintering additives.

Specimen name	Temperature [°C]	Relative density [%]
SiAlON	1700	94.53 ± 0.21
10wt.%hBN-SiAlON	1775	98.83 ± 0.41
20wt.%hBN-SiAlON	1775	99.58 ± 0.23
30wt.%hBN-SiAlON	1775	96.20 ± 0.67
30wt.%cBN-SiAlON	1775	86.77 ± 0.01

The new specimens were characterised with SEM and EDS to analyse the effects of adding the sintering additives on the microstructure of the materials. Figure 4.9 shows the microstructure of the pure SiAlON specimen after FAST processing. Although some pores are still present in the analysed area, the level of porosity was significantly reduced, compared to the specimen prepared without sintering additives (Figure 4.5). It was observed that the material is no longer characterised by a 'snow flake' microstructure and that the grains are separated by an intergranular phase

(bright contrast). The majority of these grains are equiaxed and shows a hexagonal morphology.

As previously mentioned, Si_3N_4 -based ceramics can exist as two major crystalline phases, namely α and β . The specimens analysed in this chapter were prepared using α -SiAlON feedstock and, therefore, it was expected to find a microstructure consisting of small equiaxed grains. However, Figure 4.9 shows that a small amount of elongated grains is present in the material, which are typically observed in β -SiAlON. There are studies which report the formation of rod-like grains in α -SiAlON, instead of the more common equiaxed morphology. It was observed that the development of elongated grains occurred in systems characterised by a composition rich in O, Al and when excess Y_2O_3 is used as the sintering additive (Ahmed et al., 2020; Mandal, 1999; Ye et al., 2003). For this reason, the presence of rod-like grains observed in Figure 4.9 may be the result of adding Y_2O_3 - Al_2O_3 sintering aids prior to FAST processing.

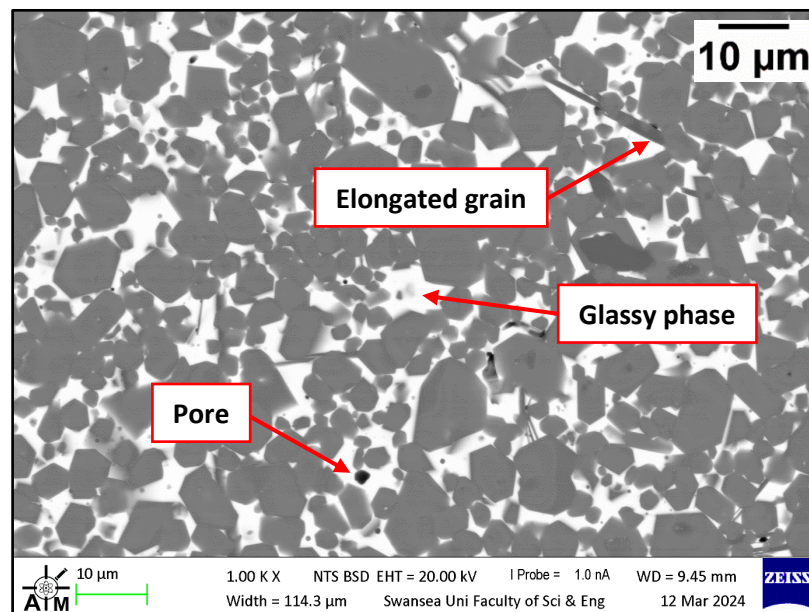


Figure 4.9 Microstructure of SiAlON after the addition of Y_2O_3 and Al_2O_3 sintering additives.

The microstructure of SiAlON contains a glassy phase separating the SiAlON grains, in a similar fashion to Si_3N_4 -based ceramics. EDS analysis was conducted to reveal the composition of both the SiAlON grains and the intergranular glassy phase. It was found that the grains contain Si (36.5 ± 3.1 wt.%), N (25.5 ± 2.4 wt.%), Al (20.2 ± 1.5

wt.%), Y (10.8 ± 0.2 wt.%) and O (7.0 ± 2.8 wt.%). Like α -Si₃N₄, α -SiAlON has an hexagonal crystal structure with (Si,Al)(O,N)₄ tetrahedra and modifying cations can partially occupy the interstitial positions created in the (Si,Al)-(N,O) network. It is well-known that the metal ions present in the sintering additive can diffuse in these interstitial sites (El-Amir et al., 2021). As the specimen was fabricated using a sintering additive containing Y, this element was incorporated into the interstitial sites of the α -SiAlON structure. Regarding the intergranular glassy phase, Figure 4.10 shows that it mainly consists of Y (52.1 ± 1.1 wt.%), Si (26.1 ± 0.5 wt.%), O (12.2 ± 0.7 wt.%), Al (5.8 ± 0.6 wt.%) and N (3.7 ± 0.3 wt.%). It was observed that the intergranular phase was almost absent in the initial trials, when no sintering aids were present in the powder mixtures. Once Y₂O₃-Al₂O₃ was subsequently added, a reaction between the sintering aids with part of the nitride occurred, forming a liquid-phase, which solidified into glass at the grain boundaries during cooling (El-Amir et al., 2021). Therefore, the addition of sintering aids promoted the formation of an intergranular phase and allowed to achieve better densification, as shown by the Archimedes' density measurements (Table 4.5).

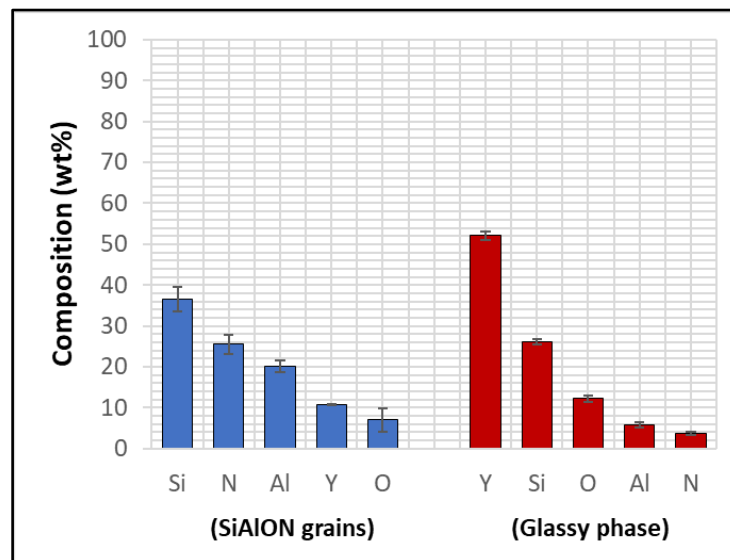


Figure 4.10 EDS phase elemental analysis of the phases present in SiAlON, which were previously highlighted in Figure 4.9.

Furthermore, it was observed that the sintering aids interacted with the phases containing BN. Figure 4.11 was captured on the 30wt.%hBN-SiAlON specimen and

three different regions can be distinguished: the first region consists of SiAlON with little presence of the intergranular phase (1); the second region consists of SiAlON grains separated by the glassy phase (2); the third region is characterised by hBN rich phases (3). This inhomogeneity could be caused by improper mixing of the powders, which led to the development of the glassy phase in certain areas and not in others. Moreover, there are areas where the hBN phase is not well dispersed with the SiAlON phase. It is expected that using a mixing method during the preparation of the powders, such as ball-milling, could enhance the homogeneity in the material. In addition to this, increasing the dwell time could potentially homogenise the material further, although it may affect characteristics of the material, such as grain size.

A magnified SEM image of the 30wt.%hBN-SiAlON specimen is shown in Figure 4.12 and it revealed the presence of a bright phase within the darker hBN-rich regions. EDS mapping was conducted, which confirmed that the dark phase is hBN, as expected. In addition to this, the results of EDS analysis suggested that the bright phase found in this region is likely to be a glassy phase as it contained Y diffused from the sintering additive, in a similar fashion to the intergranular phase located between the SiAlON grains.

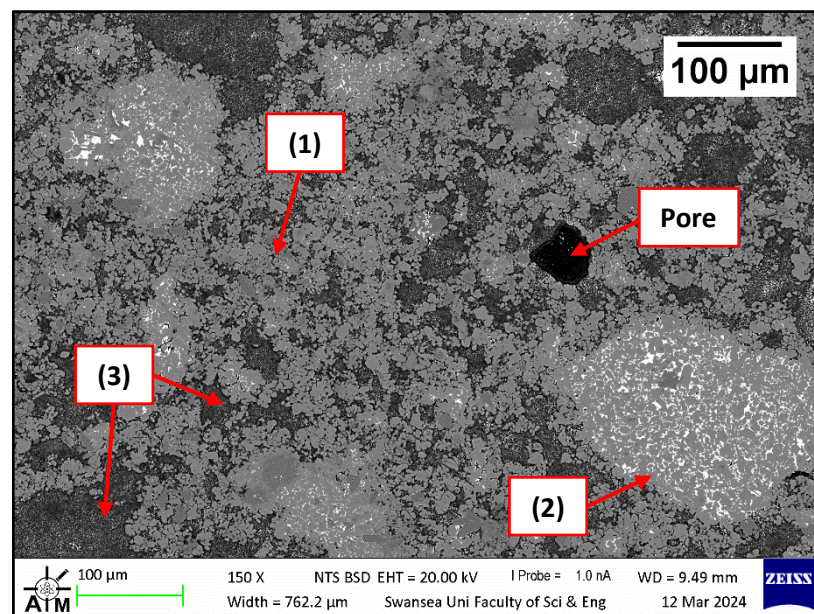


Figure 4.11 Microstructure of 30wt.%hBN-SiAlON after the addition of Y_2O_3 and Al_2O_3 sintering additives.

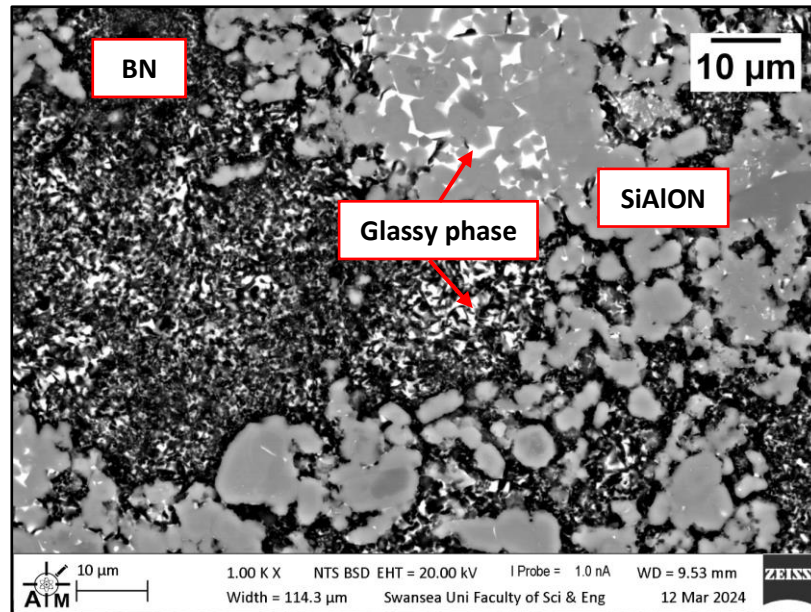


Figure 4.12 Image of the 30wt.%hBN-SiAlON microstructure.

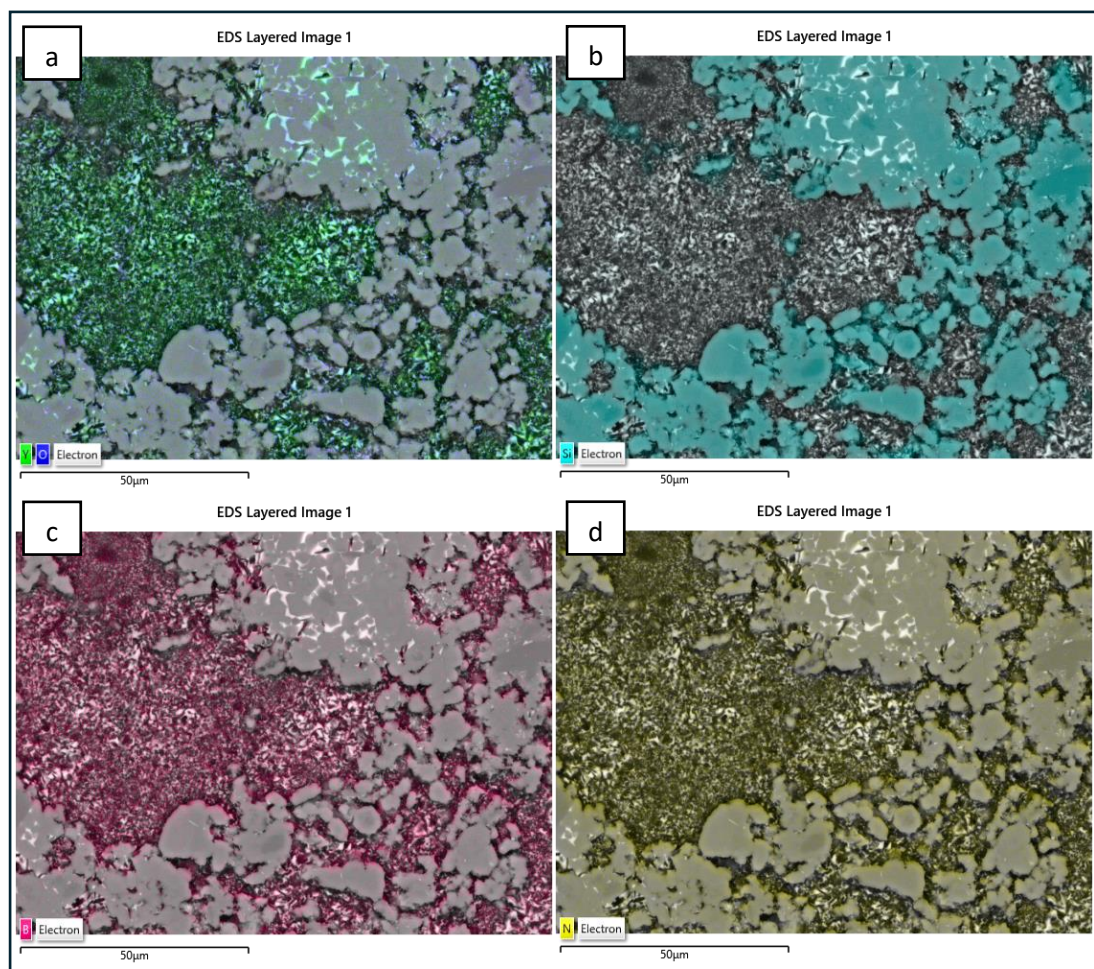


Figure 4.13 EDS mapping of 30wt.%hBN-SiAlON highlighting areas containing Y, O (a), Si (b), B (c) and N (d).

The microstructure of 30wt.%cBN-SiAlON is shown in Figure 4.14. As observed for the 30wt.%hBN-SiAlON specimen, it is possible to distinguish dark contrast regions that are rich in BN (1) and areas where the SiAlON grains are separated by the intergranular glassy phase (2), as illustrated in the image captured at 1000X magnification (Figure 4.15). EDS elemental mapping was performed (Figure 4.16) and confirmed that cBN is found in the dark contrast region of the sample, as shown by the B and N maps; in addition to this, it is also shown that the glassy phase containing Y is located within the cBN rich zones, as previously reported for the SiAlON-hBN specimens. The phases present in SiAlON and SiAlON-BN after the addition of sintering additives were analysed with XRD, which was performed according to the procedures outlined in Chapter 2, Section 2.2.4. The diffraction patterns obtained for the five materials are found in Figure 4.17. The results of XRD revealed that the main phase in each material is α -SiAlON; however, the peaks obtained in the analysis are those of Y containing SiAlON, because of the reaction between the nitride and Y present in the sintering aids mixture, as explained earlier. For the specimens with SiAlON-hBN and SiAlON-cBN composition, the Y-SiAlON phase co-existed with hBN and cBN respectively, as expected. No other phases were detected in the materials after FAST processing.

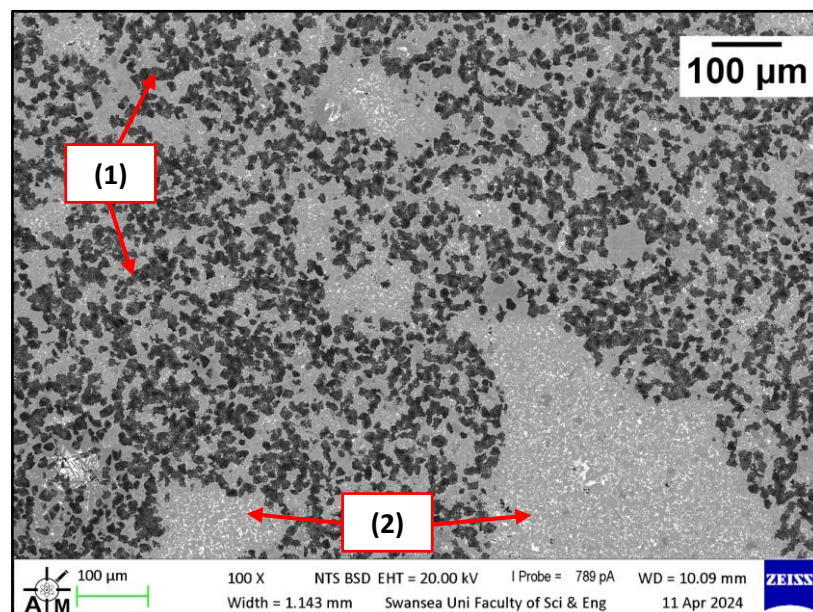


Figure 4.14 Microstructure of 30wt.%cBN-SiAlON after the addition of Y_2O_3 and Al_2O_3 sintering additives, showing BN rich (1) and SiAlON rich areas (2).

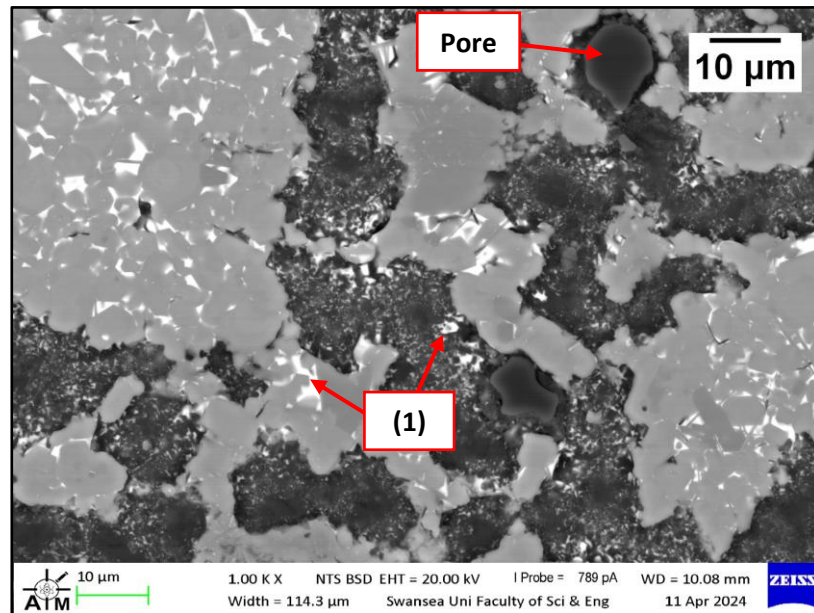


Figure 4.15 Magnified image of 30wt.%cBN-SiAlON showing details of the glassy phase (1).

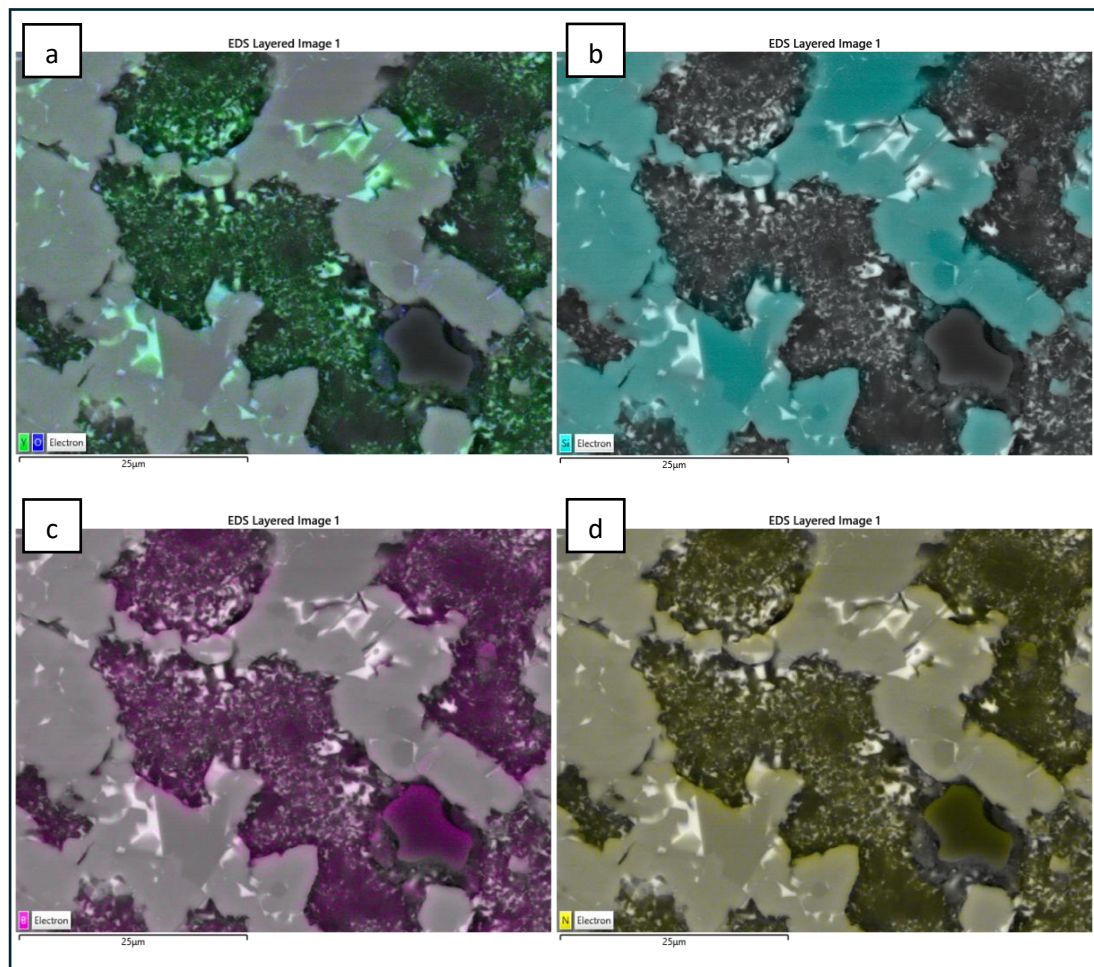


Figure 4.16 EDS mapping of 30wt.%cBN-SiAlON highlighting areas containing Y, O (a), Si (b), B (c) and N (d).

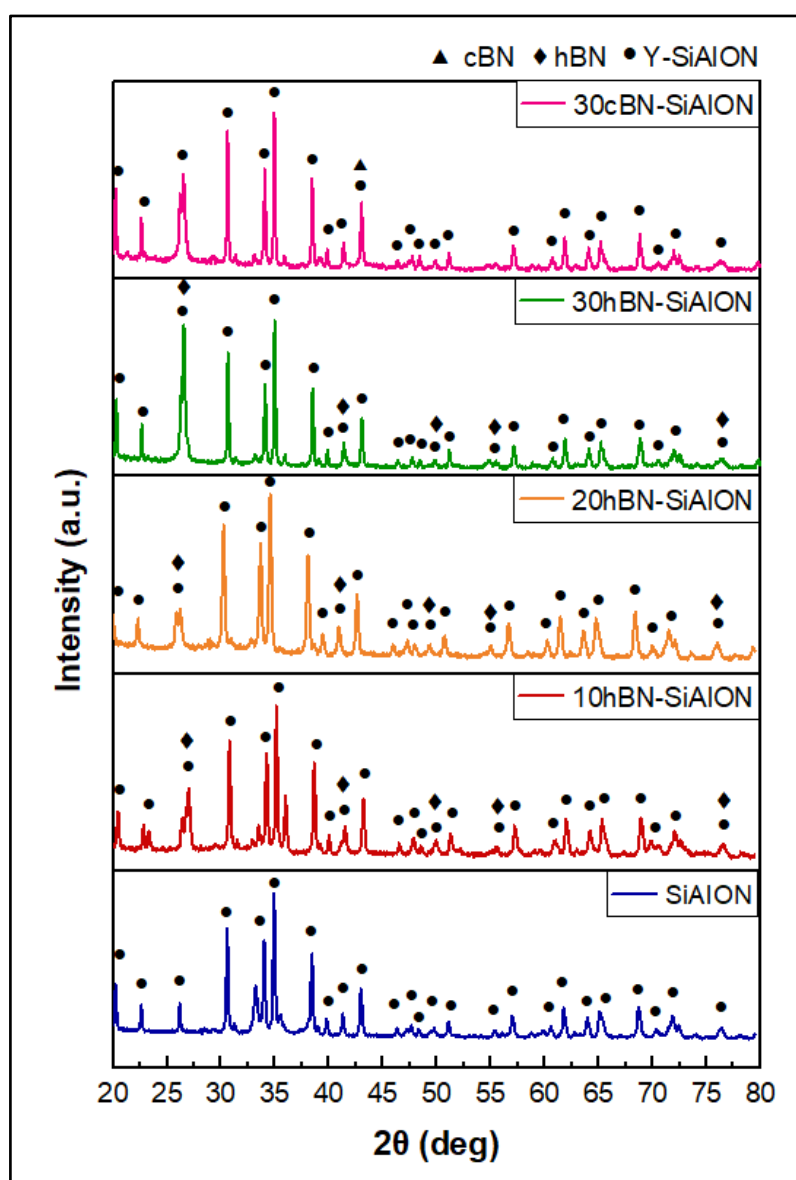


Figure 4.17 Diffraction patterns of the SiAlON and SiAlON-BN composites after FAST processing.

4.1.7 Static Immersion Testing

The specimens produced with FAST, namely SiAlON, 10wt.%hBN-SiAlON, 20wt.%hBN-SiAlON, 30wt.%hBN-SiAlON and 30wt.%cBN-SiAlON were tested in Zn-Al (Zn-0.3wt%Al) and Zn-Al-Mg (Zn-1.5wt%Al-1.5wt%Mg) baths to assess the corrosion behaviour of these materials in liquid Zn alloy. Coatings with an Al content around 0.3wt% are referred to as GI coatings and are used to produce automotive full finish premium grade product. Zn-Al-Mg coatings are thinner and have become popular

within the automotive industry for reducing the weight of vehicles. Tata Steel's ZODIAC CG line produces both Zn-Al (GI) and Zn-Al-Mg coatings. Static immersion testing was conducted following the procedures discussed in Chapter 2, Section 2.4.1. The molten metal baths were kept at a temperature of 465 °C and, after 5 weeks of exposure to Zn-Al and Zn-Al-Mg, the samples were removed from each bath. Subsequently, the residual Zn was removed with HCl solution.

The cross-section of SiAlON and the SiAlON-BN specimens after immersion in Zn-Al and Zn-Al-Mg baths are shown in Figure 4.18 and Figure 4.19 respectively. The SEM images revealed that the corrosion behaviour of these materials was analogous to that of the ceramics investigated in the previous chapter. Unlike SS 316L (Figure 3.20, Figure 3.21), there were no intermetallic particles on the surface of the material after exposure to molten metal and, moreover, no sub-surface diffusion layers were detected, suggesting the SiAlON and SiAlON-BN specimens were inert to Zn, Al and Mg. This observation is supported by the results of EDS elemental analysis, which was conducted at the interface, where contact with the Zn alloy occurred, as well as in the bulk of the materials for both the SiAlON and BN phases. The average element composition of the 30wt.%hBN-SiAlON specimens tested in Zn-Al and Zn-Al-Mg are shown in Figure 4.20 and Figure 4.21 respectively. EDS analysis did not detect evidence of corrosion of these materials after exposure to Zn alloy. Mg was detected on the samples immersed in Zn-Al-Mg; however, due to the low levels (< 0.2), it is likely they are traces of residual alloy which were not eliminated during pickling. In addition to this, the results of EDS analysis showed that the composition measured at the interface is the same as that measured in the bulk of the material. The analysis conducted in the other SiAlON specimens showed an identical behaviour.

The absence of dissolution-diffusion processes with the molten metal bath indicates that SiAlON and SiAlON-BN can be considered for making pot roll journal bearings with extended service life, alongside the ceramics investigated in Chapter 1. The inertness to molten Zn of SiAlON and SiAlON-BN could solve the problems related to strip vibrations around the gas knives section of the galvanising line. Furthermore, the results of static immersion testing conducted in this study confirmed that SiAlON and

its composites are suitable for use in baths containing both Zn-Al and Zn-Al-Mg, as changing bath composition did not affect the corrosion behaviour of these materials.

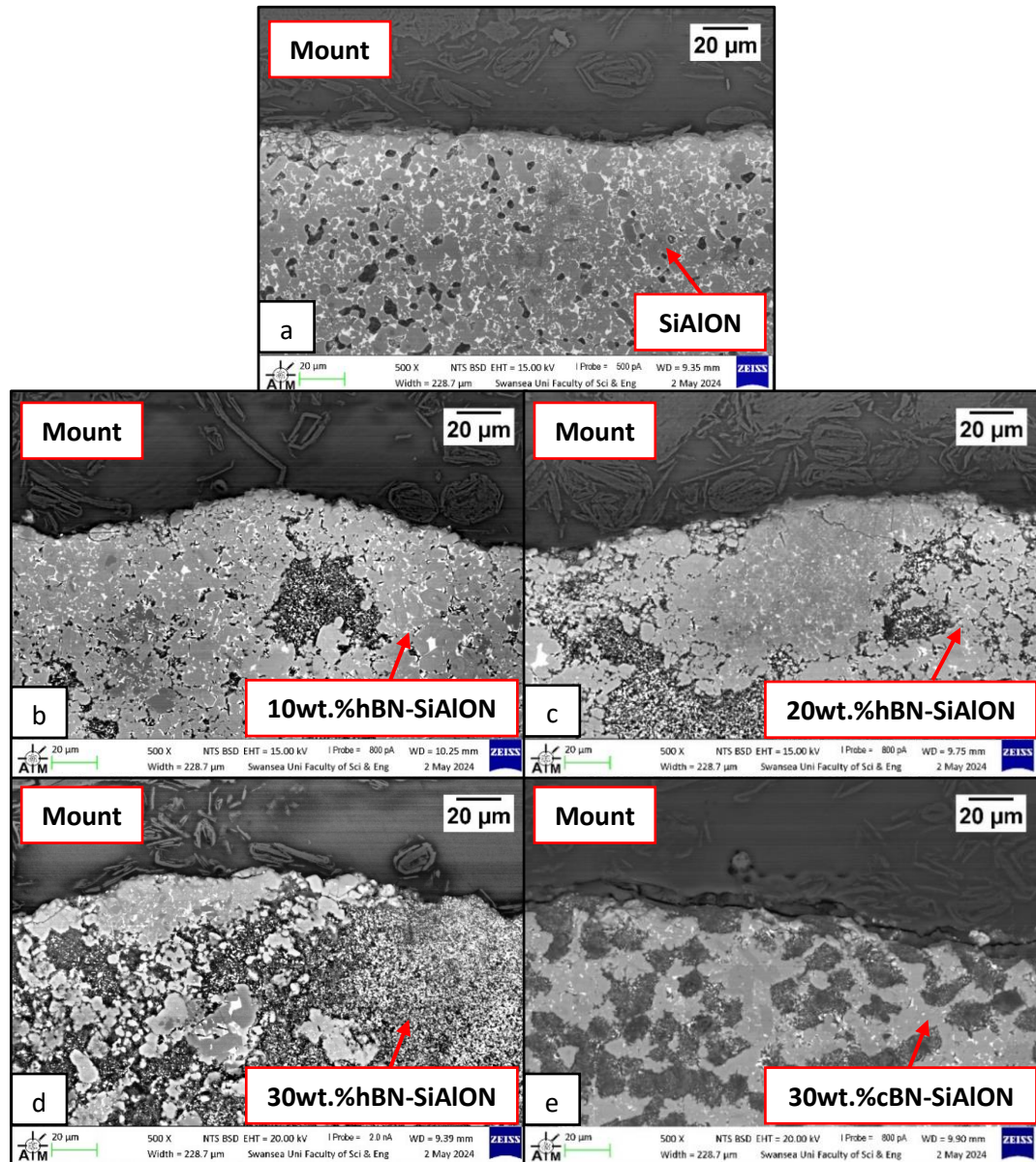


Figure 4.18 SEM cross-sections of the specimens prepared with FAST, namely SiAlON (a), 10wt.%hBN-SiAlON (b), 20wt.%hBN-SiAlON (c), 30wt.%hBN-SiAlON (d) and 30wt.%cBN-SiAlON (e), after immersion in Zn-Al.

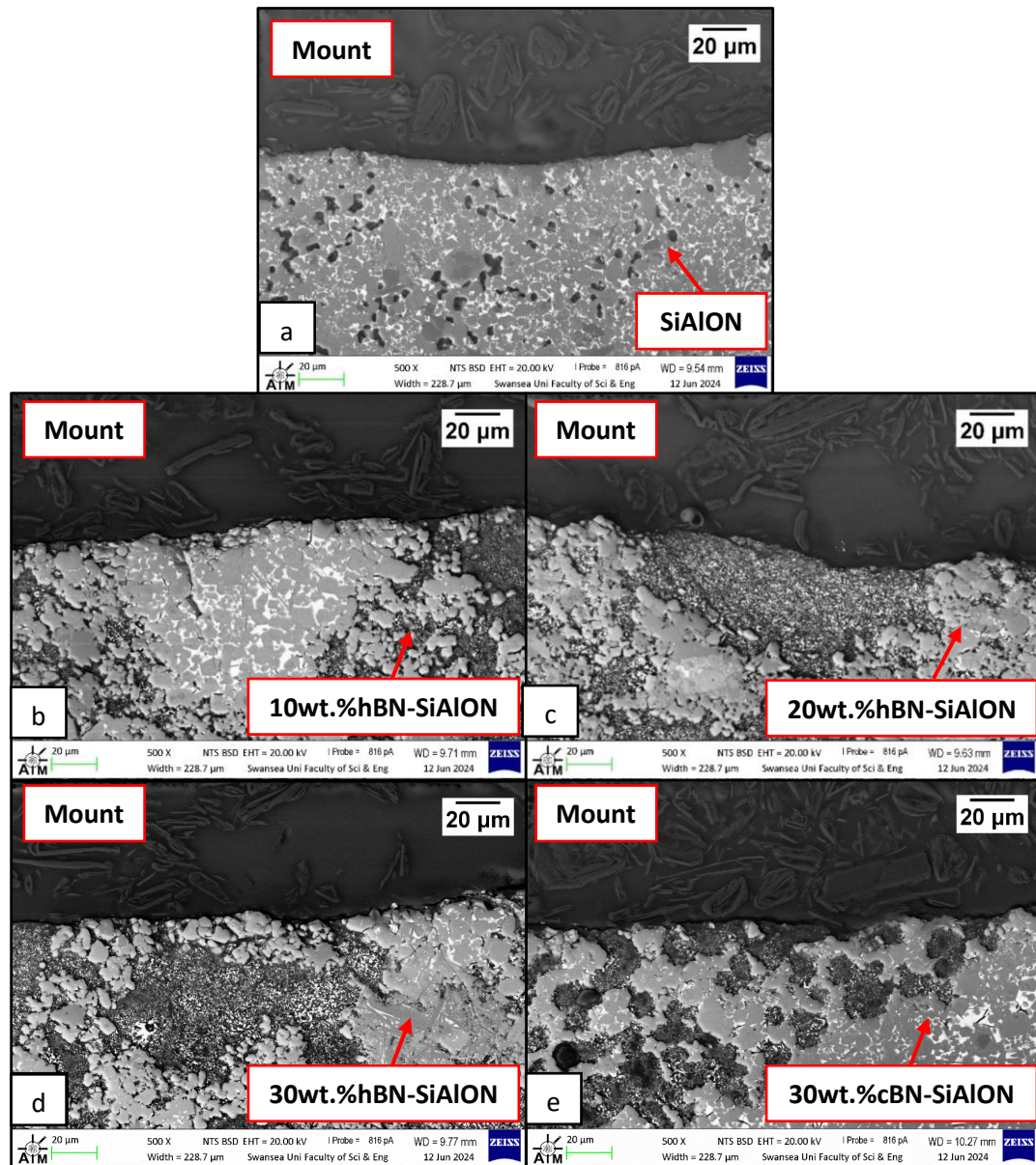


Figure 4.19 SEM cross-sections of the specimens prepared with FAST, namely SiAlON (a), 10wt.%hBN-SiAlON (b), 20wt.%hBN-SiAlON (c), 30wt.%hBN-SiAlON (d) and 30wt.%cBN-SiAlON (e), after immersion in Zn-Al-Mg.

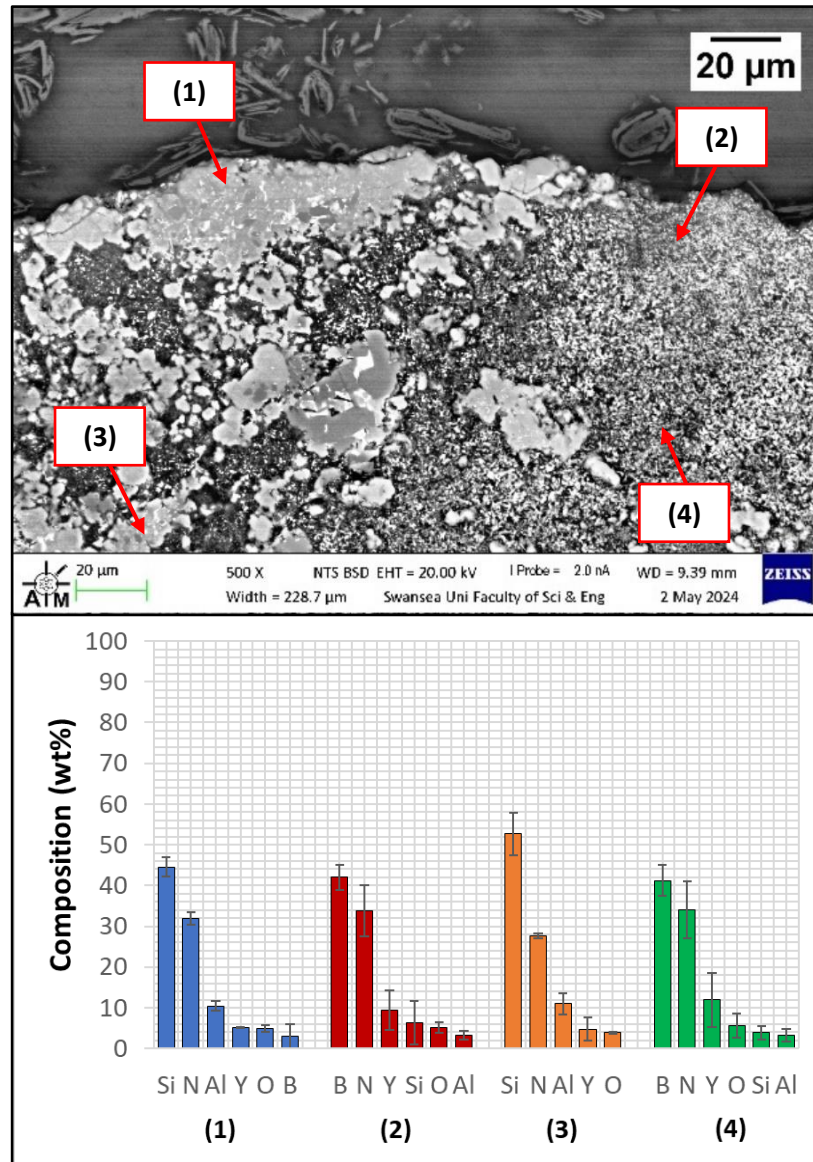


Figure 4.20 Results of EDS analysis on 30wt.%hBN-SiAlON, showing the average element composition of the SiAlON and BN rich phases at the interface (1, 2) and in the bulk of the material (3, 4), after exposure to Zn-Al.

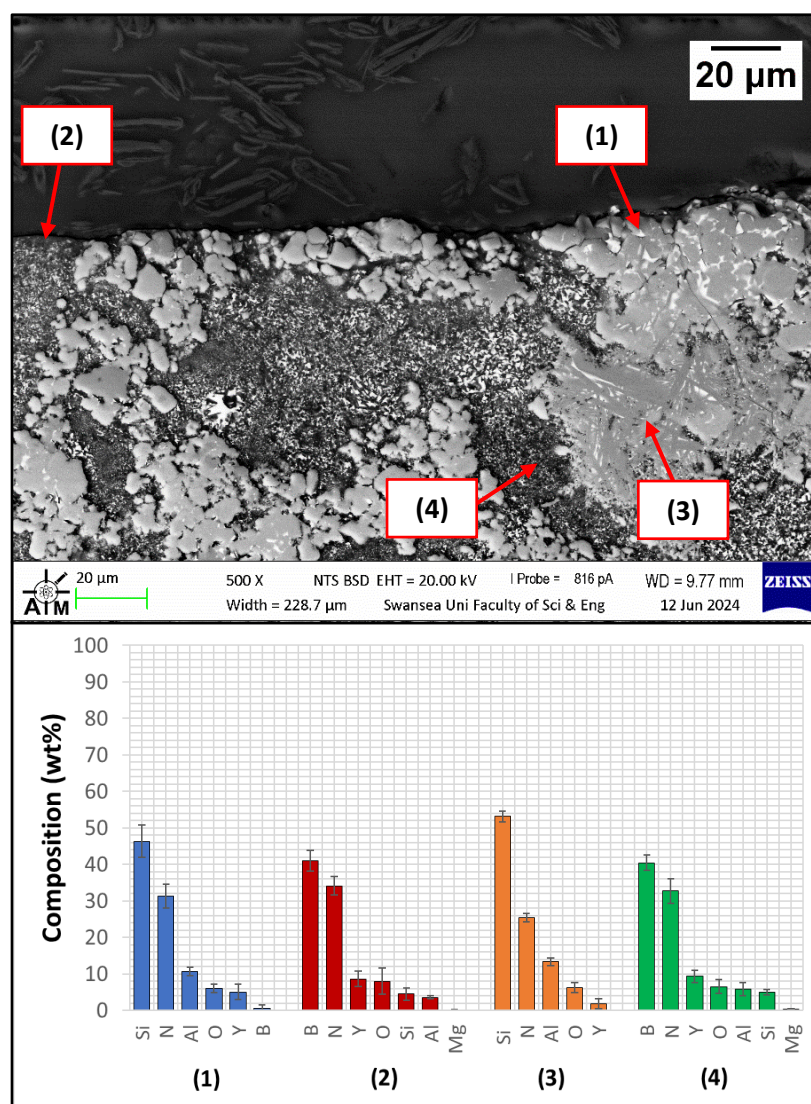


Figure 4.21 Results of EDS analysis on 30wt.%hBN-SiAlON, showing the average element composition of the SiAlON and BN rich phases at the interface (1, 2) and in the bulk of the material (3, 4), after exposure to Zn-Al-Mg.

4.1.8 Pin-on-Disc Wear Testing

The pin-on-disc tribometer discussed in Chapter 2, Section 2.3.2, was used to determine the COF of the SiAlON-BN composites prepared with FAST. The purpose of the experiment was to compare the tribological performance of pure SiAlON with that of SiAlON-hBN and SiAlON-cBN and to understand whether adding hBN enabled to reduce friction with the counterpart during sliding contact. The 60 mm diameter specimens fabricated with FAST were used as the 'discs' for wear testing. The

rotations of the moving platform were set at 150 rpm, which corresponds to a sliding speed of 9.42 m/min, and the duration of sliding contact was extended to 1 hour. Like the previous experiments, the SiC ball bearing was pressed with a constant load of 2 N onto the rotating discs and the test was carried out under dry sliding conditions and at room temperature.

Curves of the measured COF of the five SiAlON-based specimens are shown in Figure 4.22. It is possible to notice that the COF followed a similar profile to those observed in the ceramics examined previously. The COF increases as sliding with the SiC pin is initiated; once a peak was reached, it started to decrease until it stabilises to steady-state values. The values reported in Table 4.6 refer to the average COF obtained in the last 10 minutes of sliding, when steady state conditions were observed in all the ceramics. The results of pin-on-disc testing showed that the five SiAlON-based specimens displayed a similar COF during steady-state regime. Although the experiments discussed in the previous chapter demonstrated that hBN is a lubricious material, adding hBN to SiAlON did not produce an improvement of the tribological properties of the material, as the COF of SiAlON-hBN was similar to that obtained for the pure SiAlON and SiAlON-cBN specimens. The maximum COF was measured on the 30wt.%hBN-SiAlON specimen (0.60 ± 0.01), which was slightly higher than the COF of pure SiAlON (0.55 ± 0.01). Furthermore, Figure 4.22 shows that the COF curves of 20wt.%hBN-SiAlON (red curve) and 30wt.%cBN-SiAlON (orange curve) are below that of SiAlON (green curve) during the initial stages of sliding; however, the measured COF is still high.

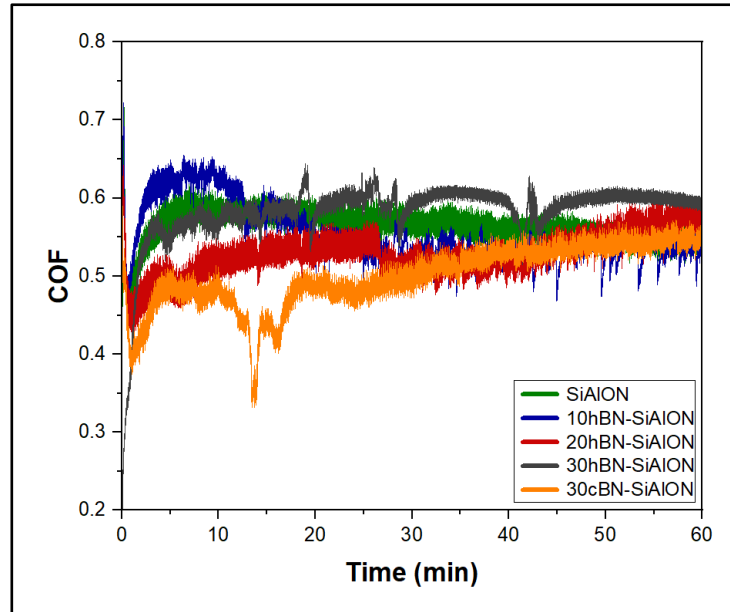


Figure 4.22 COF curves of the SiAlON and SiAlON-BN specimens prepared with FAST.

Table 4.6 COF of the SiAlON and SiAlON-BN specimens during steady-stage regime.

Material	COF
SiAlON	0.55±0.01
10wt.%hBN-SiAlON	0.53±0.01
20wt.%hBN-SiAlON	0.56±0.02
30wt.%hBN-SiAlON	0.60±0.01
30wt.%cBN-SiAlON	0.54±0.01

It is evident that the inclusion of hBN did not drastically lower the COF of SiAlON. This is in contrast to the findings reported in other studies, which concluded that hBN additions improved the tribological properties of ceramic materials, as discussed in Section 4.1.1. In addition to this, these studies demonstrated that the hBN content is critical for it to act as a solid lubricant. When small quantities of hBN are present, flakes are released continuously and hBN particles are, subsequently, crushed by the pin into smaller flakes, which fills the pores, cracks and grooves of the material, leading to a reduction of the COF. If the hBN exceeds a 'critical value', the mechanical properties of the material deteriorate due to the soft nature of hBN, which in some cases resulted in an increase of the COF (Carrapichano et al., 2002; Zhao et al., 2018). This observation can explain why none of the compositions investigated in this work enabled to significantly reduce the COF of SiAlON. Moreover, the poor homogeneity

of the materials discussed earlier may have affected the tribological properties of the materials, since there are regions where the BN phase is absent, as shown in Figure 4.11.

Additions of cBN, on the other hand, are not expected to result in a loss of mechanical properties due to the hard nature of the cubic phase. The COF of 30wt.%cBN-SiAlON was found to be slightly lower than the other materials during the initial stages of sliding and this can be related to the thermal conductivity of the material relative to pure SiAlON. The thermal conductivity of cBN at room temperature is approximately 13 W/cm.K, meaning that the thermal conductivity of the material is very high and it is second only to diamond. Materials with high thermal conductivity are known to dissipate heat better and this typically results in a lower COF (Berger, 2020; Stachowiak & Batchelor, 2013).

4.1.9 Summary of SiAlON-BN Composites

SiAlON and SiAlON-BN composites were prepared using FAST and the corrosion behaviour of these materials was investigated by conducting static immersion tests in liquid Zn-Al and Zn-Al-Mg for five weeks. Material characterisation after testing revealed that changing bath composition had no effect on the performance of the materials in molten metal. The SiAlON and SiAlON-BN ceramics remained completely inert to molten metal after five weeks of exposure. No corrosion products were identified on the materials, showing superior performance compared to materials such as SS 316L, which have been reported to be severely attacked by Zn alloy. The results of pin-on-disc wear testing showed that the COF of SiAlON and SiAlON-BN is similar during steady-state regime and that the additions of hexagonal BN did not produce significant changes to the COF.

Based on the observations made from the static immersion tests, it is possible to conclude that SiAlON and SiAlON-BN can be used as materials for developing galvanising pot roll bearings with extended service life, alongside the ceramics investigated in Chapter 3. It was previously mentioned that, in order to overcome the problem of brittleness, coatings are preferred compared to sintered bulk ceramics.

Although steel reacts with liquid Zn alloy, it is more ductile and if it is protected by a thin layer of inert ceramic material, the formation of corrosion products detrimental to the bearing service life can be prevented. For this reason, experiments were conducted to investigate the properties of ceramic coatings. It was decided to choose Al_2O_3 as the coating material, due to its wear and chemical resistance, as well as the known difficulties in thermal spraying nitride ceramics (Shahien, 2018). In addition to this, a local supplier with expertise in developing thermal spray coatings of Al_2O_3 was found.

4.2 Al_2O_3 Coatings

4.2.1 Introduction

Various coatings have been examined as a method for developing bearings with extended durability. For example, thermal sprayed coatings consisting of WC particles embedded in a Co-based matrix have been applied to the bearings to enhance their wear resistance (Shi et al., 2018; Zhang et al., 2004). However, it was previously shown that these coatings were affected by thickness reduction, suggesting that WC-Co was deteriorated in molten metal. Degraded coatings can affect the lifetime of the bearings if they can no longer shield the underlying material from the attack of liquid Zn. Therefore, it is clear that chemical inertness is a requirement for developing coatings offering protection to bearing materials, such as steels, which are known to be corroded in the galvanising bath.

Ceramic materials show promise due to their inertness in molten metal, which was verified by the findings obtained so far in this study. Al_2O_3 was previously tested as sintered bulk ceramic and was found to remain completely unreactive in Zn-Al and Zn-Al-Mg after five weeks of exposure. Moreover, Al_2O_3 was observed to remain unreactive even when used as a coating, in Zn baths with Al content below 0.14wt.%. The ceramic was applied via thermal spraying and was reported to have good bonding with stainless steel (Nag et al., 2021). At present, no information exists regarding the behaviour of Al_2O_3 coatings in baths containing Zn-Al-Mg and the performance of

ceramic coatings may be different from that observed in sintered bulk ceramics. Therefore, this section analyses the performance of Al_2O_3 coatings applied to SS 316L via HVOF technology (Chapter 1, Section 1.9.2), in galvanising baths containing Zn-Al and Zn-Al-Mg. The corrosion behaviour was compared with uncoated SS 316L to determine whether it can offer protection to stainless steel from the attack of liquid metal. To achieve this, the coating must remain unreactive in molten metal and act as a barrier against diffusion of molten Zn alloy into steel. In addition to this, the Al_2O_3 coatings were examined for structural integrity after exposure to molten metal at high temperatures. These investigations enabled to assess the potential of Al_2O_3 coatings for application in continuous galvanising lines. The findings presented in this section were published in the following paper:

- “ Al_2O_3 Coatings for Protection of Stainless Steel 316L against Corrosion in Zn-Al and Zn-Al-Mg”. In: *Coatings* 2024, 14(5), 606. DOI: 10.3390/coatings14050606.

4.2.2 Material Characterisation Before Testing

The specimens used in this study consisted of 20 mm × 20 mm × 5 mm plates of SS 316L, which were coated with a 250 µm thick Al_2O_3 layer. The coating was applied via the HVOF thermal spray process, which was carried out by Engineered Performance Coatings (Cardiff, UK). SEM images of the as-received Al_2O_3 coating obtained with the BSD detector are shown in Figure 4.23. The cross-section of the specimen (Figure 4.23a) shows a dark grey phase, which is the ceramic coating, and a light grey phase, which is the SS 316L substrate. A high-magnification image of the surface of the Al_2O_3 coating is illustrated in Figure 4.23b, showing the presence of pores in the as-received coatings. EDS was performed on the surface of the Al_2O_3 and on the SS 316L substrate to identify the elements present in the specimen. The analysis revealed that only Al and O were present, as expected. The content of Al and O was approximately 57 ± 0.5 wt.% and 43 ± 0.4 wt.%, respectively, which corresponded to approximately 40 mol% for Al and 60 mol% for O; therefore, the results of EDS agreed with the expected stoichiometry. The average composition of the coating and of the SS 316L substrate

is shown in Figure 4.24. X-ray diffraction patterns of the as-received Al_2O_3 coatings (Figure 4.25) allowed the identification of the phases present in the ceramic. The diffractogram showed that the majority of the peaks corresponded to hexagonal aluminium oxide (corundum); however, several peaks revealed the presence of cubic aluminium oxide ($\text{Al}_{2.66}\text{O}_4$). There are several variants of aluminium oxide (Huang, Qiu, et al., 2023), and this phase is one of the known transition phases, which is characterised by a face-centred cubic crystal (fcc) structure as opposed to the stable phase with a hexagonal close-packed (hcp) structure (Kaunisto et al., 2023). Other studies identified the cubic phase in Al_2O_3 coatings and attributed its presence to the faster cooling of the Al_2O_3 particles hitting the target substrate during the thermal spray process (Nag et al., 2021).

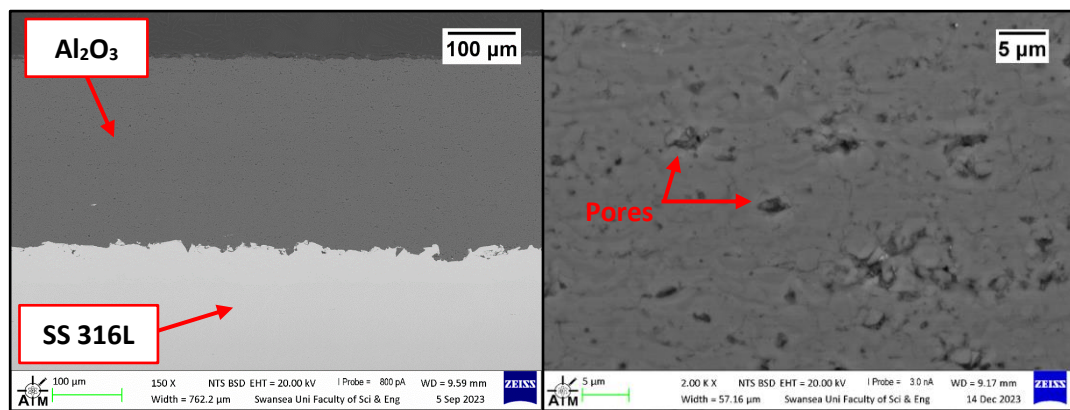


Figure 4.23 As-received specimen (a); details of pores in the Al_2O_3 coating (b).

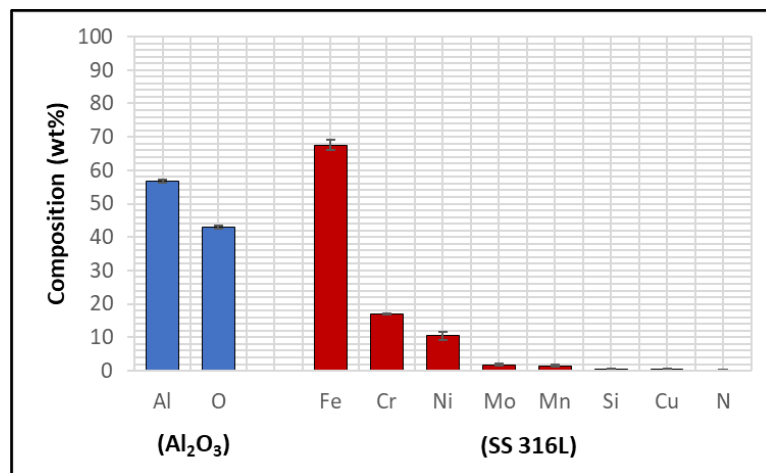


Figure 4.24 EDS average elemental composition of the as-received specimens.

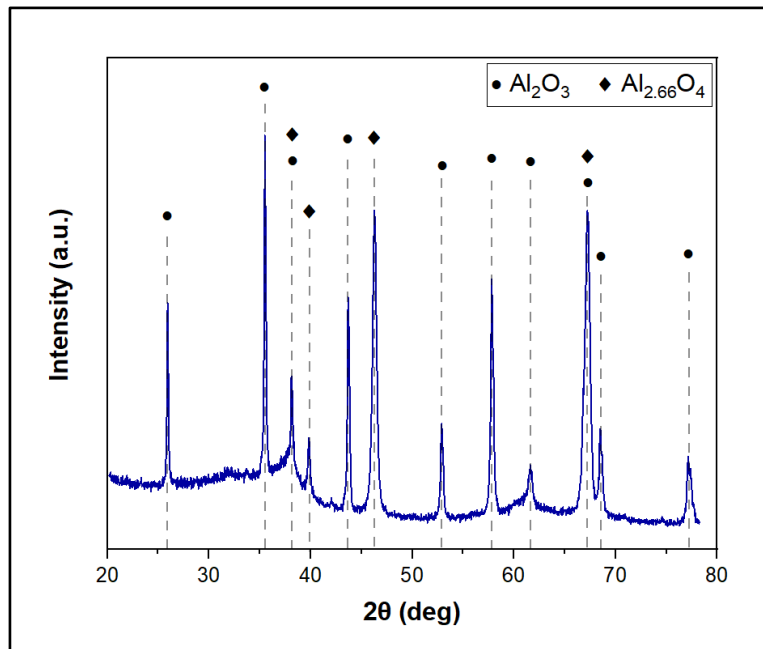


Figure 4. 25 X-ray diffraction patterns for the as-received Al_2O_3 coatings.

4.2.3 Static Immersion Testing

4.2.3.1 Zn-Al Bath

The procedures followed for static dip testing of the coatings were previously outlined in Chapter 1, Section 2.4.1. The Al_2O_3 coatings were immersed in Zn-Al and Zn-Al-Mg for five weeks and they were extracted from the molten metal bath after 1 week intervals. The SEM images of the coatings shown in Figure 4.26a-b and Figure 4.26c-d were captured after 1 week and 3 weeks of testing, respectively. All the tested specimens analysed in this study were characterised by cracks that developed in the ceramic coating. Horizontal cracks started to form during the early stages of testing, as they were observed in the images captured after 1 week of exposure to molten Zn-Al. Furthermore, fragments of the coatings detached from the specimen, resulting in localised spallation, as shown in Figure 4.26b. It is possible to observe that the coating spalled in the proximity of a horizontal crack, as indicated in the figure. The cracks observed in the Al_2O_3 coatings after static immersion testing were not present in the untested specimen, as shown in Figure 4.23. Therefore, they developed after

exposure to molten metal at high operating temperatures. Unlike the uncoated SS 316L specimen, no products of reactions between SS 316L and liquid Zn-Al were observed, suggesting that Al_2O_3 is capable of protecting the steel from the attack of liquid Zn-Al after 1 week of testing. Moreover, the Al_2O_3 coating was found to remain inert to liquid Zn-Al, as no reaction products accumulated at the interface between the ceramic and the molten metal. However, the presence of cracks in the Al_2O_3 coating could be detrimental to the performance of the materials in liquid Zn alloy if Zn infiltration through these cracks and subsequent reaction with SS 316L occurred.

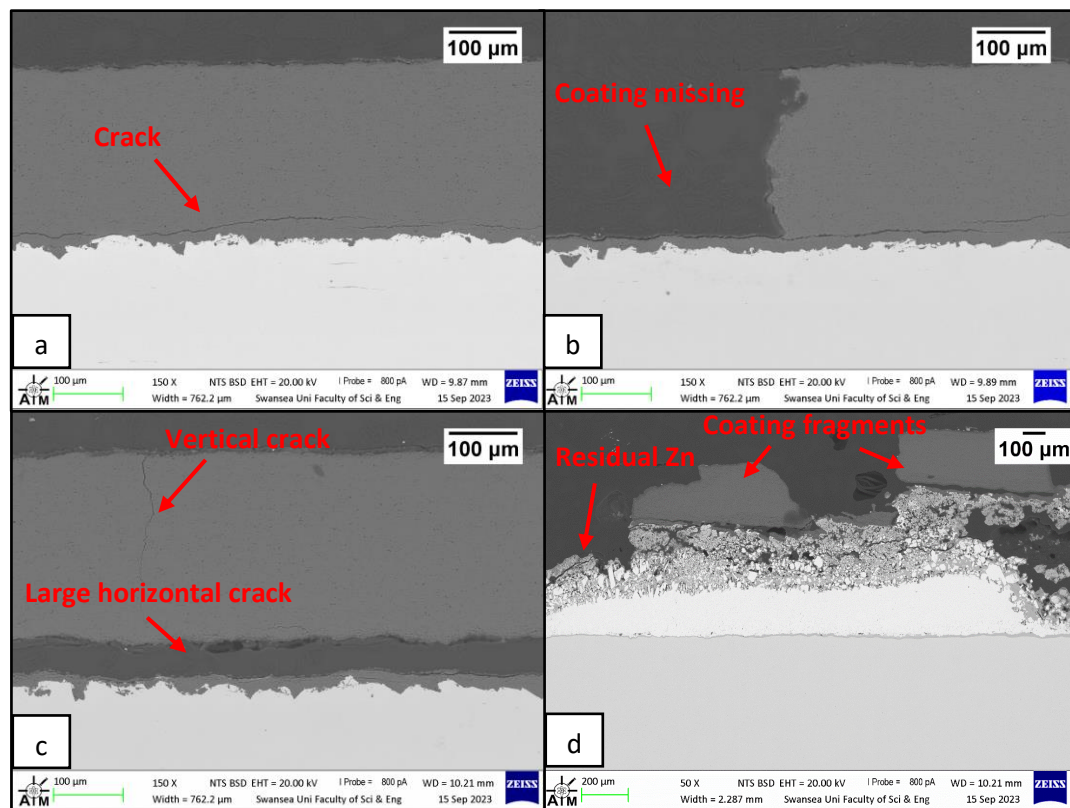


Figure 4.26 Cross-sections of Al_2O_3 coated SS 316L after 1 week (a, b) and 3 weeks (c, d) of static immersion testing in Zn-Al.

After 3 weeks of testing in Zn-Al, severe coating degradation occurred. Both horizontal cracks and vertical cracks were observed in the ceramic coating. The large horizontal crack observed in Figure 4.26c shows that most of the coating detached from the steel substrate, leaving the surface of the steel protected only by a thin ($\sim 20\ \mu\text{m}$) layer of Al_2O_3 , which again prevented the formation of corrosion products on the steel. Figure

4.26d shows that the breakdown of the Al_2O_3 coating occurred, as fragments of the coatings were observed in the SEM image. The bright phase detected between the coating fragments and the steel was residual Zn-Al, which solidified upon removal of the specimen from the molten metal bath; its presence suggested that liquid Zn-Al reached the surface of the steel specimen, causing it to be exposed to molten metal. As a result, a reaction layer developed (Figure 4.27a) in a similar fashion to that seen on the uncoated SS 316L specimen previously discussed (Chapter 3, Figure 3.20a). EDS phase elemental analysis (Figure 4.27b) revealed that the diffusion layer mainly contained Al (41 ± 0.6 wt.%), Fe (29.7 ± 1.1 wt.%) and Zn (19.9 ± 1 wt.%), and its composition was similar to that observed previously in the uncoated SS 316L specimen (Chapter 3, Figure 3.20 b).

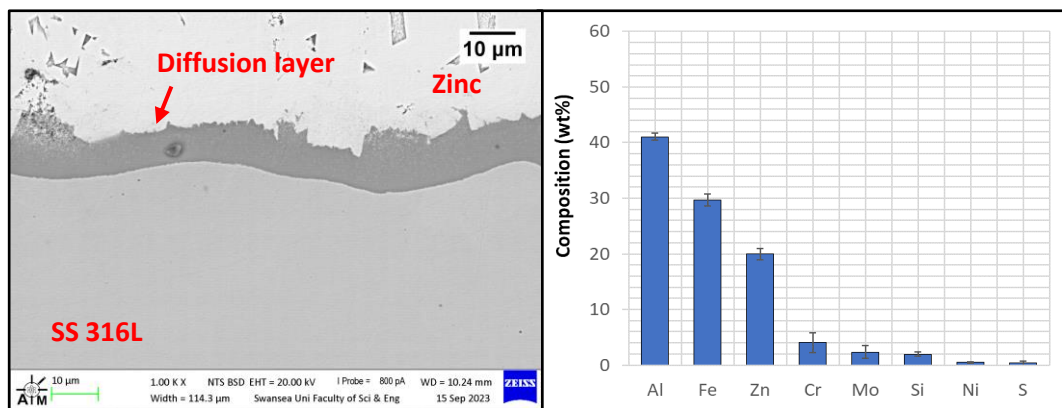


Figure 4.27 Details of the diffusion layer observed after the breakdown of the Al_2O_3 coating and subsequent contact with Zn-Al (a); EDS phase elemental analysis of the diffusion layer (b).

4.2.3.2 Zn-Al-Mg Bath

The SEM images shown in Figure 4.28 were captured after 4 weeks of immersion in Zn-Al-Mg. Some similarities were observed with the specimens immersed in Zn-Al, such as spallation and breakdown of the coatings (Figure 4.28a), as well as the presence of cracks (Figure 4.28b). It is evident from Figure 4.28b-c that the liquid Zn alloy penetrated through cracks that formed in the coating. Moreover, contact occurred between the steel and the molten metal, as observed in the specimens immersed in Zn-Al. This contact was facilitated by the spallation of the Al_2O_3 coating,

which exposed SS 316L to the attack of the liquid Zn-Al-Mg. Consequently, corrosion products are formed on the surface of SS 316L. However, further degradation was detected on the coatings immersed in the Zn-Al-Mg bath.

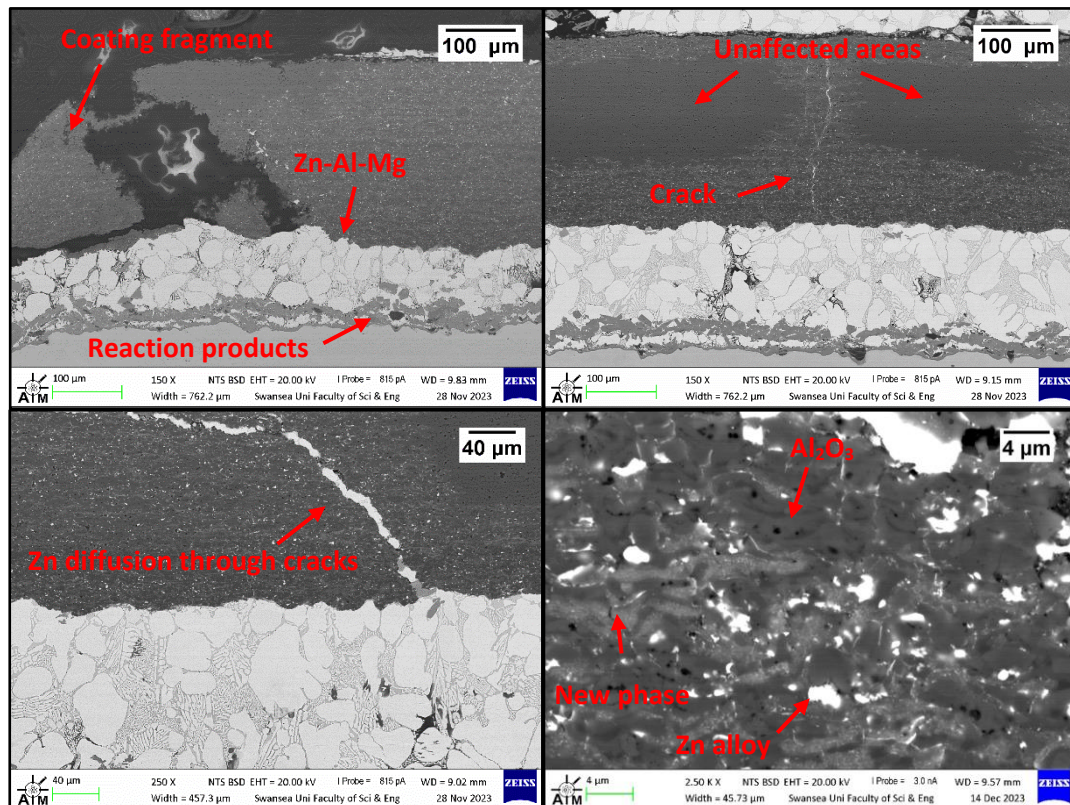


Figure 4.28 Cross-sections of the Al_2O_3 coatings after 4 weeks of immersion in Zn-Al-Mg: spallation of the coating (a); details of cracks and areas of the coating affected by degradation in molten metal (b); Zn diffusion through cracks (c); details of the three phases (d).

Figure 4.28 shows that certain regions of the coatings deteriorated in molten metal, whereas other areas remained unaffected (Figure 4.28b). These areas were identified in the proximity of the surfaces where contact with Zn occurred, as well as near cracks where liquid Zn alloy permeated, suggesting that the Al_2O_3 coatings interacted with the molten Zn-Al-Mg. The details of these interactions are shown in Figure 4.28d, and the SEM image showed three phases: a bright phase, which was the Zn that penetrated through pores and cracks present in the coating; a dark grey phase, which was the Al_2O_3 in the coating; a light grey phase, which was a new phase as it was

absent in the as-received Al_2O_3 coating (Figure 4.23). In addition to this, the new phase was absent in all the coatings tested in the Zn-Al bath. Therefore, its formation is likely to be related to the presence of Mg in the Zn-Al-Mg bath.

To confirm this, EDS mapping was performed in the regions of the coatings where the new phase was detected, and the results are shown in Figure 4.29. It was observed that some areas of the coating were rich in Mg; these areas corresponded to the new phase. Moreover, the analysis showed that the new phase was low in Al, suggesting that a reaction occurred with the molten metal bath. It is postulated that Al_2O_3 was reduced by the Mg present in the bath, forming MgO in the coating. It is well known that Al_2O_3 can be reduced by Mg metal following the reaction $3\text{Mg} + \text{Al}_2\text{O}_3 = 2\text{Al} + 3\text{MgO}$. According to the Ellingham diagram, the free energy of the formation of Mg is more negative than Al at 465 °C, and the line for the $2\text{Mg} + \text{O}_2 = 2\text{MgO}$ reaction lies below the $4/3\text{Al} + \text{O}_2 = 2/3 \text{Al}_2\text{O}_3$ reaction (Liu et al., 2013; University of Cambridge, 2022; Zhang et al., 2022). This observation suggested that MgO formed in the coatings after submergence in Zn-Al-Mg and can explain the results obtained from the EDS analysis. The reduction of Al_2O_3 by molten Mg does not normally occur at low temperatures due to slow kinetics. However, the cracks and pores observed in this study may have provided 'diffusion channels' for Mg metal and led to an increase in the surface area of Al_2O_3 . As a result, the higher surface area is postulated to have improved the kinetics of the reduction reaction.

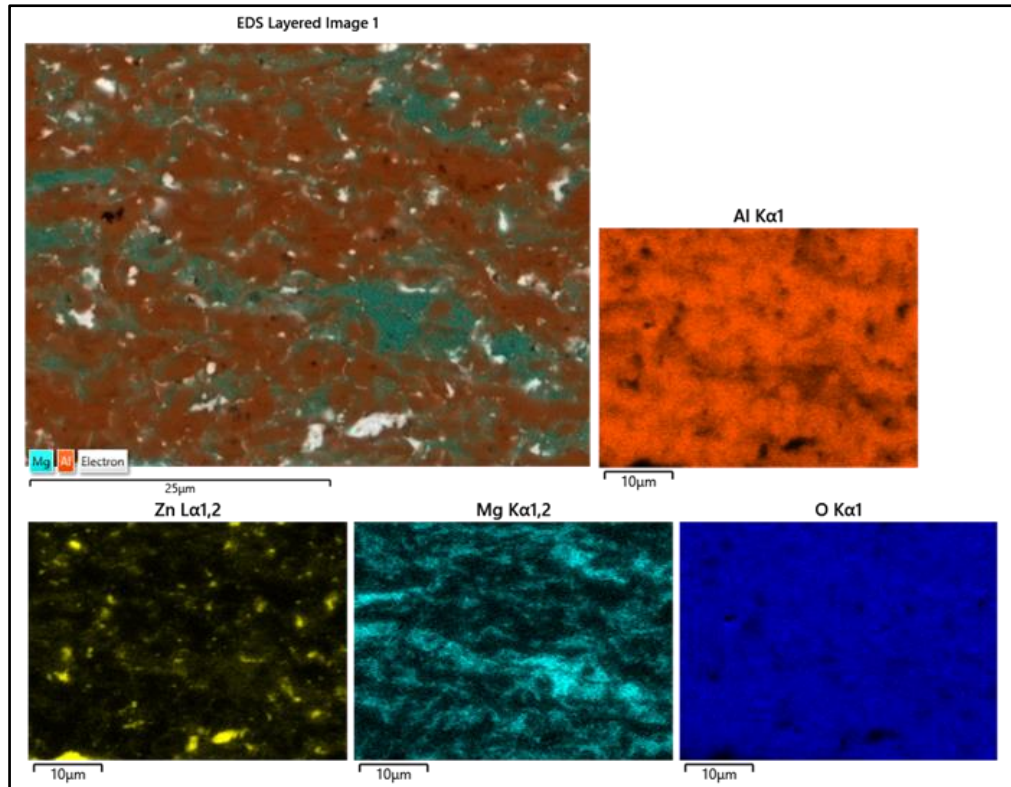


Figure 4.29 EDS maps of Al_2O_3 coating after immersion in Zn-Al-Mg.

4.2.4 Analysis of Coating Failure

The results of static immersion testing revealed that the Al_2O_3 coatings were damaged in the molten metal bath, even when no reactions between the ceramic and the liquid Zn alloy were observed, as shown in the specimens immersed in Zn-Al. Material characterisation of the coatings after exposure to molten metal at high temperatures has identified the presence of cracks that developed in the ceramic coating. The formation of cracks in ceramic and cermet coatings after exposure to high temperatures was reported in other studies in the literature (Dong et al., 2006; Hiroaki Mizuno & Junya Kitamura, 2007; Noda et al., 2008; Wang et al., 2019). In addition to this, cracking was linked to stress generated between materials with dissimilar CTE values (Huang, Qiu, et al., 2023; Huang, Zhang, et al., 2023). Therefore, the cause for the development of cracks was attributed to the thermal expansion mismatch between the coating and substrate materials, which resulted in the formation of stresses responsible for inducing the cracking.

In this study, dilatometry was performed to measure the CTE of Al_2O_3 and SS 316L at a temperature analogous to that of each Zn bath used for the static tests (Figure 4.30). The CTEs recorded at $\sim 465^\circ\text{C}$ for Al_2O_3 and SS 316L were 8.2×10^{-6} and $21.2 \times 10^{-6} \text{ K}^{-1}$, respectively, suggesting that the steel substrate expanded more than the Al_2O_3 coating due to its higher CTE. The difference in CTE of $13 \times 10^{-6} \text{ K}^{-1}$ between the two materials caused a thermal expansion mismatch and generated tensile stresses, which probably made the ceramic coating prone to vertical cracking. In addition to this, the larger expansion of the steel substrate relative to the ceramic coating resulted in horizontal cracks near the interface between Al_2O_3 and SS 316L, triggering the delamination effects previously discussed.

SEM images of the coatings showed that a breakdown of the coating occurred, and a possible failure mechanism was identified (Figure 4.31). As the specimens were immersed in the molten metal bath, contact with liquid Zn alloy occurred. Due to the high temperature and the large difference between the CTE of the substrate and coating material, cracks started to develop in the Al_2O_3 coating. These cracks acted as 'channels' for liquid Zn alloy to diffuse in the ceramic coating and to reach the underlying steel substrate. When the steel became exposed to the attack of liquid Zn alloy, corrosion products started to form below the coating. The accumulation of these reaction products led to the generation of stresses, and the coating was forced to detach, as illustrated in Figure 4.26d. This potential failure mechanism was observed in other studies which investigated the performance of ceramic coatings in liquid Zn, such in Wang et al. (2019).

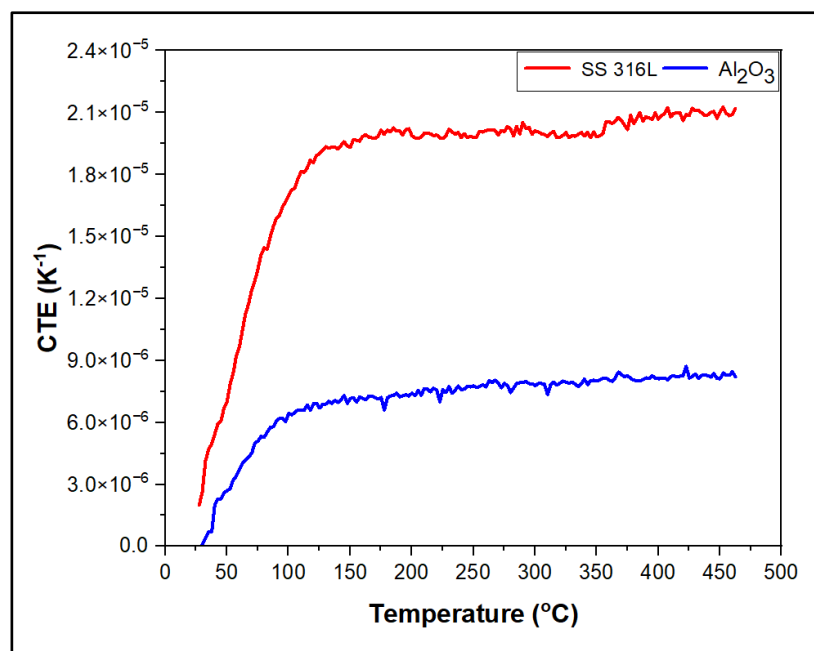


Figure 4.30 CTE of SS 316L and Al₂O₃ as a function of temperature in the range of 35–465 °C.

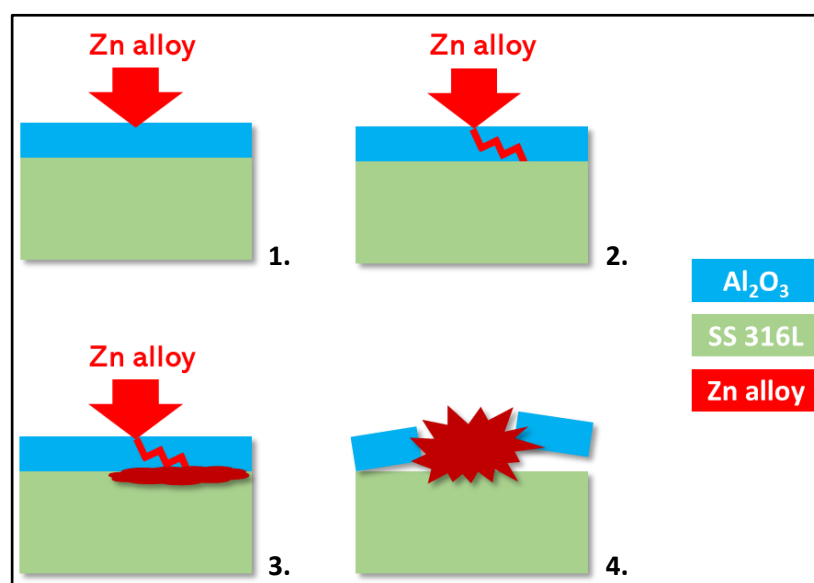


Figure 4.31 Failure process of the Al₂O₃ coatings after exposure to molten metal at high temperature.

It was previously shown that the Al₂O₃ coatings remained inert in liquid Zn-Al and shielded SS 316L from the attack of molten metal until coating breakdown occurred. Therefore, they have the potential to increase the service life of the bearings beyond the current five-week campaign for the production of Zn-Al coatings. However,

optimisation of the ceramic coatings/substrate system is required to prevent cracking and breakdown. Several solutions were identified to minimise the thermal expansion mismatch:

1. Replacing the substrate or coating material, or both, to reduce the difference between the CTE values. The substrate used in this work was made of SS 316L, which is known to be more corrosion resistant than other steel grades and it has previously been used for making the pot rolls in CG lines. However, other grades, such as the 400 series ferritic and martensitic stainless steels have a lower thermal expansion compared to austenitic 316L (Matthews & James, 2010). Moreover, among the ceramics investigated in this work, there are materials with higher CTE compared to Al_2O_3 . For example, 3YSZ was reported to have a CTE of approximately $10 \times 10^{-6} \text{ K}^{-1}$ at 465 °C (Hayashi et al., 2005).
2. Reducing the thickness of the coating. There is evidence that coating thickness plays an important role in determining the coating ductility. Thick coatings are known to spall more easily and, therefore, lowering the thickness can prevent cracking and spallation. However, as the thickness decreases, the level of interconnected porosity increases (Matthews & James, 2010). For this reason, trials should be conducted to determine acceptable limits on the coating thickness.
3. Multilayer and composition gradient coatings. The introduction of one or more materials between the ceramic and the steel, with intermediate CTEs will enable to achieve a more gradual transition in thermal expansion properties, which can reduce the mismatch as well as the risk of cracking. Some studies developed composition gradient coatings where the ratio of ceramic-to-metallic material is varied from the metallic-rich substrate to the ceramic-rich coating to achieve a better gradient transition (Dong et al., 2006; Matthews & James, 2010; H. Mizuno & J. Kitamura, 2007).

4.2.5 Summary of Al₂O₃ Coatings

In this work, Al₂O₃ coatings were deposited onto SS 316L to shield the steel from the attack of liquid Zn. Static testing was conducted to compare the performance of the Al₂O₃ coatings against that of as-received SS 316L specimens. The corrosion behaviour of the coatings was studied after exposure to Zn-Al and Zn-Al-Mg galvanising baths. It was concluded that the Al₂O₃ coatings were damaged following exposure to molten metal at high temperatures.

The difference between the CTEs of Al₂O₃ and SS 316L was approximately $13 \times 10^{-6} \text{ K}^{-1}$ and led to stress-induced cracking, which would be detrimental to the service life of the bearings, as they provided paths for the liquid Zn alloy to permeate and react with SS 316L. As a result, spallation and breakdown of the Al₂O₃ coatings occurred. Unlike SS 316L, the Al₂O₃ coatings showed excellent corrosion resistance after immersion in Zn-Al; however, examination of the coatings immersed in Zn-Al-Mg revealed possible interactions with the molten metal bath due to the reduction of Al₂O₃ by molten Mg. Therefore, the use of bearings coated with Al₂O₃ should be limited to hot-dip galvanising baths containing Zn-Al composition in order to avoid coating degradation and the risk of incurring frequent line stops.

The resistance of the Al₂O₃ coatings to damage by the molten Zn alloy baths holds promise that ceramic coatings can be used in the development of new bearing coatings for galvanising, although the tendency of the coating to fail due to the mismatched CTEs of the coating and the underlying substrate requires further investigation of an optimal coating/substrate coupling to be undertaken.

Chapter 5

Dynamic Testing of Materials in Zn Alloy

5.1 Introduction

The corrosion behaviour of the materials tested so far has been examined by conducting static immersion tests in liquid Zn. However, as previously explained in Chapter 1, Section 1.8.4, the behaviour of materials with the industrial molten metal bath under dynamic condition could differ from that observed during static testing. In the dynamic situation, the pot furniture material experiences chemical attack from the liquid metal and dynamic wear due to the sliding of bearing material under stress. To simulate the operation of the bearings in the hot-dip galvanising bath, dynamic testing was conducted using a bespoke wear testing rig, which was discussed in Chapter 2, Section 2.4.2.2. The dynamic test specimens were in the form of a rotating round bar and a static pad of similar or dissimilar material, depending on the aims of the test. The bar and pad samples were submerged in the Zn bath to determine the corrosion behaviour of the materials. Moreover, the rig allowed to assess the tribological performance of a material pair at conditions similar to those observed on the line and, therefore, more valuable information can be obtained compared to tests involving dry sliding contact, such as pin-on-disc testing.

This section of the thesis focuses on analysing the performance of three different pair materials by conducting dynamic tests in Zn-Al and Zn-Al-Mg. The first test involved using a Wallex6™ bar coated with HVOF WC-Co and an uncoated Wallex6™ pad. This material pair is found in the bearings of the pot rolls used in ZODIAC and, for this reason, its performance was used as the benchmark. The second pair replaced the pad material with Wallex4™ and, following the work conducted by Faulkner (2020), it could be a potential upgrade to the bearing system currently used in the ZODIAC CG line. The third pair involved using a SS 316L bar coated with HVOF Al₂O₃ and a Wallex6™ pad. Throughout Chapter 1, the benefits of introducing ceramic materials

in pot roll bearings systems were comprehensively discussed and experiments were conducted earlier to study the interactions of Al_2O_3 with Zn alloy. However, so far the performance of Al_2O_3 was investigated based on the results of static testing only. The details of the materials experimented in this chapter are summarised in Table 5.1. The content of this chapter was included in a paper entitled “Dynamic Testing of Materials for Galvanising Pot Roll Bearings with Improved Performance”, which is currently under review for publication.

Table 5.1 Material combinations chosen for dynamic testing.

Material pair no.	Bar	Pad
1	Wallex6 TM coated with HVOF WC-Co	Wallex6 TM
2	Wallex6 TM coated with HVOF WC-Co	Wallex4 TM
3	SS 316L coated with HVOF Al_2O_3	Wallex6 TM

5.2 Characterisation of As-received Samples

Images were taken on the as-received samples to illustrate the microstructures of materials before exposure to Zn-Al and Zn-Al-Mg. Cross-sections were captured on as-received WC-Co/Wallex6TM and Al_2O_3 /SS 316L bar specimens (Figure 5.1). The as-received pad specimens, namely Wallex6TM and Wallex4TM, are shown in Figure 5.2.

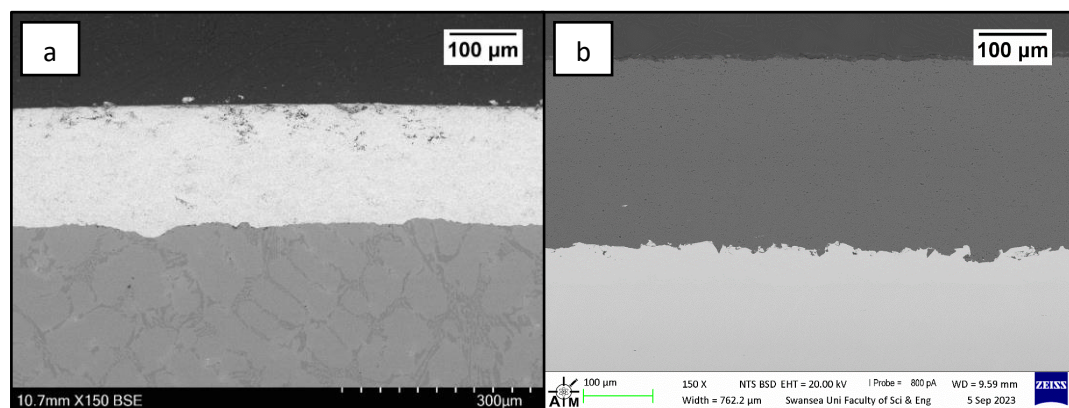


Figure 5.1 Cross-sections of WC-Co/Wallex6TM (a) and Al_2O_3 /SS 316L (b).

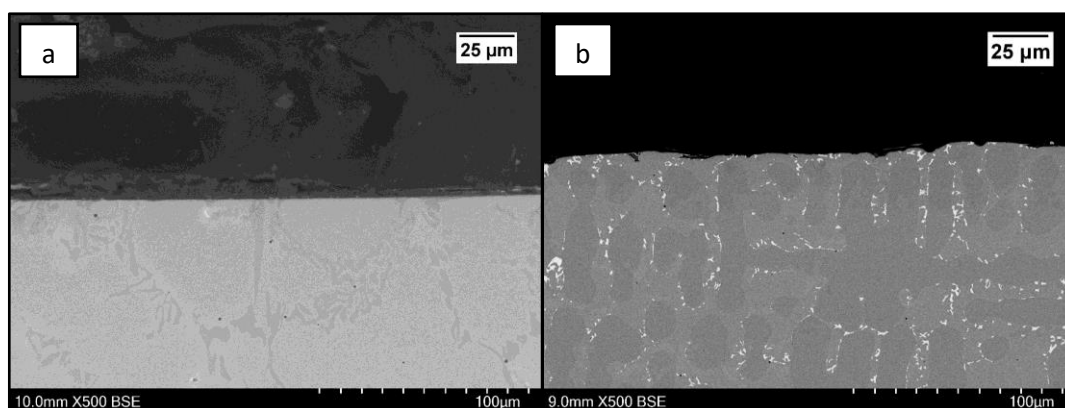


Figure 5.2 Cross-sections of Wallex6™ (a) and Wallex4™ (b) pad specimens.

The materials tested in the previous experiments were characterised earlier in this study. Microstructural examinations of Wallex6™ and Al₂O₃/SS 316L are respectively found in Chapter 3, Section 3.2.1 and Chapter 4, Section 4.2.2. This section focuses on describing the microstructure of Wallex4™, which was not tested in any of the previous experiments.

The composition of Wallex4™ provided by the supplier is shown in Table 5.2 and the microstructure of the material is illustrated in Figure 5.3a. The SEM image showed the presence of three regions, which corresponded to three different phases. EDS analysis was conducted to determine the composition of these phases and is shown in Figure 5.3b. EDS revealed the presence of a dark grey phase (1), which is a solid solution matrix phase containing Co (56.1 ± 0.4 wt.%), Cr (27.8 ± 0.2 wt.%), W (11.8 ± 0.2 wt.%), Ni (2.7 ± 0.2 wt.%) and Fe (1.6 ± 0.1 wt.%). In addition to this, Figure 5.3a shows the presence of two eutectic phases. The bright phase (2) is made of W (57.0 ± 0.7 wt.%), Co (23.0 ± 0.7 wt.%), Cr (18.8 ± 0.2 wt.%), Ni (0.8 ± 0.0 wt.%) and Fe (1.3 ± 0.1 wt.%), whereas the light grey phase (3) contains Co (44.9 ± 3.6 wt.%), Cr (34.9 ± 2.7 wt.%), W (17.1 ± 1.1 wt.%), Ni (1.8 ± 0.1 wt.%) and Fe (1.3 ± 0.1 wt.%). It was observed that the bright eutectic phase has a greater portion of W compared to the Co-rich matrix; in addition to this, the composition of the dark grey phase is similar to that of the matrix, with greater Cr and W content. The composition does not significantly differ from Wallex6™ (Table 3.2); however, Wallex4™ was found to have lower Co content (47.2 wt.%) and higher W additions (14.3 wt.%) compared to Wallex6™, which contained Co (59.1 wt.%) and W (3.8 wt.%). In addition to this, Wallex4™ is a cheaper

option compared to Wallex6™: Wallex4™ samples were purchased for £64.82 per unit and Wallex6™ samples were purchased for £126.40 per unit. Therefore, the cost of Wallex4™ was half the price required for procuring Wallex6™ samples of the same dimensions.

Table 5.2 Wallex4™ alloy composition provided by the supplier.

Material	%Fe	%Cr	%Ni	%Mn	%Si	%Co	%C	%W	%Mo
Wallex4™	1.7	30.4	2.6	0.6	0.8	BAL	0.9	14.3	1.5

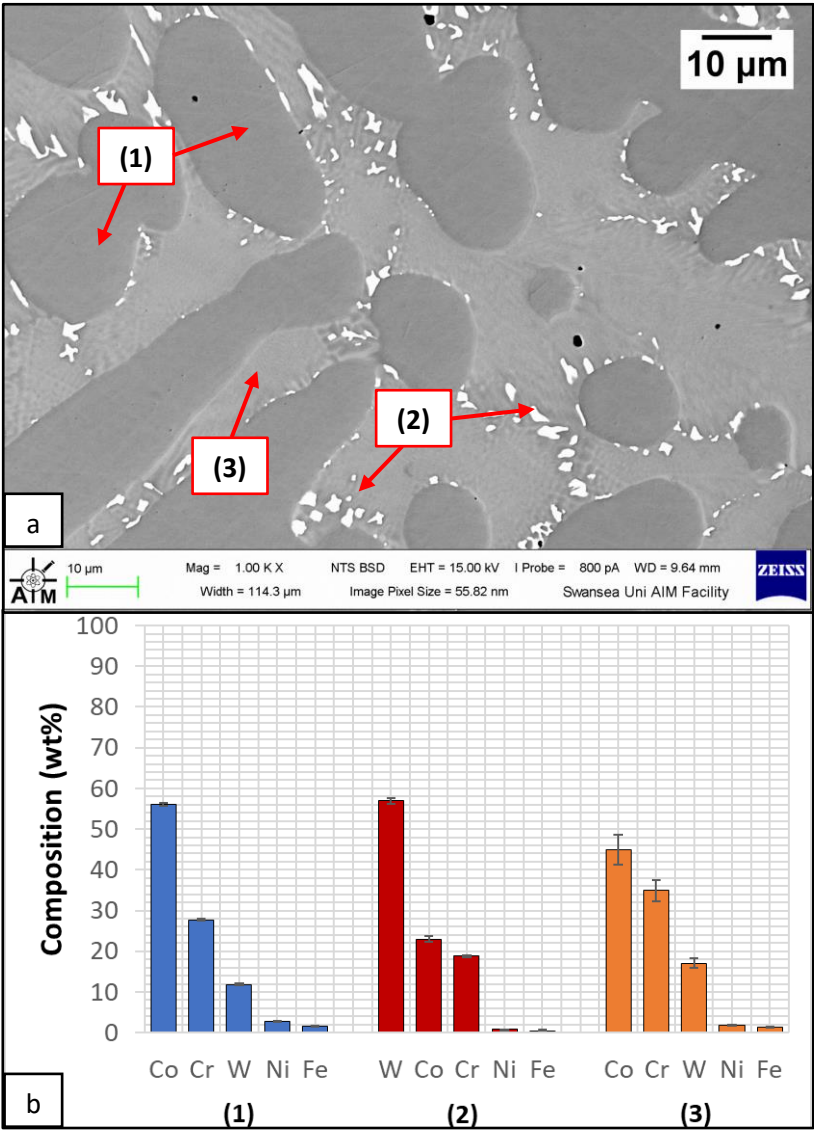


Figure 5.3 Microstructure of Wallex4™ (a); Elemental phase composition of Wallex4™ (b).

5.3 Dynamic Testing

This section discusses the results of dynamic wear testing. The experimental procedures followed for these experiments were previously outlined in Chapter 2, Section 2.4.2.3. Since ZODIAC has the capability of producing both GI and MagiZinc® coatings, the three material pairs in Table 5.1 were tested in Zn-0.3wt%Al (Zn-Al) and Zn-1.5wt%Al-1.5wt%Mg (Zn-Al-Mg) bath compositions. The tests were carried out by setting the bar speed at 300 rpm and the specimens were extracted from the bath after 48 hours of immersion in liquid Zn alloy. Higher immersion times would have increased the risk of incurring in unplanned stoppages, due to material building up at the surface when the bar was in motion (Figure 5.4).

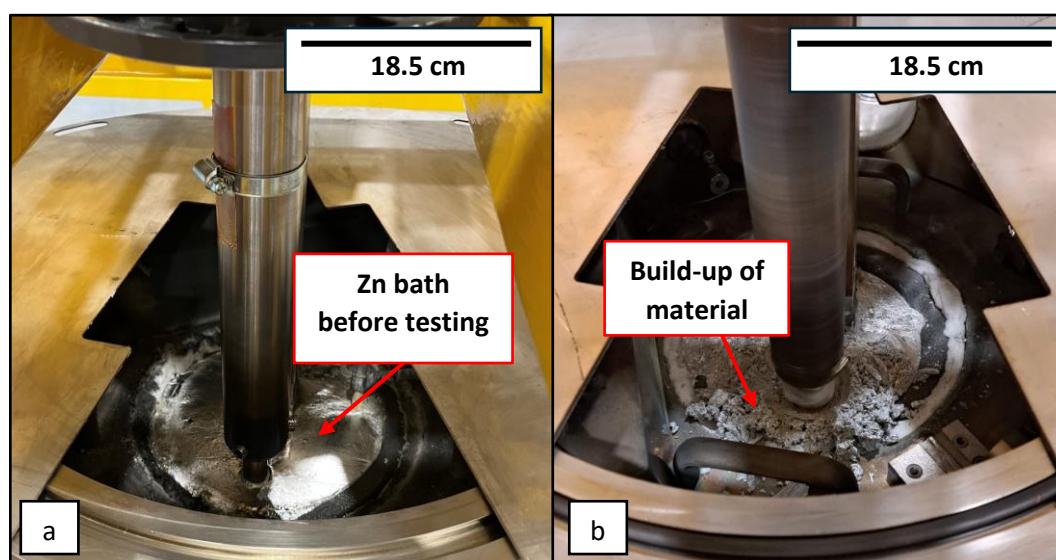


Figure 5.4 Photograph of the Zn bath before testing (a); Dross formation during testing (b).

This build-up could be the result of dross formation in the bath, which was subsequently confirmed by the analysis of the cross-sections of the tested specimens. However, it was noticed that zinc oxide phases were present within the residual Zn layer that solidified onto the specimens. Figure 5.5a illustrates a cross-section of a WC-Co/Wallex6™ bar after testing and bulbous phases were found in the Zn layer (1), whose composition is shown in Figure 5.5b. It is believed that oxidation of the surface of the Zn bath occurred, although these bulbous phases were not detected in the static baths, where no build-up of material was observed. Therefore, the Zn oxide

phases could have been introduced into the bath by the turbulence generated by the movement of the bar, causing these phases to buildup in the proximity of the samples, such as the specimen illustrated in Figure 5.5.

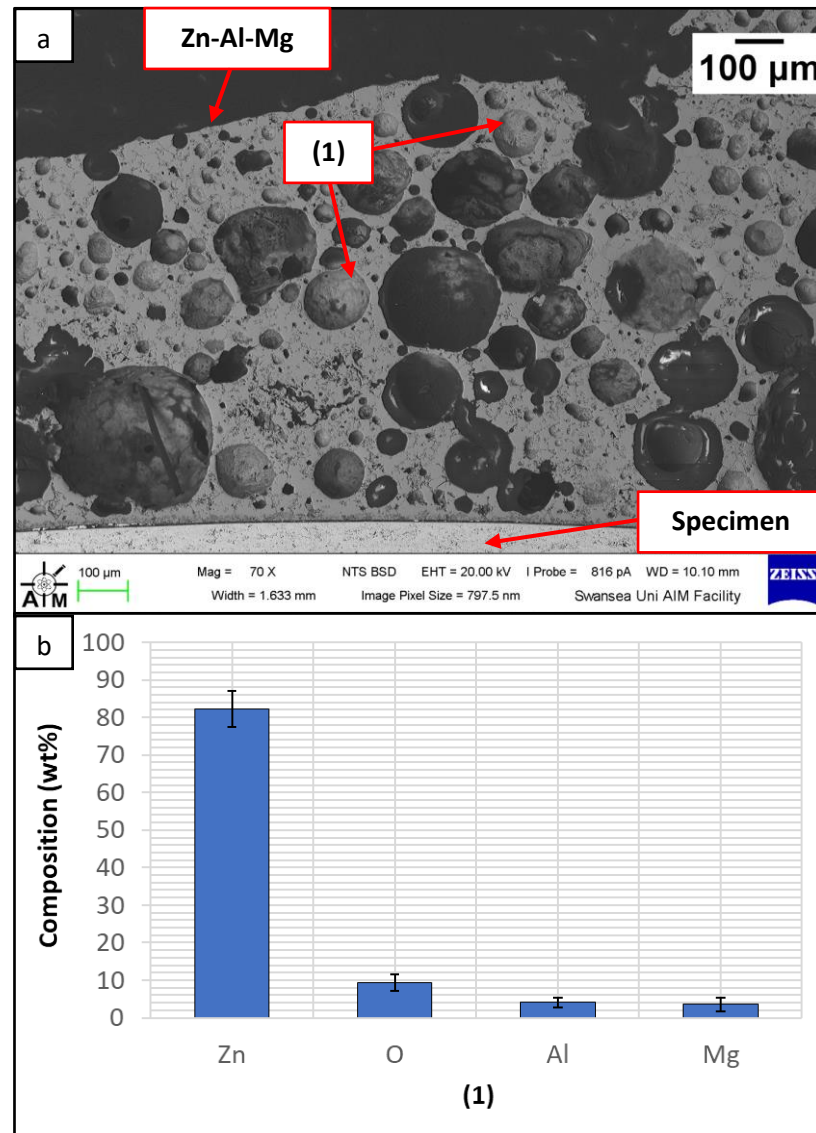


Figure 5.5 Cross-section of the WC-Co/Wallex6™ bar after immersion in Zn-Al-Mg, showing the oxide phases forming on the residual Zn layer (a); Composition of the oxide phases observed in this layer (b).

5.3.1 Wallex6™ with HVOF WC-Co vs Wallex6™

In this chapter, the cross-sections of each material pair were examined, in order to assess the corrosion behaviour of the materials during sliding contact in liquid Zn alloy. The first test was conducted using a Wallex6™ bar coated with HVOF WC-Co coating and an as-received Wallex6™ pad. These materials are used respectively for the sleeve and bushing components of the bearing system used in ZODIAC.

Figure 5.6a shows a cross-section of the WC-Co/Wallex6™ bar after 48 hours of testing in Zn-Al. Although an oxide layer formed on the surface of WC-Co after static testing (Figure 3.22 – Figure 3.23), Figure 5.6a shows that this layer is absent in the bar specimen. The absence of an oxide layer can be the result of the shorter duration of exposure to molten metal compared to the static tests and that limited dissolution of Co into the melt occurred during the 48 hours. In addition, the coatings did not show signs of damage such as cracks, which could have provided pathways for liquid Zn alloy to permeate through the coating and corrode the Wallex6™ base metal. The absence of wear damage in the coating could be the result of the hardness of the counterpart, which is softer than WC-Co and, therefore, it was unable to inflict damage to the bar, as later discussed in Section 5.3.4.

Although the WC-Co coating protected Wallex6™ from the attack of liquid Zn-Al, the analysis of the cross-section revealed that intermetallic compounds formed on the contact surface, as illustrated in the high magnification image (Figure 5.6b). These compounds were absent in the as-received specimen (Figure 5.1). The results of EDS phase elemental analysis conducted in this region (Figure 5.6c) showed that the intermetallic compounds are Zn-based phases and mainly contain Al (42.6 ± 0.9 wt.%) and Co (29.3 ± 0.9 wt.%), with traces of Fe, W and Ni. Previous studies reported the presence of intermetallic phases on the surface of WC-Co coatings (Seong et al., 2001; Tani et al., 1994). Co is known to have a strong affinity for Al present in the melt and, for this reason, Co-Al particles can develop in liquid Zn baths containing Al (Zhang & Tang, 2004). In this study, Co is contained in the WC-Co coating of the bar specimen, as well as in the Wallex6™ pad.

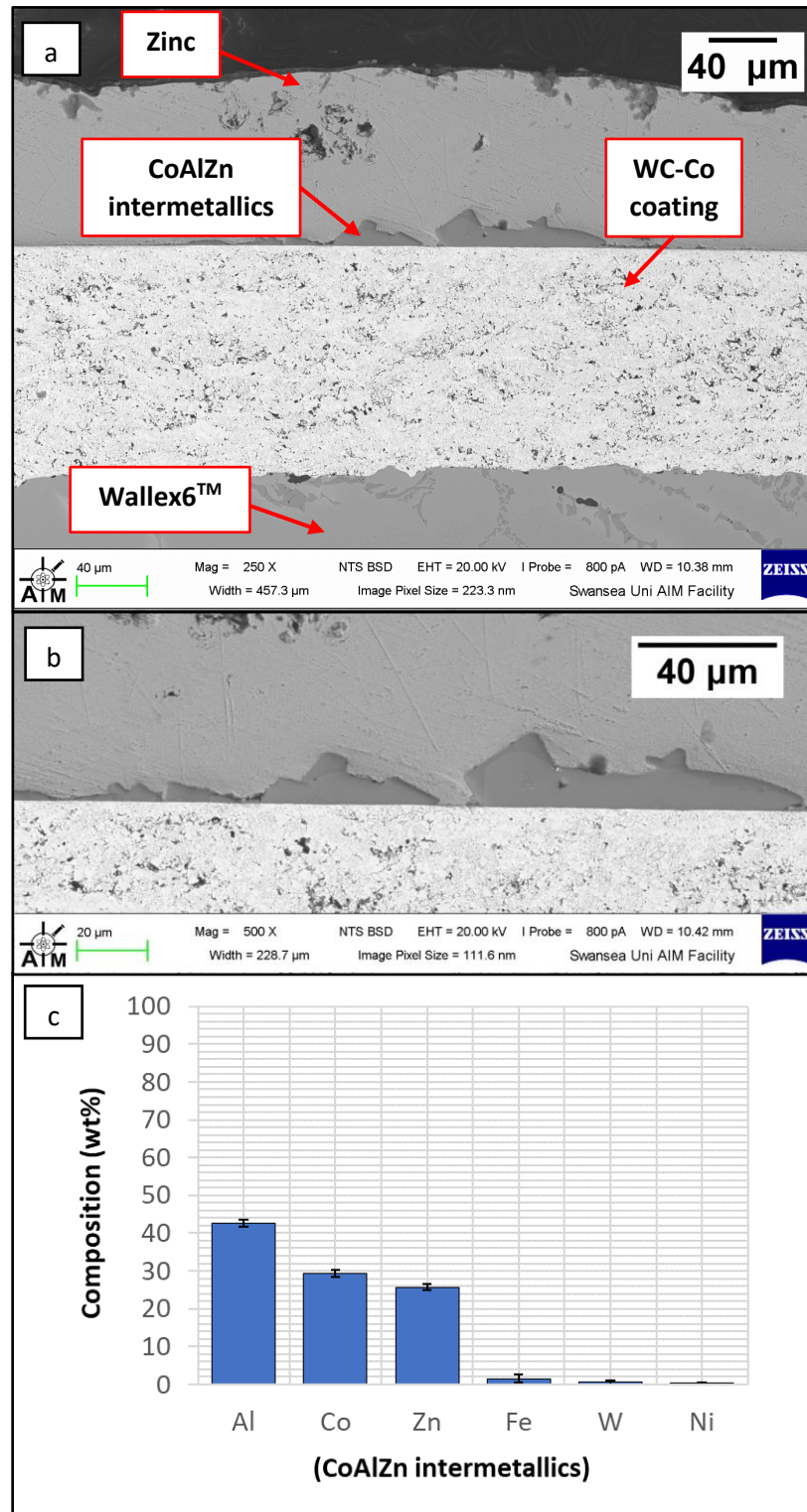


Figure 5.6 SEM image of WC-Co/Wallex6™ bar after testing in Zn-Al (a); high magnification image showing the intermetallic compounds (b); EDS phase elemental analysis of the intermetallic compounds (c).

Co-rich surfaces are known for being ideal sites for the attachment of intermetallic compounds existing in the liquid metal bath (Zhang & Tang, 2004). Experiments were performed by Zhang (2003) on Stellite 6 bearings in GI and it was found that Co-based aluminides were present on the bushing surface as a result of the reaction between the wear particles generated during testing and the Zn alloy bath. Therefore, the presence of aluminides illustrated in Figure 5.6 could be related to the adhesion of these particles to the coating surface. However, the formation of Al-Co-Zn intermetallic compounds in WC-Co coatings can be the result of the corrosion of the Co-rich matrix phase in the coatings by the Zn bath. As discussed by Seong et al. (2001) and Tani et al. (1994), Co reacted with the Al present in the Zn bath due to Co dissolution into the melt, leading to the formation of Al-rich compounds containing Co and Zn.

The Wallex6™ pad was found to react with the molten metal bath, after exposure to Zn-Al. Cross-sections of the specimens were analysed within the contact region (Figure 5.7), where contact with the counterpart occurred, as well as in the unworn region (Figure 5.8) and they were compared to the as-received specimen (Figure 5.2). The SEM image captured on the contact surface (Figure 5.7a) showed that two phases were present at the interface of the alloy. A magnified image of the same area (Figure 5.7b) suggested that one of these phases was a thin ($\sim 0.4 \mu\text{m}$) reaction layer, which developed beneath the surface of the sample and it was only interrupted by the CoCrWMo eutectic phases present in the alloy, meaning that the diffusion layer did not form at locations where the eutectic phases were present. EDS analysis was conducted (Figure 5.7c) and it revealed that the surface of the material was covered with a layer of Zn containing small amount of Co ($6.5 \pm 0.8 \text{ wt.}\%$), which is believed to have diffused into the melt from the alloy (1). The subsurface reaction layer (2) was found to mainly contain Co ($37.7 \pm 1.4 \text{ wt.}\%$), Zn ($26.6 \pm 2.5 \text{ wt.}\%$), Cr ($15.3 \pm 0.6 \text{ wt.}\%$) and Al ($12.8 \pm 0.4 \text{ wt.}\%$). Similar findings were obtained by Zhang (2003) who reported the formation of a layer of cobalt-based aluminides of Al-Co-Zn-Cr-Fe-W on the contact surface of a Stellite 6 bearing after exposure to GI.

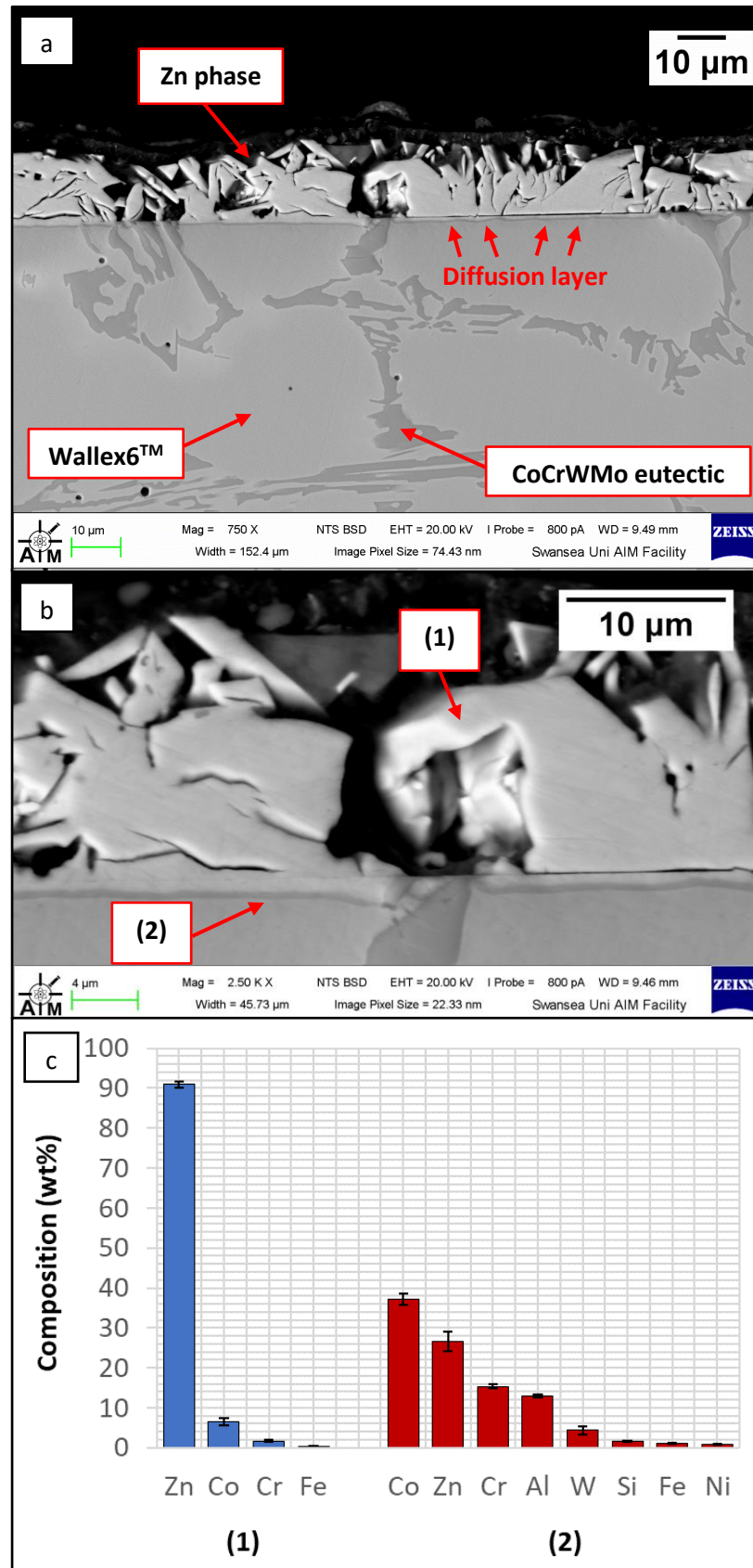


Figure 5.7 (a) SEM image of Wallex6™ pad after testing in Zn-Al captured on the contact surface; (b) high magnification image; (c) Results of EDS phase elemental analysis.

Figure 5.8a was captured within the unworn region, which is the area where the bar and pad specimens were not in contact with each other. EDS point spectrum analysis was performed to reveal the composition of the phases observed in this area (Figure 5.8b). The results clearly showed the presence of dross phases (2) within the top Zn phase (1) and on top of the surface in contact with molten Zn-Al. These Zn-based intermetallic compounds were found to mainly contain Al (45.9 ± 1.0 wt.%), Co (17.1 ± 1.2 wt.%), Fe (14.5 ± 1.0 wt.%) and small amounts of Cr and W.

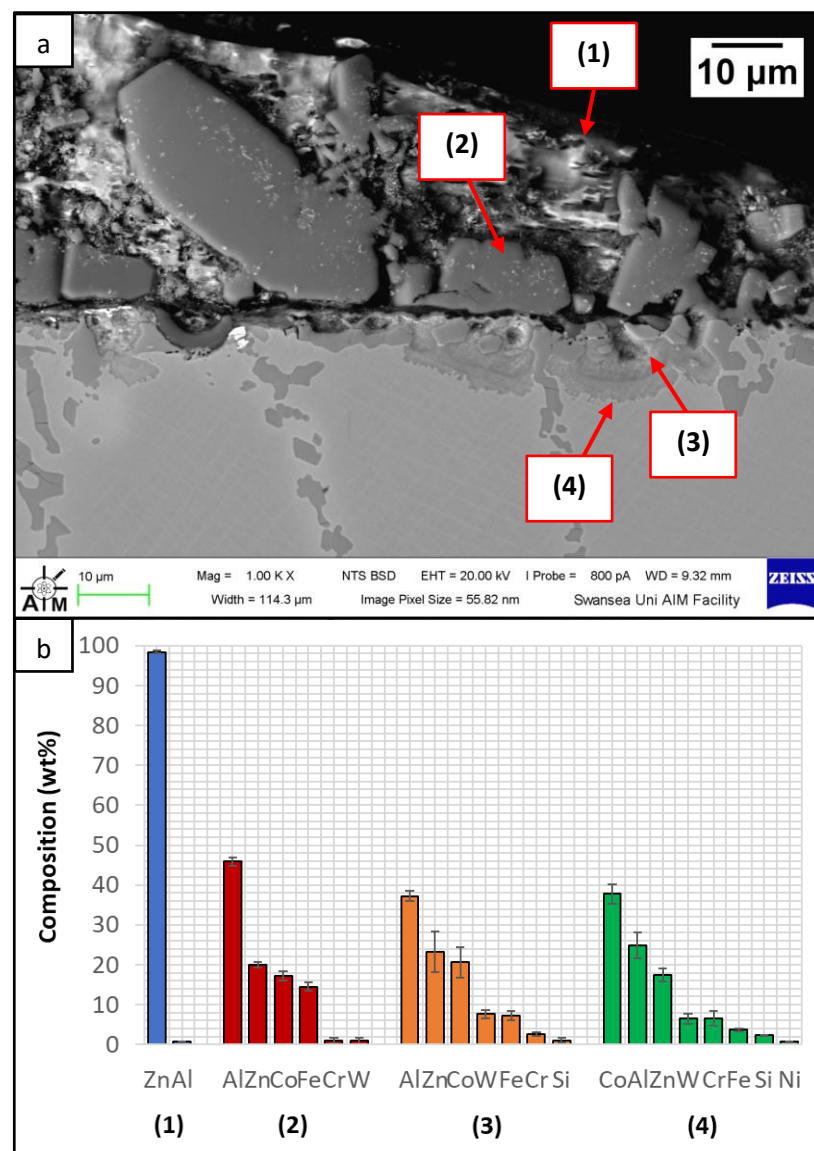


Figure 5.8 SEM image of Wallex6™ pad after testing in Zn-Al within the unworn region (a); EDS point spectrum analysis of the phases present in the unworn region (b).

Co has a strong affinity for Al and there is evidence that the Co solid solution phase of Co-Cr-W alloys reacts with the Al contained in liquid Zn baths (Zhang & Tang, 2003). The products of this reaction are CoAl particles forming on the sample surface. The information obtained in the present study showed that Fe was contained in the CoAl intermetallic compounds after testing in Zn-Al. This finding aligns with previous studies, which reported that CoAl particles transformed to FeAl complexes, as the exposure to liquid Zn alloy increased because of the presence of dissolved Fe in the Zn alloy (Seong et al., 2001; Zhang & Tang, 2004). In Figure 5.8, (3) and (4) respectively denote the region within the subsurface reaction layer and the interface between the reaction layer and the bulk of the alloy. It was observed that Al was present in the reaction layer, whereas the Co content diminished compared to the unreacted Co-solid solution phase (Figure 3.2). The Co content was found to increase in the vicinity of the interface with the Co-solid solution phase, indicating that Co was depleted from the reaction layer below the surface. In addition to this, it was observed that the diffusion layer is thicker ($\sim 10 \mu\text{m}$) compared to that present beneath the contact surface, where removal of material occurred.

The same material pair was characterised after testing in Zn-Al-Mg. The cross-section of the WC-Co/Wallex6™ bar specimen was analysed (Figure 5.9a) and it was observed that particles of intermetallic compounds were present (Figure 5.9b), showing similar behaviour to Zn-Al. However, the results of EDS analysis (Figure 5.9c) revealed that these particles contained more Fe ($18.5 \pm 1.2 \text{ wt.}\%$) than Co ($12.9 \pm 1.6 \text{ wt.}\%$), whereas the intermetallic particles grown in Zn-Al were richer in Co.

The present literature highlights that the solubility of Fe in liquid Zn alloy depends on the Al content. The solubility limit is defined as “the maximum concentration of solute atoms that may dissolve in the solvent to form a solid solution” (Callister & Rethwisch, 2013). In this experiment, the solubility limit corresponds to the maximum quantity of Fe that can dissolve in the Zn bath with the addition of Al for GI and Al-Mg for MagiZinc®. The solubility limit of Fe in Zn-Al was determined from the experiments conducted by Tang (2000) and it is a function of temperature (Ilinca et al., 2007). Figure 5.10 shows a phase diagram constructed for the Zn-rich corner of the Zn-Al-Fe system, based on the more recent experiments conducted by McDermid et al. (2007).

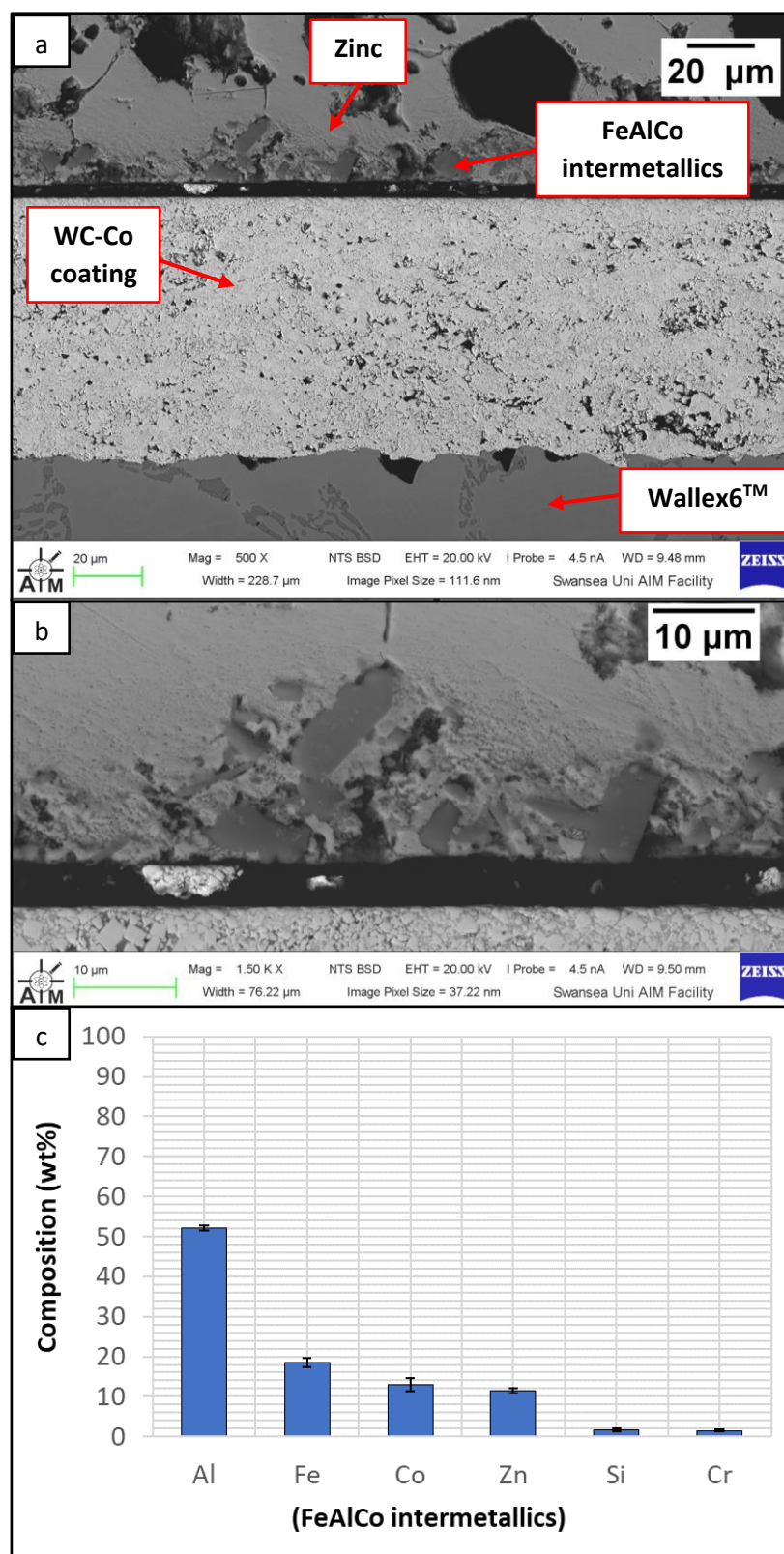


Figure 5.9 SEM image of WC-Co/Wallex6™ bar after testing in Zn-Al-Mg (a); high magnification image showing the intermetallic compounds (b); EDS phase elemental analysis of the intermetallic compounds (c).

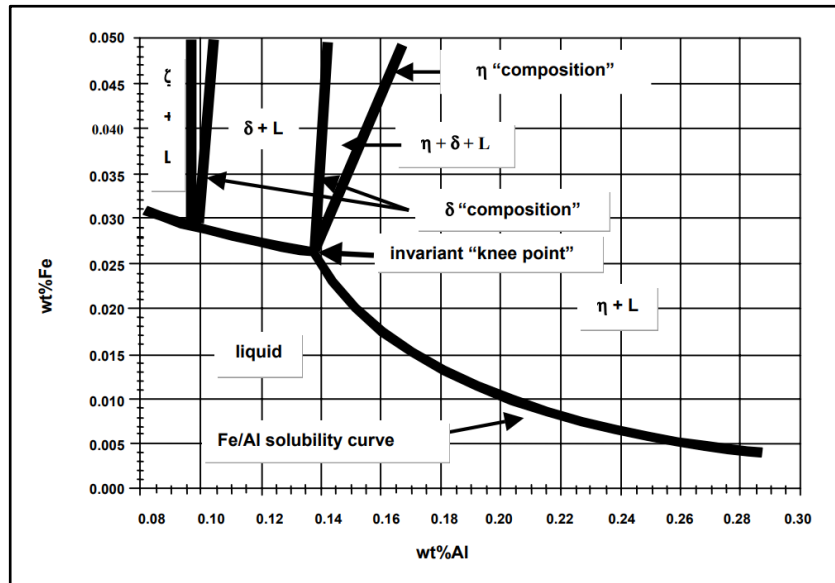


Figure 5.10 Phase diagram showing the Zn-rich corner of the Zn-Al-Fe system at 460 °C. The diagram illustrates the Fe solubility limit for Al concentrations up to ~ 0.3 wt.% Al (McDermid et al., 2004).

The diagram shows the Fe solubility limits for Al concentrations up to approximately 0.3 wt.% at 460 °C. The area under the Fe/Al solubility curve indicates the region where Fe and Al remain in solution. It can be observed that this area decreases as the Al content in the bath is increased. Intermetallic dross compounds between Fe and Al do not form below the solubility limit. However, FeAl intermetallic phases form when the Fe solubility is exceeded (Kuperus, 2018; Marder & Goodwin, 2023). Al tends to react with Co dissolved in the melt at low Al contents (Matthews & James, 2010). The strong affinity of Co for Al could justify the higher Co content in the intermetallic phases observed in this study for the Zn-Al bath with 0.3 wt.% Al.

The Zn-Al-Mg bath contains 1.5 wt.% Al and 1.5 wt.% Mg. The Fe-Al phase diagram with the addition of 1.5% Mg is shown in Figure 5.11. Although the presence of Mg did not significantly alter the Fe/Al solubility in the phase diagram, it can be observed that the area under the solubility line is small as the Al content is increased from the GI composition to the levels encountered in the Zn-Al-Mg bath. Therefore, the Fe solubility is even smaller at higher Al content and this is believed to have increased the Fe content in the intermetallic phases detected in the specimens immersed in Zn-Al-Mg.

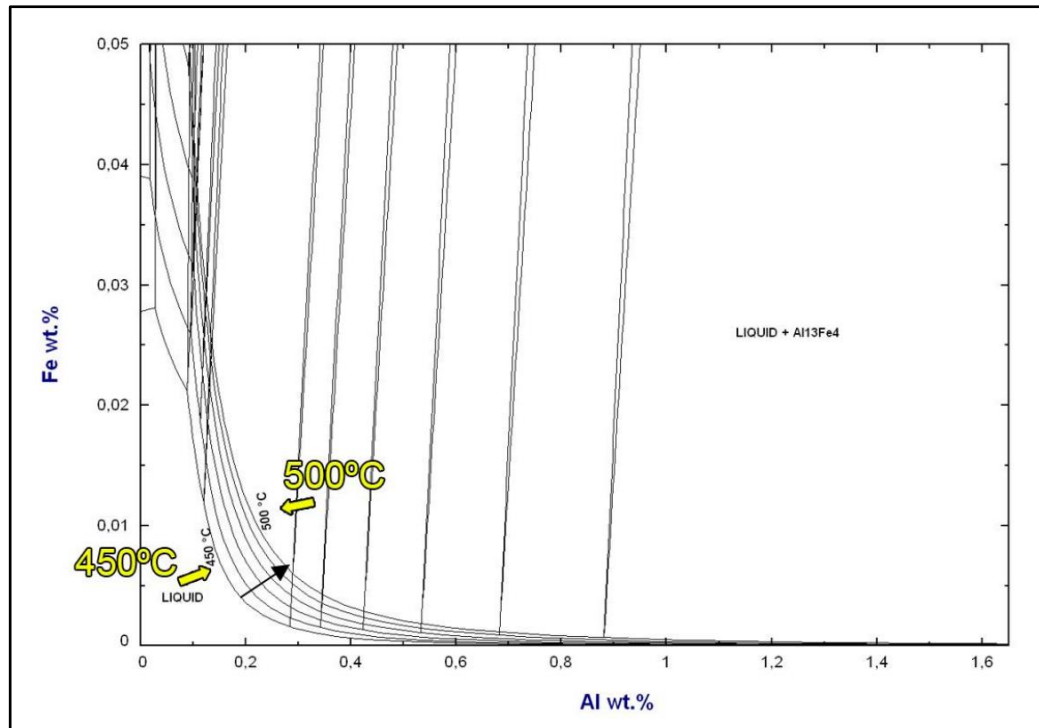


Figure 5.11 Phase diagram of the Zn-Al-Fe system at 460 °C for 1.5 wt.% Mg additions. Fe solubility lines are shown in the temperature range between 450 °C and 500 °C (Kuperus, 2018).

Regarding the pad specimens, Figure 5.12a was captured on the Wallex6™ pad after testing in Zn-Al. The image shows the area of contact and chemical analysis was carried out within this region (Figure 5.12b). The results showed that the sample was covered with a layer of mainly residual Zn (1) and that the interface was characterised by a high Zn and Al content (2). Co is also present in this region, as well as the majority of the other elements present in the alloy before testing. For this reason, it is possible that this layer was characterised by a combination of dross and debris originating from the contact with the bar.

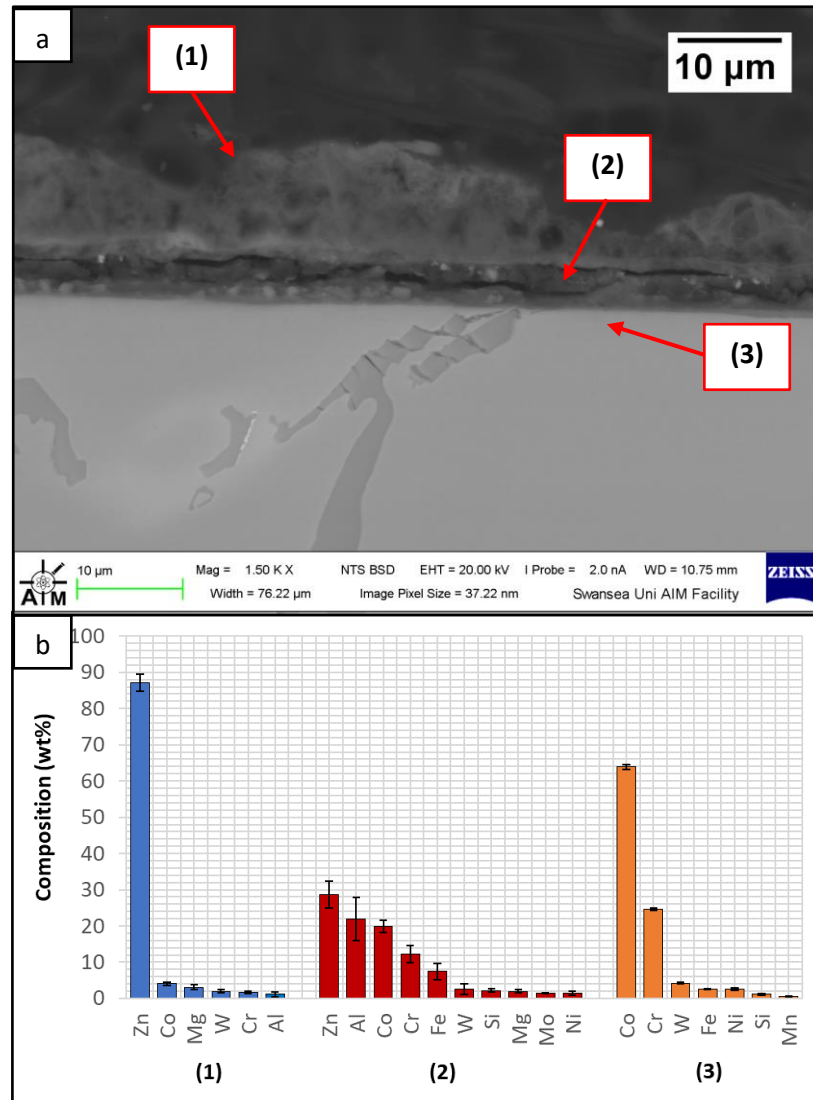


Figure 5.12 SEM image of Wallex6™ pad after testing in Zn-Al-Mg captured on the contact surface (a); high magnification image (b); results of EDS phase elemental analysis (c).

Furthermore, the SEM image in Figure 5.12 highlighted that a subsurface reaction layer was absent (3), as material was continuously removed by the harder WC-Co bar. This observation was confirmed by the results of EDS, which revealed that no Zn, Al and Mg diffused into the alloy. Outside the contact region (Figure 5.13), the behaviour was similar to that observed in Zn-Al. CoAlZn intermetallic compounds grew on the surface of the material (1) and a diffusion layer formed beneath the surface of the sample (2). This reaction layer contained Al (35.1 ± 1.5 wt.%) and Co (30.9 ± 5.3 wt.%), whereas outside this layer, the composition changed to Co (39.9 ± 2.4 wt.%) and Al

(26.6 ± 2.9 wt.%), indicating Co depletion from the reaction layer. The introduction of Mg into the bath did not alter the corrosion behaviour of the pad material.

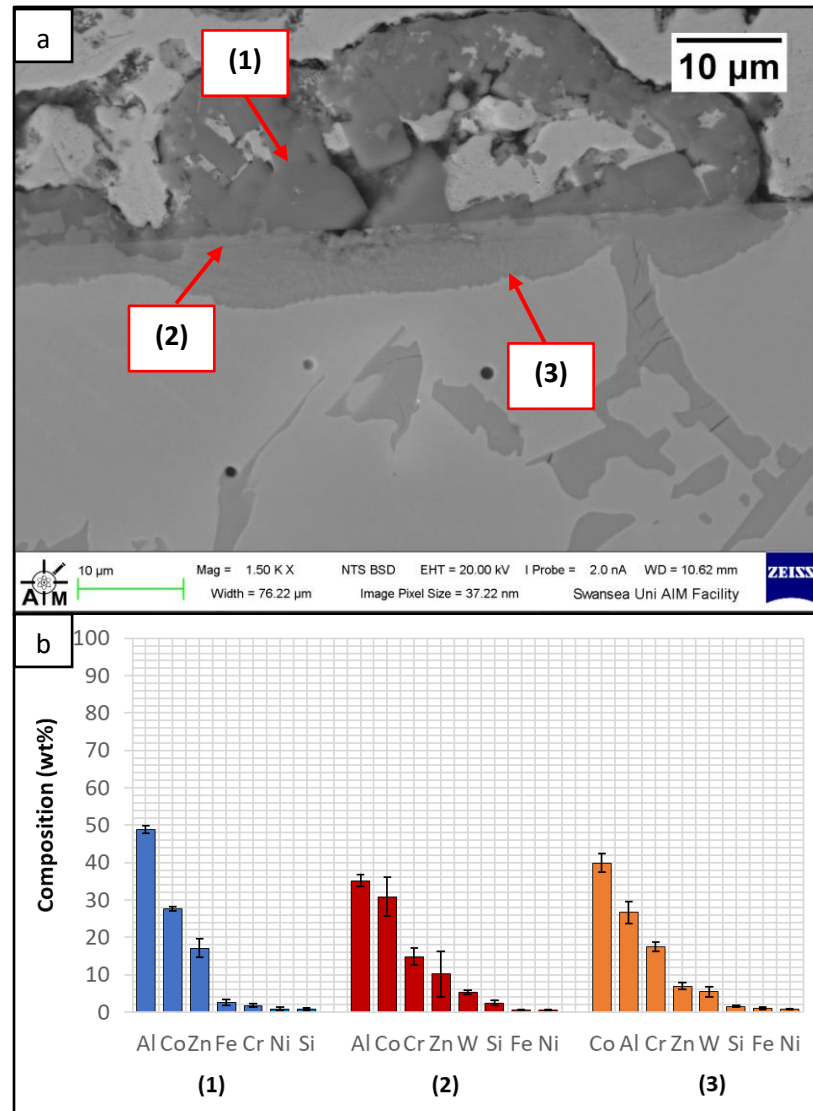


Figure 5.13 SEM image of Wallex6™ pad after testing in Zn-Al-Mg captured on the unworn region (a); EDS point spectrum analysis of the phases present in the unworn region (b).

5.3.2 Wallex6™ with HVOF WC-Co vs Wallex4™

The first of the two potential upgrades to the material pair used in ZODIAC involved replacing Wallex6™ with Wallex4™. The bar specimen used in the experiment was again coated with WC-Co applied via HVOF, as described in Chapter 3, Section 3.2.1.

Figure 5.14a was captured on the WC-Co/Wallex6™ bar after sliding against the Wallex4™ pad in Zn-Al. A similar behaviour to the bar specimens analysed previously can be observed. The Wallex6™ base metal remained unreactive in Zn-Al, as the WC-Co coating prevented exposure to the molten metal bath. No cracks and other signs of damage to the coating were observed after the experiment. In a similar fashion to the coatings discussed in the previous section, the image was compared to the as-received specimen (Figure 5.1) and the samples tested under static conditions (Figure 3.22 and Figure 3.23). The oxide layer formed during static testing was again absent and a layer of intermetallic particles formed on the surface. EDS phase elemental analysis (Figure 5.14b) revealed the composition of the intermetallic particles, which contained Al (48.6 ± 0.2 wt.%), Fe (18.6 ± 0.4 wt.%), Zn (17.6 ± 0.3 wt.%) and Co (13.5 ± 0.4 wt.%).

No intermetallic compounds were detected on the surface of the pad specimen, as shown in Figure 5.15a. EDS point spectrum analysis (Figure 5.15b) was conducted in the region near the surface exposed to molten Zn-Al and it was found that both Zn and Al diffused into the alloy, as observed in the Wallex6™ pad tested in the previous experiment. However, the reaction layer present in Wallex4™ appeared to be less homogenous compared to the diffusion layer observed in Wallex6™. This is evidenced by the results of EDS analysis, which displayed variation of elemental composition, as illustrated by the measured standard deviation of the average values shown in Figure 5.15b. Outside the contact region (Figure 5.16a), several corrosion products were identified, and the composition of the new phases was investigated (Figure 5.16b). Intermetallic dross phases were found on the surface of the alloy (1), which contained Al (44.2 ± 2.6 wt.%), Co (23.4 ± 4.0 wt.%), Zn (22.3 ± 3.1 wt.%) and Fe (3.4 ± 1.0 wt.%). The results of EDS showed that the composition of the dross was similar to that of the intermetallic particles found on the bar specimen (Figure 5.14), although it contained 9.9 wt.% more Co and 15.2 wt.% less Fe. A subsurface reaction layer was still present (2), where both Al and Zn were detected, and the Zn content was lower compared to the dross phase. The Co and Cr content measured in this layer was found to be lower compared to the as-received specimen (Figure 5.2). The results of EDS analysis showed that the reaction layer contained Co (36.3 ± 7.0 wt.%) and Cr

(2.9 ± 0.7 wt.%), whereas the solid solution phase of the as-received specimen contained Co (56.1 ± 0.4 wt.%) and Cr (27.8 ± 0.2 wt.%). Therefore, the analysis suggested that the depletion of these elements from the reaction layer occurred. Moreover, it was observed that the CoCrW eutectic phase present in Wallex4™ reacted with the molten metal bath as highlighted in the EDS maps (Figure 5.17), which shows Al diffusion from the bath.

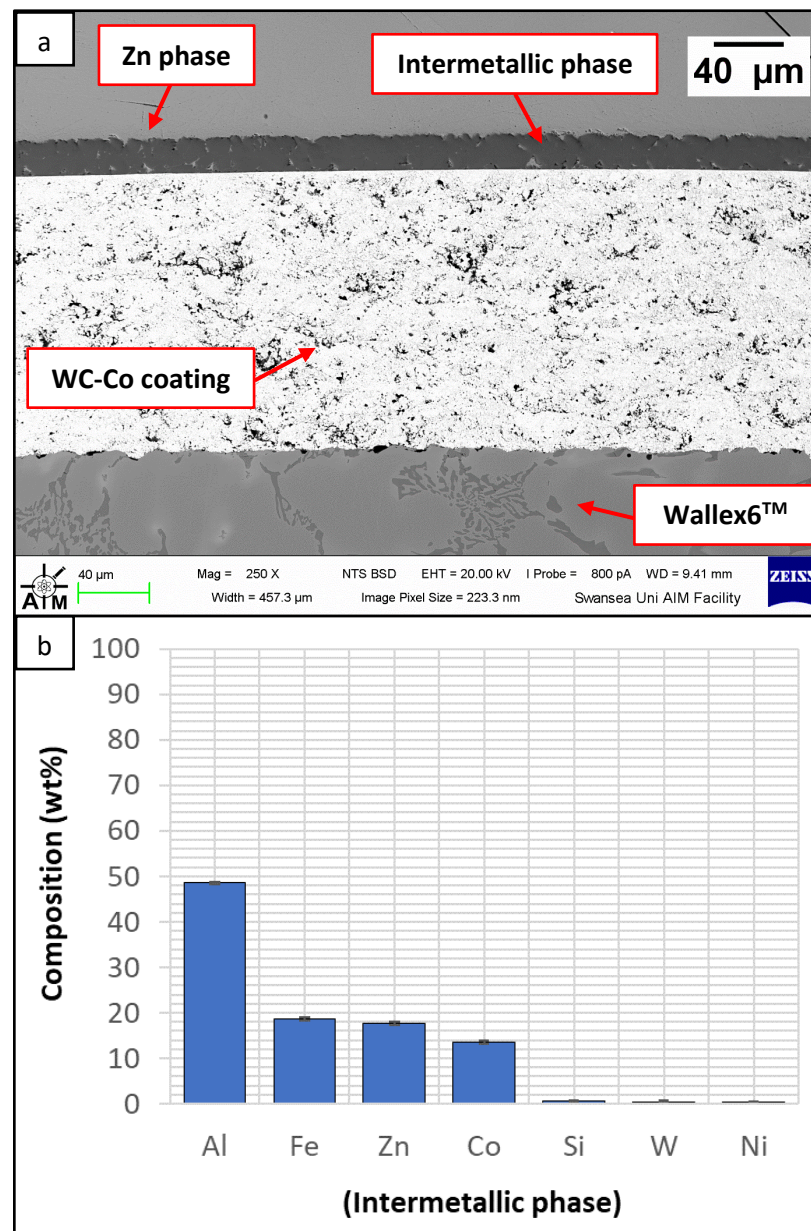


Figure 5.14 SEM image of WC-Co/Wallex6™ bar after testing in Zn-Al (a); EDS phase elemental analysis of the intermetallic compounds (b).

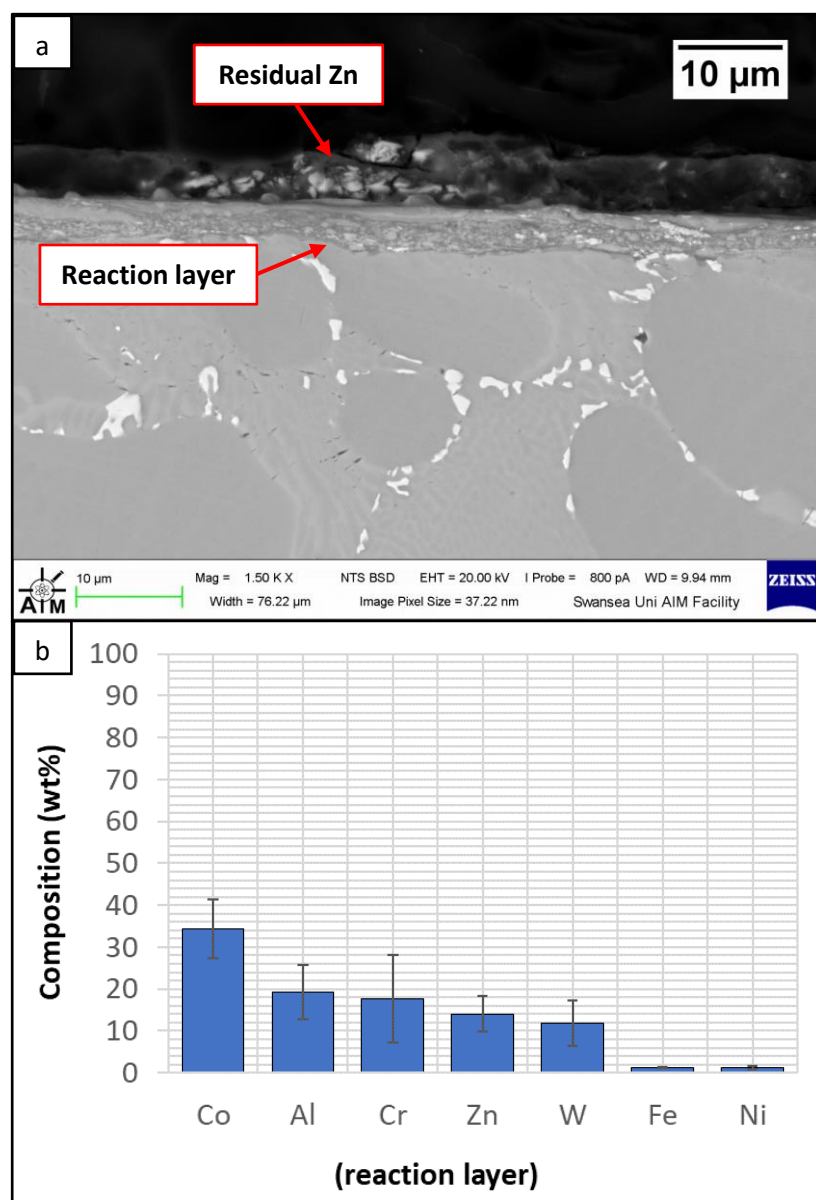


Figure 5.15 SEM image of the contact region of Wallex4™ after testing in Zn-Al (a); EDS phase elemental analysis of the reaction layer (b).

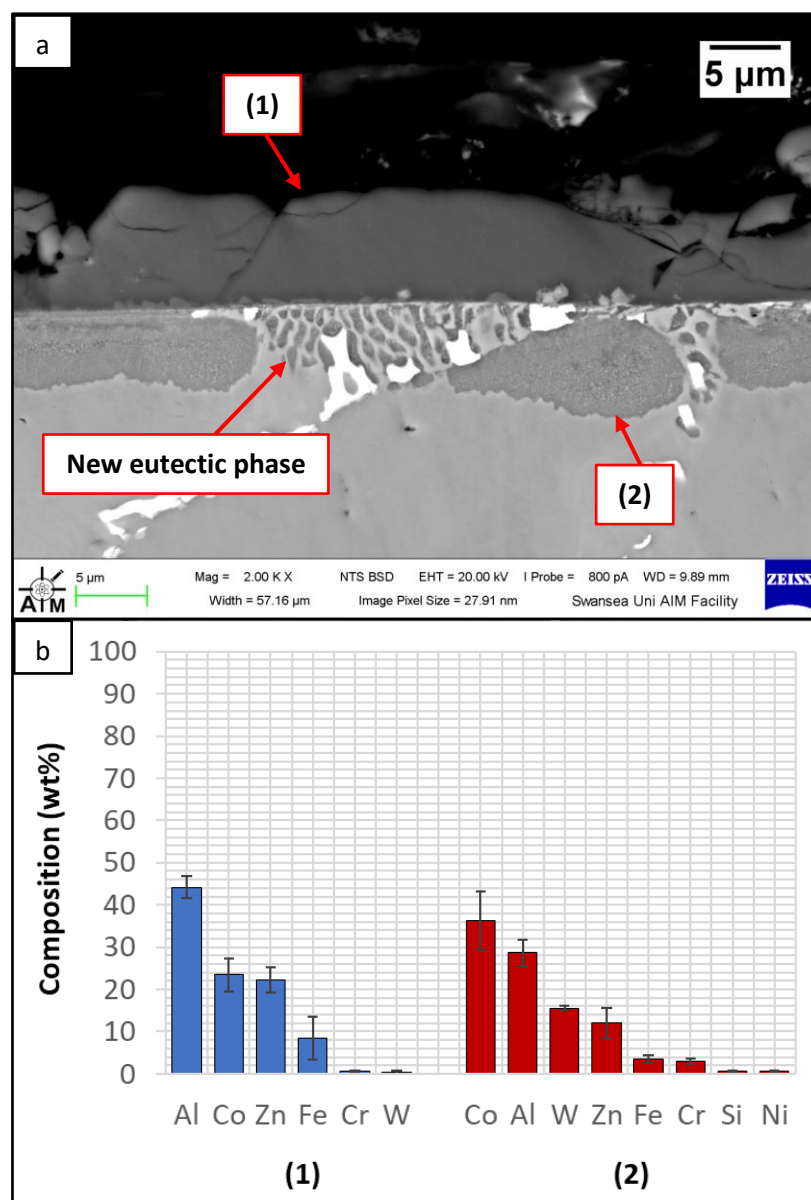


Figure 5.16 SEM image captured within the unworn region of the Wallex4TM pad after testing in Zn-Al (a); EDS phase elemental analysis of the corrosion products (b).

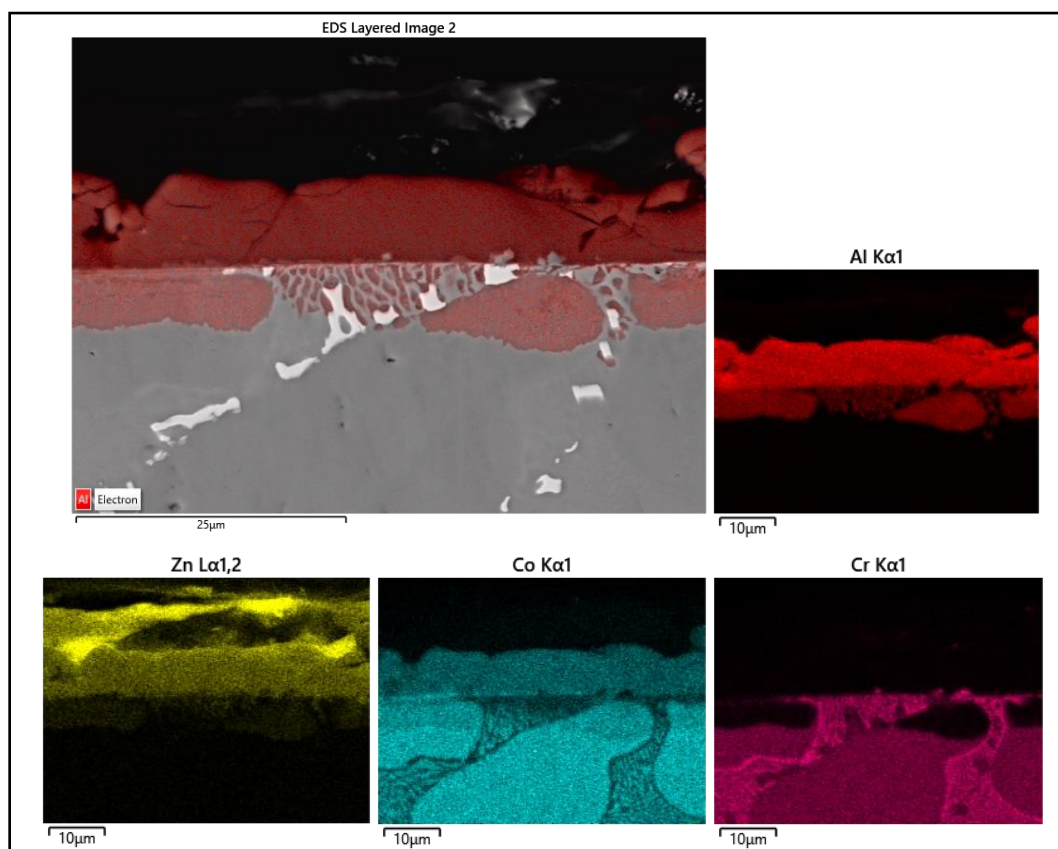


Figure 5.17 EDS mapping of the elements present in Wallex4™ after testing in Zn-Al.

A similar corrosion behaviour was observed in the samples immersed in Zn-Al-Mg. Figure 5.18 illustrates that reaction products developed onto the WC-Co coating (1), which were found to mainly contain Al (45.3 ± 3.7 wt.%), Zn (19.4 ± 5.8 wt.%), Co (11.7 ± 1.7 wt.%) and Fe (10.3 ± 1.2 wt.%). The reaction products of this specimen formed a distinct layer and their presence confirms that the Co matrix of the thermal sprayed coating reacts with the elements present in the bath. No reaction with Mg was detected, as observed in the previous material pair. The Wallex4™ pad did not show any evidence of reaction with Zn-Al-Mg within the contact region, as observed previously (Figure 5.19). At the interface with the Zn phase, the alloy mainly contained Co (55.0 ± 0.6 wt.%), Cr (27.5 ± 0.4 wt.%), W (10.9 ± 0.5 wt.%), Ni (2.4 ± 0.1 wt.%), Fe (1.56 ± 0.13 wt.%) and Zn (1.16 ± 0.4 wt.%). Al and Mg were not detected in this region.

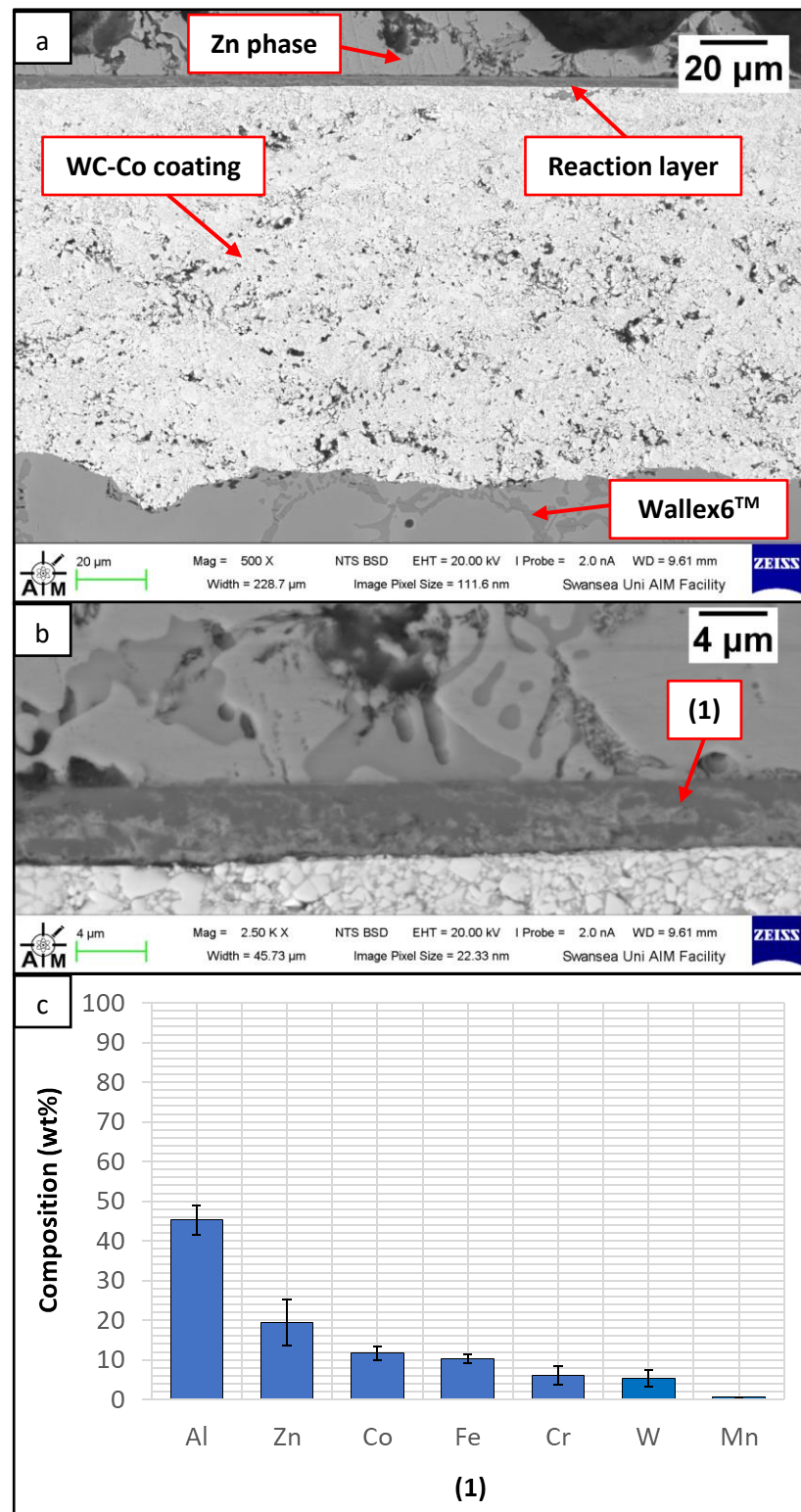


Figure 5.18 SEM image of WC-Co/Wallex6™ bar after testing in Zn-Al-Mg (a); high magnification image showing the reaction layer (b); EDS phase elemental analysis of the intermetallic compounds (c).

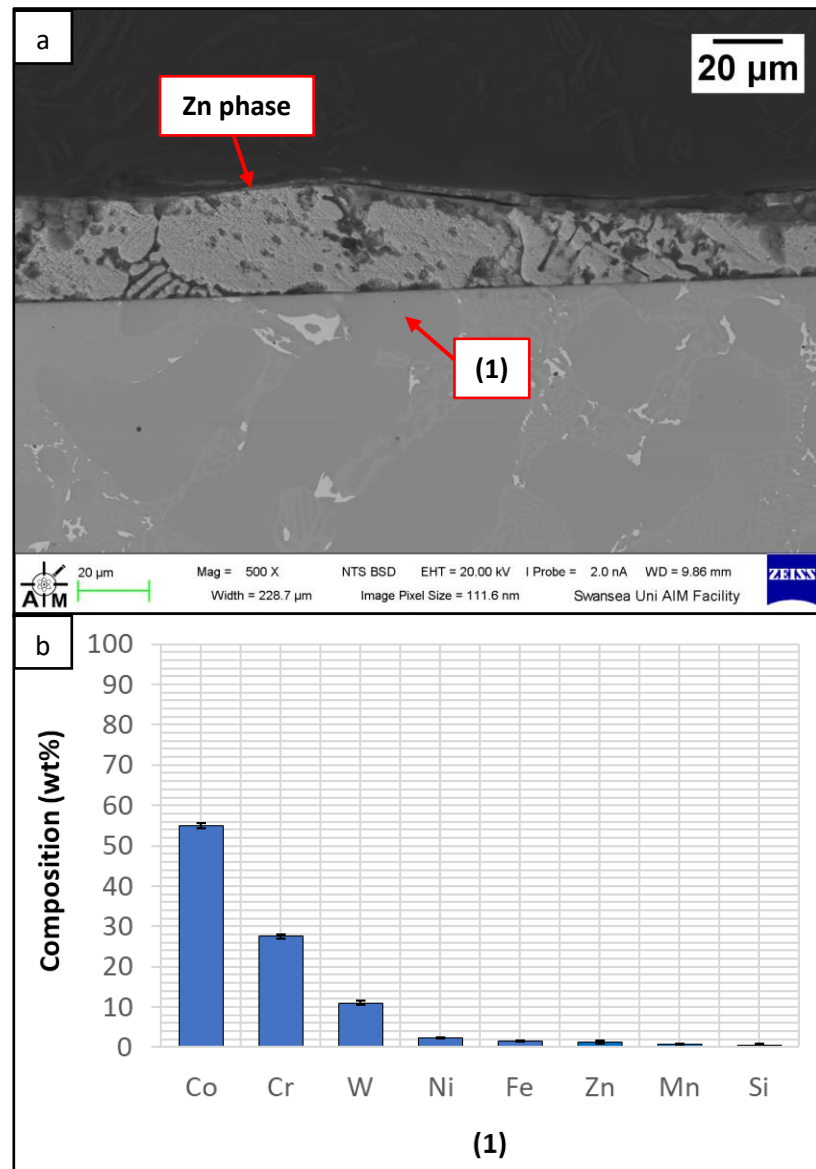


Figure 5.19 SEM image of the contact region of Wallex4™ after testing in Zn-Al-Mg (a); EDS phase elemental analysis of the reaction layer (b).

Figure 5.20 shows that AlCoZn dross was again present within the unworn region (1); in addition to this, CoCrW particles were present within this layer (2), which are likely to be wear debris from the alloy due to their composition. Al diffused into the Co solid solution phase forming a subsurface reaction layer (3), as well as in the CoCrW eutectic phases, in a similar fashion to the specimen tested in Zn-Al. The reaction layer was found to contain Al (8.22 ± 4.5 wt.%) and only small amounts of Mg (~ 0.1 wt.%). Similarly, EDS elemental mapping showed that mostly Al diffused into the eutectic phases from the molten metal bath (Figure 5.21). Overall, changing bath from Zn-Al

to Zn-Al-Mg did not alter the interactions between the materials and the liquid metal significantly. Wallex4™ was corroded in both baths and WC-Co reacted with Al. Moreover, the corrosion behaviour of Wallex4™ showed similarities with Wallex6™, due to the similar chemical composition of the two alloys. The Co-rich solid solution phase of both alloys was attacked by molten Zn and Al forming diffusion layers and, additionally, they developed a layer of Co-Al-Fe-Zn intermetallic phases on the surface.

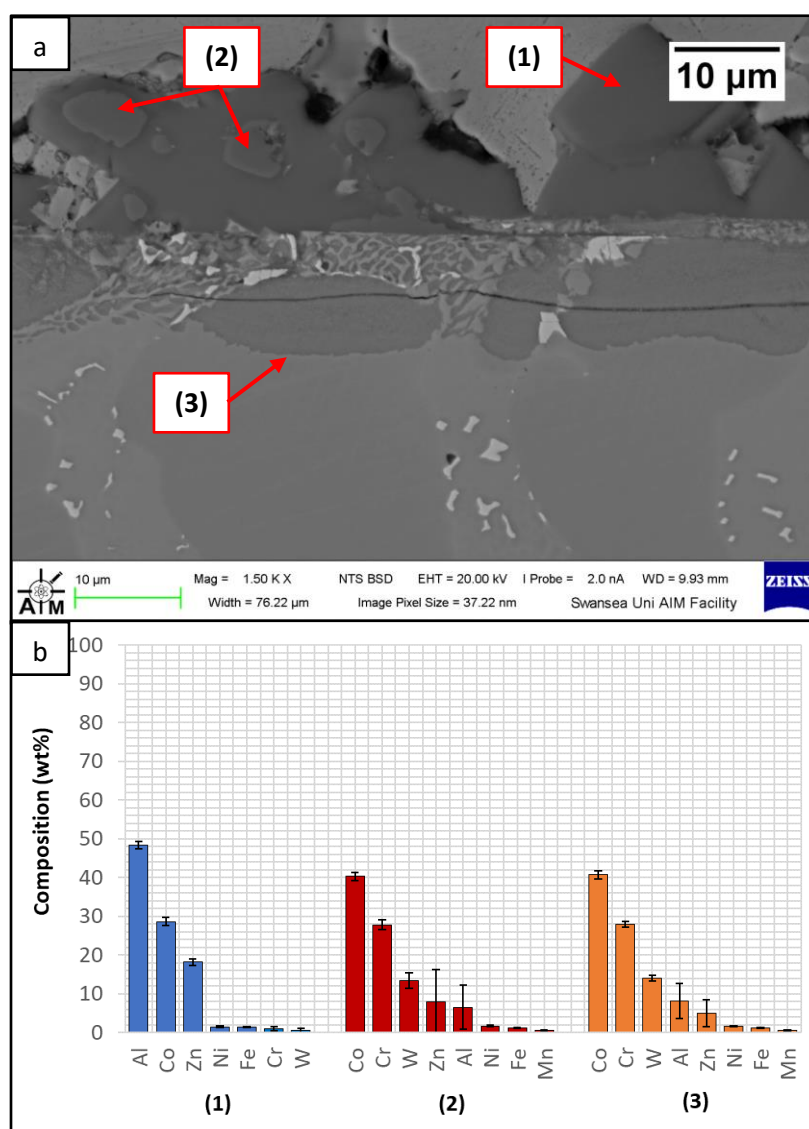


Figure 5.20 SEM image of the unworn region of Wallex4™ pad after testing in Zn-Al-Mg (a); EDS phase elemental analysis of the corrosion products (b).

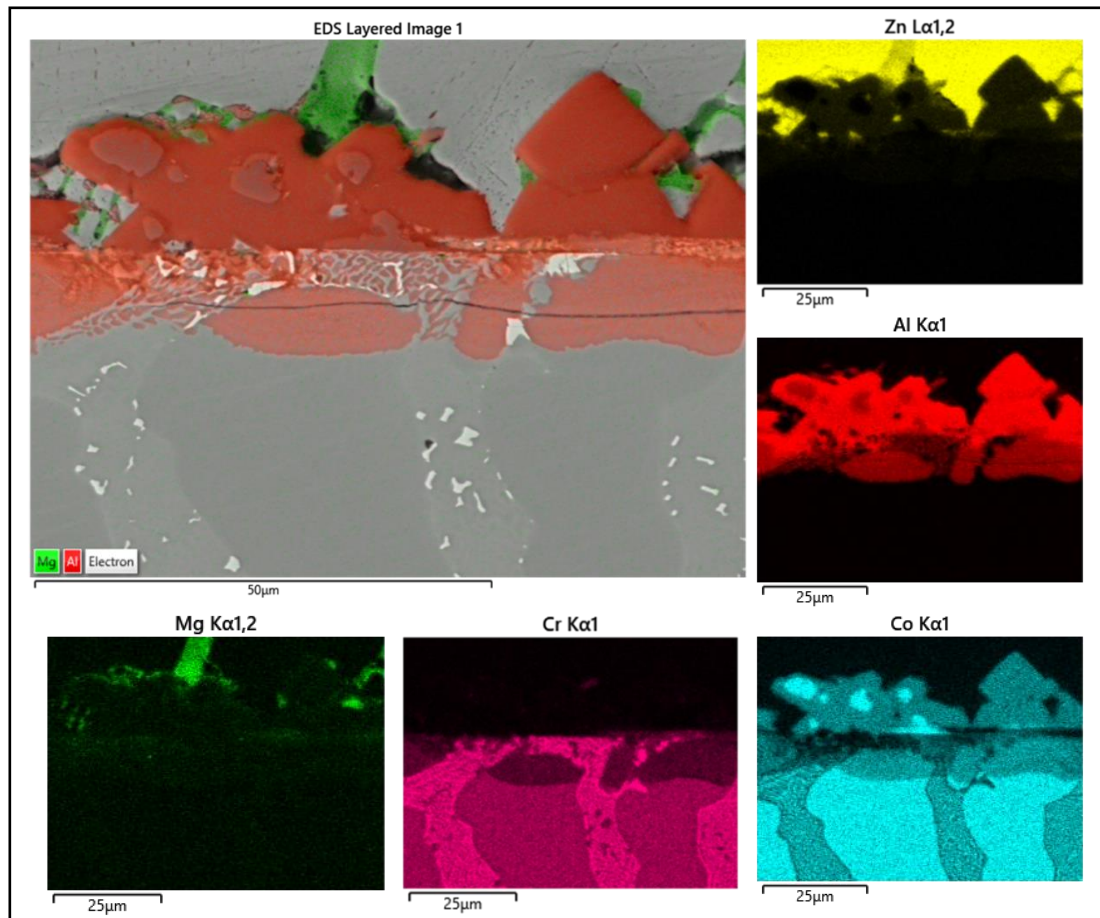


Figure 5.21 EDS mapping of the elements present in Wallex4™ after testing in Zn-Al-Mg.

5.3.3 SS 316L with HVOF Al₂O₃ vs Wallex6™

In the last material pair, WC-Co was replaced with a HVOF Al₂O₃ ceramic coating. Al₂O₃ coatings were previously investigated by conducting static immersion tests and the results were discussed in Chapter 4, Section 4.2. The same coating was applied onto a SS 316L round bar for dynamic testing and it was fabricated with a thickness of 250 µm. The SS 316L/Al₂O₃ bar was coupled with a static Wallex6™ pad specimen.

Visual inspection of the bars tested in Zn-Al (Figure 5.22a) and Zn-Al-Mg (Figure 5.22b) after extraction from each molten metal bath evidenced clear signs of damage on the ceramic coatings, leaving areas of the SS 316L specimen unprotected. Examination of the bar after 48 h of testing in Zn-Al with SEM (Figure 5.23) confirmed that structural damage occurred in the Al₂O₃ coating, as both vertical and horizontal cracks are

present. These cracks were not observed in the as-received specimen (Figure 5.1). The large horizontal crack in the SEM image shows that the coating was forced to separate from the steel bar, in a similar fashion to the mechanism observed after the static immersion tests. It was previously shown (Chapter 4, Section 4.2.4) that cracks and spallation of the coating can be linked to stresses developing due to the large thermal expansion mismatch between Al_2O_3 and SS 316L. Due to the similarities with the results obtained from the previous static tests, it was concluded that the large difference between the coefficients of thermal expansion (CTEs) of the two materials was the reason for the coating damage observed after dynamic testing. The CTEs recorded at $\sim 465^\circ\text{C}$ for Al_2O_3 and SS 316L were 8.2×10^{-6} and $21.2 \times 10^{-6} \text{ K}^{-1}$ respectively (Figure 4.30). However, despite suffering from significant damage, the ceramic coatings remained completely inert to Zn-Al and dross phases, which were observed to build up on WC-Co, were absent in Al_2O_3 .

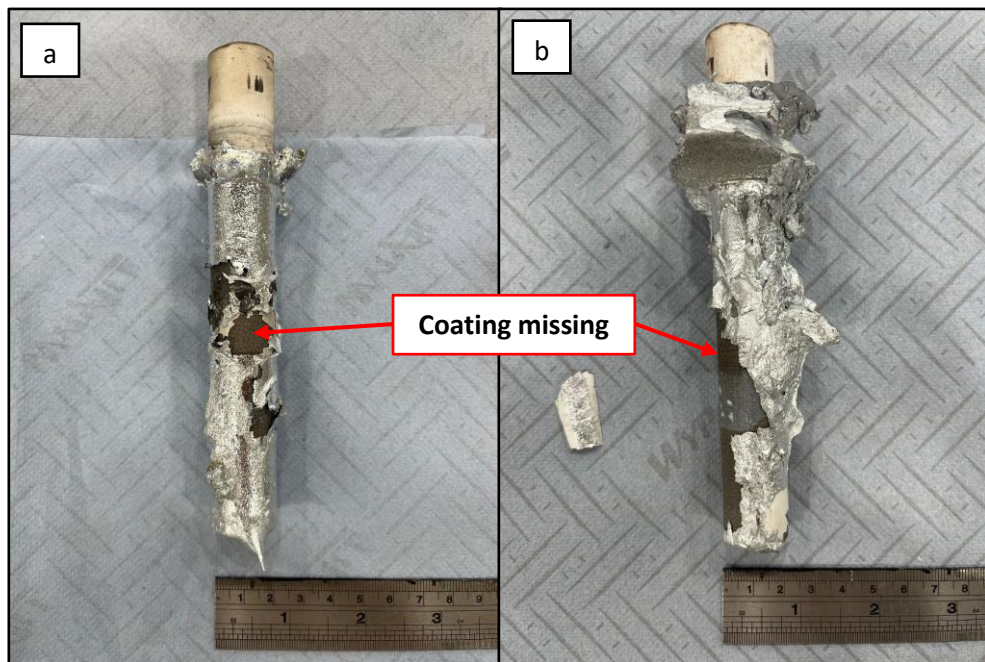


Figure 5.22 Visual inspection of the bar specimens tested in Zn-Al (a) and Zn-Al-Mg (b).

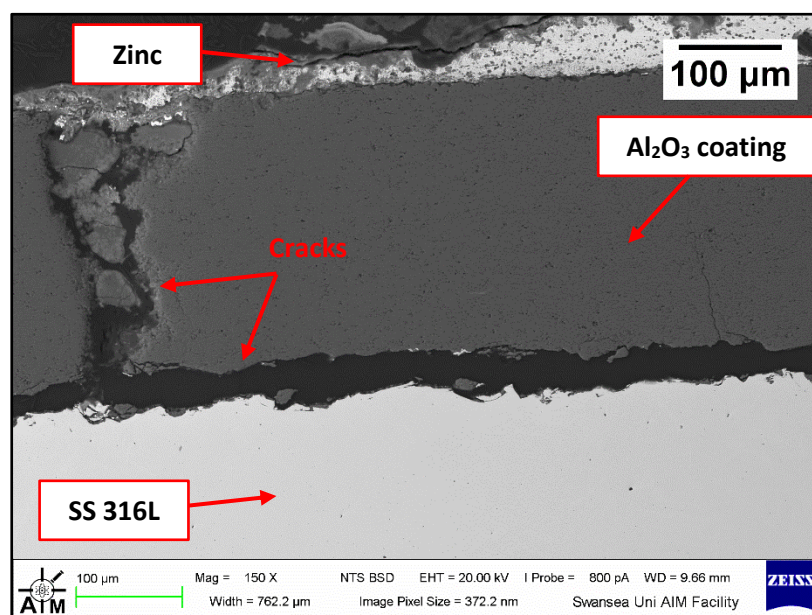


Figure 5.23 Cross-section of the Al₂O₃/SS 316L bar after dynamic testing in Zn-Al.

The contact region of the Wallex6™ counterpart after testing in Zn-Al is shown in Figure 5.24a. The image revealed that no reaction products developed on the contact surface of Wallex6™. It is again theorised that the absence of a distinct reaction layer is associated with the continuous removal of material that occurred during sliding contact. However, EDS analysis (Figure 5.24b) was conducted in the region immediately below the surface of the material exposed to wear and it was found that Zn (30.7 ± 5.6 wt.%) and Al (16.0 ± 3.8 wt.%) diffusion still occurred at the interface.

Within the unworn region, the corrosion behaviour of the Wallex6™ pad was identical to that exhibited in the previous tests. Figure 5.25 shows that intermetallic particles of Al-Co-Zn-Fe composition are present on the surface of the alloy (1). Furthermore, a subsurface reaction layer developed and it was found that Al was contained within this layer (37.2 ± 1.0 wt.%) and at the interface with the Co-solid solution phase of Wallex6™ (23.4 ± 1.3 wt.%), which are respectively indicated as location (2) and (3) in Figure 5.25. This result confirmed that Al diffused from the melt into the alloy. In addition to this, the amount of Co at location (2) is low (19.7 ± 0.5 wt.%) relative to the as-received sample (47.2 wt.%). On the other hand, at location (3), a Co content closer to that present in the bulk of the material was detected (39.8 ± 3.1 wt.%), suggesting that Co depletion from the diffusion layer occurred.

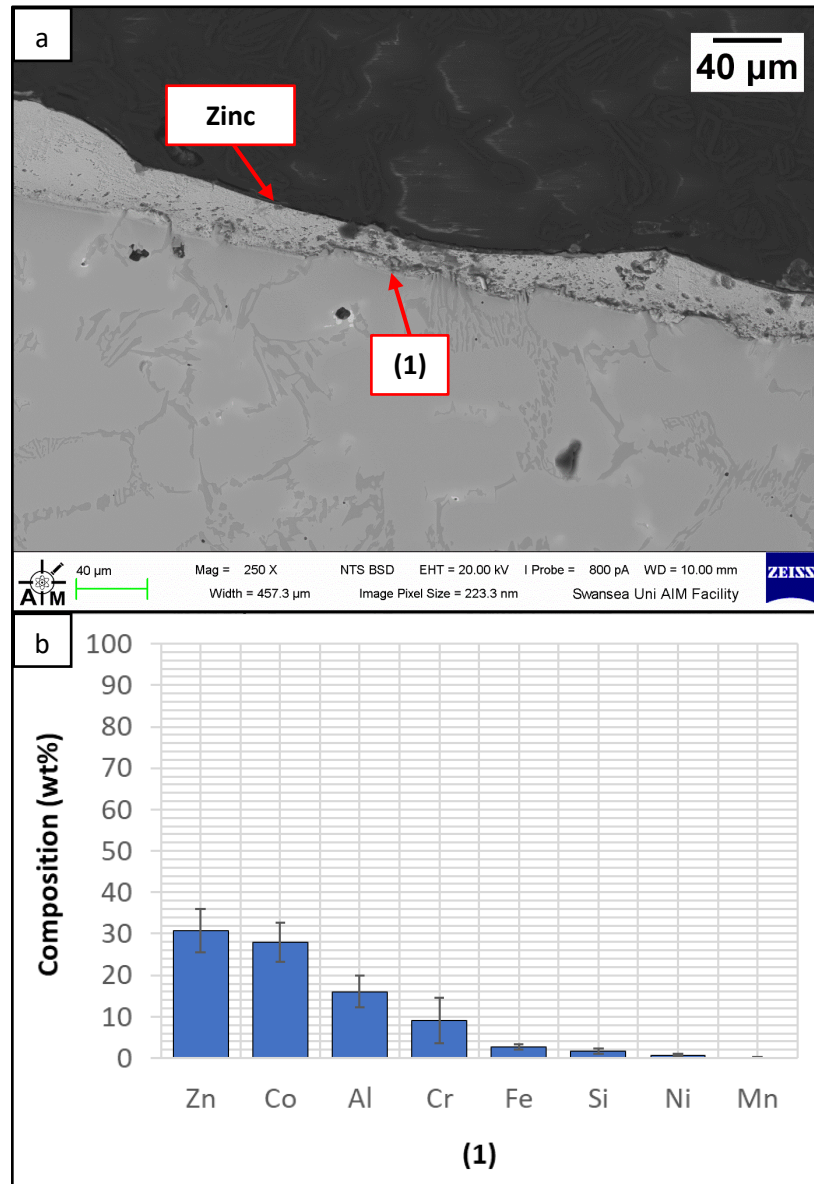


Figure 5.24 Cross-section of the contact region of the Wallex6™ pad after testing in Zn-Al (a); EDS phase elemental analysis carried out at the interface with the molten metal bath (b).

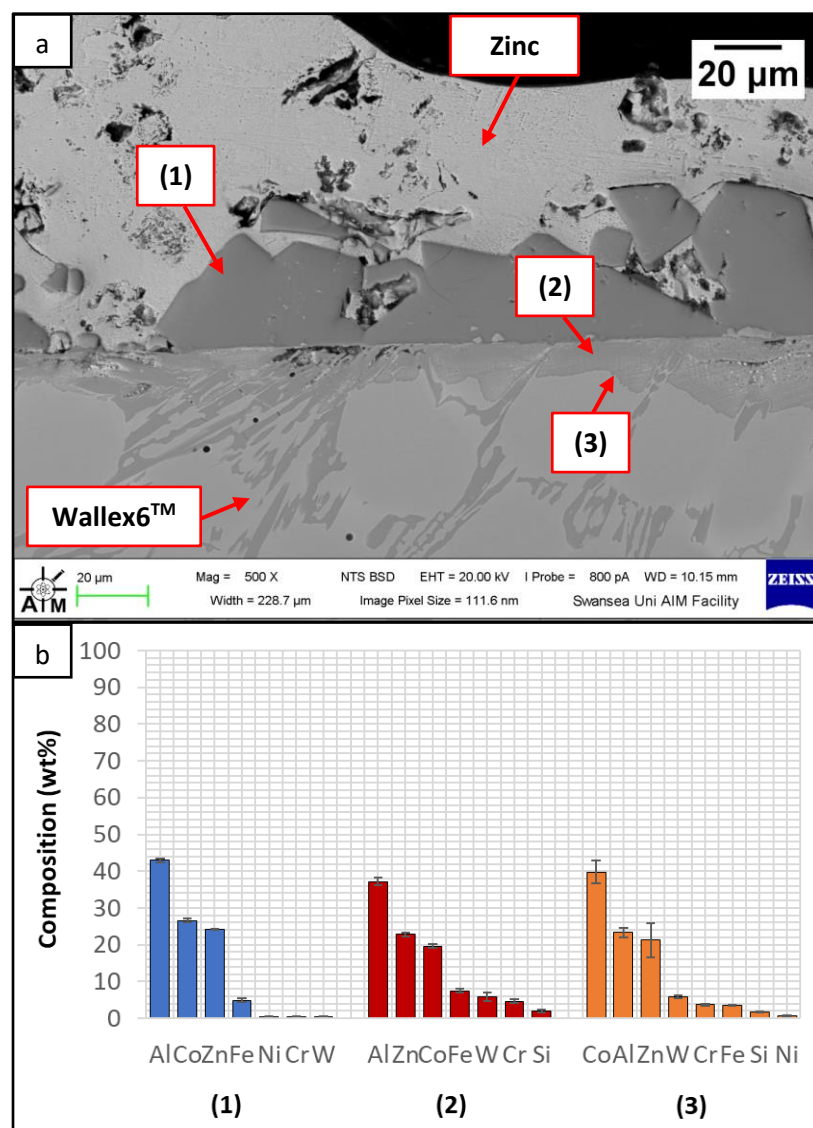


Figure 5.25 Cross-section of the unworn region of the Wallex6™ pad after testing in Zn-Al (a); EDS phase elemental analysis of the corrosion products (b).

The specimens immersed in Zn-Al-Mg showed a similar corrosion behaviour. The analysis of the cross-section of the bar revealed that no dross build-up layer was present on the ceramic coating, which did not undergo chemical reactions with the molten metal bath (Figure 5.26). This observation is in contrast to the findings that were obtained earlier in this work (Chapter 4, Section 4.2.3.2), which highlighted a possible reduction of the Al_2O_3 coating by the Mg present in the molten metal bath. However, the duration of exposure of the coating to molten Zn-Al-Mg was shorter in the dynamic tests compared to the static immersion tests, which could explain the absence of Mg diffusion into the coating. Although the coating was inert to Zn-Al-Mg,

it was again prone to cracking and spallation (Figure 5.27). No evidence of Zn infiltration in these cracks was found and, therefore, it is believed they formed during cooling after extraction from the molten metal bath.

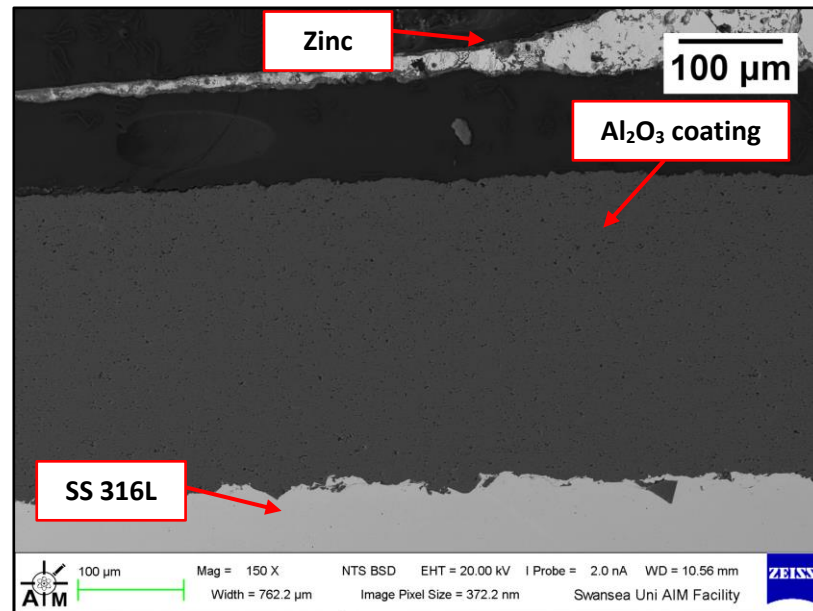


Figure 5.26 Cross-section of Al_2O_3 /SS 316L bar after dynamic testing in Zn-Al-Mg.

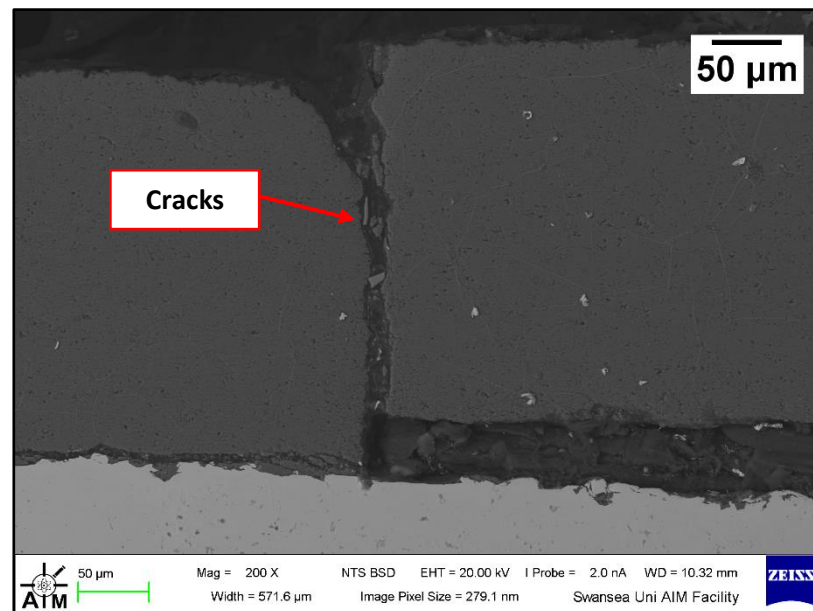


Figure 5.27 Cracks within the Al_2O_3 coating after dynamic testing in Zn-Al-Mg.

The Wallex6™ pad specimen reacted with the liquid metal bath in a similar fashion to the samples characterised previously. Within the wear region, no reaction layer was observed (Figure 5.28a) and the results of EDS analysis carried out at the interface (1) showed that Al did not diffuse into the alloy (Figure 5.28b).

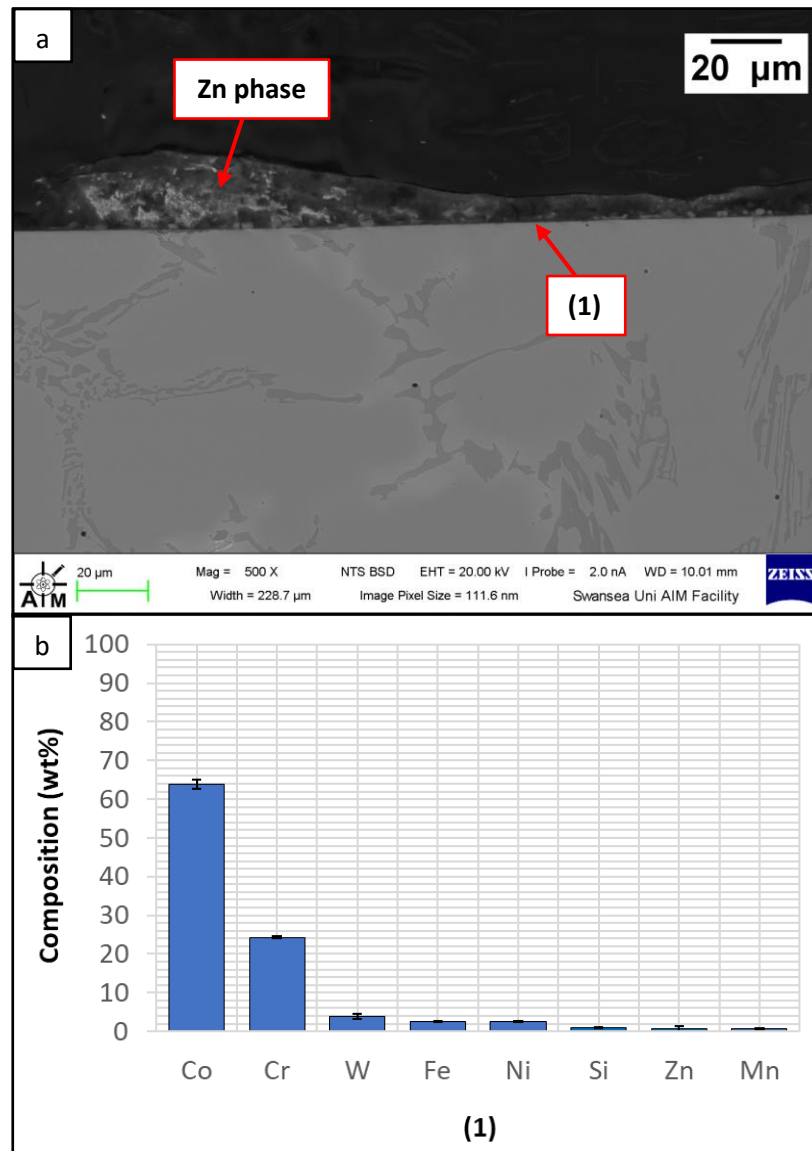


Figure 5.28 Cross-section of the contact region of the Wallex6™ pad after testing in Zn-Al-Mg (a); results of EDS phase elemental analysis of the contact surface (b).

Within the unworn region, cross intermetallic phases deposited onto the surface. Figure 5.29a shows two types of reaction products: a CoAl phase containing Zn (16.3 ± 1.1 wt.%) and a different CoAl phase with low content of Zn (1.6 ± 0.3 wt.%). Co depletion from the diffusion layer occurred, as shown by the results of EDS analysis (Figure 5.29b) which was carried out at the interface with molten metal (3) and at the interface between the subsurface reaction layer and the bulk of the material (4).

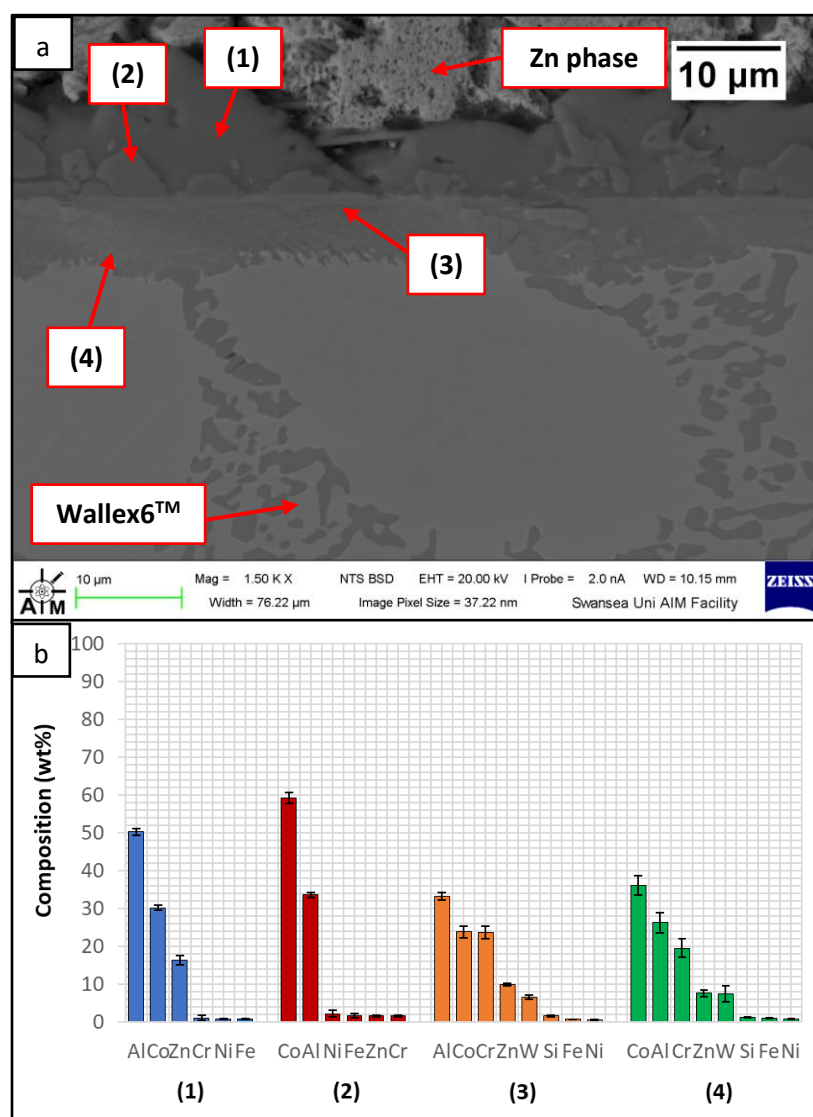


Figure 5.29 Cross-section of the unworn region of the Wallex6™ pad after testing in Zn-Al-Mg (a); EDS phase elemental analysis of the corrosion products (b).

Overall, the results of the dynamic corrosion tests showed that the ceramic coating is the only material which remained inert during the 48 hours of dynamic testing. It showed better performance compared to the WC-Co coatings, whose Co matrix reacted with the molten metal bath forming intermetallic compounds at the interface with the molten metal bath. Although previous studies highlighted that baths with Al content above 0.3 wt.% reduced the corrosion rate of WC-Co (Seong et al., 2001), the results of the present study showed that the coatings corroded both in Zn-Al and Zn-Al-Mg to a similar extent. The two Co-based alloys, namely Wallex6™ and Wallex4™, were severely corroded after exposure to molten metal. The reactivity of Wallex4™ was found to not significantly differ from that of Wallex6™, due to their similar chemical composition. Therefore, it did not show superior performance at the chosen testing conditions. The introduction of Mg did not affect the corrosion behaviour of the coupling pairs with the surrounding environment.

However, in order to investigate on the effect of the higher Al content in Zn-Al-Mg, the amount of Al, Co and Zn contained within the reaction layers of the pad specimens was tabulated for both Zn-Al (Table 5.3) and Zn-Al-Mg (Table 5.4). Graphs showing the concentration of these elements and the thickness of the diffusion layers are found in Figure 5.30 and Figure 5.31 respectively. It was observed that the content of Al within the reaction layer decreased after changing bath composition from Zn-Al to Zn-Al-Mg. On the other hand, the reaction layers contained more Co, suggesting that less depletion of Co from these layers occurred in the Zn-Al-Mg baths. Furthermore, the diffusion of Zn into the alloy diminished in the Zn-Al-Mg bath with higher Al concentration. An analogous behaviour was observed on the SS 316L specimens tested earlier in this study, due to the inhibition of the reaction between the SS 316L and the molten Zn in the bath (Chapter 3, Section 3.3.2.1). A decrease in the depth of the diffusion layer was also observed in the Wallex6™ specimens, as shown in Figure 5.31, although no significant change was detected in Wallex4™.

Table 5.3 Main composition of the reaction layer of the pads after testing in Zn-Al.

Coupling pair	Pad Material	Al [wt.%]	Co [wt.%]	Zn [wt.%]
Wallex6™/WC-Co vs Wallex6™	Wallex6™	37.3 ± 1.2	20.6 ± 3.8	23.3 ± 5.1
Wallex6™/WC-Co vs Wallex4™	Wallex4™	28.6 ± 3.2	36.3 ± 7.0	12.0 ± 3.6
SS 316L/Al ₂ O ₃ vs Wallex6™	Wallex6™	37.2 ± 1.0	19.7 ± 0.5	22.8 ± 0.5

Table 5.4 Main composition of the reaction layer of the pads after testing in Zn-Al-Mg.

Coupling pair	Pad Material	Al [wt.%]	Co [wt.%]	Zn [wt.%]
Wallex6™/WC-Co vs Wallex6™	Wallex6™	35.2 ± 1.5	30.9 ± 5.3	10.01 ± 6.2
Wallex6™/WC-Co vs Wallex4™	Wallex4™	8.2 ± 4.5	40.8 ± 1.0	5.0 ± 3.4
SS 316L/Al ₂ O ₃ vs Wallex6™	Wallex6™	33.2 ± 1.0	23.8 ± 1.6	9.8 ± 0.3

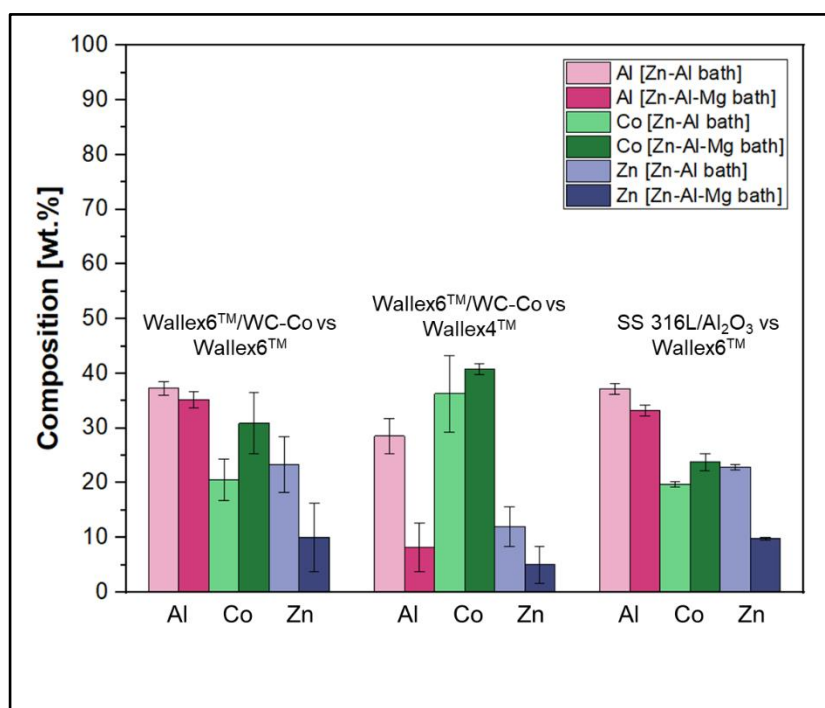


Figure 5.30 Concentration of Al, Co and Zn in the diffusion layer of the pad specimens after exposure to Zn-Al and Zn-Al-Mg.

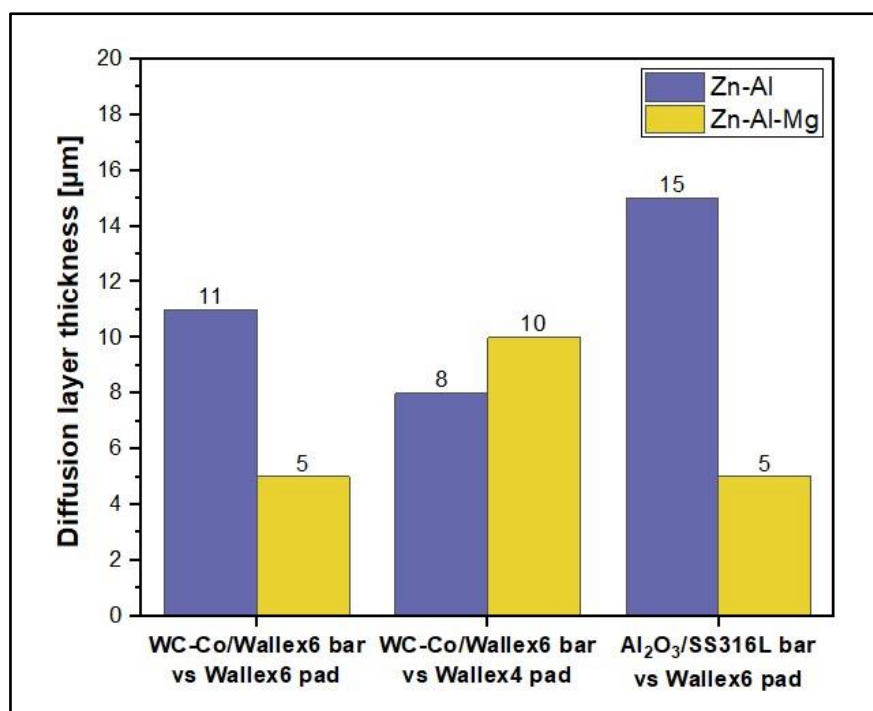


Figure 5.31 Average thickness of the diffusion layers developed in the pads for each coupling.

5.3.4 Phase Identification

The results of dynamic testing in Zn alloy showed that corrosion products developed in WC-Co coatings as well as in Wallex6TM and Wallex4TM. Since the matrix phase in each of these materials contains Co and (W, Cr) carbides have been demonstrated to have high stability in liquid Zn, the corrosion of these materials is the result of the reaction between the Zn bath and the Co, as well as the Fe, present in their microstructures. It is reported that, according to the Co-Zn phase diagram, CoZn, Co₅Zn₂₁ and CoZn₁₃ are the Zn-rich phases that are thermodynamically stable at 465 °C. However, previous work (Xibao, 2003), which analysed the corrosion behaviour of Co-Cr-W alloys in liquid Zn, showed that only Co₅Zn₂₁ was present on the surface of the alloy. In addition to this, the corrosion products were composed of Fe₁₁Zn₄₀ and Fe₄Zn₉. As explained earlier, Co and Fe react with the Al present in the bath and it is reported that CoAl and Fe₂Al₅ can form (Seong et al., 2001). The formation of new phases after exposure to Zn alloy is also a function of kinetics, explaining why phases that are known to be thermodynamically stable do not form.

To identify the phases that developed during dynamic testing, the tested specimens were analysed with XRD. The analysis was carried out following the procedures outlined in Chapter 2, Section 2.2.4. A cross-section of the Wallex6™ bar with WC-Co coating that was immersed in Zn-Al was analysed first. As the phases are present only on the surface of the WC-Co coating and not in the bulk of the alloy, a collimator was used to improve the detectability of the new phases. The results of the analysis are illustrated in Figure 5.32. It was observed that only Zn and WC phases were shown in the diffractogram, suggesting that the new phases could not be detected with XRD, even when a collimator was used, due to being located at the interface and because of their thickness, which was previously measured to be in the order of $\sim 10\text{ }\mu\text{m}$.

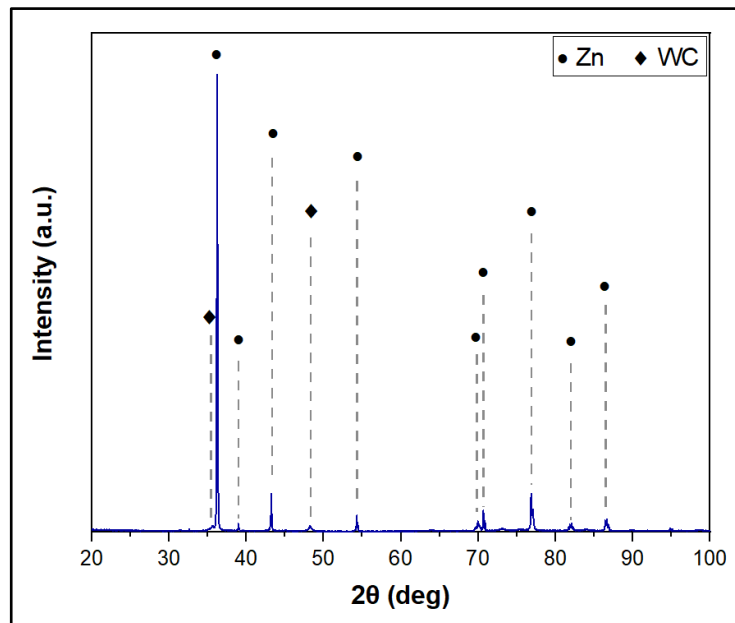


Figure 5.32 XRD carried out on a Wallex6™ bar with WC-Co after immersion in Zn-Al.

The analysis was repeated on the Wallex4™ pads tested in Zn-Al. This time the collimator was disconnected as the surface of the material was scanned, instead of the cross-section. The analysis was performed on a pickled sample without the top Zn layer. The results are found in Figure 5.33 and more peaks were shown in the diffractogram. These peaks were matched with those of Fe, C, Cr, Mo, Zn and Fe₃C. However, none of the expected phases present in the materials were identified. This suggests that the new phases that formed in the materials may not be present in the

database used for matching the XRD peaks, making the identification process of these new phases challenging with the available XRD tools.

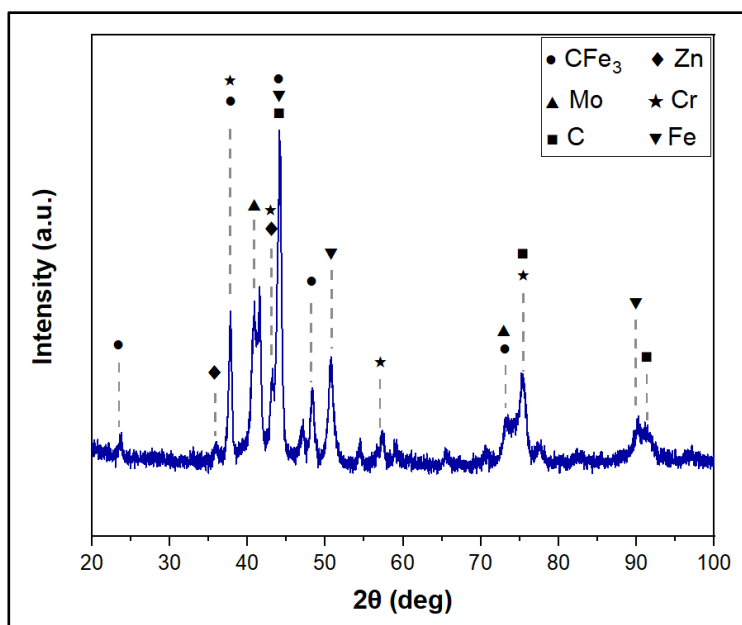


Figure 5.33 XRD carried out on a Wallex4™ pad after immersion in Zn-Al.

5.3.5 Wear Scar Analysis

The bar displacement and the wear coefficient of each pad specimen after 48 hours was calculated according to the procedures previously outlined in Chapter 2, Section 2.4.2.3. The results are summarised in Table 5.5 for Zn-Al and Table 5.6 for Zn-Al-Mg. These values were plotted in Figure 5.34. Moreover, the percentage change of these parameters after changing bath from Zn-Al to Zn-Al-Mg was calculated (Table 5.7).

Table 5.5 Wear coefficient and displacement after testing in Zn-Al.

Coupling pair	Pad Material	Wear coefficient $k \times 10^{-6}$ [mm ³ N ⁻¹ m ⁻¹]	Displacement [mm]
Wallex6™/WC-Co vs Wallex6™	Wallex6™	26.3	0.80
Wallex6™/WC-Co vs Wallex4™	Wallex4™	30.9	1.01
SS 316L/Al ₂ O ₃ vs Wallex6™	Wallex6™	9.7	0.46

Table 5.6 Wear coefficient and displacement after testing in Zn-Al-Mg.

Coupling pair	Pad Material	Wear coefficient $k \times 10^{-6}$ [mm ³ N ⁻¹ m ⁻¹]	Displacement [mm]
Wallex6™/WC-Co vs Wallex™	Wallex6™	4.5	0.21
Wallex6™/WC-Co vs Wallex4™	Wallex4™	1.3	0.10
SS 316L/Al ₂ O ₃ vs Wallex6™	Wallex6™	3.6	0.21

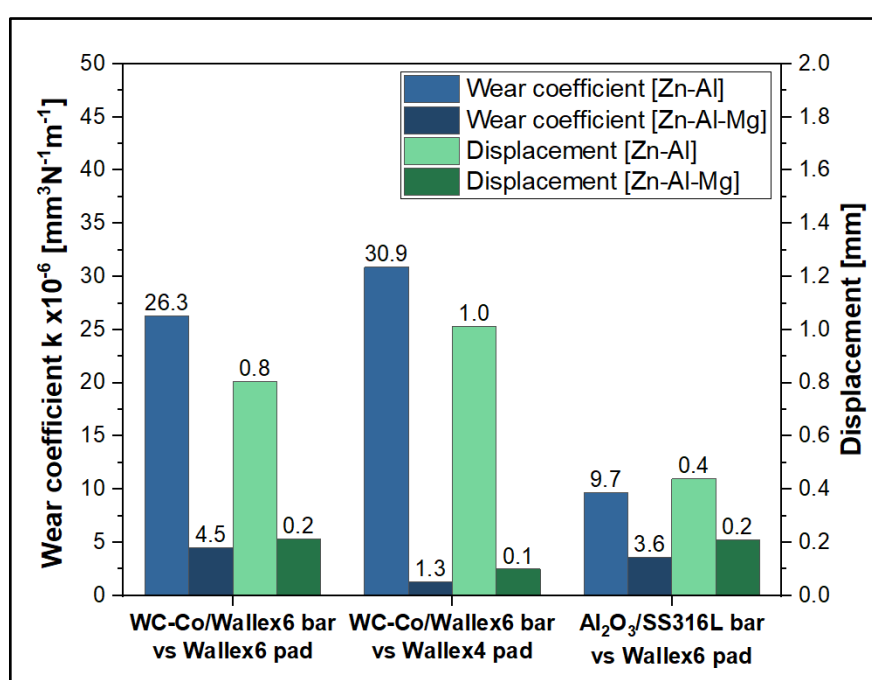


Figure 5.34 Plot of the wear coefficients and values of displacement after dynamic testing.

Table 5.7 Percentage change of wear coefficient and displacement after changing bath from Zn-Al to Zn-Al-Mg.

Coupling pair	Pad Material	Percentage decrease wear coefficient	Percentage decrease displacement
Wallex6™/WC-Co vs Wallex™	Wallex6™	83%	74%
Wallex6™/WC-Co vs Wallex4™	Wallex4™	96%	90%
SS 316L/Al ₂ O ₃ vs Wallex6™	Wallex6™	63%	54%

The results of the wear tests conducted in Zn-Al highlighted that Al₂O₃/SS 316L had the lowest value of displacement (0.46 mm) and inflicted the lowest wear damage on its counterpart ($k = 9.7 \times 10^{-6} \text{ mm}^3\text{N}^{-1}\text{m}^{-1}$). The hardness of the materials in the current bearing configuration was previously measured by Faulkner (2020). It was found that the hardness of spherical WC lied between 2100-2500 HV, which is significantly higher than the hardness of Wallex6TM (400 HV) and Wallex4TM (570 HV). As a result, it is believed that the WC-Co coatings inflicted severe wear damage to their softer counterparts on the contact surface, due to the greater hardness of the WC particles. This observation aligns with the findings of Zhang (2005), who reported that WC particles could easily scar the surface of Stellite alloys. The hardness of Al₂O₃ was measured to be approximately 1680 HV (Chapter 3, Section 3.4.5) and, therefore, it inflicted less wear damage on its counterpart.

However, previous studies (Zhang, 2005) demonstrated that the wear process of materials in liquid Zn is complex, due to the chemical reactions with the molten metal bath and the complexity of the intermetallic compounds. For this reason, surface damage or removal of materials during sliding contact can involve multiple mechanisms. It is reported that wear debris can form following the breakup of the materials as well as of the intermetallic compounds. Wear debris was found to react with the elements present in the molten metal, forming particles which could easily plough the contacting surfaces (Zhang, 2005; Zhang et al., 2001). In this work, the CoAl phases observed on the surface of WC-Co were absent on the Al₂O₃ coating, due to the inertness of the ceramic material. The CoAl phase is hard and can groove the bearing surfaces (Zhang & Tang, 2003). For this reason, it is theorised that the absence of Co-based aluminides on the Al₂O₃ coating contributed to reduce the wear damage on the Wallex6TM counterpart. Figure 5.35 illustrates a comparison of the wear scars after testing in Zn-Al with 3D imaging.

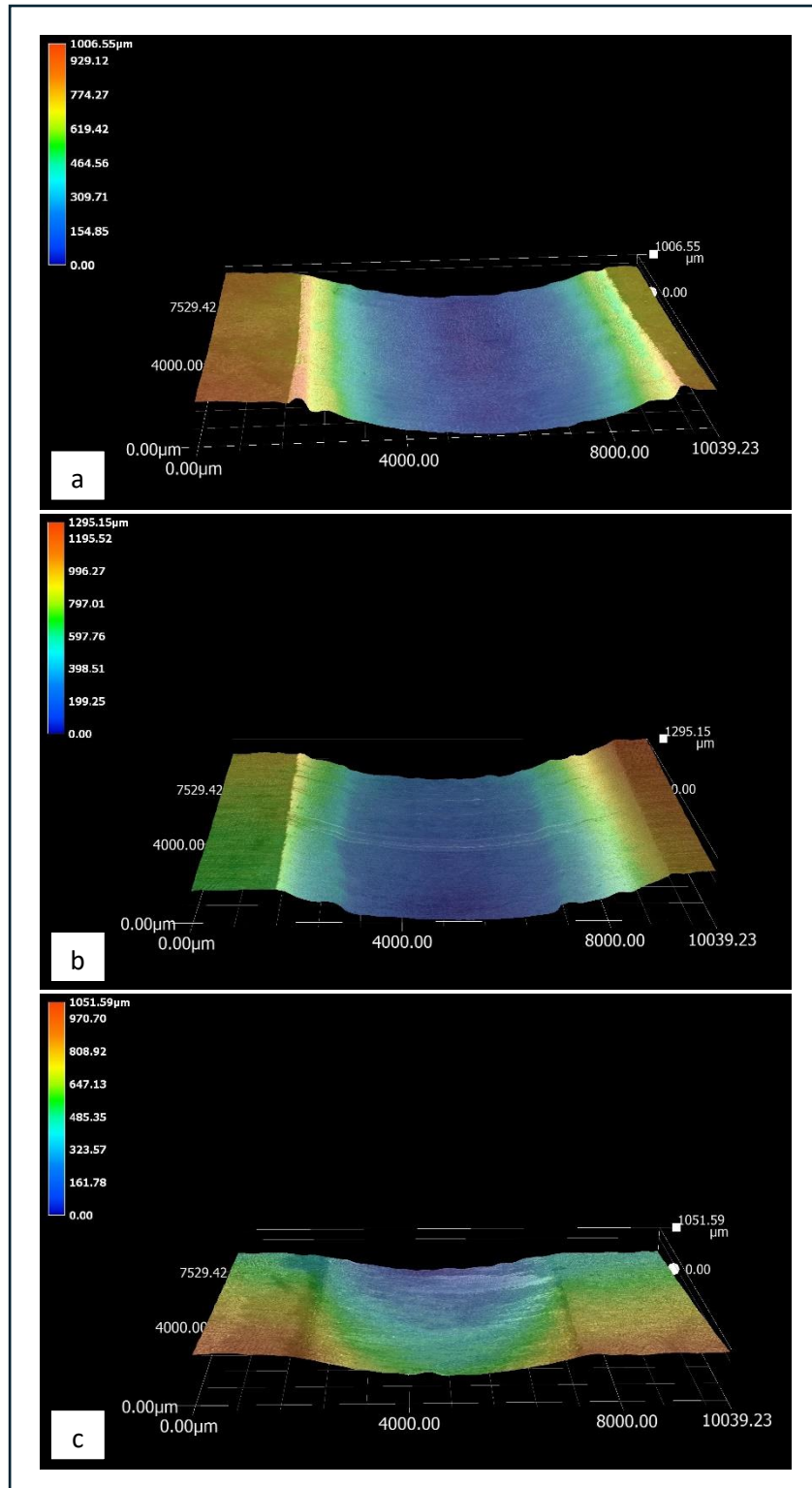


Figure 5.35 3D imaging of the wear scars produced on the specimens tested in Zn-Al: Wallex6™ after sliding with Wallex6™/WC-Co (a); Wallex4™ after sliding with Wallex6™/WC-Co (b); Wallex6™ after sliding with SS 316L/Al₂O₃ (c).

The measurements of displacement and wear coefficients obtained for the specimens tested in Zn-Al-Mg revealed that the Wallex4™ pad exhibited the highest wear resistance (0.1 mm displacement, $k = 1.3 \times 10^{-6} \text{ mm}^3\text{N}^{-1}\text{m}^{-1}$), although less wear damage was observed in all the pad specimens immersed in Zn-Al-Mg compared to Zn-Al, as shown in Table 5.7. Similar reaction products formed in the two molten metal baths; however, the composition of the reaction layers formed at high Al concentration was found to vary from that measured on the samples tested in Zn-Al. It was earlier explained that Wallex™ pads tested in Zn-Al-Mg exhibited less corrosion by molten Zn after 48h of exposure to the liquid metal. It is reported that during the rotation of submerged pot roll bearings, cracks initiate in the reaction layer and at its interface with the bulk of the material. This process is followed by the detachment of the corrosion products and of the bearing materials, resulting in the formation of wear debris, which can inflict further damage to the contact surfaces (Zhang, 2005). Therefore, it is plausible that the specimens submerged in Zn-Al-Mg displayed less wear damage due to their limited corrosion relative to the Zn-Al bath, which reduced the likelihood of breakage of the corrosion products and, consequently, the rate of material removal at the testing conditions chosen for the experiments. The higher wear resistance exhibited in Zn-Al-Mg can be visualised with the 3D images of the contacting surfaces (Figure 5.36).

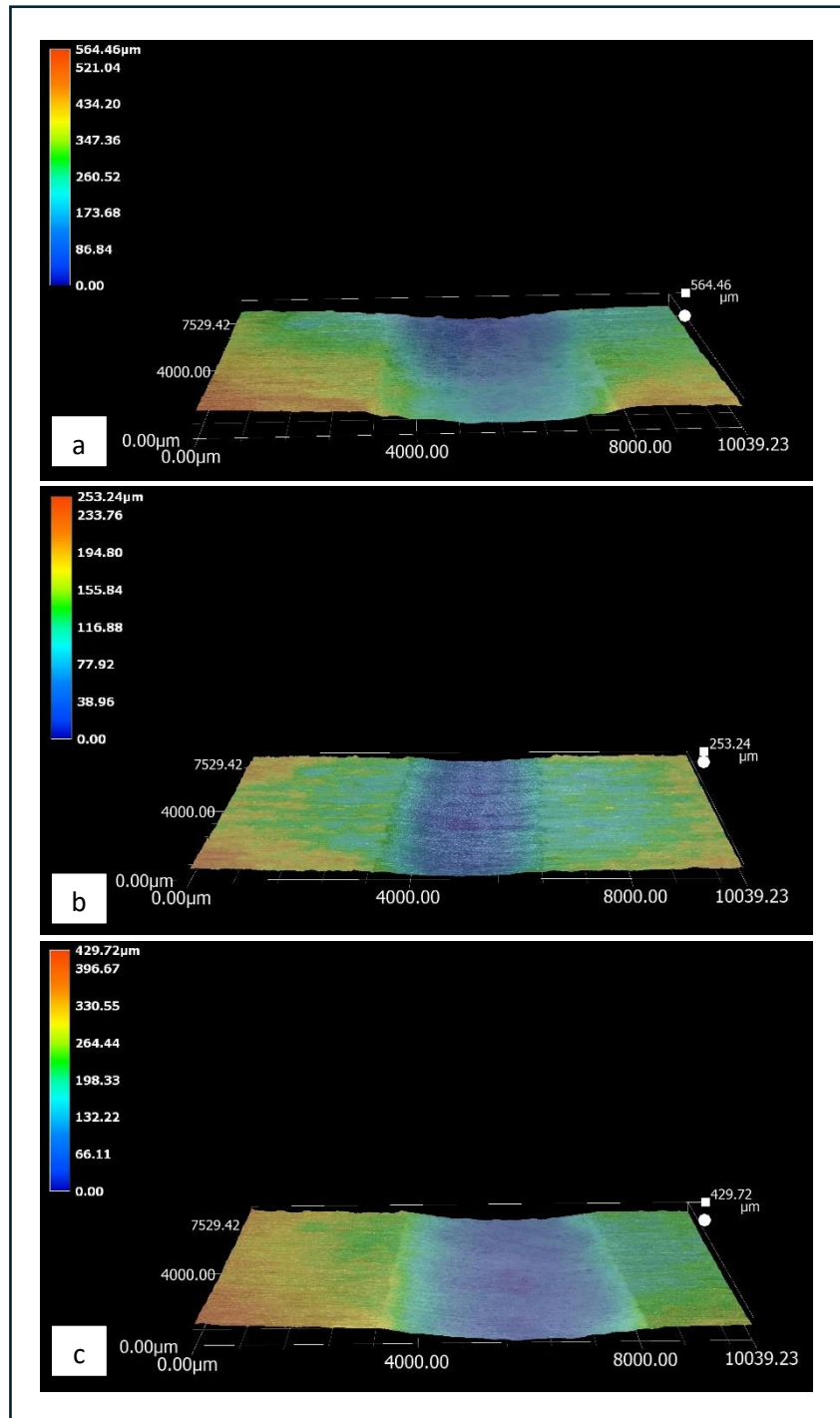


Figure 5.36 3D imaging of the wear scars produced on the pad specimens tested in Zn-Al-Mg: Wallex6™ after sliding with Wallex6™/WC-Co (a); Wallex4™ after sliding with Wallex6™/WC-Co (b); Wallex6™ after sliding with SS 316L/Al₂O₃ (c).

5.4 Summary

Dynamic wear testing in molten Zn alloy was conducted to assess the corrosion behaviour and wear resistance of three material pairs using a bespoke wear testing rig. Like the previous static immersion tests, the experiments were performed in Zn-Al and Zn-Al-Mg bath compositions. After exposure to Zn-Al, the Co matrix of the WC-Co coatings was attacked by the molten metal, mainly forming Co-based aluminides. On the other hand, an Al_2O_3 coating remained completely inert after 48 hours dynamic testing, validating the results of static immersion testing. All the WallexTM grades were corroded by molten Zn-Al, due to Al and Zn diffusion into the alloys. Little evidence of reaction products was found on the contact surface, possibly due to material removal in that region through wear. The presence of Mg in the Zn-Al-Mg bath did not significantly vary the corrosion behaviour as no interactions with the materials were detected, including the Al_2O_3 coating; however, the diffusion of Zn into the WallexTM pads was reduced by approximately 60% in the Zn-Al-Mg bath compared to Zn-Al.

The wear scar on the pad specimens was analysed after testing and it was found that all the materials tested in Zn-Al-Mg exhibited less wear damage. It was postulated that the higher Zn diffusion into the materials tested in Zn-Al contributed to the removal of material during sliding contact with the counterpart. Out of the three material couplings investigated in this study, minimal wear damage in both Zn-Al and Zn-Al-Mg was only obtained by pairing the Wallex6TM with a Al_2O_3 /SS 316L, due to the inertness of the ceramic material compared to WC-Co. The results of dynamic testing confirmed that the introduction of ceramic materials has the potential to improve the performance of galvanising pot roll bearing systems. Despite the similar corrosion behaviour, replacing Wallex6TM with Wallex4TM in the current bearing system may still lead to financial benefits, due to the lower cost of Wallex4TM.

Conclusions and Reflections

Conclusions

The limited service life of the galvanising pot hardware, such as the pot roll bearings, is a bottleneck to production and quality of galvanised steel strip steel. The main cause for the severe deterioration experienced by the journal bearings is the reaction occurring between the bearing materials and the Zn alloy bath. This project examined the corrosion behaviour of ceramic materials with potential for use as galvanising bearing materials with extended service life.

Static testing in Zn-Al and Zn-Al-Mg was conducted on ceramics available commercially, namely hBN, BN Grade M26, Macor®, AlN-BN, 3YSZ, Si₃N₄ and Al₂O₃. The performance of these materials was compared to that of two benchmarks, namely SS 316 and HVOF WC-Co coatings. The results of static testing showed that the two benchmarks were severely corroded in liquid Zn alloy after 5 weeks of exposure to molten metal. Conversely, evidence of corrosion was not found in the ceramic materials, which remained inert to both Zn-Al and Zn-Al-Mg. The wear behaviour under dry sliding conditions and at room temperature was found to vary significantly between the ceramics investigated in this study. 3YSZ, Si₃N₄ and Al₂O₃ showed superior wear resistance, whereas hexagonal BN displayed the lowest coefficient of friction.

SiAlON and hexagonal BN composites were produced with the intention of combining high wear resistance and lubricious properties. The content of hBN was varied from 10 wt.% to 30 wt.% and samples for testing were fabricated using Field Assisted Sintering Technology. The corrosion and wear resistance of SiAlON-hBN was compared to samples containing 100 wt.% SiAlON, as well as the hard cubic phase of BN. No substantial differences were found between the samples tested in the experiment, as the materials displayed the same corrosion resistance in Zn-Al and Zn-Al-Mg, and the coefficient of friction was not lowered by the additions of BN lubricant.

The brittleness of ceramics may limit their use as bearing materials; however, ceramics can be coated onto ductile materials, such as steel, and shield the bearing from the attack of the molten metal bath. Static immersion tests were conducted on Al_2O_3 coatings to compare their performance against sintered bulk Al_2O_3 . While the material remained inert in Zn-Al after 5 weeks, interactions with the Mg bath were observed, potentially restricting the use of this material in galvanising baths containing Zn-Al only. Additionally, Al_2O_3 coating showed evidence of cracking and spallation due to the large thermal expansion mismatch with the steel substrates.

The behaviour of Al_2O_3 coatings was also investigated by conducting dynamic testing using a bespoke testing rig. Al_2O_3 was coupled with Wallex6™ and its performance was compared to WC-Co coatings on Wallex6™ coupled with Wallex6™ and Wallex4™. It was shown that out of the three material couplings investigated in this study, minimal wear damage in both Zn-Al and Zn-Al-Mg was only obtained when using the Al_2O_3 /Wallex6™ pair, due to the inertness of the ceramic material compared to WC-Co.

Novelty of the Research

The research in this thesis has displayed novelty and adds to the extensive body of research that has previously explored the reactions between Zn alloy and galvanising pot hardware materials. Despite the existence of studies which investigated the use of ceramics to make bath hardware with extended durability in molten Zn, only a small selection of materials was previously experimented. The majority of the existing studies determined the short-term performance of materials in Zn alloy and the effect of changing the bath composition on the corrosion behaviour of the materials was not explored. Lack of information was found on the interactions with galvanising baths containing Mg. The present work focused on the long-term performance of ceramic materials and the experiments were conducted in baths containing Zn-Al, as well as Zn-Al-Mg, in order to study the effect of changing the chemistry of the bath. Furthermore, a bespoke testing rig was designed to permit dynamic testing of new bearing materials without the need of conducting online wear testing.

Industrial Uptake

The experiments conducted in this project enabled to analyse the properties of ceramics to assess whether these materials can be used for making galvanised pot roll bearings with improved performance. The work presented in this thesis demonstrated that the corrosion behaviour of ceramics in liquid Zn alloy is superior to that of materials which have been traditionally used to make the hardware components in CG lines, such as SS 316L, WC-Co and Wallex6TM alloys. While these materials reacted with the molten metal, forming complex intermetallic compounds which are detrimental to the lifetime of the journal bearings, the use of ceramic materials did not lead to the formation of intermetallic phases after exposure to the molten metal bath. The findings obtained in this project highlighted that the range of ceramics with potential to resist the attack of the hot dip galvanised bath is very broad. No intermetallic phases developed on the ceramics after immersion testing in Zn-Al and Zn-Al-Mg during the five weeks of static testing and even under dynamic conditions, outperforming the current bearing materials. As a result, the service life of journal bearings which are not subjected to deterioration in liquid Zn alloy can be extended beyond the current five-week campaign, as excessive strip vibrations will be prevented, as well as defects in the coating attributed to poor control of the gas knives. Therefore, the investigations discussed in the thesis suggested that the use of ceramic materials can lead to an increase in production yield with high financial reward, considering that the sales value of production for automotive grade galvanised steel can reach up to £40,000 per hour.

Future Work

It was concluded that ceramic materials have potential to increase the longevity of bearing life, which is key for the economical profitability of the hot dip galvanising line. Although the results obtained from the corrosion tests holds promise that ceramic coatings can be used in the development of new journal bearing systems, the tendency of the coatings to fail due to thermal expansion mismatch may pose new

challenges. Therefore, future work should be focused on further optimisation of the coatings, which may require exploring alternatives to Al_2O_3 coatings, such as ZrO_2 , or the use of multilayer structures that can reduce the difference between the coefficients of thermal expansion of the materials. The identification of the phases formed after exposure to Zn alloy can be performed with techniques, such as EBSD, which may allow to overcome the limitations of using XRD. The testing rig discussed in Chapter 5 can be used by research and industrial staff to facilitate the development of the new ceramic coatings.

Bibliography

Abdelbary, A., & Chang, L. (2023). 7 - Lubrication and surface engineering. In A. Abdelbary & L. Chang (Eds.), *Principles of Engineering Tribology* (pp. 295-343). Academic Press. <https://doi.org/10.1016/B978-0-323-99115-5.00012-8>

Adeniyi, A. S., Ahmed, B. A., Hakeem, A. S., Patel, F., Bakare, A. I., Ul-Hamid, A., Khan, A. A., Ehsan, M. A., & Khan, T. I. (2019). The Property Characterization of α -Sialon/Ni Composites Synthesized by Spark Plasma Sintering. *Nanomaterials*, 9(12), 1682. <https://doi.org/10.3390/nano9121682>

Ahmed, B. A., Laoui, T., & Hakeem, A. S. (2020). Development of calcium stabilized nitrogen rich α -sialon ceramics along the $\text{Si}_3\text{N}_4:1/2\text{Ca}_3\text{N}_2:3\text{AlN}$ line using spark plasma sintering. *Journal of Advanced Ceramics*, 9(5), 606-616. <https://doi.org/10.1007/s40145-020-0400-y>

Angeli, G., Brisberger, R., Bülter, M., Diez, L., Filthaut, C., Fischer, W., Koll, T., Maiwald, T., Pesci, C., & Richter, A. (2014). The new family of European ZM coatings—a promising option for the automotive industry. Proc. of 4th International European Conference on Steels in Cars and Trucks (SCT), Braunschweig, Germany.

Azimi, A., Ashrafizadeh, F., Toroghinejad, M. R., & Shahriari, F. (2012). Metallurgical assessment of critical defects in continuous hot dip galvanized steel sheets. *Surface and Coatings Technology*, 206(21), 4376-4383. <https://doi.org/10.1016/j.surfcoat.2012.04.062>

Ba, E. C. T., Dumont, M. R., Martins, P. S., Drumond, R. M., Martins da Cruz, M. P., & Vieira, V. F. (2021). Investigation of the effects of skewness R_{sk} and kurtosis R_{ku} on tribological behavior in a pin-on-disc test of surfaces machined by conventional milling and turning processes. *Materials Research*, 24. <https://doi.org/10.1590/1980-5373-MR-2020-0435>

Balakrishnan, S., Baker, C. E., & Rahnejat, H. (2010). 18 - Fundamentals of hydrodynamic journal bearings: an analytical approach. In H. Rahnejat (Ed.), *Tribology and Dynamics of Engine and Powertrain* (pp. 591-614). Woodhead Publishing. <https://doi.org/10.1533/9781845699932.2.591>

Basu, B., Kalin, M., & Kumar, B. V. M. (2020). *Friction and Wear of Ceramics: Principles and Case Studies*. Wiley.

Beentjes, P., Bottema, J., Salgin, B., & Vrenken, J. (2021). An Innovative GI with Improved Gallling and Surface Properties for Exposed Automotive Applications. 12th International Conference on Zinc and Zinc Alloy Coated Steel Sheet, Virtual Conference

Berger, L. I. (2020). *Semiconductor Materials*. CRC Press.

Brant, J. A., Brunetta, C. D., & Aitken, J. A. (2013). 5.09 - Chalcogenides and Nonoxides. In J. Reedijk & K. Poeppelmeier (Eds.), *Comprehensive Inorganic Chemistry II (Second Edition)* (pp. 213-283). Elsevier. <https://doi.org/10.1016/B978-0-08-097774-4.00510-6>

Bright, M., & Ensminger, A. (2004). Identification of Failure Mechanisms in Correcting Roll Bearings of a Continuous Galvanizing Line. Galvanizer's Association Annual Meeting, Charleston, SC, USA.

Bright, M. A. (2007). *Dissolution and diffusion characteristics of 316L stainless steel in molten zinc containing variable concentrations of aluminum*. PhD Thesis. West Virginia University. Morgantown, WV, USA.

Bruce, R. W. (2012). *Handbook of Lubrication and Tribology, Volume II: Theory and Design, Second Edition*. CRC Press.

Brunnock, M. S., Jones, R. D., Jenkins, G. A., & Llewellyn, D. T. (1996). Durability of bath hardware materials in continuous galvanizing. 88th Galvanizers Association Meeting Chicago, IL, USA.

Callister, W. D., & Rethwisch, D. G. (2013). *Materials Science and Engineering: An Introduction, 9th Edition: Ninth Edition*. John Wiley and Sons, Incorporated.

Cao, Y., Du, L., Huang, C., Liu, W., & Zhang, W. (2011). Wear behavior of sintered hexagonal boron nitride under atmosphere and water vapor ambiances. *Applied Surface Science*, 257(23), 10195-10200. <https://doi.org/10.1016/j.apsusc.2011.07.018>

Carrapichano, J. M., Gomes, J. R., & Silva, R. F. (2002). Tribological behaviour of Si₃N₄-BN ceramic materials for dry sliding applications. *Wear*, 253(9), 1070-1076. [https://doi.org/10.1016/S0043-1648\(02\)00219-3](https://doi.org/10.1016/S0043-1648(02)00219-3)

Chakraborty, A., & Ghassemi-Armaki, H. (2021). Evaluation of Initiation and Propagation of LME Cracks on the Galvanised 3G-AHSS Using Interrupted Resistance Spot-Welding Method. 12th International Conference on Zinc and Zinc Alloy Coated Steel Sheet, Virtual Conference

Chakraborty, A., Ghosh, R., Sudan, M., & Mondal, A. (2022). Improvement in hot dip galvanized coating microstructure and properties by pre-metallic deposition on steel surface: A comprehensive review. *Surface and Coatings Technology*, 449, 128972. <https://doi.org/10.1016/j.surfcoat.2022.128972>

Chen, L., Yi, D., Wang, B., Liu, H., & Wu, C. (2016). Mechanism of the early stages of oxidation of WC-Co cemented carbides. *Corrosion Science*, 103, 75-87. <https://doi.org/10.1016/j.corsci.2015.11.007>

Chen, W., Zhang, D., & Ai, X. (2017). Effect of load on the friction and wear characteristics of Si₃N₄-hBN ceramic composites sliding against steels. *Ceramics International*, 43(5), 4379-4389. <https://doi.org/10.1016/j.ceramint.2016.12.084>

Chen, X., Li, C., Bai, X., Wang, H., Xu, S., & Song, S. (2019). Microstructure, Mechanical Properties, Abrasive Wear, and Corrosion Behavior in Molten Zinc of Boride-Based Coatings in Situ Synthesized by an HVOF Spraying Process. *Coatings*, 9(10), 665. <https://doi.org/10.3390/coatings9100665>

Childs, P. R. N. (2019). 5 - Journal bearings. In P. R. N. Childs (Ed.), *Mechanical Design Engineering Handbook (Second Edition)* (pp. 167-230). Butterworth-Heinemann. <https://doi.org/10.1016/B978-0-08-102367-9.00005-6>

Chinn, R. E., & Chinn, R. (2002). *Ceramography: Preparation and Analysis of Ceramic Microstructures*. ASM International.

Dallin, G. W. (2015). *Galvanizing – 2015*. Retrieved 26 January 2025 from <https://www.galvinfo.com/wp-content/uploads/sites/8/2017/12/Galvanizing-2015.pdf>

Davis, J. R. (1994). *Stainless Steels*. ASM International.

Dhande, D. Y., & Pande, D. W. (2018). Multiphase flow analysis of hydrodynamic journal bearing using CFD coupled Fluid Structure Interaction considering cavitation. *Journal of King Saud University - Engineering Sciences*, 30(4), 345-354. <https://doi.org/10.1016/j.jksues.2016.09.001>

Dong, Y., Yan, D., He, J., Zhang, J., & Li, X. (2006). Degradation behaviour of ZrO₂-Ni/Al gradient coatings in molten Zn. *Surface and Coatings Technology*, 201(6), 2455-2459. <https://doi.org/10.1016/j.surfcoat.2006.04.029>

Eiceman, G. A., Karpas, Z., & Hill, H. H. (2013). *Ion Mobility Spectrometry, Third Edition*. Taylor & Francis.

El-Amir, A. A. M., El-Maddah, A. A., Ewais, E. M. M., El-Sheikh, S. M., Bayoumi, I. M. I., & Ahmed, Y. M. Z. (2021). Sialon from synthesis to applications: an overview. *Journal of Asian Ceramic Societies*, 9(4), 1390-1418. <https://doi.org/10.1080/21870764.2021.1987613>

El-Eskandarany, M. S. (2020). 12 - Utilization of ball-milled powders for surface protective coating. In M. S. El-Eskandarany (Ed.), *Mechanical Alloying (Third Edition)* (pp. 309-334). William Andrew Publishing. <https://doi.org/10.1016/B978-0-12-818180-5.00012-1>

Escott, L. J., Penney, D. J., Das, A., & Thomas, D. (2021). Effects of Heat Treatments on the Morphology and Mechanical Properties of a CoCrW Alloy for Hot Dip Galvanising Applications. 12th International Conference on Zinc and Zinc Alloy Coated Steel Sheet, Virtual Conference.

Faulkner, R. (2020). *Material Selection and Mechanical Design of Submerged Galvanising Bath Journal Bearings*. EngD Thesis. Cardiff University, Cardiff, UK

Faulkner, R., Evans, S., Clarke, A., Penney, D., & Collins, N. (2017). Static Immersion Testing of Laser Clad Coatings for Journal Bearing Applications. 11th International Conference on Zinc and Zinc Alloy Coated Steel Sheet, Tokyo, Japan.

Faulkner, R., Penney, D., & Bright, M. (2021). *Offline Simulation of Galvanising Bath Journal Bearings as a Cost Effective Solution to Improve Line Performance and Mitigate Risk*. 12th International Conference on Zinc & Zinc Alloy Coated Steel Sheet, Virtual Conference.

Goodwin, F., Chang, K., & Sikka, V. (2002). Development of a New Generation of Bath Hardware Materials. Galvanizers Association 94th Meeting, Dearborn, MI, USA.

Gossuin, T., & Moreas, G. (2021). Cleanliness Measurement by Innovative Libs Method. 12th International Conference on Zinc and Zinc Alloy Coated Steel Sheet, Virtual Conference.

Gražulis, S., Chateigner, D., Downs, R., Yokochi, A., Quirós, M., Lutterotti, L., Manakova, E., Butkus, J., Moeck, P., & Le Bail, A. (2009). Crystallography Open Database - An Open-Access

Collection of Crystal Structures. *Journal of applied crystallography*, 42, 726-729. <https://doi.org/10.1107/S0021889809016690>

Griffin, R., Hooper, K., Charbonneau, C., & Baker, J. (2021). Comparative Study of Radiative Heating Techniques for Fast Processing of Functional Coatings for Sustainable Energy Applications. *Johnson Matthey Technology Review*, 66. <https://doi.org/10.1595/205651322X16260797478755>

Gulbransen, E. A., & Andrew, K. F. (1951). The Kinetics of the Oxidation of Cobalt. *Journal of The Electrochemical Society*, 98(6), 241. <https://doi.org/10.1149/1.2778139>

Hayashi, H., Saitou, T., Maruyama, N., Inaba, H., Kawamura, K., & Mori, M. (2005). Thermal expansion coefficient of yttria stabilized zirconia for various yttria contents. *Solid State Ionics*, 176(5), 613-619. <https://doi.org/10.1016/j.ssi.2004.08.021>

Henry, J., Chen, X., Law, R. V., & Hill, R. G. (2018). The investigation of the crystalline phases development in Macor® glass-ceramic. *Journal of the European Ceramic Society*, 38(1), 245-251. <https://doi.org/10.1016/j.jeurceramsoc.2017.07.030>

Herrmann, M., Schulz, I., Bales, A., Sempff, K., & Hoehn, S. (2008). "Snow flake" structures in silicon nitride ceramics – Reasons for large scale optical inhomogeneities. *Journal of the European Ceramic Society*, 28(5), 1049-1056. <https://doi.org/10.1016/j.jeurceramsoc.2007.09.022>

Huang, W., Qiu, H., Zhang, Y., Zhang, F., Gao, L., Omran, M., & Chen, G. (2023). Microstructure and phase transformation behavior of Al₂O₃–ZrO₂ under microwave sintering. *Ceramics International*, 49(3), 4855-4862. <https://doi.org/10.1016/j.ceramint.2022.09.376>

Huang, W., Zhang, Y., Lu, J., Gao, L., Zhang, F., Chen, J., Omran, M., & Chen, G. (2023). Effect of sintering time on the microstructure and stability of Al₂O₃–ZrO₂ composite powders under microwave-assisted sintering. *Ceramics International*, 49(6), 8993-8999. <https://doi.org/10.1016/j.ceramint.2022.11.054>

Hutchings, I., & Shipway, P. (2017). *Tribology : Friction and Wear of Engineering Materials*. Elsevier Science & Technology.

Ilinca, F., Ajersch, F., Baril, C., & Goodwin, F. E. (2007). Numerical simulation of the galvanizing process during GA to GI transition. *International Journal for Numerical Methods in Fluids*, 53(10), 1629-1646. <https://doi.org/10.1002/fld.1376>

Jarosinski, W., Quets, J., Wang, D., Belov, V., & Klyman, A. S. (2013). *Thermal Spray Coated Rolls for Molten Metal Baths* (US Patent No. US 8,507,105 B2).

Kara, F., Küçük, Y., Özbek, O., Özbek, N. A., Gök, M. S., Altaş, E., & Uygur, İ. (2023). Effect of cryogenic treatment on wear behavior of Slei pner cold work tool steel. *Tribology International*, 180, 108301. <https://doi.org/10.1016/j.triboint.2023.108301>

Kaunisto, K., Lagerbom, J., Honkanen, M., Varis, T., Lambai, A., Mohanty, G., Levänen, E., Kivikytö-Reponen, P., & Frankberg, E. (2023). Evolution of alumina phase structure in thermal plasma processing. *Ceramics International*, 49(13), 21346-21354. <https://doi.org/10.1016/j.ceramint.2023.03.263>

- Khaliq, A., Alghamdi, A. S., Ramadan, M., Subhani, T., Rajhi, W., Haider, W., & Hasan, M. M. (2022). Intermetallic Compounds Formation during 316L Stainless Steel Reaction with Al-Zn-Si Coating Alloy. *Crystals*, 12(5), 735. <https://doi.org/10.3390/cryst12050735>
- Kuklik, V., & Kudlacek, J. (2016). *Hot-Dip Galvanizing of Steel Structures*. Elsevier Science.
- Kuperus, M. (2018). *The delamination process of the dross build-up structure on submerged hardware in Zn-Al and Zn-Mg-Al baths: An empirical study*. Master's Thesis. Delft University of Technology, Delft, Netherlands.
- Łatka, L., Pawłowski, L., Winnicki, M., Sokołowski, P., Małachowska, A., & Kozerski, S. (2020). Review of Functionally Graded Thermal Sprayed Coatings. *Applied Sciences*, 10(15), 5153. <https://doi.org/10.3390/app10155153>
- Lee, S. M., Lee, S. K., Paik, D.-J., & Park, J. H. (2017). Effect of Initial Iron Content in a Zinc Bath on the Dissolution Rate of Iron During a Hot Dip Galvanizing Process. *Metallurgical and Materials Transactions A*, 48(4), 1788-1796. <https://doi.org/10.1007/s11661-017-3966-4>
- Li, X., Gao, Y., Pan, W., Zhong, Z., Song, L., Chen, W., & Yang, Q. (2015). Effect of hBN content on the friction and wear characteristics of B4C-hBN ceramic composites under dry sliding condition. *Ceramics International*, 41(3, Part A), 3918-3926. <https://doi.org/10.1016/j.ceramint.2014.11.074>
- Liu, J., Suryanarayana, C., Ghosh, D., Subhash, G., & An, L. (2013). Synthesis of Mg-Al₂O₃ nanocomposites by mechanical alloying. *Journal of Alloys and Compounds*, 563, 165-170. <https://doi.org/10.1016/j.jallcom.2013.01.113>
- Liu, X., Barbero, E., Xu, J., Burris, M., Chang, K.-M., & Sikka, V. (2005). Liquid metal corrosion of 316L, Fe₃Al, and FeCrSi in molten Zn-Al baths. *Metallurgical and Materials Transactions A*, 36(8), 2049-2058. <https://doi.org/10.1007/s11661-005-0325-7>
- Liu, X., Zhao, X., & Yang, F. (2020). Room-Temperature and High-Temperature Wear Behaviors of As-Sprayed and Annealed Cr₃C₂-25NiCr Coatings Prepared by High Velocity Air-Fuel Spraying. *Coatings*, 10(11), 1090. <https://doi.org/10.3390/coatings10111090>
- Lv, H. P., Wang, J., Yan, Y. G., An, Q. Z., Nie, P. L., & Sun, B. D. (2010). Characterisation of detonation sprayed Mo-Co-Cr-B alloy coatings. *Materials Science and Technology*, 26(8), 950-955. <https://doi.org/10.1179/026708309X12459430509373>
- Ma, R. N., Cao, X., Du, A., Herd, A., & Dai, C. (2014). Metal/Ceramic Laminar Composite Immersion Heater for Heating Hot Dip Galvanizing Zinc Kettle. *Applied Mechanics and Materials*, 665, 90-94. <https://doi.org/10.4028/www.scientific.net/AMM.665.90>
- Ma, R. N., Du, A., Wu, J. J., & Cao, X. M. (2010). Corrosive Wear Behavior of Several Materials Coupled with Si₃N₄ in the Molten Zinc. *Applied Mechanics and Materials*, 34-35, 1804. <https://doi.org/10.4028/www.scientific.net/AMM.34-35.1804>
- Maaß, P., Peißker, P., & Ahner, C. (2011). *Handbook of Hot-dip Galvanization*. Wiley.

- Mabbett, I., Elvins, J., Gowenlock, C., Glover, C., Jones, P., Williams, G., & Worsley, D. (2014). Addition of carbon black NIR absorber to galvanised steel primer systems: Influence on NIR cure of polyester melamine topcoats and corrosion protection characteristics. *Progress in Organic Coatings*, 77(2), 494-501. <https://doi.org/10.1016/j.porgcoat.2013.11.015>
- Mandal, H. (1999). New developments in α -SiAlON ceramics. *Journal of the European Ceramic Society*, 19(13), 2349-2357. [https://doi.org/10.1016/S0955-2219\(99\)00111-9](https://doi.org/10.1016/S0955-2219(99)00111-9)
- Marder, A., & Goodwin, F. (2023). *The Metallurgy of Zinc Coated Steels*. Elsevier Science. <https://doi.org/10.1016/C2020-0-04502-0>
- Marder, A. R. (2000). The metallurgy of zinc-coated steel. *Progress in Materials Science*, 45(3), 191-271. [https://doi.org/10.1016/S0079-6425\(98\)00006-1](https://doi.org/10.1016/S0079-6425(98)00006-1)
- Matthews, S. J., & James, B. (2010). Review of Thermal Spray Coating Applications in the Steel Industry: Part 2—Zinc Pot Hardware in the Continuous Galvanizing Line. *Journal of Thermal Spray Technology*, 19, 1277-1286. <https://doi.org/10.1007/s11666-010-9519-7>
- McDermid, J., Baril, É., & Goodwin, F. (2004). Galvanizing Bath Management During Galvanize to Galvanneal and Galvanneal to Galvanize Product Transitions. 6th International Conference on Zinc and Zinc Alloy Coated Steel Sheet, Chicago, IL, USA.
- McDermid, J. R., Kaye, M. H., & Thompson, W. T. (2007). Fe Solubility in the Zn-Rich Corner of the Zn-Al-Fe System for Use in Continuous Galvanizing and Galvannealing. *Metallurgical and Materials Transactions B*, 38(2), 215-230. <https://doi.org/10.1007/s11663-007-9028-3>
- Menezes, P. L., Nosonovsky, M., Ingole, S. P., Kailas, S. V., & Lovell, M. R. (2013). *Tribology for Scientists and Engineers: From Basics to Advanced Concepts*. Springer New York.
- Messier, D. R., Riley, F. L., & Brook, R. J. (1978). The α/β silicon nitride phase transformation. *Journal of Materials Science*, 13(6), 1199-1205. <https://doi.org/10.1007/BF00544725>
- Mizuno, H., & Kitamura, J. (2007). MoB/CoCr Cermet Coatings by HVOF Spraying against Erosion by Molten Al-Zn Alloy. *Journal of Thermal Spray Technology*, 16(3), 404-413. <https://doi.org/10.1007/s11666-007-9046-3>
- Mizuno, H., & Kitamura, J. (2007). *Thermal Spray Coating and Thermal Spray Powder* (United States Patent No. US7862911B2).
- Nag, A., Bhadu, M. K., Bijalwan, P. K., & Pathak, A. S. (2021). Investigation of selected HVOF and plasma sprayed coatings for sustained performance in molten zinc. *Corrosion Science*, 180, 109177. <https://doi.org/10.1016/j.corsci.2020.109177>
- Neale, M. J. (2013). *Bearings: A Tribology Handbook*. Elsevier Science.
- Niebuhr, D. (2007). Cavitation erosion behavior of ceramics in aqueous solutions. *Wear*, 263(1), 295-300. <https://doi.org/10.1016/j.wear.2006.12.040>
- Noda, N.-A., Yamada, M., Sano, Y., Sugiyama, S., & Kobayashi, S. (2008). Thermal stress for all-ceramics rolls used in molten metal to produce stable high quality galvanized steel sheet.

Engineering Failure Analysis, 15(4), 261-274.
<https://doi.org/10.1016/j.engfailanal.2007.03.003>

Nouri, A., & Sola, A. (2019). Powder morphology in thermal spraying. *Journal of Advanced Manufacturing and Processing*, 1(3), e10020. <https://doi.org/10.1002/amp2.10020>

Okamoto, H. (2007). Fe-Zn (Iron-Zinc). *Journal of Phase Equilibria and Diffusion*, 28(3), 317-318. <https://doi.org/10.1007/s11669-007-9051-8>

Özbek, N. A., & Özbek, O. (2022). Effect of cryogenic treatment holding time on mechanical and microstructural properties of Sverker 21 steel. *Materials Testing*, 64(12), 1809-1817. <https://doi.org/10.1515/mt-2022-0207>

Pagilla, P. R., Garimella, S. S., Dreinhoefer, L. H., & King, E. O. (2001). Dynamics and control of accumulators in continuous strip processing lines. *IEEE Transactions on Industry Applications*, 37(3), 934-940. <https://doi.org/10.1109/28.924778>

Park, T. J., Choi, Y. S., & Kim, Y. H. (2021). Influence of Surface Roughness of Full Hard Steel on Spangle of Galvanized Steel and Actual Application Results. 12th International Conference on Zinc and Zinc Alloy Coated Steel Sheet, Virtual Conference.

Parthasarathy, V., Kang, S. J., Krishnaswamy, A., Barbero, E., Chang, K., Irwin, C., & Goodwin, F. (2004). Long-time Performance of Pot Hardware in Continuous Galvanising Line. 6th International Conference on Zinc and Zinc Alloy Coated Steel Sheet, Chicago, IL, USA.

Pearcey, O., Brown, H., Marincic, I., & Tham, J. (2021). The Evolution of Coating Control Systems as the Need for New Coated Products Expands. *BHM Berg- und Hüttenmännische Monatshefte*, 166(11), 525-534. <https://doi.org/10.1007/s00501-021-01161-8>

Popp, M., & Sternagel, R. (1999). Hybrid ceramic and all ceramic anti friction bearings. 8th European Symposium, Toulouse, France.

Rachamalla, V. V. (2006). *A model of stabilizer roll bearing for a continuous hot-dip galvanizing line*. Master's Thesis. West Virginia University, Morgantown, WV, USA.

Rahnejat, H. (2010). *Tribology and Dynamics of Engine and Powertrain: Fundamentals, Applications and Future Trends*. Woodhead Publishing.

Rai, V. K., Srivastava, R., Nath, S. K., & Ray, S. (1999). Wear in cast titanium carbide reinforced ferrous composites under dry sliding. *Wear*, 231(2), 265-271. [https://doi.org/10.1016/S0043-1648\(99\)00127-1](https://doi.org/10.1016/S0043-1648(99)00127-1)

Reid, R. (2018). *Inorganic Chemistry*. ED-Tech Press.

Reusch, F., Umwelttechnik, D., Rudolph, S., & Nitride, B. (2015). Use of Boron Nitride Coatings with Aluminum Casting Technology. Proceedings of the 8th International Aluminium Extrusion Technology Seminar, Orlando, USA

Roy, S., Zhang, X., Puthirath, A. B., Meiyazhagan, A., Bhattacharyya, S., Rahman, M. M., Babu, G., Susarla, S., Saju, S. K., Tran, M. K., Sassi, L. M., Saadi, M. A. S. R., Lai, J., Sahin, O., Sajadi, S. M., Dharmarajan, B., Salpekar, D., Chakingal, N., Baburaj, A., . . . Ajayan, P. M. (2021).

Structure, Properties and Applications of Two-Dimensional Hexagonal Boron Nitride. *Advanced Materials*, 33(44), 2101589. <https://doi.org/10.1002/adma.202101589>

Saravanan, P., & Srikanth, S. (2018). Surface Defects and their Control in Hot Dip Galvanized and Galvannealed Sheets. *International Journal of Advanced Research in Chemical Science*, 5, 11-23.

Seong, B. G., Hwang, S. Y., Kim, M. C., & Kim, K. Y. (2001). Reaction of WC-Co coating with molten zinc in a zinc pot of a continuous galvanizing line. *Surface and Coatings Technology*, 138(1), 101-110. [https://doi.org/10.1016/S0257-8972\(00\)01136-1](https://doi.org/10.1016/S0257-8972(00)01136-1)

Shahien, M. (2018). Reactive Plasma Spray: A Method for Nitride Coatings Deposition in Thermal Spray. In (pp. 299-332). <https://doi.org/10.4018/978-1-5225-4194-3.ch012>

Shi, Y., Tong, J., Zheng, Q., Rao, S., Jin, H., & Rao, S. (2018). Analysis About the Failure Mechanism of the Sleeves in Sink Roll System. *Journal of Failure Analysis and Prevention*, 18(1), 183-188. <https://doi.org/10.1007/s11668-018-0395-7>

Shinozaki, N., Suenaga, M., & Mukai, K. (1999). Wettability of Zirconia and Alumina Ceramics by Molten Zinc. *Materials Transactions, JIM*, 40(1), 52-56. <https://doi.org/10.2320/matertrans1989.40.52>

Stachowiak, G., & Batchelor, A. W. (2004). *Experimental Methods in Tribology*. Elsevier Science.

Stachowiak, G., & Batchelor, A. W. (2013). *Engineering Tribology*. Elsevier Science & Technology.

Stavros, J. S. (1999). *Boron Nitride-Silicate Sealant* (United States Patent No. 5,869,144).

Subramanian, K., Murugesan, S., Mohan, D. G., & Tomków, J. (2021). Study on Dry Sliding Wear and Friction Behaviour of Al7068/Si₃N₄/BN Hybrid Composites. *Materials*, 14(21), 6560. <https://doi.org/10.3390/ma14216560>

Tang, N.-Y. (2000). Determination of liquid-phase boundaries in Zn-Fe-Mx systems. *Journal of Phase Equilibria*, 21(1), 70-77. <https://doi.org/10.1361/105497100770340444>

Tang, N. Y., Daniel, L., & Zhang, K. (2010). Performance of Submerged Hardware in Continuous Galvanizing. *Corrosion Science and Technology* 9(3), 116-121.

Tang, N. Y., & Goodwin, F. (2001). *A Study of Defects in Galvanized Coatings*. 5th International Conference on Zinc and Zinc Alloy Coated Steel Sheet, Brussel, Belgium

Tani, K., Tomita, T., Kobayashi, Y., Takatani, Y., & Harada, Y. (1994). Durability of Sprayed WC/Co Coatings in Al-added Zinc Bath. *ISIJ International*, 34(10), 822-828. <https://doi.org/10.2355/isijinternational.34.822>

Tobół, D. (2019). Impact of Mechanical Processes as a Pre-Sulphonitriding Treatment on Tribology Properties of Selected P/M Tool Steels. *Materials*, 12, 3431. <https://doi.org/10.3390/ma12203431>

University of Cambridge. (2022). *Dissemination of IT for the Promotion of Materials*

Science (DoITPoMS). Retrieved 19 March 2024 from https://www.doitpoms.ac.uk/tlplib/ellingham_diagrams/ellingham.php

Wang, L., Zhou, Y., Chen, G., Xu, P., & Rao, S. (2015). Analysis on dominant influencing factors of on-line life cycle in sink roll system and effective improved methods. *Engineering Failure Analysis*, 58, 8-18. <https://doi.org/10.1016/j.engfailanal.2015.08.004>

Wang, Q., Zhang, J. W., Zhang, L., Liu, H. J., & Zeng, C. L. (2019). Stability investigation of electrodeposited zirconium diboride ceramic coatings in molten zinc. *Materials and Corrosion*, 70(3), 492-502. <https://doi.org/10.1002/maco.201810401>

Wang, Y., Wan, W., Mao, J., Tian, L., & Li, R. (2020). Microstructure and Wear Behavior of Plasma-Sprayed TiO₂-SiAlON Ceramic Coating. *Coatings*, 10(12), 1268. <https://doi.org/10.3390/coatings10121268>

Watson, T., Mabbett, I., Wang, H., Peter, L., & Worsley, D. (2011). Ultrafast near infrared sintering of TiO₂ layers on metal substrates for dye-sensitized solar cells. *Progress in Photovoltaics: Research and Applications*, 19(4), 482-486. <https://doi.org/10.1002/pip.1041>

Weston, N., Thomasa, B., & Jacksona, M. (2020). Exploitation of field assisted sintering technology (FAST) for titanium alloys. *MATEC Web of Conferences*, 321, 02006. <https://doi.org/10.1051/mateconf/202032102006>

Williams, J. (2023). *The development of surface treatments on galvanised steel products for the automotive industry utilising a chemcoater*. EngD Thesis. Swansea University, Swansea, UK

Xiao, Y., Shi, W., Luo, J., & Liao, Y. (2014). The tribological performance of TiN, WC/C and DLC coatings measured by the four-ball test. *Ceramics International*, 40(5), 6919-6925. <https://doi.org/10.1016/j.ceramint.2013.12.015>

Xibao, W. (2003). Corrosion of Co-Cr-W alloy in liquid zinc. *Metallurgical and Materials Transactions B*, 34(6), 881-886. <https://doi.org/10.1007/s11663-003-0094-x>

Yanar, H., Purcek, G., Demirtas, M., & Ayar, H. H. (2022). Effect of hexagonal boron nitride (h-BN) addition on friction behavior of low-steel composite brake pad material for railway applications. *Tribology International*, 165, 107274. <https://doi.org/10.1016/j.triboint.2021.107274>

Ye, F., Hoffmann, M. J., Holzer, S., Zhou, Y., & Iwasa, M. (2003). Effect of the Amount of Additives and Post-Heat Treatment on the Microstructure and Mechanical Properties of Yttrium- α -Sialon Ceramics. *Journal of the American Ceramic Society*, 86(12), 2136-2142. <https://doi.org/10.1111/j.1151-2916.2003.tb03621.x>

Ye, F., Hou, Z., Zhang, H., Liu, L., & Zhou, Y. (2010). Spark plasma sintering of cBN/ β -SiAlON composites. *Materials Science and Engineering: A*, 527(18), 4723-4726. <https://doi.org/10.1016/j.msea.2010.04.034>

- Yin, L., Zhao, K., Ding, Y., Wang, Y., He, Z., & Huang, S. (2022). Effect of hBN addition on the fabrication, mechanical and tribological properties of Sialon materials. *Ceramics International*, 48(6), 7715-7722. <https://doi.org/10.1016/j.ceramint.2021.11.319>
- Yu, Z., Chen, M., Chen, K., Xie, D., Zhu, S., & Wang, F. (2019). Corrosion of enamel with and without CaF₂ in molten aluminum at 750 °C. *Corrosion Science*, 148, 228-236. <https://doi.org/10.1016/j.corsci.2018.12.016>
- Yu, Z., Chen, M., Li, F., Zhu, S., & Wang, F. (2020). Synergistic effect of corrosion and wear of the 316 stainless steel in molten zinc alloy at 460 °C. *Corrosion Science*, 165, 108411. <https://doi.org/10.1016/j.corsci.2019.108411>
- Yu, Z., Chen, M., Wang, J., Li, F., Zhu, S., & Wang, F. (2021). Enamel coating for protection of the 316 stainless steel against tribo-corrosion in molten zinc alloy at 460 °C. *Journal of Materials Science & Technology*, 65, 126-136. <https://doi.org/10.1016/j.jmst.2020.04.079>
- Zhang, C. (2014). 17 - Understanding the wear and tribological properties of ceramic matrix composites. In I. M. Low (Ed.), *Advances in Ceramic Matrix Composites (Second Edition)* (pp. 401-428). Woodhead Publishing. <https://doi.org/10.1016/B978-0-08-102166-8.00017-7>
- Zhang, H. (2016). 2 - Surface characterization techniques for polyurethane biomaterials. In S. L. Cooper & J. Guan (Eds.), *Advances in Polyurethane Biomaterials* (pp. 23-73). Woodhead Publishing. <https://doi.org/10.1016/B978-0-08-100614-6.00002-0>
- Zhang, J., Deng, C., Song, J., Deng, C., Liu, M., & Zhou, K. (2013). MoB–CoCr as alternatives to WC–12Co for stainless steel protective coating and its corrosion behavior in molten zinc. *Surface and Coatings Technology*, 235, 811-818. <https://doi.org/10.1016/j.surfcoat.2013.08.052>
- Zhang, J., Liu, Y., Babamiri, B. B., Zhou, Y., Dargusch, M., Hazeli, K., & Zhang, M.-X. (2022). Enhancing specific energy absorption of additively manufactured titanium lattice structures through simultaneous manipulation of architecture and constituent material. *Additive Manufacturing*, 55, 102887. <https://doi.org/10.1016/j.addma.2022.102887>
- Zhang, K. (2003). Wear of cobalt-based alloys sliding in molten zinc. *Wear*, 255(1), 545-555. [https://doi.org/10.1016/S0043-1648\(03\)00050-4](https://doi.org/10.1016/S0043-1648(03)00050-4)
- Zhang, K. (2005). On the Selection of Materials for Improved Performance of Pot Bearings. AISTech - Iron and Steel Technology Conference Proceedings, Charlotte, NC, USA.
- Zhang, K., Battiston, L., & Goodwin, F. (2001). Friction and Wear Characteristics of Materials in Molten Zinc. 5th International Conference on Zinc and Zinc Alloy Coated Steel Sheet, Brussels, Belgium.
- Zhang, K., & Tang, N.-Y. (2004). Reactions of Co based and Fe based superalloys with a molten Zn – Al alloy. *Materials Science and Technology*, 20(6), 739-746. <https://doi.org/10.1179/026708304225017300>
- Zhang, K., Tang, N.-Y., Goodwin, F. E., & Sexton, S. (2007). Reaction of 316L stainless steel with a galvanizing bath. *Journal of Materials Science*, 42(23), 9736-9745. <https://doi.org/10.1007/s10853-007-1978-y>

Zhang, K., & Tang, N. Y. (2003). On the wear of a cobalt-based superalloy in zinc baths. *Metallurgical and Materials Transactions A*, 34(10), 2387-2396. <https://doi.org/10.1007/s11661-003-0301-z>

Zhang, K., Tang, N. Y., & Goodwin, F. (2004). Research and development of pot bearings in continuous galvanizing. 6th International Conference on Zinc and Zinc Alloy Coated Steel Sheet, Chicago, USA.

Zhao, Y., Wang, Y., Yu, Z., Planche, M.-P., Peyraut, F., Liao, H., Lasalle, A., Allimant, A., & Montavon, G. (2018). Microstructural, mechanical and tribological properties of suspension plasma sprayed YSZ/h-BN composite coating. *Journal of the European Ceramic Society*, 38(13), 4512-4522. <https://doi.org/10.1016/j.jeurceramsoc.2018.06.007>

Zhou, Y., Yang, L., & Huang, Y. (2013). *Micro- and Macromechanical Properties of Materials*. Taylor & Francis.

Zhu, X., & Sakka, Y. (2008). Textured silicon nitride: processing and anisotropic properties. *Science and Technology of Advanced Materials*, 9(3), 033001. <https://doi.org/10.1088/1468-6996/9/3/033001>